Optical Magnetometry and Micromagnetic Simulations of Three-Dimensional Magnetic Nanostructures

Submitted by Matthew Hunt, to Cardiff University as a thesis for the degree of Doctor of Philosophy in Physics, September 2017

Abstract

This thesis describes the magnetic properties of three-dimensional (3D) magnetic nanostructures fabricated using two-photon lithography (TPL) and measured by the magneto-optical Kerr effect (MOKE), with supporting micromagnetic simulations.

Simulations were performed on individual cylindrical nanowires composed of permalloy (Py) with diameter 50nm and length 1.5µm. Hysteresis loops were taken where the external field was applied at angles of 0^o, 35.25^o, 54.75^o, 70.5^o and 90^o with respect to the wire axis. From investigating the visualisations of the magnetisation it was observed that Bloch point domain walls were propagated down the wire during the switching process. The resulting hysteresis loops were compared with those generated from simulations performed on tetrapod structures in the principle directions [100], [110] and [111]. It was found that the [100] and [110] loops were reproducible from the individual wire loops where the field angles matched. However, the [111] loop could not be reproduced due to domain wall propagation through the vertex.

Angled 3D nanowires and 3D magnetic structures in tetrapod geometry made of cobalt (Co) were fabricated using two-photon lithography and electrodeposition. From SEM imaging, the nanowires in both structures were found to have an elliptical profile with feature sizes of 750±40nm lateral width, 910±30nm length perpendicular to the wire axis and approximately 8µm length for the individual nanowires, and feature sizes of 610±55nm lateral width, 900±75nm length perpendicular to the wire axis and approximately 6.5µm length for the nanowires comprising the tetrapods. MOKE measurements were performed on 300µmx300µm arrays of both, in the polar and longitudinal geometries. It was found that the polar MOKE loops were comparable between the two structures, whereas the longitudinal MOKE loops for tetrapods showcased unexpected transition events at higher fields and could not be reproduced from the measurements of the single wires.

Declaration and Statements

DECLARATION

This work has not been submitted in substance for any other degree or award at this or any other university or place of learning, nor is being submitted concurrently in candidature for any degree or other award.

Signed M.C. Hunt (candidate) Date 28/09/17

STATEMENT 1

This thesis is being submitted in partial fulfilment of the requirements for the degree of PhD.

Signed M.C. Hunt (candidate) Date 28/09/17

STATEMENT 2

This thesis is the result of my own independent work/investigation, except where otherwise stated, and the thesis has not been edited by a third party beyond what is permitted by Cardiff University's Policy on the Use of Third Party Editors by Research Degree Students. Other sources are acknowledged by explicit references. The views expressed are my own.

Signed M.C. Hunt (candidate) Date 28/09/17

STATEMENT 3

I hereby give consent for my thesis, if accepted, to be available online in the University's Open Access repository and for inter-library loan, and for the title and summary to be made available to outside organisations.

Signed M.O. Hunt (candidate) Date 28/09/17

STATEMENT 4: PREVIOUSLY APPROVED BAR ON ACCESS

I hereby give consent for my thesis, if accepted, to be available online in the University's Open Access repository and for inter-library loans **after expiry of a bar on access previously approved by the Academic Standards & Quality Committee.**

Signed M.O. Hunt (candidate) Date 28/09/17

Publications

"Two-photon Lithography for 3D Magnetic Nanostructure Fabrication", Williams, G., Hunt, M., Boehm, B. et al. Nano Res. (2017). https://doi.org/10.1007/s12274-017-1694-0

Two further publications in progress, concerning:

Detailed consideration of switching in tetrapods.

Bloch point domain wall propagation in tetrapods.

Significant Contributions

I would like to give special thanks to Gwilym Williams who performed the fabrication work necessary to produce the structures measured in Chapter 5.

I would also like to thank Dr Rolf Allenspach's group at IBM, Zurich for performing the spin-polarised SEM measurements and statistical analysis presented in Chapter 5.

The simulations presented in Chapter 4 were run on the Raven supercomputing cluster at ARCCA, Cardiff University.

Acknowledgements

I have always struggled with the effort to produce any kind of written report; as such this thesis owes its existence in no small part to the multitude of people who have helped and supported me throughout the last four years.

Firstly I would like to thank my primary supervisor Sam Ladak, whose unending supply of enthusiasm for the subject area helped motivate me throughout the years and who took me under his wing after a number of setbacks in my initial two years. Without his support, advice and dedication I would have not been able to make it through my PhD, particularly during the writing stages. I also wish to thank my secondary supervisors Sean Giblin and Dan Read for their contributions, advice and support in my endeavours.

Next I wish to thank my fellow students and colleagues in the lab: Gwilym (Ifan) Williams (good luck wherever you've ended up!), and more recently Andrew May, Arjen van den Berg and Alaa Hejazi for their comradery, help and continuing support. I would like to thank

all the ‘coffee regulars’ and PhD students/Postdocs who have provided many fun times and stories. In particular I would like to thank Adam Beachy who shared demonstrating duties with me; keep on drawing and painting and good luck with the postdoc! I would also like to say my thanks to all the workshop, office and other academic staff in the university Physics department for always being on hand and willing to help.

Outside of the university I must give my undying gratitude to my good friends Chris Noble and Zachary Wilmot for sticking with me throughout it all, enduring my techno-babble, and also for helping create characters, stories and worlds to escape to on a regular basis. See you in the skies my friends!

Mum, Dad, you’ve both been there for me during my darkest days and greatest triumphs, and through it all you have given so much to support me. Rhi, you will always be not just my sibling but also my best friend. Thank you all for being you and being there for me. And thank you for believing in me when I could not.

"All right, here's the deal. We're all stuck in a time loop of some kind. However Teal'c and I seem to be the only ones who realize it. Now there's this alien device on six thirty nine. It shoots a beam at the Stargate which…err subspace something…what?"

"Accesses the subspace field the Stargate is capable of generating. It is powered by ionization." (TEAL'C)

"In the atmosphere, right. Which is caused by…AH! I know this one…" (He thinks about it)

"Magnets!"

- Jack O'Neill, Stargate SG1, Window of Opportunity

Contents

List of Symbols

A	Area normal (vector)
A	Material exchange stiffness constant
A_E	Einstein coefficient of spontaneous emission
B, B	Magnetic flux density
C, C_0	Constant
C_{ij}	Coulomb interaction term
c	Speed of light ($3x10^8 ms^{-1}$)
d, d_x	Displacement (vector, components)
$\boldsymbol{D}$	Tensor of demagnetisation factors
D	Demagnetisation factor
d_{Vox}	Voxel diameter
E, $\mathbb{E}$, $\mathbb{E}_x$	Electric field (vector, magnitude, component)
E	Energy
E_F	Fermi energy
E_{MC}	Magnetocrystalline anisotropy energy density
E_{MS}	Magnetostatic energy density
E_{SO}	Spin-orbit energy
E_{Zeeman}	Zeeman energy density
e	Electron charge ($1.6x10^{-19}C$)
F	Force
$F(x)$	Function
f	Repetition rate of laser source
f_L	Laser noise fraction
g	g-factor
H	Magnetic field strength
$\mathbf{H_D}$	Demagnetising field
$\mathbf{H}_{eff}$	Effective magnetic field strength
$\mathbf{H}_{Ext}$	External magnetic field
H_C	Coercive field
H_W	Walker field

$\mathcal{H}$	Hamiltonian
h, $\hbar$	Planck's constant ($6.6\times10^{-34}m^2kgs^{-1}$), Planck's constant/2π
I	Intensity of incident light
I_0	Intensity at centre of laser focus
i	Square-root of -1
$\mathbf{i_c}$, i_c	Current (vector, magnitude)
Δi	Current range produced by full MOKE signal
i_D	Dark noise
i_L	Laser noise
i_S	Shot noise
J, J	Total angular momentum (vector, magnitude)
$\mathcal{J}_{ij}$	Exchange energy term
K	Anisotropy constant
K_{un}	Nth order magnetocrystalline anisotropy constants
k, k	Wave vector (vector, magnitude)
k_1, k_2, k_3	Rate constants
k_B	Boltzmann constant ($1.38\times10^{-23}m^2kgs^{-2}K^{-1}$)
k_F	Fermi wavenumber
L, L, L_z	Angular momentum (vector, magnitude, z-component)
l	Angular momentum quantum number
$\mathbf{l_d}$	Dipole length (vector)
M, M, m	Magnetisation
M^G	Photoinitiator ground state concentration
M^*	Photoinitiator excited state concentration
M_R	Remanent magnetisation
M_s	Saturation magnetisation
M_{th}	Threshold photoinitiator concentration
m_e	Mass of electron ($9.1\times10^{-31}kg$)
m^*	Effective mass
m_l	Magnetic angular momentum quantum number
m_s	Magnetic spin quantum number

N	Number of magnetic moments, spins
$N^{\uparrow}$, $N^{\downarrow}$	Number of spin-up and spin-down electrons
n_d	Number of electrons in the 3*d* band
$n^{\uparrow\downarrow}$	Concentration of spins in either up or down states
p	Magnetic pole strength
P	Polarisation
P	Soluble product concentration
P_{laser}	Peak laser power
P_0	Incident laser power
q	Charge
R	Resistance of the detector
r, r	Position vector between two bodies (vector, magnitude)
r_L	Radial distance from Gaussian beam centre
r_{th}	Threshold radius
S, S, S_z	Spin (vector, magnitude, z-component)
S_0	Entropy
s	Spin quantum number
T	Temperature
T_C	Curie temperature
U	Potential energy
V	Electric potential
Vol	Volume
V_J	Johnson noise
v, v	Linear velocity (vector, magnitude)
W_L	Domain wall width
w_0, $w(z)$	Gaussian beam widths at waist, z
Z	Atomic number
$Z^{\uparrow}$, $Z^{\downarrow}$	Density of states for spin-up and spin-down
α	Gilbert damping parameter
β	Photodetector bandwidth
γ	Gyromagnetic ratio

γ'	Precessional term
γ_L	Gyromagnetic ratio orbital
γ_s	Gyromagnetic ratio spin
δ	Two-photon absorption cross-section
ε	Dielectric constant
$\tilde{\varepsilon}$	Dielectric tensor
ε_0	Permittivity of free space ($8.85 \times 10^{-12} m^{-3} kg^{-1} s^4 A^2$)
η	Transmittance of objective lens
λ	Damping term
$\boldsymbol{\mu}$	Magnetic moment (vector)
μ_0	Permeability of free space ($4\pi \times 10^{-7} H/m$)
μ_B	Bohr magneton
μ_L	Magnetic moment of orbital angular momentum
μ_m	Magnetic moment per atom
χ	Linear susceptibility
$\rho^{\uparrow\downarrow}$	Spin density
τ	Pulse width of laser
υ	Photodetector responsivity
θ	Angle between spins
θ_K	Kerr rotation angle
ϑ	Angle with respect to magnetocrystalline axis
Φ	Quantum efficiency
ϕ	Solution for electron in coulomb potential
ϕ_A	Analyser angle
Ψ	Full wavefunction
ψ	Spatial wavefunction
Ω_0	Ground state degeneracy
ω	Frequency of incident light

List of Acronyms

AAO	Anodic aluminium oxide
AFM	Atomic force microscopy
ASI	Artificial spin ice
CEF	Crystalline electric field
CPU	Computing processor unit
EDX	Energy dispersive X-ray analysis
FEBID	Focused electron beam induced deposition
GPU	Graphical processing unit
HDD	Hard-disk drive
ITO	Indium tin oxide
LLG	Landau-Lifshitz-Gilbert (equation)
MFM	Magnetic force microscopy
MOKE	Magneto-optical Kerr effect
MPI	Message passing interface
MRAM	Magnetic random access memory
NEP	Noise equivalent power
OOMMF	Object-oriented micromagnetic framework
PEEM	Photoemission electron micrography
SEM	Scanning electron microscopy
Spin-SEM	Spin-polarised scanning electron microscopy
TEM	Transmission electron microscopy
TPL	Two-photon lithography
TPP	Two-photon polymerisation
VSM	Vibrating sample magnetometry
XMCD	X-ray magnetic circular dichroism
XRD	X-ray diffractive analysis

Chapter 1 - Introduction

Magnetism is one of the fundamental forces of nature and has been the subject of much scrutiny and development throughout human history. Today, the impact of magnetism within our technological society is far-reaching with the bulk of the world's digital information being stored on magnetic media such as magnetic tapes and hard disk drives (HDDs) (Prinz, 1998). In addition to this, cutting edge magnetic random access memory (MRAM) devices are now at market after many years of research ("Spin-transfer Torque MRAM Technology | Everspin," accessed 2018.) and pave the way to ultrafast, non-volatile memory.

Today there is an intense interest in further improving the performance and data density of such devices, requiring the further study of magnetism in the micro- and nano-metre regimes. The study of nano-magnetism for device applications has traditionally focused on two-dimensional (2D) structures due to the relative ease of fabrication with standard lithography techniques such as photo- and electron beam lithography. Great success in this field, coupled with a huge number of theoretical studies (Ferguson et al., 2015; Streubel et al., 2016) have led to an interest in expanding fabrication efforts to three-dimensional (3D) magnetic structures. From initial efforts it has been seen that in 3D geometries a plethora of new and interesting magnetic effects becomes accessible (Fernández-Pacheco et al., 2017). Fundamental examples include novel spin textures within 3D magnetic nanostructures, the impact of topographical restraints upon domain wall motion and pinning as well as a symmetry breaking Dzyaloshinskii-Moriya interaction (Fernández-Pacheco et al., 2017).

In addition, the exploitation of 3D magnetic nanostructuring may lead to a paradigm shift in magnetic memory technology. A design by S. Parkin for 'racetrack memory' (Parkin et al., 2008) uses magnetic domain walls to store digital information in long nanowires that have a 3D magnetic architecture as shown in figure 1.1. The walls are stored in series within the wire which has a folded 'U' shape. In this way the storage is now extended to three dimensions. The information is read by a magnetic tunnel junction sensor situated at the bottom of the 'U' shape which senses the stray flux from the domains within the wire. To access information stored within the wire, the domain walls are propagated through the wire using spin-polarised current so that new domains are exposed to the sensor. While this is a promising design, current fabrication techniques are not able to easily realise magnetic racetrack memory geometries.

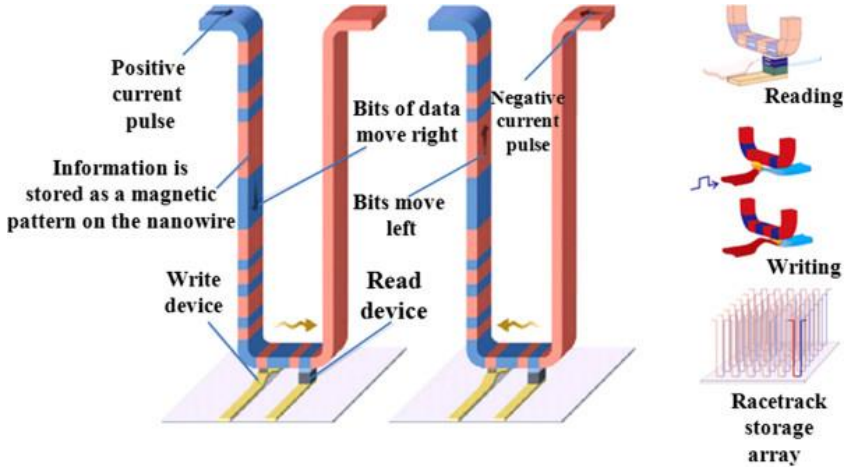

Figure 1.1: Schematic diagram of racetrack memory design. Image reproduced from Meena et al. (Meena et al., 2014).

Other studies have focused on the exotic magnetic effects observable in bulk frustrated materials known as spin ice. Such materials exist as a small number of bulk compounds where a complex 3D arrangement of magnetic moments leads to interesting physical properties, such as the phenomena of frustration and non-zero entropy values as temperature tends towards absolute zero (Harris et al., 1997; Ramirez et al., 1999). In addition, a huge range of theoretical and experimental evidence has now demonstrated that emergent quasi-particles that behave as magnetic monopoles also exist within these materials (Castelnovo et al., 2008). As these effects occur within crystal structures, the probing of them has been limited to techniques that examine bulk properties such as heat capacity, or crystallographic imaging such as neutron and muon diffraction experiments (Kadowaki et al., 2002; Lago et al., 2007). Two-dimensional artificial analogues of these systems do exist and can mimic the arrangement of moments as viewed along different planes and axes of the bulk crystals. However these often cannot capture the long-range disorder evident in their counterparts due to neglecting the 3D interactions (Cumings, 2011). As such, the ability to fabricate true 3D artificial analogues of the spin ice material would open up a plethora of experimental possibilities and allow the study of ground state ordering and magnetic monopole dynamics. In particular, emulating such atomic spins with nanoscale magnetic islands (within 3D geometries) allows the direct observation and interaction of magnetic monopole quasi-particles. However, due to the complicated structure and extended 3D lattice that would be required, such fabrication is beyond the scope of typical 3D methods in current use.

One fabrication method that has been widely used to produce large arrays of 3D cylindrical nanowires is the use of electrodeposition into anodised alumina or ion-etch templates (Da Col et al., 2014; Ohgai et al., 2008, 2006). Anodised alumina oxide (AAO) templates are fabricated by electrochemical oxidation means to produce a self-ordered hexagonal array of cylindrical pores in an oxide layer on an aluminium surface (figure 1.2). The pore diameter can be tailored from a few nanometres to several hundred nm and is typically uniform throughout the oxide layer. The template thickness is dependent upon the oxidation time which allows the cylinder length to be varied between 1-50 µm (Nasirpouri, 2007). The oxide layer can then be turned into a template for electrodeposition by depositing a thin conductive film onto the backside of the pores to act as an electrode and then removing the aluminium and oxide caps of the other surface of the layer to open the pores.

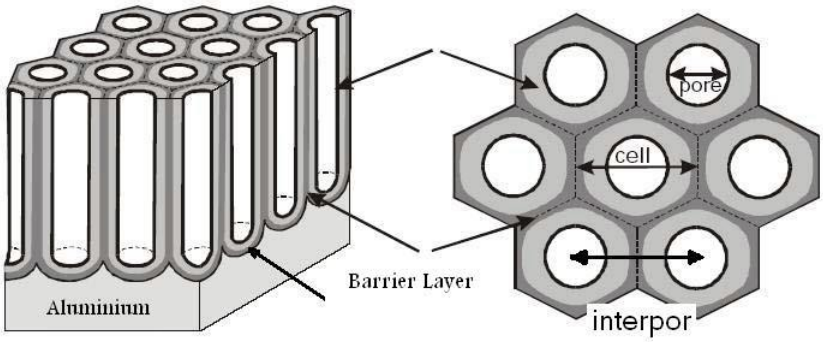

Figure 1.2: Diagram of anodic alumina oxide templates showing pore structure. Image reproduced from Nasirpouri (Nasirpouri, 2007).

Electrodeposition is a well-known process that uses an electrolytic bath and electrical current to deposit ions onto an electrode while removing ions from the counter electrode. A wide range of materials can be used in electrodeposition including the ferromagnetic transition metals iron, cobalt, nickel and their alloys. Hence, using the above templates it is possible to create cylindrical magnetic nanowires that have their long-axis perpendicular to the substrate plane. While this technique has been used to great effect, the range of geometries possible is limited to that of single-axis cylinders of varying dimensions. While it is possible to modulate the diameters of the pores to produce wires that have varying diameter across their length (Sulka et al., 2011), true freeform 3D design is beyond the technique.

Another fabrication technique in use, which is able to produce arbitrary 3D geometries, is focused electron beam induced deposition (FEBID). The basic principle of FEBID is to

introduce a precursor gas that contains the desired material to be deposited to a substrate where upon it is adsorbed onto the surface. An electron beam is then focused on the area and the bombardment of electrons breaks down the precursor molecules, leaving the desired material as a deposit and removing the remaining volatile constituents (figure 1.3). In this manner the material deposit can be grown, and by translation and rotation of the stage the direction of growth can be controlled to produce free-form structures. As the technique does not rely upon a flat substrate it is possible to produce complex arrangements of branching structures. The technique has previously produced measurable 3D magnetic nanostructures (Fernández-Pacheco et al., 2013). However, the FEBID process is very complex and depends upon a large number of experimental parameters. Coupled with the slow growth time of structures this leads to great difficulty in the reproducibility of structures (Wanzenboeck et al., 2014). Additionally, the required use of precursor molecules limits the number of potential materials that can be deposited with the technique, and the non-desired constituents typically result in a large amount of impurities within the completed structure (van Dorp and Hagen, 2008).

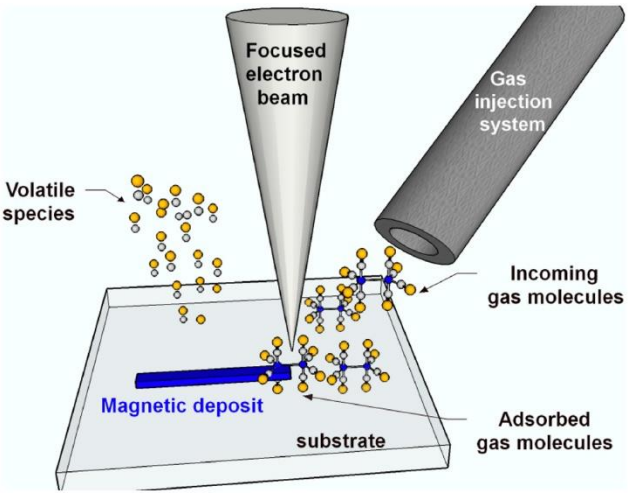

Figure 1.3: Schematic of focused electron beam induced deposition process. Image reproduced from Teresa et al. (Teresa et al., 2016).

To address the limitations of these two techniques, a new approach to 3D fabrication is required. Two-photon lithography (TPL) is a direct laser-writing lithography technique that has previously been employed in fields such as micro-optics, microfluidics and microbiology (Brigo et al., 2017; Maruo, 2016; Thiele et al., 2017). TPL exploits a non-linear optical process to expose photoresist within a highly localised region only, which can be scanned through the resist layer to expose patterned volumes in a manner analogous to macroscopic 3D printers (figure 1.4). This technique has the powerful ability to fabricate

structures of arbitrary 3D geometry at the micro- and nano-scale, but its use in nano-magnetism has so far not been explored. Using TPL, it is possible to produce templates of complex 3D nanostructures within thick layers of photoresist used in standard lithography. These templates can then be used with electrodeposition to produce freeform 3D nanostructures. This combination provides the true 3D design capabilities possible with FEBID coupled with the wide material range, purity and largescale fabrication from template-based electrodeposition. By using this technique, the large-scale fabrication of complex 3D magnetic nano-lattices is now within reach, as are previously unattainable geometries.

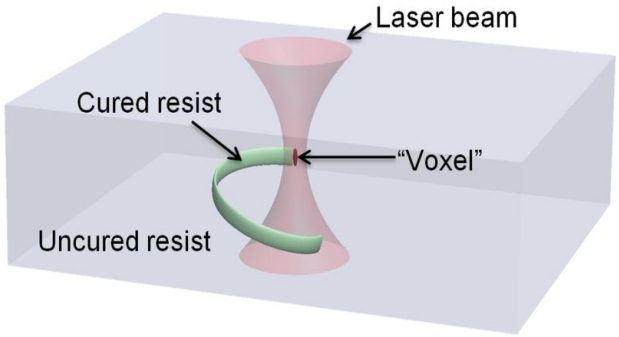

Figure 1.4: Diagram of two-photon lithography process. Exposed resist track shown in green. Image reproduced from Saha et al. (Saha et al., 2017).

The aim of this thesis is to explore the use of TPL and electrodeposition to produce 3D magnetic nanostructures, with the long-term goal of realising a 3D artificial spin ice (ASI) structure. In order to investigate the behaviour of 3D nanowires when placed into a spin ice geometry, preliminary micromagnetic simulations were performed using cylindrical nanowires in the single-domain (at remanent magnetisation) regime and a 'tetrapod' structure comprised of four such wires. The latter complex structure mimics the 3D spin arrangement found in pyrochlore spin ices and so could be used as the basis for a 3D ASI lattice. Following from these simulations, arrays of 3D nanowires and tetrapods were experimentally fabricated and studied. As the fabrication efforts were unable to reach the single-domain regime, a set of additional supporting simulations were performed to provide an insight into the reversal mechanism of multi-domain 3D nanowires. The thesis is laid out in the following manner:

Chapter 2 covers the required background theory for understanding the physics discussed in later chapters. A detailed look at ferromagnetism is presented, including contributions from various energy terms: the exchange interaction, shape anisotropy, magnetocrystalline

anisotropy and demagnetisation energy. Magnetic domain theory and the various types of domain wall for planar and cylindrical nanowires is also discussed with reference to existing literature. A review of the key features of spin ice is presented, from the emergence of magnetic charges in bulk pyrochlores and residual entropy, to popular designs of artificial 2D spin ice lattices. Current attempts at fabricating artificial 3D spin ice designs are reviewed. The chapter closes by detailing the physics of two-photon polymerisation and deriving a model for feature sizes obtainable using standard photoresists.

Chapter 3 covers the experimental methodology of a magneto optical Kerr effect (MOKE) magnetometer, supporting imaging and magnetometry techniques, micromagnetic simulations and the fabrication process utilising two-photon lithography and electrodeposition. The theory of using the MOKE to probe magnetisation and observe hysteresis is detailed, followed by an overview of the magnetometer used, including its operation. A study of its calibration, including a significant look at the achievable signal to noise ratio, is included. Brief overviews of scanning electron microscopy (SEM), spin-polarised SEM (spin-SEM), energy dispersive X-ray analysis (EDX), atomic force microscopy (AFM) and vibrating sample magnetometry (VSM) are given. An introduction to micromagnetic simulations is provided, including basic theory of how the packages operate and the reasoning for using the chosen packages in the study. A short overview of the software packages is also detailed. The chapter closes by briefly presenting the fabrication procedure of 3D magnetic nanostructures utilising TPL and electrodeposition used by G Williams to produce the structures investigated in chapter 5.

Chapter 4 details the results obtained from micromagnetic simulations on cylindrical nanowires and nanowire-comprised tetrapod structures. The simulations performed on cylindrical nanowires showed the formation and propagation of Bloch point domain walls. Hysteresis loops were taken where the angle of the applied external field, with respect to the wire axis, was varied to match the angles featured in the three principle symmetry directions for the tetrapod structure. The simulations agreed with previous studies of hysteresis loops taken at various angles on similarly sized nanowires and also showed the displacement of the Bloch point core away from the nanowire axis at increasing angles. The simulations of the tetrapods showed that, with no externally applied field, the two-in/two-out and three-in/one-out states were stable, while the four-in state is unstable. The three states followed a similar trend in energies as those for bulk pyrochlore spin ice. Hysteresis loops were performed in three principle symmetry directions on the tetrapod structure. It was observed that for the [100] and [110] directions, the hysteresis loops could be

reconstructed using the loops for single nanowires; however the [111] direction loop could not be constructed in such a way. The loop for the [111] direction was scrutinised in more detail and it was observed that a Bloch point wall propagated through the wire parallel to the externally applied field and, upon entering the vertex of the tetrapod, induced the propagation of two further walls. The wire selection for these secondary walls was observed to be different on the reversal of the applied external field direction.

Chapter 5 covers the measurement studies performed on 3D cobalt nanostructures fabricated using a combination of TPL and electrodeposition. Preliminary studies on an array of vertical nanowires written at a range of powers is included, showing that the minimum lateral feature size achieved was 435nm which agreed with a theoretical model in literature. Large arrays of angled nanowires and tetrapods were imaged using an SEM and the dimensions probed, showing that the arrays were largely uniform. Hysteresis loops captured using MOKE magnetometry were performed on 3D angled nanowire arrays and tetrapod arrays. The measurements showed that it was possible to use such a magnetometer to probe 3D structures. The angled nanowires showed a sharp initial transition at low field values and were dominated by rotation of the magnetisation at high field values when the field was aligned parallel to the projection of the wire axis. The angled nanowires showed a more hard-axis type loop when the field was aligned perpendicular to the projection of the wire axis. Supporting micromagnetic simulations of large, multi-domain nanowires were included in the discussion of the nanowire reversal mechanism. Spin-polarised SEM images were performed by IBM Zurich on one of the tetrapod samples which allowed for the remanent domain structure to be observed. The upper surface of a wire in the structure was seen to be multi-domain with a preference for domains to align with the wire axis, while the vertex was seen to retain a complex domain structure even after application of a field magnitude in excess of the coercive field. The domain patterns were found to be comparable to those observed in multi-domain nanowires found in the literature and the supporting simulations. The magnetometry results for the tetrapods showed similar loops when the field was applied both parallel and perpendicular to the projection of the lower wires on the substrate. However, both loops showed multiple switching events that could not be reproduced from the loops performed on the single angled nanowires. A reversal mechanism was proposed based on the observations from the single nanowire discussion and existing literature.

Chapter 6 summarises the results obtained over the course of the PhD and provides recommendations for future studies, including improvements for fabricating 3D magnetic structures using two-photon lithography and electrodeposition.

Chapter 2 - Background Theory

2.1 Introduction and basic concepts

This chapter details some of the underlying principles and theories of the areas of physics studied in this thesis. Magnetism, in particular ferromagnetic materials, is detailed, as are spin ice materials and the two-photon lithography process.

2.1.1 Magnetic moments

A fundamental concept to understanding the results in this thesis is that of the magnetic moment and its response to an external magnetic field. There are two standard definitions of the magnetic moment; the first is as a dipole moment between two hypothetical magnetic charges (magnetic monopoles) analogous to an electric dipole (Brown, 1962), and the second is as an enclosed current loop. These are shown in figure 2.1.

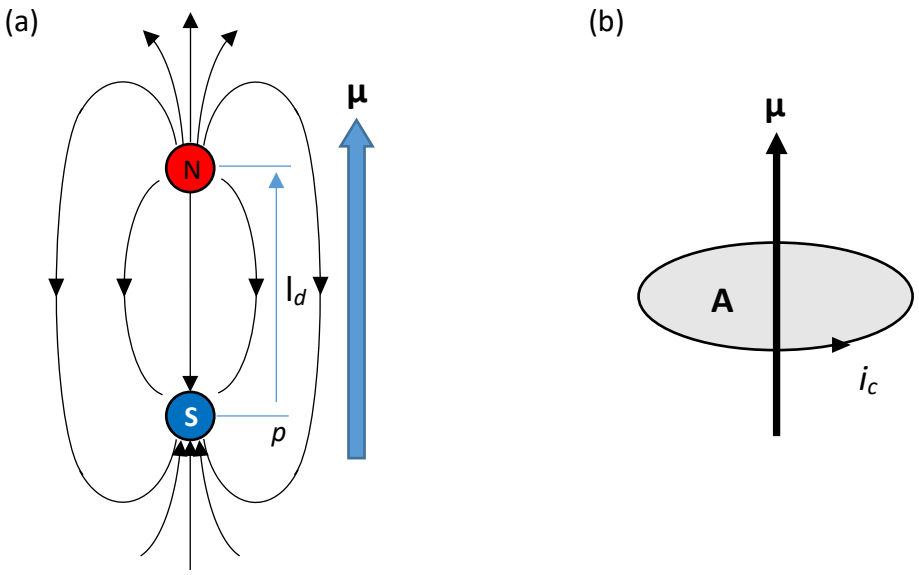

Figure 2.1: Diagram representation of a magnetic moment: (a) Dipole model with two poles of equal strength separated by a finite distance, (b) Current loop and enclosed area.

In the case of the dipole model the magnetic moment is simply defined as the product between the strength of the magnetic poles and the vector distance between them:

$$\boldsymbol{\mu} = p\mathbf{l}_d \tag{2.1}$$

where $\boldsymbol{\mu}$ is the magnetic moment vector, p is the magnetic pole strength and $\mathbf{l}_d$ is the separation vector between the poles.

In the case of a current loop it can be shown via Stoke's theorem (O'Handley, 2000) that the magnetic moment is the product of the current with the area the loop encloses:

$$\boldsymbol{\mu} = i_c \mathbf{A} \tag{2.2}$$

where $\boldsymbol{\mu}$ is the magnetic moment vector, i_c is the current and **A** is the normal vector of the area enclosed by the current loop.

The magnetic field from a moment can be defined in terms of magnetic flux density, *B,* or magnetic field strength, *H,* which are related by the permeability of free space μ_0. The field outside of a magnetic dipole has the form (O'Handley, 2000):

$$\mathbf{B} = \mu_0 \mathbf{H} = \frac{\mu_0}{4\pi}\left[\frac{3\mathbf{r}(\boldsymbol{\mu}\cdot\mathbf{r})}{r^5} - \frac{\boldsymbol{\mu}}{r^3}\right] \tag{2.3}$$

where **B** is the magnetic flux density vector, **H** is the magnetic field strength vector, $\boldsymbol{\mu}$ is the dipole magnetic moment and **r** is the position vector from the dipole (with magnitude *r*).

When a free magnetic moment, $\boldsymbol{\mu}$, is placed within an external magnetic field, **B**, it experiences a force, **F**, expressed by:

$$\mathbf{F} = \nabla(\boldsymbol{\mu} \cdot \mathbf{B}) \tag{2.4}$$

and the potential energy, *U*, for such a moment within a magnetic field is given by (Young and Freedman, 2008):

$$U = -\boldsymbol{\mu} \cdot \mathbf{B} \tag{2.5}$$

The above equations show the well-known and familiar result that a free magnetic moment tends to align with an externally applied field.

Using equations 2.3 and 2.5, the dipole interaction energy between two magnetic moments can be expressed as (Ku et al., 2016):

$$U = -\frac{\mu_0}{4\pi|\mathbf{r}|^3}[3(\boldsymbol{\mu_1} \cdot \hat{\mathbf{r}})(\boldsymbol{\mu_2} \cdot \hat{\mathbf{r}}) - \boldsymbol{\mu_1} \cdot \boldsymbol{\mu_2}] \tag{2.6}$$

where *U* is potential energy, μ_0 is the permeability of free space, **r** is the position vector between the centres of the two moments ($\hat{\mathbf{r}} = \mathbf{r}/|\mathbf{r}|$ is the unit vector for **r**). From equation 2.6 it is apparent that dipoles favour a parallel arrangement when brought together end-to-end, and an anti-parallel arrangement when brought side-to-side. Hence they can be said to favour 'head-to-tail' arrangement.

2.1.2 Atomic moments and spin

Using the current loop model, and considering the simplest case of a Hydrogen atom using the Bohr model for an atom, the magnitude of the magnetic moment for the orbital motion of one electron can be calculated. Assuming that the electron orbits the nucleus in a circular loop, then the magnitude of the current is the electron charge divided by the period of the orbit, and the area is simply that of the circle enclosed. Hence, from equation 2.2:

$$\mu_L = \frac{ev}{2\pi r}(\pi r^2) = \frac{evr}{2} \tag{2.7}$$

where *e* is the charge of an electron, *r* is the distance from the nucleus to the electron and *v* is the electron's velocity.

If the angular momentum, *L*, of the electron is considered such that $L = m_e vr$ then equation 2.3 becomes (Young and Freedman, 2008):

$$\mu_L = \frac{e}{2m_e} L = \gamma_L L \tag{2.8}$$

where m_e is the mass of an electron. The factor $e/2m_e$ can also be expressed as the orbital gyromagnetic ratio, γ_L as shown.

Now, using the quantum mechanical result that *L* is quantised in the fashion (Eisberg and Resnick, 1974):

$$L^2 = \hbar^2 l(l+1) \qquad \text{and} \qquad L_z = \hbar m_l \tag{2.9}$$

where *L* is the magnitude of the angular momentum vector, L_z is the z-component of the angular momentum vector, *l* is the orbital angular momentum quantum number and m_l is the quantum number for magnetic orbital angular momentum. The quantum number m_l can take integer values in the range $-l, -l+1, \ldots 0 \ldots, l-1, l,$ and as such for a single electron with a quantum of angular momentum, $L = \hbar$, the orbital magnetic moment can be equated as:

$$\mu_L = \mu_B = \frac{e\hbar}{2m_e} \tag{2.10}$$

This numerical value is known as the Bohr magneton, μ_B, and is calculated to be $9.27 \times 10^{-24} Am^2$.

Another important source of magnetic moment in the context of magnetic materials is spin. Spin is a fundamental property of elementary particles that arises from quantum mechanics and is often described as a particle's intrinsic angular momentum, separate and

distinct from any orbital angular momentum it may have. Spin has been shown to exist via experiments such as the hyper-fine splitting of hydrogen atomic spectra lines and the Stern-Gerlach experiment where silver atoms directed through a magnetic field split into two distinct paths (Gerlach and Stern, 1922). Previously the model of quantum mechanics based on the Schrodinger equation had required three fundamental quantum numbers, but the results of these experiments prompted the need for a fourth to explain some of the subtle effects observed. When Dirac incorporated relativistic effects into the quantum mechanical model it was found that spin was predicted as a result of the changes. The spin vector is analogous to that of angular momentum such that it follows quantisation expressions of the form (Eisberg and Resnick, 1974):

$$S^2 = \hbar^2 s(s+1) \qquad \text{and} \qquad S_z = \hbar m_s \tag{2.11}$$

where S is the magnitude of the spin vector, S_z is the z-component of the spin vector, s is the spin quantum number and m_s is the magnetic spin quantum number and can take discrete values from $-s$ to $+s$ where s is ½. As such, $m_s = \pm ½$.

Using equation 2.8 in a similar analogy to angular momentum, it can now be shown that the magnetic moment associated with an electron's quantum of spin, S, is expressed as:

$$\mu_s = \gamma_s S = \pm \gamma_s \frac{\hbar}{2} \tag{2.12}$$

where the spin gyromagnetic ratio, $\gamma_s = e/m_e = 2\gamma_L$ with γ_L being the orbital gyromagnetic ratio. Hence the electron's moment is:

$$\mu_s = \pm \frac{e\hbar}{2m_e} = \pm \mu_B \tag{2.13}$$

This number is the Bohr magneton, the same as was estimated earlier for the moment due to the electron's orbital angular momentum, because the quantum of orbital angular momentum is twice that of spin and orbital gyromagnetic ratio is half that for spin. As an electron has only two values for spin orientation it is common to refer to the states as 'spin-up' and 'spin-down'.

Both spin and orbital angular momentum moments can contribute to the total magnetic moment of an atom, as such a weighting factor, *g,* is required to account for their relative contributions. The *g*-factor is equal to 1 for orbital only contribution and approximately equal to 2 (2.002319; (Odom et al., 2006)) for spin only contribution.

2.1.3 Spin-orbit interaction

As the electron has a magnetic moment from both its spin and its orbital motion the two can couple together which is described by the spin-orbit interaction. If the effect were neglected then the spin, *S* and angular momentum, *L* would be independent of each other.

If the effect is considered in its simplest terms then the spin-orbit interaction describes the effect of the electron's orbital motion on the orientation of its spin. If the classical case of a hydrogen atom is considered, then the electron in its rest frame 'sees' a positive charge in motion around it (figure 2.2). The positive charge creates a current loop generating a magnetic field that causes a preferred direction for the electron's spin to align to.

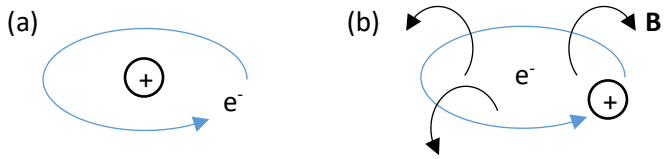

Figure 2.2: Illustration of the classical hydrogen model from (a) the proton's rest frame and (b) the electron's rest frame.

The magnetic field that is effectively generated by the positive charge is expressed from the Biot-Savart law as (O'Handley, 2000):

$$\mathbf{B} = \left(\frac{\mu_0}{4\pi}\right)\frac{\mathbf{i_c} \times \mathbf{r}}{r^3} = -\frac{Ze\mu_0}{4\pi}\left(\frac{\mathbf{v} \times \mathbf{r}}{r^3}\right) \tag{2.14}$$

where **B** is magnetic field**,** $\mathbf{i_c}$ is the current, **r** is the position vector from the electron to the charge with magnitude *r*, *Z* is the atomic number of the charge, *e* is the electronic charge, and **v** is the linear velocity of the charge.

The field can be expressed in terms of the charge's electric field (Young and Freedman, 2008):

$$\mathbf{E} = \frac{Ze}{4\pi\varepsilon_0}\frac{\mathbf{r}}{r^3} = \frac{1}{e}\frac{\partial V}{\partial r}\frac{\mathbf{r}}{r} \tag{2.15}$$

where **E** is the electric field, ε_0 is the permittivity of free space and *V* is the electric (Coulomb) potential.

And hence from equation 2.14:

$$\mathbf{B} = -\mu_0\varepsilon_0(\mathbf{v}\times\mathbf{E}) = -\frac{1}{c^2}(\mathbf{v}\times\mathbf{E}) = -\frac{1}{ec^2r}(\mathbf{v}\times\mathbf{r})\left(\frac{\partial V}{\partial r}\right) \tag{2.16}$$

and using $\mathbf{L} = \mathbf{r}\times m_e\mathbf{v}$ gives:

$$\mathbf{B} = \frac{1}{em_ec^2}\frac{1}{r}\frac{\partial V}{\partial r}\mathbf{L} \tag{2.17}$$

where *c* is the speed of light, m_e is the mass of the electron, and **L** is angular momentum.

Using equation 2.5 the energy of a spin within this field is then given by:

$$E_{SO} = \frac{1}{2m_e{}^2c^2}\frac{1}{r}\frac{\partial V}{\partial r}\mathbf{L}\cdot\mathbf{S} \tag{2.18}$$

The spin-orbit interaction is responsible for a number of effects in magnetic materials such as magnetocrystalline anisotropy, which will be discussed later in the chapter.

A consequence of the spin-orbit interaction is that spin angular momentum and orbital angular momentum are no longer independent of each other. As such, when considering effects where the spin-orbit interaction is notable, a more useful quantity is the total angular momentum **J**, where (Merzbacher, 1998):

$$\mathbf{J} = \mathbf{L} + \mathbf{S} \tag{2.19}$$

In such scenarios **J** is the 'good quantum number' in that it commutes with the Hamiltonian operator (Eisberg and Resnick, 1974). The above considers an atom with only a single electron. For an atom with multiple electrons the atomic orbital model is used where there are a number of constraints on where each electron can reside within the atom's orbitals. Most significantly, no electrons can share the same set of quantum numbers. It is known that electrons will fill orbitals from the lowest energy to highest (i.e. the 1*s* orbital is filled before the 2*s* orbital), however the filling of orbitals with multiple vacancies (e.g. *p*- or *d*-orbitals) are governed by Hund's rules. These state that (O'Handley, 2000):

1. Quantum states are filled so as to maximise total spin, i.e. an orbital will be populated by electrons of one spin exclusively before mixing spin states or creating spin-up spin-down pairs.
2. If the first rule does not apply, the quantum states are filled so as to maximise total angular momentum.
3. For partially filled orbitals, if the suborbital is less than half full the state with lowest total angular momentum *J* is filled first, and if the suborbital is more than half full the state with the highest *J* is filled first.

These rules are based largely on the Coulombic repulsion between electrons and the spin-orbit interaction for the third rule. They are important when considering the formation of magnetism in transition metals (see section 2.2.2).

The theory discussed so far has concerned magnetism for individual atoms, but when considering the magnetic properties of a bulk material there are further factors at play. For macroscopic magnetic materials, instead of individual atomic moments a more useful quantity to consider is magnetisation, **M**, which is defined as the total magnetic moment per unit volume:

$$\mathbf{M} = \frac{1}{Vol}\sum_{N} \boldsymbol{\mu} \tag{2.20}$$

where **M** is the magnetisation, *N* is the number of magnetic moments and *Vol* is volume of the material.

The potential energy density for a macroscopic sample within an external field (called the Zeeman energy) is then given in analogous fashion to equation 2.5 by:

$$E_{Zeeman} = -\mu_0 \mathbf{M} \cdot \mathbf{H}_{Ext} \tag{2.21}$$

In the absence of an external magnetic field, it is also possible for certain bulk materials to exhibit a magnetic field due to their magnetisation. This field is referred to as the 'magnetostatic' field and its associated energy is referred to as magnetostatic energy.

There are several categories of magnetism in materials which include: paramagnetism, where the moments of a material align in parallel in response to an external magnetic field; diamagnetism, where the moments align anti-parallel to an externally applied field; and Ferromagnetism. A detailed look at paramagnetism and diamagnetism can be found in *Modern Magnetic Materials* by O'Handley (O'Handley, 2000). Ferromagnetism is the category of most concern to this thesis and so is covered in detail below.

2.2 Ferromagnetism

A ferromagnetic material is one that can exhibit a spontaneous magnetisation, usually at room temperature. Above a critical temperature (the Curie temperature, T_C) the long range ordering of magnetisation vanishes, resulting in the material becoming paramagnetic (i.e. where the magnetisation responds linearly with the externally applied field). To describe ferromagnetism it is not sufficient to only consider the dipole interaction between atomic

moments. By considering the simplest case of two atomic dipoles aligned in parallel via the magnetic dipole interaction, then the energy is given approximately by (Ku et al., 2016):

$$U \approx \frac{\mu_0 {\mu_B}^2}{4\pi r^3} \tag{2.22}$$

where r is the distance between the two moments. If a spacing of an atomic diameter of approximately 1Å is used then $U \approx 8.6\text{x}10^{-24}$J, and equating that with the thermal energy (k_BT) results in a Curie temperature of approximately 0.6K. As a number of ferromagnetic materials can exhibit stable non-zero magnetisation at room temperature (300K), the dipole interaction cannot be the only mechanism governing the magnetic ordering.

2.2.1 Exchange interaction

The exchange interaction is another mechanism that contributes to the energy responsible for ferromagnetism. If two atoms, each with an unpaired electron, are considered then there are several ways they can interact. Electron shell theory has it that electrons pair up in spin-up and spin-down pairs (Eisberg and Resnick, 1974), however the electrons in the pair still have a Coulomb repulsion between them. If the Pauli Exclusion Principle (Merzbacher, 1998) is taken into account, then if both electrons share the same spin state they are forced to reside in separate orbitals (Hund's rule), and hence further apart, which reduces the Coulombic interaction. The energy difference between two anti-parallel electrons and two parallel electrons in this manner can be shown to be orders of magnitude greater than that of the dipole-dipole interaction.

As the quantum mechanical effects in metals are very complex, in order to demonstrate the basic physics involved the simpler case for a Hydrogen molecule will be considered, as demonstrated by Heitler and London and shown in figure 2.3 (Yosida, 1996). For such a system composed of two electrons each orbiting a proton, the Hamiltonian plus the inclusion of the Coulomb interaction between the electrons can be described by the following:

$$\mathcal{H}_0 = -\frac{\hbar^2}{2m_e}{\nabla_1}^2 - \frac{\hbar^2}{2m_e}{\nabla_2}^2 + V(1) + V(2) \tag{2.23}$$

$$\mathcal{H} = \mathcal{H}_0 + \frac{e^2}{4\pi\varepsilon_0 r_{12}} \tag{2.24}$$

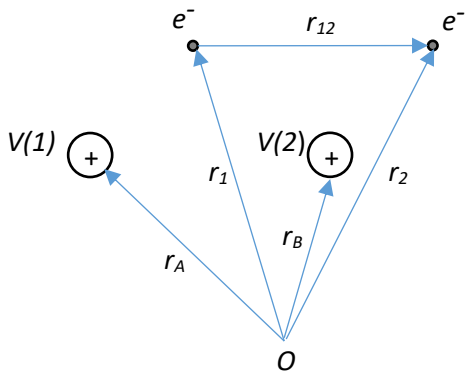

Figure 2.3: Representation of particles in the Hydrogen molecule and relevant variables; e is electron charge, r is distance, V is potential.

In the case where the Coulomb interaction can be considered negligible, it is possible to split the above into two equations, each for one of the electrons:

$$\mathcal{H}^0\psi^0 = E^0\psi^0 \tag{2.25}$$

$$\psi^0 = \phi_i(1)\phi_j(2) \tag{2.26}$$

$$E^0 = E^{(i)} + E^{(j)} \tag{2.27}$$

where ϕ is the solution for one of the electrons in their respective potential *V*. If both are under identical conditions then $E^{(i)}=E^{(j)}$. However, if the Coulomb interaction is non-negligible then by using first-order perturbation theory an additional term is added to equation 2.27 to account for it:

$$E = E^0 + \int \phi_i^*(1)\phi_j^*(2)\left[\frac{e^2}{4\pi\varepsilon_0 r_{12}}\right]\phi_i(1)\phi_j(2)\,dv \tag{2.28}$$

$$E = E^0 + C_{ij} \tag{2.29}$$

where C_{ij} is the average of the Coulomb interaction between the electrons. The addition of this term raises the overall energy states relative to the non-perturbed system. To add further to this model, the Pauli Exclusion Principle and the electrons' spin needs to be considered. The principle states that no two electrons can occupy the same quantum state in a system. Each electron can either be spin-up or spin-down and in isolation the anti-parallel configuration of spin-up to spin-down is the preferred energy state. As electrons are Fermions, to satisfy the interchangeability of their positions the spatial component of

their wavefunction must be anti-symmetric and can be given as (McQuarrie and Simon, 1997):

$$\psi^- = \phi_1(1)\phi_2(2) - \phi_1(2)\phi_2(1) \tag{2.30}$$

where $\phi_2(1)$ indicates that electron 1 is in state 2, $\phi_1(2)$ indicates electron 2 is in state 1, etc.

While the spin component is given as:

$$S = S_+(1)S_-(2) \pm S_+(2)S_-(1) \tag{2.31}$$

where $S_+(1)$indicates that electron 1 is spin-up, $S_-(2)$ indicates electron 2 is spin-down, etc. This describes a singlet (anti-parallel) state when subtracting and a triplet state (parallel) when adding.

As a consequence of equation 2.30, the electrons cannot share the same state or position as doing so causes ψ^- to equate to 0. If the simplest case where the spin and spatial components are separable variables is considered, then the full wavefunction becomes the product of the two terms:

$$\Psi = \psi(r_1, r_2)S(s_1, s_2) \tag{2.32}$$

The overall wavefunction must be anti-symmetric. Therefore, for that to be true, if the spatial component is symmetric the spin component is required to be anti-symmetric (singlet) and vice versa. Therefore the full wavefunction for both singlet and triplet spin states can be expressed as the following:

$$\Psi_S = \left(\frac{1}{2}\right)^{1/2}[\phi_1(1)\phi_2(2) + \phi_1(2)\phi_2(1)]S_S\,; \quad E_S^0 = E_1 + E_2 \tag{2.33, 2.34}$$

$$\Psi_T = \left(\frac{1}{2}\right)^{1/2}[\phi_1(1)\phi_2(2) - \phi_1(2)\phi_2(1)]S_T\,; \quad E_T^0 = E_1 + E_2 \tag{2.35, 2.36}$$

The Coulomb interaction is again taken into account using perturbation theory:

$$\mathcal{J}_{ij} = \int \phi_i^*(1)\phi_j^*(2)\left[\frac{e^2}{4\pi\varepsilon_0 r_{12}}\right]\phi_i(1)\phi_j(2)\,dv \tag{2.37}$$

And so the energies for both states becomes the following:

$$E_S = E^0 + C_{ij} + \mathcal{J}_{ij} \tag{2.38}$$

$$E_T = E^0 + C_{ij} - \mathcal{J}_{ij} \tag{2.39}$$

$\mathcal{J}_{ij}$ here is known as the exchange energy. Either state can have lower energy depending on the sign of $\mathcal{J}$, with the triplet (parallel spins) state preferred if $\mathcal{J} > 0$, as is the case for ferromagnetic materials. The exchange energy can be written in the formulation presented by Heisenberg:

$$\mathcal{H} = -2\sum_{i<j} \mathcal{J}_{ij} S_i \cdot S_j \tag{2.40}$$

2.2.2 Magnetism in transition metals

Figure 2.4 illustrates what is known as the Slater-Pauling curve – how the magnetic moment per atom varies with atomic number for transition metals in the 3*d* orbital band (Williams et al., 1983). It should be noted that for the pure ferromagnetic metals, iron Fe, cobalt Co and nickel Ni, the moment per atom measured in Bohr magnetons have been measured as 2.2μ_B for Fe, 1.7 μ_B for Co and 0.6 μ_B for Ni (O'Handley, 2000). The behaviour shown by the Slater-Pauling curve can be explained by considering the exchange interaction and band models for the binding electrons of the metallic atoms.

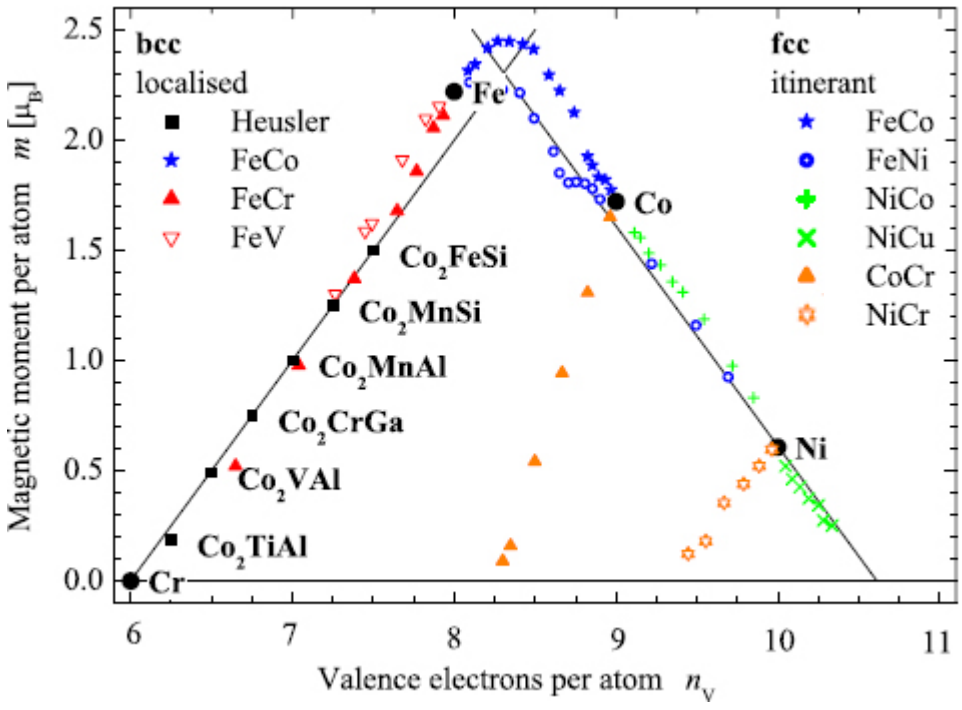

Figure 2.4: Slater-Pauling curve for transition metals in 3d band. Image reproduced from Balke et al. (Balke et al., 2008).

When atoms are brought together to form solids, the atomic levels broaden. For transition metals the outer orbitals are the 4*s* and 3*d* orbitals, with the number of *d* electrons varying

the most between metals, and it is the *d* electrons that give rise to the magnetic behaviour observed. The states in the lower half of the band are bonding states (i.e. favour anti-parallel spins) while those in the upper half of the band are anti-bonding states (i.e. favour parallel spins). Hence, the first half of the 3*d* metal series (vanadium V, chromium Cr, manganese Mn) exhibit antiferromagnetism because the Fermi energy level, E_F, lies in the bonding part of the 3*d* band, whereas for the latter half (Fe, Co, Ni) E_F lies in the anti-bonding part.

In addition, if the exchange interaction is considered then it must create an imbalance between the number of spin-up and spin-down states in the 3*d* electron band (figure 2.5); this can be understood in terms of Hund's first rule – states are filled with parallel spins first. The 3*d* band can hold 10 electrons (5 each of up and down) and without the exchange interaction an imbalance would be an excited state; however because of the large number of available states the exchange energy cost becomes preferable (Jiles, 2015). If the electronic structures of iron and nickel are considered in this manner as shown in figure 2.5, then the variation of magnetic moment with the average number of valence electrons as depicted on the right hand side of the Slater-Pauling curve can be explained in terms of a simple model.

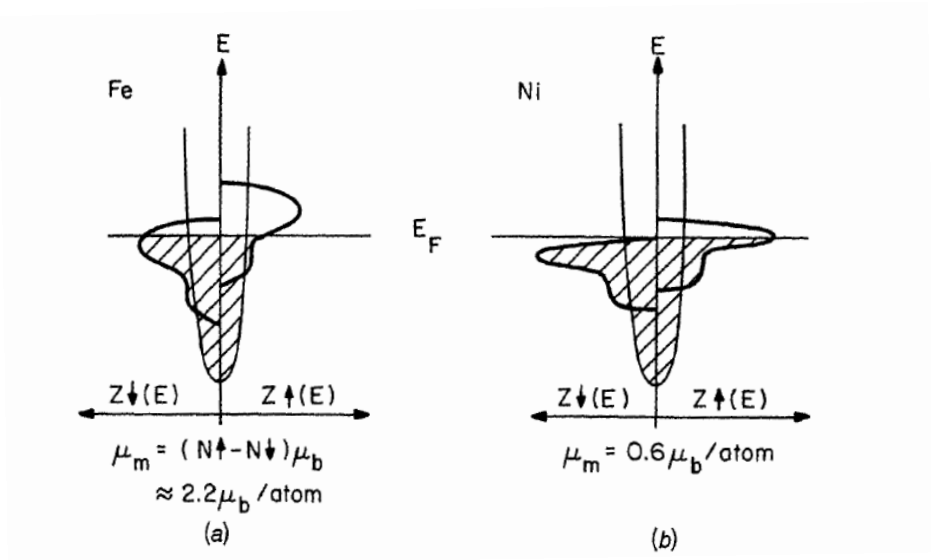

Figure 2.5: Simple illustration of 3d band splitting and filling of states for (a) iron and (b) nickel. E_F is the Fermi-level energy, $Z^{\uparrow}$ and $Z^{\downarrow}$ are density of states for spin-up and spin-down respectively and $N^{\uparrow}$ and $N^{\downarrow}$ are the number of spin-up and spin-down electrons present respectively. Image reproduced from O'Handley (O'Handley, 2000).

Iron has 8 valence electrons spread across the 4*s* and 3*d* bands, while nickel has 10. Experimental measurements have shown that iron has slightly less than 1 (0.95) electron occupying the 4*s* band on average, which leaves 7.05 electrons on average in the 3*d* band. Therefore, if the total number of *d* electrons per atom is the sum of the electrons in the spin-up and spin-down sub-bands ($N^{\uparrow} + N^{\downarrow}$), and the observed magnetic moment of iron ($2.2\mu_B$) is the difference ($N^{\uparrow} - N^{\downarrow}$), then that leads to $N^{\uparrow} = 4.62$ and $N^{\downarrow} = 2.42$; i.e. both sub-bands are partially occupied. Nickel in comparison has 0.6 electrons in the 4*s* band on average, resulting in 9.4 electrons in the *d* band. This leads to sub-band populations of $N^{\uparrow} = 5$ and $N^{\downarrow} = 4.4$ meaning that only the down band has partial occupancy. This is illustrated in figure 2.5 by the fermi-level position for the two metals.

To expand this to alloys where the number of valence electrons is averaged and hence no longer an integer, further simplifications of the model can be made. This forms the basis of the 'rigid-band' model where it is assumed that the shape of the *s* and *d* bands is fixed as the number of valence electrons changes. While the model is a crude approximation it is sufficient to explain the trend for alloying shown by the Slater-Pauling curve. In the rigid-band model the effect of varying the alloy concentrations is to move the Fermi-energy level relative to the fixed density of states. If the assumption is made that exchange causes 5 of the 3*d* electrons to be spin-up (as is the case for nickel) and the remainder spin-down, then the magnetic moment per atom can be expressed as:

$$\mu_m = (10 - n_d)\mu_B \tag{2.41}$$

where μ_m is the magnetic moment per atom, n_d is the number of electrons in the 3*d* band and μ_B is the Bohr magneton. This equation is a straight line with gradient of -1, showing the trend of the Slater-Pauling curve for the strongly ferromagnetic materials on the right hand side and indicates that alloys and metals with similar numbers of electrons in the *d* band will have a similar moment per atom. Given that the only materials of interest within this thesis are Co and permalloy ($Ni_{81}Fe_{19}$) the left hand side of the Slater-Pauling curve will not be considered here.

2.2.3 Indirect exchange

There can also be an exchange interaction at the boundaries between multi-layer or multi-grain materials, or other systems where electron separation is greater than would be expected to support direct exchange interaction (e.g. 4*f* electrons in rare-earth metals). This is referred to as indirect exchange and occurs because the free conduction electrons of

the material become polarised at one site and thus transfer the spin information to another. A model describing this interaction was developed independently by Ruderman and Kittel, as well as by Kasuya and by Yosida, and so is referred to as the RKKY interaction and is described below (Kasuya, 1956; Ruderman and Kittel, 1954; Yosida, 1957).

If the case of an impurity placed within an electron gas is considered, then the background charge redistributes to compensate for the introduced impurity charge. In doing so the electron gas forms a Fourier series of charge oscillations that sum to cancel the impurity charge. However the Fermi energy of the gas ($h^2k_F^2/2m_e$) sets a lower limit for the wavelength of these oscillations which leaves them to be characterised by a wave number $k \geq k_F$. These are known as Friedel oscillations. A similar case happens for a magnetic impurity in the gas if $k_F^{\uparrow} \neq k_F^{\downarrow}$. The spin density around such an impurity can be expressed as (O'Handley, 2000):

$$\rho\uparrow\downarrow(r) = n\uparrow\downarrow\left[1 \pm \frac{9n\uparrow\downarrow}{E_F}\pi J S^z F(2k_F^{\uparrow\downarrow}r)\right] \tag{2.42}$$

where $\rho^{\uparrow\downarrow}$ is the spin density, $n^{\uparrow\downarrow}$ is the concentration of spins in either up or down states, E_F is the Fermi energy, J is total angular momentum, S^z is spin, k_F is the Fermi wave vector, r is distance from the impurity and where F is the following function:

$$F(x) = \frac{\sin(x) - x\cos(x)}{x^4} \tag{2.43}$$

Equation 2.42 describes a spin density that shows damped oscillations with distance from the impurity. The spin polarisation is proportional to the function $F(x)$ and can be expressed for large values of x as:

$$\rho\uparrow - \rho\downarrow \approx \frac{n^2}{E_F} J\langle S^2\rangle \frac{\cos(2k_F r)}{(k_F r)^3} \tag{2.44}$$

The magnetic impurity that creates this oscillating spin polarisation is a localised moment whose spin-dependant direct exchange with the conduction electrons affects electrons that have spin-up differently to those that have spin-down. As these oscillations carry spin information away from the moment that created them, they can then interact with other moments that are beyond the range of the direct exchange interaction. The Hamiltonian describing the exchange with a second moment is expressed as:

$$\mathcal{H}_{RKKY} = S_i \cdot S_j \frac{4J^2 m^* k_F^r}{(2\pi)^3} F(2k_F r) \tag{2.45}$$

where $\mathcal{H}$ is the Hamiltonian and m^* is the effective mass of the electron.

This model describes the indirect exchange interaction between moments via interactions with conduction electrons. This interaction is weaker than that described by the direct exchange present in 3*d* metals such as cobalt and so is unlikely to play a role in continuous samples.

2.2.4 Magnetocrystalline anisotropy

While the exchange energy is responsible for aligning neighbouring atomic moments, other energies contribute to the production of a larger scale spin texture assumed by a ferromagnet. Magnetic anisotropy applies a constraint on the orientation of the magnetisation of a material. The relevant types of anisotropy for the structures considered in this thesis are magnetocrystalline anisotropy and shape anisotropy.

Magnetocrystalline anisotropy is due to the spin-orbit interaction and the interaction of the atomic orbital angular momentum with the crystalline ordering of the material, and causes the magnetisation to preferentially point along a crystallographic axis. An electron's orbital angular momentum is oriented to an axis and the orbital, upon rotation of the axis, can only be transformed into an equivalent and degenerate orbital that does not contain an electron in the same state (Laan, 1998). The degeneracy of an orbital can be influenced by its surroundings in such a way as to limit the number of possible transformations and so constrain the allowed orientations of the orbital magnetic moment. This is illustrated for the case of orbitals within a long range crystal lattice by the simplified model below (O'Handley, 2000).

The distribution of charge between different atomic orbitals can have symmetry dependent on the orbital's angular momentum (e.g. *p* orbitals are less symmetric than *s* orbitals), and the crystalline electric field (CEF) can also have a separate symmetry, as illustrated by simple representation in figure 2.6. In the case where either has a large number of symmetry directions ($L_z = 0$ or CEF = 0) then there is only a very weak anisotropy as the atomic orbitals can assume any orientation with respect to the CEF (and in the $L_z = 0$ case there is no spin-orbit interaction). However, if both have a limited number of symmetry directions ($L_z \neq 0$ *and* CEF ≠ 0) then the orbital has preferable orientations with respect to the CEF. In this case, if the spin-orbit interaction is non-zero, then the spin moments are coupled to the orbital and so will prefer a direction relative to the CEF, leading to a stronger anisotropy.

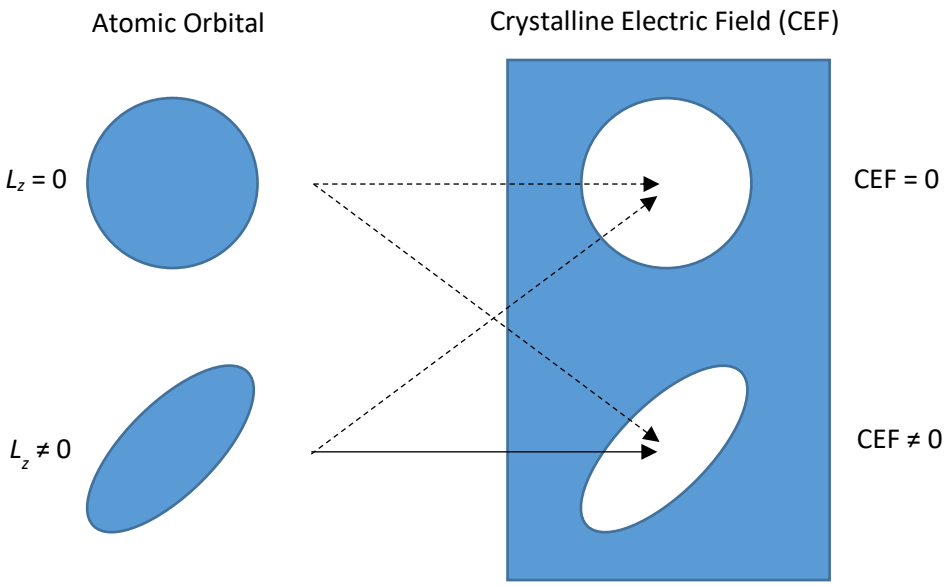

Figure 2.6: Simple 2D representation of the role of orbital angular momentum (L_z) and crystalline electric field (CEF) in determining magnetocrystalline anisotropy. Dashed arrows represent combinations with weak/no anisotropy, solid arrow represents combination with strong anisotropy.

When there is magnetocrystalline anisotropy, an external field will cause a torque on the spin, **S**, which may be coupled to the orbital angular momentum, **L**. If the crystal field energy is stronger than the spin-orbit interaction (CEF > **L**·**S**), then μ_s will respond to the external field while the μ_L response will be suppressed and so the material exhibits weak anisotropy. If the spin-orbit interaction is greater than the crystal field energy (CEF < **L**·**S**) then the external field acts on the total magnetic moment $\mu_J = \mu_L + \mu_s$ and so has to act against the pull of the crystal field which may be very strong, and hence the material exhibits strong anisotropy. A material axis is defined as 'easy' where the external field required to magnetise the sample to saturation is smaller when compared to 'hard' axes. For the case of hexagonal close packed (hcp) Cobalt, the c-axis is its easy axis while the basal planes are hard axes.

For uniaxial materials the energy density of magnetocrystalline anisotropy can be expressed as a power series (O'Handley, 2000):

$$E_{MC} = \sum_n K_{un} \sin^{2n} \vartheta \tag{2.46}$$

Where ϑ is the angle between the magnetisation and magnetocrystalline axis and K_{un} are nth order magnetocrystalline anisotropy constants. It should be noted that 0^{th} order constant K_{u0} is independent of magnetisation and so has no meaning for anisotropy.

For cobalt in *hcp* the magnetocrystalline energy is often expressed to second order (O'Handley, 2000):

$$E_{MC} = K_{u1} \sin^2 \vartheta + K_{u2} \sin^4 \vartheta \qquad (2.47)$$

where K_{u1} and K_{u2} are anisotropy constants and ϑ is the angle between the magnetisation and magnetocrystalline axis, which is parallel to the c-axis of the crystal for this case. For cobalt, the anisotropy constants are reported as $K_1 = 4.5 \times 10^5 Jm^{-3}$ and $K_2 = 1.4 \times 10^5 Jm^{-3}$ at room temperature (Cantu-Valle et al., 2015). As both values are positive this indicates that the c-axis for hcp cobalt is the easy axis.

Permalloy ($Ni_{81}Fe_{19}$) exhibits zero magnetocrystalline anisotropy and so for permalloy samples shape anisotropy effects constrain the magnetisation (Yin et al., 2006). This makes permalloy an attractive material for studying the effects of geometry on magnetic properties.

2.2.5 Demagnetising field and shape anisotropy

Demagnetising fields and their associated energy are the result of long-range magnetostatic interactions. If a uniformly magnetised sample is considered it can be considered using the dipole model to have magnetic charges residing at opposite surfaces of the magnetisation axis (figure 2.7). Under this consideration, there is a field directed through the material that opposes the magnetisation and it is this field that is known as the demagnetising field.

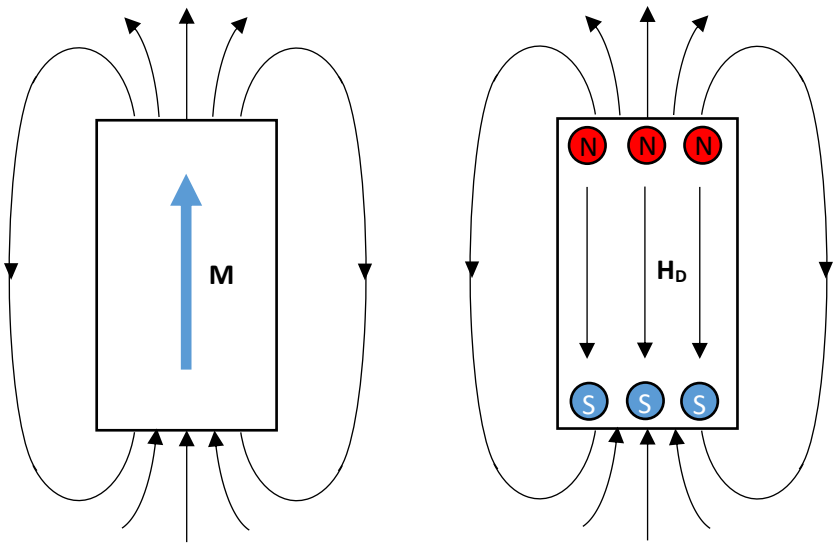

Figure 2.7: Illustration of demagnetising field $\mathbf{H_D}$ *arising from magnetisation* **M**.

The demagnetising field and associated magnetostatic energy density can be written for a general case as (O'Handley, 2000):

$$\mathbf{H_D} = -\boldsymbol{D} \cdot \mathbf{M} \tag{2.48}$$

$$E_{MS} = -\frac{\mu_0}{2}\mathbf{M} \cdot \mathbf{H_D} \tag{2.49}$$

where $\mathbf{H_D}$ is the demagnetising field, $\boldsymbol{D}$ is a tensor of demagnetisation factors, $\mathbf{M}$ is magnetisation, E_{MS} is the energy density and μ_0 is the permeability of free space.

Shape anisotropy is the tendency for the magnetisation to have a preferential axis for magnetisation due to the demagnetising field, and is proportional to the difference in demagnetisation field between two orthogonal axes, i.e. from equation 2.26:

$$H_{Shape} = M\left(D_x - D_y\right) = M\Delta D \tag{2.50}$$

As the structures examined in Chapters 4 and 5 are mostly comprised of high aspect ratio (aspect ratios of the order of 30 and 10 respectively) cylindrical nanowires, the shape anisotropy for infinite cylinders is considered here. For the case of a general ellipsoid the demagnetising factors sum to unity (SI units), and for the case of an infinite cylinder where the cylinder axis is parallel with the z-axis, the factors are simply D_{11}= D_{22} = 0.5 with remaining factors equal to zero. If a magnetisation vector in the x-z plane is considered, with θ being the angle the vector makes with respect to the z-axis (and hence cylinder axis), then the energy associated with shape anisotropy becomes (Osborn, 1945):

$$E_{MS} = \frac{1}{2}\mu_0 {M_S}^2 \begin{bmatrix} \sin\theta \\ 0 \\ \cos\theta \end{bmatrix} \begin{bmatrix} 1/2 & 0 & 0 \\ 0 & 1/2 & 0 \\ 0 & 0 & 0 \end{bmatrix} \begin{bmatrix} \sin\theta \\ 0 \\ \cos\theta \end{bmatrix} \tag{2.51}$$

$$E_{MS} = \frac{1}{4}\mu_0 {M_S}^2 \sin^2\theta \tag{2.52}$$

As can be seen from this expression, it is preferential for the magnetisation to align with the cylinder axis, i.e. when θ = 0°.

As shape anisotropy and magnetocrystalline anisotropy are competing energy terms, it is worth considering at what aspect ratio for a cylinder does shape anisotropy become dominant. By setting the shape anisotropy energy term to be greater than or equal to the magnetocrystalline energy term the following expression is obtained:

$$E_{MC} \leq \frac{1}{2}\mu_0 {M_S}^2 \Delta D \tag{2.53}$$

which can be rearranged for ΔD:

$$\Delta D \geq \frac{2E_{MC}}{\mu_0 {M_S}^2} \tag{2.54}$$

Using the material parameters for hcp Cobalt, E_{MC} = 5.9x10^{5}Jm^{-3} and M_s = 1425x10^{3}Am^{-1} (Cantu-Valle et al., 2015), then $\Delta D \geq 0.46$. For a cylinder of finite length the demagnetising factors have to be approximated using the formulations for an ellipsoid. Using the relationships $\Delta D = D_x - D_z$, $D_x = D_y$ and $D_x + D_y + D_z = 1$, then the calculated value for D_z using the previous result is D_z=0.025. From Okoshi's work, this D_z value corresponds to a cylinder of aspect ratio of approximately 7 (defined as cylinder length/diameter) (Okoshi, 1965). As the cobalt nanowires studied in this thesis have aspect ratios of approximately 10, it is therefore expected that shape anisotropy will contribute more than magnetocrystalline anisotropy for them.

2.2.6 Magnetic domains

The exchange coupling is a relatively short range force and as such over larger areas the dipole interaction is important. If every moment is aligned in the same direction, as in figure 2.8(a), then this energy becomes a significant contribution to the overall energy of the material.

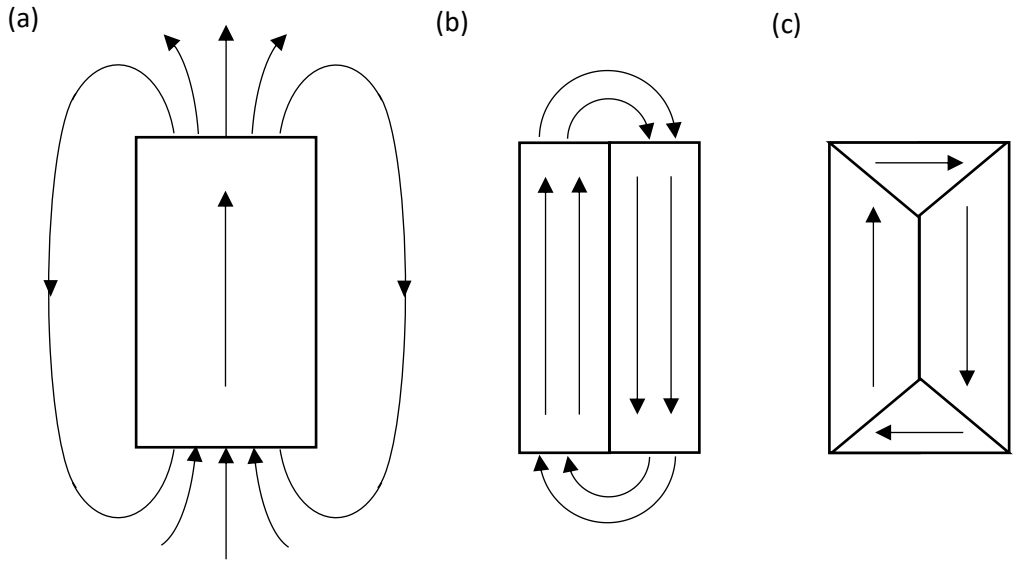

Figure 2.8: Representation of reduction of demagnetisation energy by forming closed loops; (a) single domain, (b) partial closed loop by two anti-parallel domains, (c) complete flux closure from four orthogonal domains.

To reduce this dipolar energy, bulk ferromagnetic materials have a tendency to form distinct regions called magnetic domains (Hubert and Schäfer, 1998). By aligning domain regions anti-parallel the overall magnetostatic energy is reduced (figure 2.8(b)) and the fields from each tend to cancel. With multiple domains the material can form flux closure loops to eliminate most of the extraneous magnetic field and minimise the magnetostatic energy (figure 2.8(c)). This is why not all ferromagnetic samples have a spontaneous magnetic field (i.e. a piece of iron does not typically act as a permanent magnet).

If two anti-parallel domains have only an atomic boundary between them, then the exchange energy at that boundary will be very large (O'Handley, 2000);

$$E_{ij} = -2S^2\mathcal{J}\cos\theta_{ij} = 2S^2J \tag{2.55}$$

where θ_{ij} = 180° = π radians.

If instead the angle between adjacent spins is changed incrementally across *N* spins, then this energy is reduced by a factor of approximately π/*N*. If *N* is sufficiently large then equation 2.55 can be expanded to (O'Handley, 2000):

$$E_{ij} \approx S^2\mathcal{J}{\theta_{ij}}^2 \approx S^2\mathcal{J}\left(\frac{\pi}{N}\right)^2 \tag{2.56}$$

Evidently this relation favours very large N, tending towards infinity if only exchange energy is considered. However, anisotropy competes with it and so N becomes the balancing factor between the two. The region of material that the N atoms takes up is known as a domain wall. There are a number of different types of domain wall which depend on the geometry of the magnetic structure being investigated.

For thin films the standard examples are the Bloch wall, where the magnetisation rotates out of the film plane, and the Néel wall, where the magnetisation rotates within the plane of the film. Bloch walls are more favourable as the film thickness increases as the magnetostatic energy due to the out of plane component decreases. Because of this, Néel walls become more preferential at low thicknesses (Hubert and Schäfer, 1998). Nanowires exhibit their own types of domain walls and are covered in more detail in section 2.3.

The theoretical width of a 180° domain wall in a uniaxial crystal is given by (Hubert and Schäfer, 1998):

$$W_L = \pi\sqrt{\frac{A}{K}} \tag{2.57}$$

where W_L is the wall width, A is the material exchange stiffness constant and K is an anisotropy constant. For cobalt with parameters A=3.1x10^{-11}Jm^{-1} and K=4.5x10^{5}Jm^{-3} (Cantu-Valle et al., 2015), the typical wall width calculated using equation 2.57 is W_L=26nm; and for permalloy with parameters A=1.3x10^{-11}Jm^{-1} and $K=\frac{1}{2}\mu_0 M_S^2$=4.6x10^{5}Jm^{-3} (using equation 2.50 assuming ΔD=1 and M_s=860x10^{3}Am^{-1}) (Gunnarsson et al., 2005), the typical wall width is W_L=17nm.

2.2.7 Hysteresis

A common practice when investigating magnetic samples is to examine hysteresis loops, which describe how the magnetisation changes as a function of applied external field over a cycle from H_{Ext} = 0 to H_{Ext} = H to H_{Ext} = -H and finally to H_{Ext} = H once more (Hubert and Schäfer, 1998). An example of such a loop without the initial 0 to H segment is shown in figure 2.9.

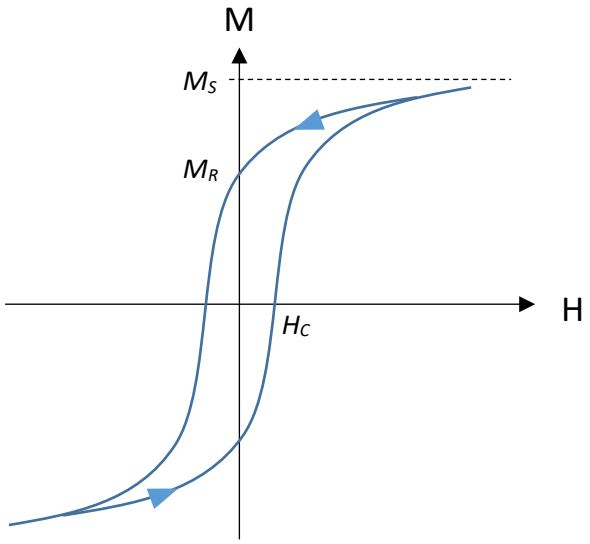

Figure 2.9: Sketch representation of a typical ferromagnetic hysteresis curve.

With no externally applied field, domains arrange to reduce the demagnetisation energy (figure 2.10(a)). In the presence of a small external field, the domain walls are displaced in such a way to increase the volume of the domains with the largest components of M with respect to H (figure 2.10(b)). As the applied field increases, this process continues until eventually a point is reached where the domain wall motion is completely pinned (figure 2.10(c)). At this point there are often domains that remain unaligned with respect to the external field. As the field is increased further the magnetisation in these domains must rotate to align with the field (figure 2.10(d)) so as to reduce the potential energy. This

rotation is energetically costly as the magnetisation must be rotated away from 'easy-axes' within the material, i.e. preferable magnetisation directions due to anisotropy. When the external field is further increased there comes a point where the magnetisation of the sample is fully aligned with the external field (figure 2.10(e)) and the sample is at saturation (M_S in figure 2.9).

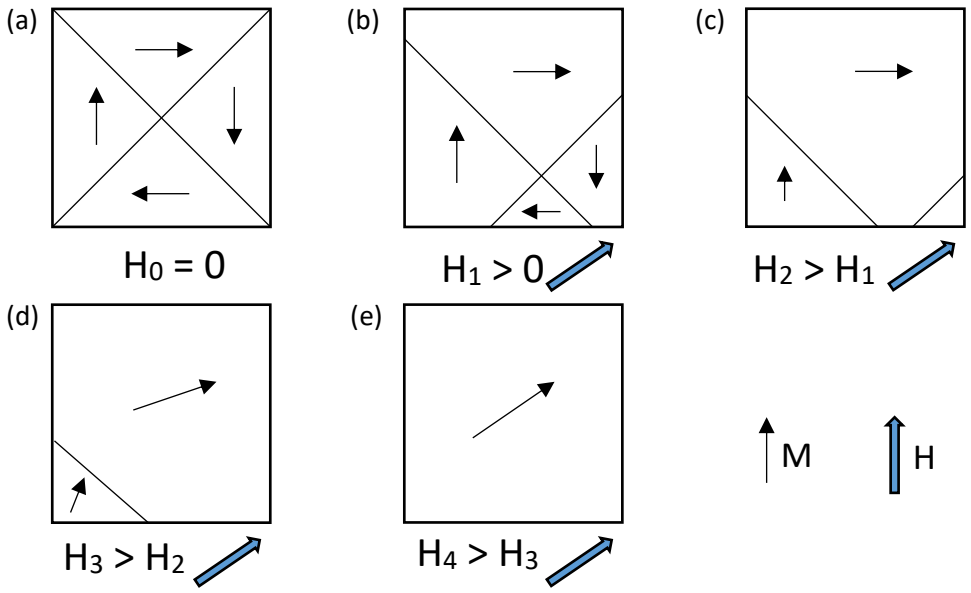

Figure 2.10: Two-dimensional representation of domain size changes with an externally applied field; (a) domain pattern with no external field, (b) domain pattern with an externally applied field greater than zero, (c) point where all wall motion is pinned, (d) onset of rotation of magnetisation, (e) sample at saturation magnetisation. Black arrows indicate the direction of the magnetisation, M, for the domains; blue arrows represent the direction of the applied external field, H.

When the field is reduced, the magnetisation rotates back to its easy-axes without hysteresis (i.e. rotation of the magnetisation is a largely reversible process). As the field is decreased further, domain walls begin moving across the sample again. The motion of the domain walls can be impeded due to defects in the material, and so tends to consist of abrupt jumps between localised energy minimums (known as Barkhausen jumps or noise). Because of this, domain wall motion causes energy to be lost and is an irreversible process, leading to the M-H curve opening, exhibiting hysteresis. This also tends to result in a remanent magnetisation (M_R in figure 2.9) for the material when the external field is reduced to zero. The field applied in the reverse direction that is required to return the magnetisation to 0 is known as the coercive field (H_C in figure 2.9) (O'Handley, 2000).

2.3 Domain walls in magnetic nanowires

Nanowires exhibit a large shape anisotropy favouring one dimension, that of the wire axis. If the material has a low or negligible magnetocrystalline anisotropy (such as permalloy, $Ni_{81}Fe_{19}$) then the shape anisotropy dominates. Provided that the nanowire dimensions are sufficiently small, nanowires tend to consist of a single domain, or for longer lengths, a series of alternating domains separated by walls. As the other dimensions are more constrained than in thin films or bulk material, the type of domain walls that arise have more simplistic forms. During hysteresis cycles where the external field has a component parallel with the wire axis, the magnetisation reversal is typically driven by the nucleation and propagation of domain walls along the wire (Del Atkinson et al., 2003).

2.3.1 Planar nanostrips

For 2D planar nanowire strips, the commonly observed walls are the transverse (figure 2.11(a)), vortex (figure 2.11(b)) and asymmetric transverse walls (figure 2.11(c)) domain walls. A transverse wall is similar to a Néel wall in a thin film: the magnetisation rotates by 180° within the plane of the nanowire. The vortex wall features a closed flux loop around a central core that points out of the wire plane. The asymmetric transverse wall is similar to the transverse wall but with the transverse component canted at an angle. The dimensions of the wire play an important part in determining which of these wall types is preferable, as shown by the phase diagram in figure 2.12. Generally, in thicker and wider nanowires vortex domain walls are more energetically favourable due to a reduction in magnetostatic energy perpendicular to the strip when compared to transverse walls. In thinner wires this magnetostatic energy contributes less than the contribution of exchange energy from forming a vortex and so transverse walls are the preferred type (McMichael and Donahue, 1997). Asymmetric transverse walls occupy a transitional region between these two walls above a threshold width.

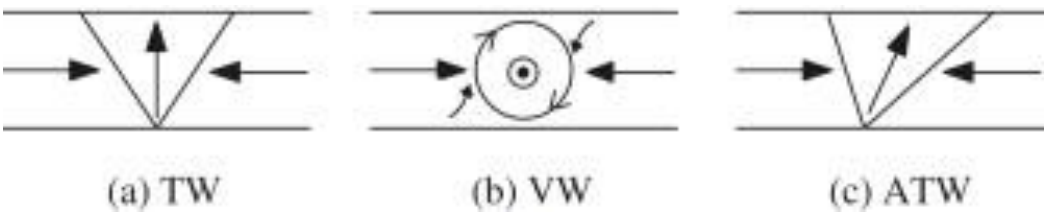

Figure 2.11: Schematic representation of magnetisation in domain walls in a 2D nanowire strip; (a) Transverse wall, (b) Vortex wall, (c) Asymmetric transverse wall. Image reproduced from Nakatani et al. (Nakatani et al., 2005).

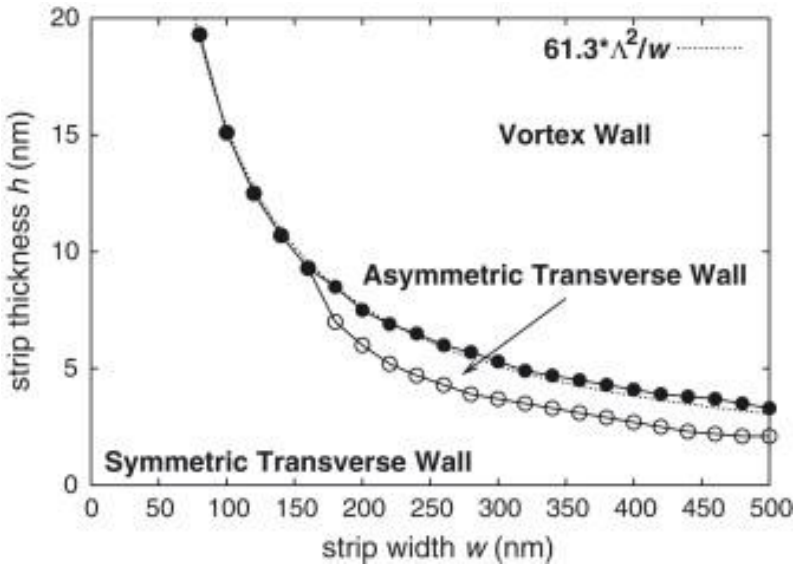

Figure 2.12: Phase diagram of domain wall types in planar nanowires. Image reproduced from Nakatani et al. (Nakatani et al., 2005).

The propagation of domain walls through nanowires is of particular interest for real-world applications. It has been shown that it is possible to propagate domain walls through a nanowire by the application of an external magnetic field and/or the application of an electric current through the wire (Salhi and Berger, 1993). For the purposes of this thesis it is field-driven motion (i.e. application of an external magnetic field only) that is of most interest. In planar nanowires, when a domain wall is driven by either method and propagates through the wire, the velocity of the walls through the wire is initially linear with field. At a critical point however, the velocity abruptly decreases before slowly returning to a linear increase again at much higher driving potentials; however in this second regime the domain walls are topologically unstable (figure 2.13). This effect is known as the Walker breakdown of domain wall velocity, and for field-driven walls the field value at which it occurs is called the Walker field (Schryer and Walker, 1974). The Walker field depends on the sample geometry and can be expressed as (Mougin et al., 2007):

$$H_W = 2\pi\alpha M_s |D_y - D_x| \tag{2.58}$$

where H_W is the Walker field, α is the intrinsic Gilbert damping parameter (see section 3.9), M_s is the saturation magnetisation and D_x, D_y are demagnetisation factors (see section 2.2.5).

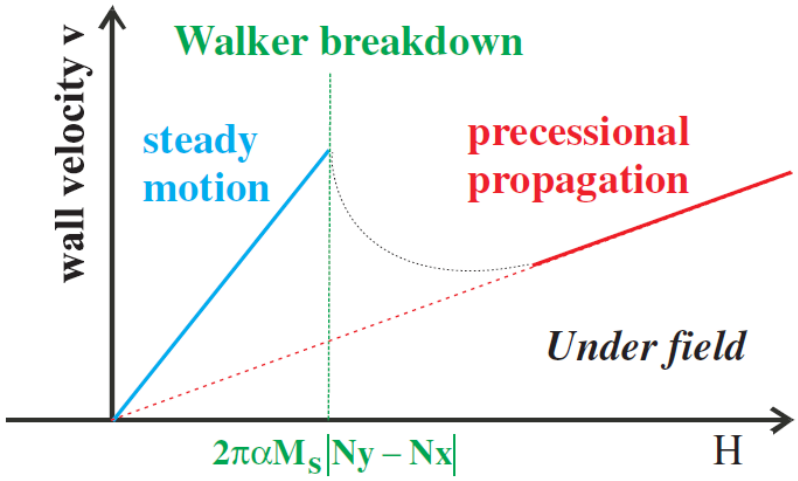

Figure 2.13: Diagram showing the relationship between field-driven only domain wall velocity and applied external field, including Walker breakdown. Image reproduced from Mougin et al. (Mougin et al., 2007).

This phenomenon is due to the nucleation of anti-vortex cores at the edges of the wall caused by attempted precession around the applied field. These nucleations cause the wall to periodically switch chirality (Nakatani et al., 2003).

Domain wall motion in planar magnetic nanostrips has been studied extensively; the discussion here will focus upon efforts to reduce or suppress the onset of Walker breakdown, the pinning of domain walls within nanostrips and the behaviour of domain walls at nanostrip junctions. Atkinson *et al.* measured the domain wall velocity in a 200nm wide permalloy track with two 90° curved bends and observed an extremely high velocity of 1500ms^{-1} at an applied external field of 4.9mT. This result did not agree with micromagnetic simulations which implied the onset of Walker breakdown at 1.5mT. The author put forward the suggestion that the discrepancy was due to the domain wall changing shape in such a way to accommodate a higher than expected speed (D. Atkinson et al., 2003). As a possible explanation for this, by looking at the work of Kunz *et al*. and Bryan *et al*., it was observed that an external field applied transverse to the wire length altered the width of transverse domain walls with a dependence on the wall chirality, and also that this change in wall width could enhance the wall velocity and shift the onset of Walker breakdown to a higher field magnitude (Bryan et al., 2008; Kunz and Reiff, 2008). Given the curved 90° bends present in Atkinson *et al*.'s study, it is possible that the increased speed observed was due to this effect. As part of this thesis concerns the application of external fields at non-orthogonal angles to nanowires (which can be

separated into an axial drive-field and a transverse offset) it will be of note if similar or unexpected behaviour occurs in cylindrical wires.

Using micromagnetic simulations Seo *et al.* showed that under the application of an oblique field to nanostrips the Walker breakdown occurs at two field values and that within the range between the two breakdown occurrences the chirality of the wall in motion can be selectively switched by the external field (Seo et al., 2010). Such control of the wall chirality is important for pinning effects, for as shown by Atkinson *et al*. the chirality of a wall dictates whether it is pinned or not at triangular notches engineered into a nanostrip (Atkinson et al., 2008). This was also shown experimentally by Eastwood *et al*. for vortex domain walls. An obliquely applied field can stabilise the chirality of the vortex wall, which allows for control of its pinning upon notch defects in the strip (Eastwood et al., 2011). The pinning of domain walls at topographical defects is notable and has been considered as a way to store information for computer memory as noted by the above references. As this study ultimately looks at nanowire junctions, the pinning of walls at such junctions should be considered.

Faulkner *et al*. fabricated three-wire nanostrip Y-junctions and investigated the domain wall dynamics for such structures. It was observed that when a domain wall was injected into one of the two input wires the wall would become pinned at the junction, which causes the coercive field of the structure to be reduced compared to one without any injected domain walls. When a domain wall was injected into each of the two input wires they would combine and cause the remaining wire to switch, reducing the coercive field further compared to the single domain wall case (Faulkner et al., 2003). It is also shown by Allwood *et al*. that it is possible to clone a domain wall using a Y-junction; i.e. a single domain wall travelling in one wire can split at the junction and create two domain walls with the same chirality that travel through the two remaining wires. They show that this cloning behaviour exists over a large range of wire widths for both the input and output wires, and that it is possible to further clone domain walls with successive junctions (Allwood et al., 2007). Petit *et al*. investigated the domain wall motion for a T-shaped junction of nanowires. They found that the T-junction acted as a gate for domain wall movement in the two parallel wires for transverse walls: when the magnetisation of the transverse wire was parallel with the chirality of the wall it was able to move freely across the junction, and when the magnetisation was anti-parallel the wall was strongly pinned at the junction (Petit et al., 2008). For a similarly T-shaped system but with the transverse wire disconnected from the parallel wires, O'Brien *et al*. observed that the stray field of a transverse wall passing the

transverse wire could induce switching of the transverse wire (O'Brien et al., 2012a). For systems with multiple domain walls, Kunz showed that for thin wires it is possible via control of the domain wall topology to cause collisions between two walls that either annihilate or preserve the two walls. The latter case can be used to depin one wall using another wall while preserving its information. The author warns however that in thicker films the walls will annihilate regardless because the magnetisation can rotate out of plane (Kunz, 2009). The interactions between domain walls with each other and at junctions may have relevance to similar situations arising in cylindrical wires, notably for the structures later considered in this thesis, which can exhibit both Y-shaped and cross-shaped junctions depending on the field geometry and component of magnetisation observed. However, all of the above are effects observed in 2D structures; when moving to 3D cylindrical nanowires the extra degree of freedom has an important effect on the domain walls observed and their dynamics.

2.3.2 Cylindrical nanowires

For 3D cylindrical nanowires two main types of domain wall, transverse (figure 2.14(a)) and Bloch point (figure 2.14(b)) domain walls, can be observed. The transverse wall is analogous to the transverse wall that appears in planar nanowires with the magnetisation rotating perpendicular to the wire axis. Bloch point domain walls are characterised by a localised point where the magnetisation vanishes; around this point the magnetisation forms a closed loop. In a similar fashion to planar nanowire strips, transverse walls are preferable in cylindrical wires with small diameters, while Bloch point walls are more favourable at larger diameters (figure 2.15). A third type of domain wall, asymmetric-transverse domain walls (figure 2.14(c)), are allowed as a metastable state but occupy the same regime as Bloch point walls though at a higher energy (figure 2.15) and so are less favourable (Ferguson et al., 2015).

Bloch point domain walls in particular have garnered some interest for research. Unlike 3D transverse walls, Bloch point domain walls have chirality and so can potentially act as bit carriers for digital media. They are also remarkably stable as the vortex ring provides flux closure and is topologically protected (Da Col et al., 2014), and have an intrinsic pinning effect at low-field values. This is due to the nature of the Bloch point being an atomically sharp change which causes the lattice to pin the wall at low fields.

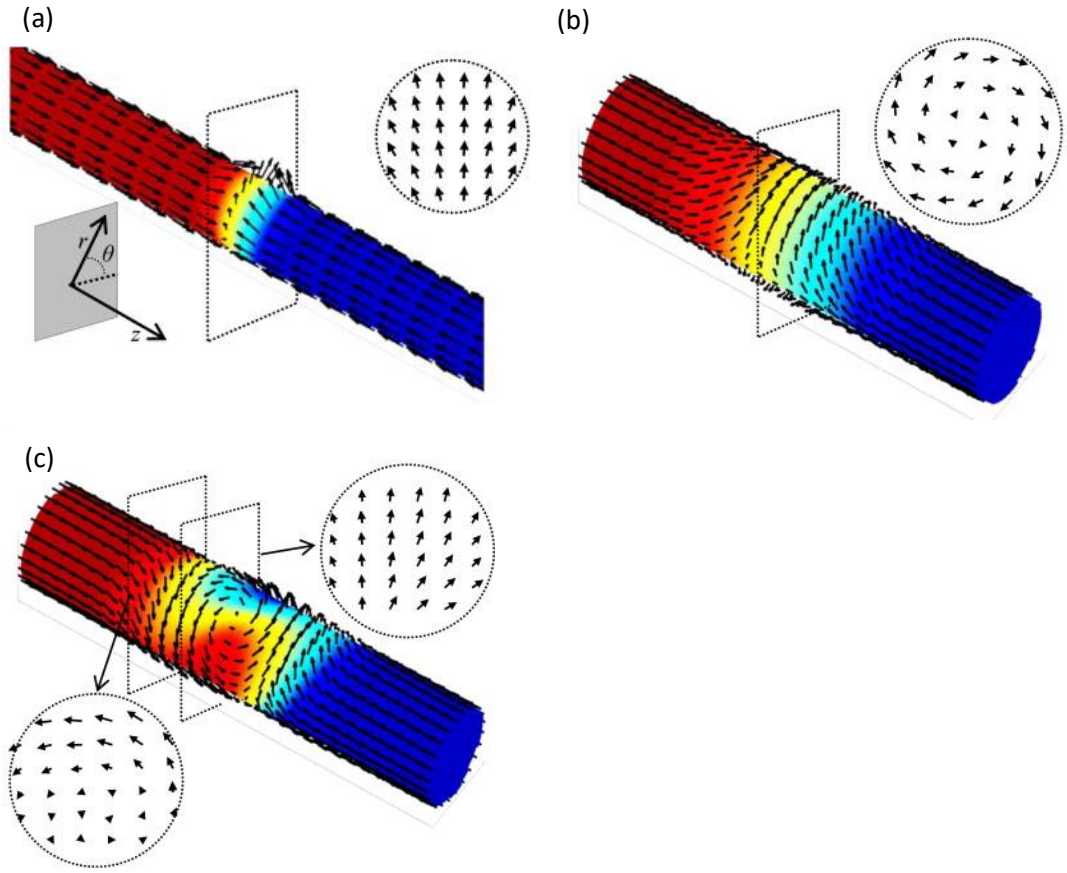

Figure 2.14: Schematic representation of magnetisation in domain walls in a 3D cylindrical nanowire; (a) Transverse wall, (b) Bloch point wall, (c) Anti-transverse wall. Image reproduced from Ferguson et al. (Ferguson et al., 2015).

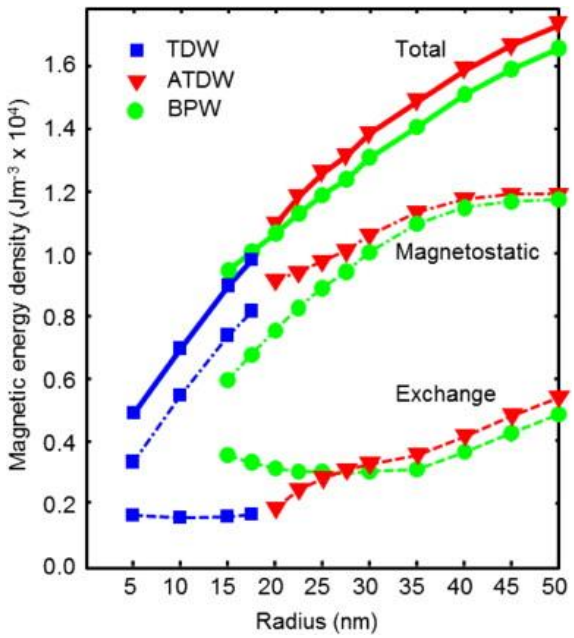

Figure 2.15: Phase diagram for domain wall energy contributions in cylindrical nanowires. Image reproduced from Ferguson et al. (Ferguson et al., 2015).

A large portion of the literature concerning domain walls in cylindrical nanowires has so far focused on the pinning of current-driven walls at constrictions, protrusions, or modulations in the nanowire diameter (Thiaville et al., 2005; Wieser et al., 2010). However one of the notable features of cylindrical nanowires explored in simulations is the absence of Walker breakdown. Yan *et al*. show that for current-driven transverse walls in permalloy nanowires the 3D nature of the wire allows the walls to rotate without changing shape as they propagate and hence avoid the effect of nucleation of turbulence-causing features due to precession. As a result, domain walls in cylindrical nanowires can reach much higher velocities before destabilising, about an order of magnitude greater than those typically seen in planar nanowires (Yan et al., 2010). Other simulation studies show this to be the case for field-driven domain walls, with Forster *et al*. showing that it applies to both transverse and Bloch point domain walls in simulated cobalt nanowires. In their study they observe transverse walls exclusively for diameters <20nm and Bloch point domain walls exclusively for diameters >20nm. They report that the velocity of the Bloch point walls exceed that of the transverse wall by a factor of 1.3, and observe velocities up to approximately 2000ms^{-1} (Forster et al., 2002). Piao *et al*. also show the velocity of Bloch point domain walls up to 2000ms^{-1} in simulations for an external field of 150mT in permalloy wires of diameter 50nm and length 2μm and that even at such high fields they maintain their shape. Their study also observed the intrinsic pinning of Bloch point domain walls with no observable motion for applied fields less than 32mT (Piao et al., 2013). It should be noted that while the Walker breakdown phenomena is absent, there is still a fundamental limit to the velocity of domain walls in 3D nanowires due to the onset of spin-wave emission – which is known as the spin Cherenkov effect (Yan et al., 2011).

The lack of experimental domain wall studies for cylindrical nanowires is due to the difficulty in both fabrication of more complex nanowires as well as the challenge in probing the domain pattern across the structure diameter. Efforts have been made to address this second point with the existence of Bloch-point domain walls being shown experimentally by Da Col *et al*. Their study used both surface and transmission X-ray magnetic circular dichroism – photoemission electron micrography (XMCD-PEEM) to observe the magnetic contrast of a Bloch point domain wall as well as its transmission shadow, and confirm its presence in an electrodeposited permalloy nanowire of diameter 70nm. The study also mentions that the wall was mobile under applied fields of 1-10mT (Da Col et al., 2014). Another study by Biziere *et al.* used electron holography in conjunction with transmission electron micrography (TEM) and micromagnetic simulations to probe the domain wall

structure in electrodeposited nickel nanowires with diameters between 55-85nm. In that diameter range they observed the walls transition from transverse into a hybrid structure (Biziere et al., 2013).

As of writing there appear to be no studies performed, simulation or experimental, of cylindrical nanowire junctions. This is likely again due to the great difficulty in fabricating such structures using the widely available techniques. As such, the overall aim of the PhD was to make use of the ability of two-photon lithography to place cylindrical nanowires into the spin geometry found in bulk spin ice materials, as a first step to investigating the properties and fabrication of complex 3D magnetic nanowire junctions and 3D artificial spin ice. Spin ice is discussed in the next section.

2.4 Spin ice

Spin ice is a class of material that has been the subject of much research in the last decade due to its interesting magnetic and physical properties. Chief amongst these are that they exhibit frustration and monopole-like defects.

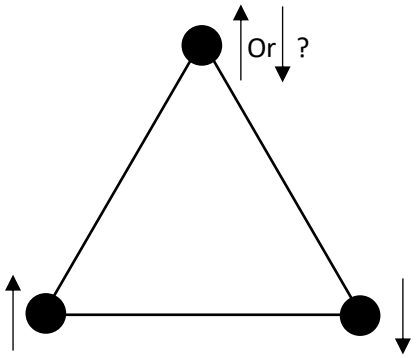

Figure 2.16: Example of a frustrated system. If three spins are arranged on an equilateral triangle the first two placed will align anti-parallel, the third however is frustrated as both spin-up and spin-down contribute equally to the energy distribution.

Frustration is defined as when the pairwise interactions within a system cannot be simultaneously satisfied. The classical example is that of three spins that have an anti-ferromagnetic interaction (i.e. preference to align anti-parallel) placed at the vertices of an equilateral triangle (figure 2.16). The first two spins placed align anti-parallel, minimising their energy, however the final spin creates the same energy regardless of its spin state (Claudine Lacroix, 2011). As the three spins are identical this creates a six-fold degenerate

ground state for the system. One of the earliest natural frustrated systems that was realised was ordinary water ice (Pauling, 1935).

Spin ice takes its name for sharing similar geometrical frustration as found in ordinary water ice in its hexagonal crystal form, where the proton (hydrogen atom) displacement between oxygen ions is on a tetrahedral lattice with four protons surrounding each oxygen atom. Each proton can be either close to, or far from, the central oxygen atom which leads to a six-fold degenerate minimum energy state, leading to frustration. Common spin ice materials are pyrochlore oxides, which have a chemical formula in the form of $A_2B_2O_7$ where A and B represent metals. For spin ice cases, A represents a rare earth magnetic ion (for example Dysprosium, Dy or Holmium, Ho). In pyrochlore spin ices the magnetic ions are similarly arranged on a tetrahedral lattice (figure 2.17(a)) and the crystal field constrains the magnetic spins (Bramwell and Gingras, 2001) to point into or out of the tetrahedron (figure 2.17(b)), analogous to the proton displacement in water ice (figure 2.17(c)). Spin ice also follows the 'ice rules' in analogous fashion, with the two-in/two-out state being preferable. This can be represented by the sum of the four spins, S_Δ, for each tetrahedral cell equating to 0:

$$\sum_\Delta S_\Delta^{z_1} + S_\Delta^{z_2} + S_\Delta^{z_3} + S_\Delta^{z_4} = 0 \qquad (2.59)$$

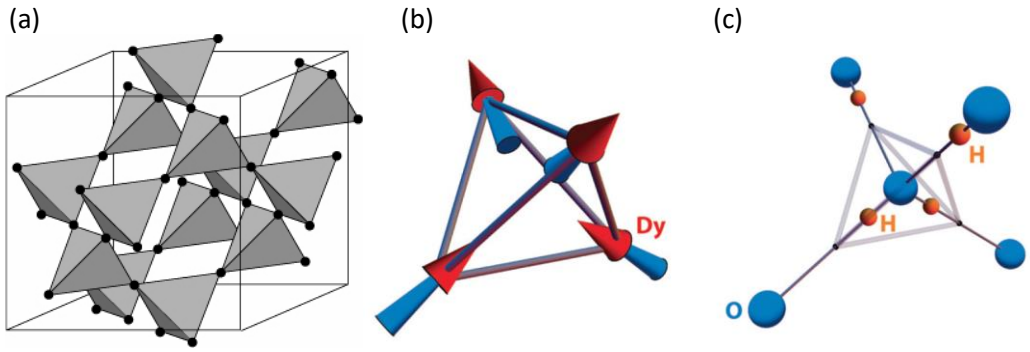

Figure 2.17: (a) Representation of the magnetic ion arrangement in a pyrochlore crystal lattice, image reproduced from Elhajal et al. (Elhajal et al., 2004)*, (b) Spin representation of a unit cell from the lattice shown in (a) with Dysprosium ions, (c) Representation of tetrahedral cell in water ice crystal showing proton (Hydrogen) displacement being analogous to spins in (b). Image reproduced from Castelnovo et al.* (C. Castelnovo et al., 2012).

An interesting property of spin ice that can also be observed in water ice is that, due to the effects of frustration, they have a non-zero residual entropy as temperature tends towards

absolute zero. An estimate of a value for this entropy for spin ice can be derived following the arguments Pauling used to estimate a value for water ice (Claudine Lacroix, 2011). For a system of N spins in a pyrochlore lattice there are $N/2$ upward and downward tetrahedra, which leads to $(2^4)^{N/2} = 4^N$ microstates. This however is an overestimate of the actual number of microstates as each spin is shared between two tetrahedra. To account for this Pauling's reasoning is used: the ground state for each tetrahedra is satisfied by the two-in/two-out state, which is met by 6 of the $2^4 = 16$ possible configurations of the four spins. In this case 2^2 states can be allocated per tetrahedra instead, and assuming that 6/16 satisfy the constraint then the ground state degeneracy, Ω_0 is:

$$\Omega_0 = (2^2)^{\frac{N}{2}} \left(\frac{6}{16}\right)^{\frac{N}{2}} = \left(\frac{3}{2}\right)^{\frac{N}{2}} \tag{2.60}$$

And so the corresponding entropy S_0 is:

$$S_0 = k_B \ln \Omega_0 = \frac{N k_B}{2} \ln\left(\frac{3}{2}\right) = 1.68 \mathrm{Jmol^{-1}K^{-1}} \tag{2.61}$$

Experimental measurements have been found to agree with this model (X Ke, 2007).

Another of the notable effects observed in pyrochlore spin ice is the emergence of monopole-like defects in the bulk material. These occur when the spins are in a three-in/one-out or one-in/three-out arrangement. If the spins are thought of using the magnetic dipole model (section 2.1.1) then each can be considered a pair of equal and opposite magnetic charges, and from the spin ice constraints each charge can be considered to lie within a tetrahedra on either end of the spin. Using this 'dumbbell' model (Jaubert and Holdsworth, 2011) it can be seen that for a two-in/two-out state the total charge in the tetrahedra is zero, but for a three-in/one-out state or vice versa there is a net magnetic charge at the localised area of $2p$ (where p is the charge of one of the poles comprising the spin). It should be noted that the creation of one of these monopole-like charges also creates an equal and opposite charge in an adjacent tetrahedra and breaks the ice rules. Due to the crystal lattice however, the monopoles can be moved separately through the bulk lattice by reversal of spins, allowing them to behave like delocalised magnetic charges within the bulk material that can be shown to obey a magnetic version of Coulomb's law (Castelnovo et al., 2008). These charges behave as dipoles where there is a tensionless string (known as a Dirac string) between the pole pairs. Such magnetic charges have been observed experimentally in bulk spin ice and manipulated to produce a magnetic equivalent of current (Bramwell et al., 2009).

While the physics of bulk spin ice is interesting, there are limited options for varying the material parameters, such as lattice spacing, as the crystal make up defines many of these. As such, in addition to studies on the pyrochlore bulk spin ice crystals, strides have been made in developing 2D artificial spin ice which can also exhibit properties such as monopole defects (Ladak et al., 2010). These are created by fabricating a lattice of elongated nano-islands from a magnetic material that are of small enough dimensions to be single-domain, such that the magnetisation of each is constrained along the island axis and approximates a classical Ising spin. Two types that have seen much attention are the square and Kagomé lattices (unit cells shown in figure 2.18).

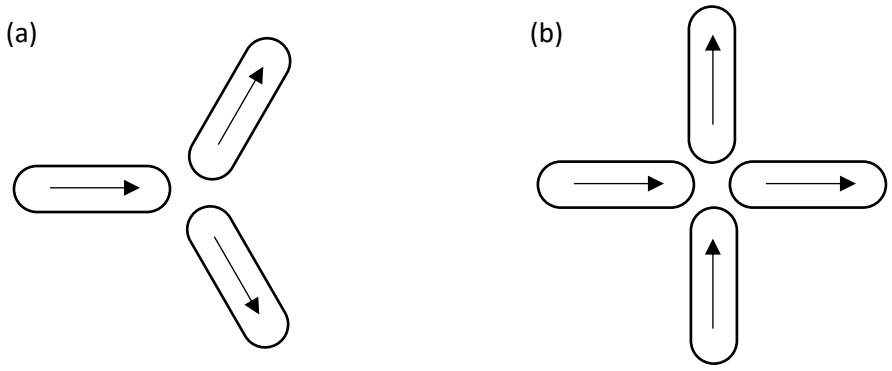

Figure 2.18: (a) Representation of unit cell for Kagomé lattice in one-in/two-out state; (b) Representation of unit cell for square lattice in two-in/two-out state.

The simplest way to realise a 2D equivalent of spin ice is by arranging spins such that four meet at a vertex in a square geometry (R. F. Wang et al., 2006). This arrangement maintains the possible configurations from a pyrochlore vertex, however the square arrangement does not allow for equal interaction energy between the four islands as the separation distance for opposite islands is greater than that for adjacent, leading to a further separation of energies within the two-in/two-out state. This also has the effect of creating a single long-range ordered antiferromagnetic ground state (Cumings, 2011). As a consequence any monopoles that nucleate are constrained by a string of finite tension. Hence the monopoles in these systems are not equivalent to those seen in the bulk material.

The Kagomé lattice is comprised of three islands arranged at 120^{o} at each vertex. This arrangement mimics the pattern of spins in a pyrochlore lattice when viewed along the [111] direction if the out of plane spins are ignored (Qi et al., 2008). While the interaction energy is identical for the three islands, the possible energy states are limited to

degenerate two-in/one-out and vice versa, or three-in/out. Crucially, these systems do not possess the fourth out-of-plane spin, and so are not ideal to capture the physics of bulk spin ice.

In addition to the disconnected islands type of artificial spin ice, versions that are a connected network of nanowires have also been investigated. For these the monopole-like defects and their movement through the lattice are governed by domain wall motion. Ladak *et al*. have shown across two studies that the monopole defects observable in such connected networks are the result of the pinning of domain walls at the structure vertices. They have shown this for cobalt honeycomb lattices with wire dimensions 1000nm by 100nm by 20nm both in micromagnetic simulations and experimentally with close agreement using magnetic force microscopy (MFM). The domain walls are seen to be injected into the lattice from its edges. It is then observed that either a single domain wall or a pair of domain walls can create the monopole defect, and additionally that the introduction of domain walls can be controlled by use of a patterned injection pad (Ladak et al., 2010; S. Ladak et al., 2011). In the above studies it was noted that for permalloy systems only the domain wall pair method of domain wall introduction exists, and in a follow up study they look in detail at the pinning of the two walls due to the repulsive interaction between them. They map the potential energy well of the interaction and discuss a model for the interaction (Sam Ladak et al., 2011). Similar cases are expected to arise in a junction of cylindrical nanowires; however the differing nature of the domain walls could lead to other effects being observed.

In true spin ice, the interaction at the vertices has perfect symmetry. However as the 'spins' in artificial spin ice are not point sources this is not necessarily the case. This is highlighted by Rougemaille *et al*. in their consideration of the vertices in disconnected island Kagomé lattices – they observe from simulations that the magnetisation at the ends of the islands facing into the vertex begins to curl which breaks the symmetry of the 'forbidden' 3-in/out state. However, they make note that such an effect may not be observable in real samples due to extrinsic factors such as the alignment of the external field or slight variations in the nanopatterning between the islands (Rougemaille et al., 2013).

In connected lattices there is also the issue of path selectivity of the domain walls. Zeissler *et al.* show in their study that the path chosen by a transverse domain wall at a Y-junction in a honeycomb lattice is influenced by the chirality of the wall, which leads to non-random Dirac chain paths taken by the monopole defects through the lattice. They suggest the

inducement of Walker breakdown to suppress this non-random selection due to the chirality-switching behaviour that occurs in the regime above the Walker field (Zeissler et al., 2013). This chirality based path selection at Y-junctions is also shown to exist for vortex walls by Pushp *et al*. who go into a detailed consideration of topological charges of the wall leading edge and the vertex. They introduce methods of controlling the injected domain wall chirality and use their model to explain the formation of Dirac chains in a honeycomb lattice (Pushp et al., 2013). However a study in response to this performed by Walton *et al*. show in simulations at zero-temperature that the propagation field for vortex walls in such a lattice is greater than the Walker field, and as such the induced chirality switching of the walls due to this removes the predictable path selection. They then go on to confirm that this is also the case experimentally at room temperature (Walton et al., 2015).

Less has been done on connected square artificial spin ice lattices, however a study by O'Brien *et al*. on the interaction of two domain walls at a cross-shaped vertex indicated complex behaviour. They observed that walls of the same chirality assisted each other in depinning from the vertex, whereas walls of opposite chirality had asymmetric depinning behaviour and could even suppress the depinning of walls from the vertex (O'Brien et al., 2012b).

When considering a 3D artificial spin ice or nanowire junction, it is unknown whether such constraints on path selection should occur as the extra degree of freedom should allow transverse walls to rotate to avoid pinning effects, while the Bloch point domain wall is highly symmetric.

There have been some recent attempts at fabricating artificial 3D spin ice, such as by stacking the orthogonal arrays of nano-islands comprising a square lattice so that the distance between the dipolar interactions is equivalent for all spins (Chern et al., 2014). In this case however there remains a long-range ordered ground state that is absent in pyrochlore spin ice. Another attempt filled the inverse space of an opal lattice creating a tetrahedral-like lattice of connected cobalt where the ice-rules could be applied (Mistonov et al., 2013). In this approach, however, the local magnetisation of a basic unit is very inhomogeneous, and parameters such as spacing are again restricted by that of the opal lattice.

2.5 Two-photon polymerisation

Two-photon lithography (TPL) shares much in common with standard photolithography; the key difference is that TPL makes use of a 3rd order optical process rather than direct absorption of single photons.

In typical photolithography a chemical resist is used as a medium to form lithography templates. The resists contain a number of photoinitiators that undergo a transition upon absorbing a photon matching the energy difference between the transition states. This transition triggers a chemical change within the resist, causing either polymerisation (negative resist) or de-polymerisation (positive resist). This is a linear reaction in the form:

$$\mathbf{P}(\omega) = \varepsilon_0 \chi(\omega)\mathbf{E}(\omega) \tag{2.62}$$

where **P** is the induced polarisation in the material, ε_0 is the permittivity of free space, χ is the linear susceptibility of the material, **E** is the electric field component of the incident light and ω is the frequency of the incident light. The amount of light absorbed by the material is proportional to the intensity of the incident light, which in turn is proportional to the energy squared.

In general however, the response of a material to light need not be linear in which case the above can be expanded to (Andrzejewska, 2016):

$$\mathbf{P} = \mathbf{P^{(1)}} + \mathbf{P^{(2)}} + \mathbf{P^{(3)}} + \cdots \tag{2.63}$$

where

$$\mathbf{P^{(1)}} = \varepsilon_0 \chi^{(1)}\mathbf{E}$$

$$\mathbf{P^{(2)}} = \varepsilon_0 \chi^{(2)}\mathbf{E} \cdot \mathbf{E}$$

$$\mathbf{P^{(3)}} = \varepsilon_0 \chi^{(3)}\mathbf{E} \cdot \mathbf{E} \cdot \mathbf{E}$$

Etc.

From above, the rate of single-photon absorption is proportional to $\mathbf{E \cdot P^{(1)}}$. It follows that the ability to absorb two photons depends on the square of the intensity and so is proportional to $\mathbf{E \cdot P^{(3)}}$. As such, two-photon polymerisation (TPP) is a 3rd order optical process where two photons, each with energy less than the energy difference between states, are absorbed near-simultaneously to trigger the transition (figure 2.19). As this is a higher order process, TPP can only occur in a region where the intensity of incident

photons is above a threshold value. Due to this requirement TPP is usually constrained to a region within the focal point of a highly focused laser.

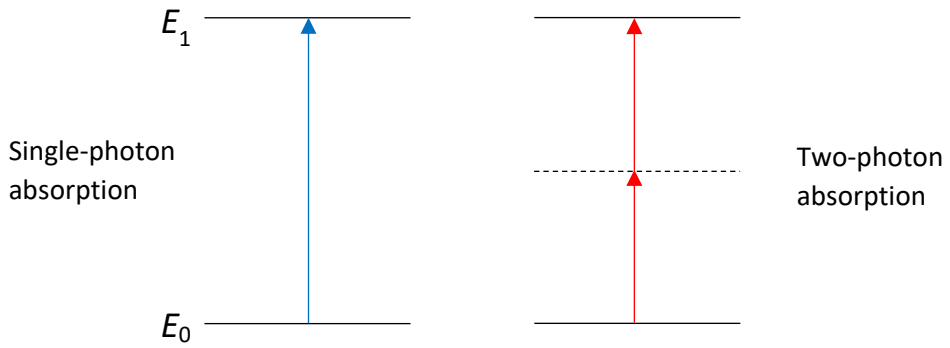

Figure 2.19: Representation of the energy schemes for single and two-photon absorption.

Because of the localised nature of this process, compared to the blanket-area effect of standard photolithography, it is possible to use the TPP region as a voxel (3D pixel) by translating the focal point throughout the resist layer. In this way, arbitrary volumes of the resist can be exposed in an analogous fashion to 3D additive manufacturing (Jeon et al., 2006).

If the case for a positive photoresist is considered, then the dimensions of the voxel can be determined by starting from the rate equations for the chemical reaction of the photoinitiators, following the derivation presented by Cao *et al.* (Cao et al., 2013). In positive resist an organic compound forms a stable polymer, which is decomposed when exposed to light of appropriate wavelength for the contained photoinitiators to form volumes that are soluble and able to be removed in a development process. The initial excitation is a reversible reaction, with the elevation of an amount of the photoinitiator in the ground state (M^G) to the excited state (M^*). The excited state can then undergo a non-reversible reaction to form the soluble product (P). As such there are three rate constants (k_1, k_2, k_3) to consider:

$$M^G \underset{k2}{\overset{k1}{\rightleftharpoons}} M^* \xrightarrow{k3} P \tag{2.64}$$

It is possible to show the relation between the amount of photoinitiator in the ground state and the amount in the excited state as a function of time using the rate equations:

$$M^G = M_0 \exp\left(-\frac{k_1 k_3}{k_2 + k_3} t\right) \tag{2.65}$$

where M_0 is the initial concentration of photoinitiator in the ground state. The first rate constant k_1 can be described in terms of the absorbed incident light:

$$k_1 = \Phi\delta\left(\frac{I}{h\omega f\tau}\right)^2 \tag{2.66}$$

where Φ is the quantum efficiency of the reaction, δ is the two-photon absorption cross-section, I is the intensity of the incident light, h is Planck's constant, ω is the frequency of the incident light, f is the repetition rate of the laser source and τ is the pulse width of the laser.

The second rate constant k_2 can be approximated as roughly equal to the Einstein coefficient of spontaneous emission A_E, while the third rate constant can be considered constant for the duration of the interaction ($k_3 = C_0$). Substituting for these physical terms, equation 2.41 now becomes:

$$M^G = M_0 \exp\left[-\frac{C}{f\tau}\left(\frac{I}{h\omega}\right)^2 t\right] \tag{2.67}$$

$$C = \frac{\Phi\delta C_0}{A_E + C_0} \tag{2.68}$$

The intensity profile for a Gaussian beam is given by:

$$I = I_0\left[\frac{{w_0}^2}{w^2(z)}\right]\exp\left[\frac{-2{r_L}^2}{w^2(z)}\right] \tag{2.69}$$

where w_0 and w(z) are the beam widths at the waist and position z respectively, r_L is the radial distance from the beam centre and I_0 is the intensity at the centre of the laser focus:

$$I_0 = \frac{2\eta P_{laser}}{\pi {w_0}^2} \tag{2.70}$$

where η is the transmittance of the objective lens and P_{laser} is the peak laser power.

This allows for further substitution into equation 2.43:

$$M^G = M_0 \exp\left\{-\frac{Ct}{f\tau(h\omega)^2}\left[\frac{2\eta P_{laser}}{\pi {w_0}^2}\right]^2 \exp\left[\frac{-4{r_L}^2}{w^2(z)}\right]\right\} \tag{2.71}$$

There is obviously a threshold amount of photoinitiator that can be excited within the beam, so by setting M^G to M_{th} it is possible to rearrange for the threshold radius r_{th} and hence the diameter of the voxel, d_{Vox}:

$$d_{Vox} = 2r_{th} = w(z)\sqrt{ln\left[\frac{4C\eta^2 P_{laser}^2 t}{f\tau\left(\pi h\omega w^2(z)\right)^2 ln\frac{M_0}{M_{th}}}\right]} \tag{2.72}$$

For negative resist a similar derivation as above can be made (Zhou et al., 2015). However, where in positive resist the photoinitiator is used to make soluble regions, in negative resist the photoinitiator generates radicals which cause monomers to bond and form strong polymer chains. Hence, for negative resist, the negative region around the desired structure shape is exposed.

The structures examined in chapter 5 were all produced using a positive photoresist and the fabrication procedure is covered in the next chapter.

Chapter 3 – Methodology

3.1 Introduction

During the course of this PhD a significant amount of work has been put into the development of a magneto-optical Kerr effect (MOKE) magnetometer measurement system as a useful tool for characterising the properties of arrays of magnetic nanostructures. This section will give an outline of the underlying theory of the effect and will give details of the MOKE magnetometer's construction, operation and optimisation of the signal-to-noise ratio (SNR) on 2D structures consisting of permalloy nano-islands and on 3D structures comprised of cobalt nanowires. Another significant methodology utilised within this thesis is micromagnetic simulations. Therefore the underlying theory and initial preparation work for numerical simulations is presented, along with an overview of the types of packages used. The fabrication of magnetic nanostructures using two-photon lithography, and supporting imaging techniques are also briefly discussed.

3.2 MOKE background theory

The MOKE describes the interaction of incident polarised light with the magnetisation of a ferromagnetic material, which results in a change of the reflected light intensity and polarisation. When linearly polarised light is incident upon a metal, the oscillating electric field causes the electrons in the metal to oscillate, producing a time dependent displacement vector. The interaction can be quantified by utilising a general dielectric tensor. In a material with high symmetry such as a cubic crystal, a single dielectric constant is sufficient to describe how the electric field component of incident light is affected (Keatley, 2008):

$$\mathbf{d} = \varepsilon \mathbf{E} \tag{3.1}$$

where **d** is the displacement vector, **E** is the electric field and ε is the dielectric constant. The spontaneous magnetisation in ferromagnetic materials requires that the single dielectric constant be replaced by a general tensor, $\tilde{\varepsilon}$ (Scaife, 1989):

$$\tilde{\varepsilon} = \begin{pmatrix} \varepsilon_{xx} & \varepsilon_{xy} & \varepsilon_{xz} \\ -\varepsilon_{xy} & \varepsilon_{xx} & \varepsilon_{yz} \\ -\varepsilon_{xz} & -\varepsilon_{yz} & \varepsilon_{xx} \end{pmatrix} \tag{3.2}$$

Onsager's theorem (Curtis R. Menyuk, 2010) states that such a tensor's components are symmetric across the diagonal. Therefore, the diagonal components of equation 3.2 must be symmetric with magnetisation while the off-centre components must be anti-symmetric

(i.e. $\varepsilon_{ii}(\mathbf{M}) = \varepsilon_{ii}(-\mathbf{M})$ and $\varepsilon_{ij}(\mathbf{M}) = -\varepsilon_{ji}(-\mathbf{M})$) (Liu, 1967). It can also be shown that, to first order approximation, the diagonal elements ε_{ii} are independent of magnetisation and that the off-centre components ε_{ij} are proportional to magnetisation and zero where **M** vanishes (Curtis R. Menyuk, 2010). Therefore, if the case of a material magnetised parallel to the z-axis is considered, the above tensor becomes:

$$\tilde{\varepsilon} = \begin{pmatrix} \varepsilon_{xx} & \varepsilon_{xy} & 0 \\ -\varepsilon_{xy} & \varepsilon_{xx} & 0 \\ 0 & 0 & \varepsilon_{xx} \end{pmatrix} \tag{3.3}$$

If the incident linearly polarised light is considered to be a superposition of a left circularly polarised and a right circularly polarised source (such that $\mathbb{E}_y = i\mathbb{E}_x$ for left and $\mathbb{E}_y = -i\mathbb{E}_x$ for right) then by using equation 3.1 and equation 3.3 it follows that the dielectric constants for left (ε_+) and right (ε_-) are expressed as shown in equation 3.5 (Keatley, 2008):

$$\begin{pmatrix} d_x \\ d_y \\ d_z \end{pmatrix} = \begin{pmatrix} \varepsilon_{xx} & \varepsilon_{xy} & 0 \\ -\varepsilon_{xy} & \varepsilon_{xx} & 0 \\ 0 & 0 & \varepsilon_{xx} \end{pmatrix} \begin{pmatrix} \mathbb{E}_x \\ \pm i\mathbb{E}_x \\ 0 \end{pmatrix} =$$

$$\begin{pmatrix} (\varepsilon_{xx} \pm i\varepsilon_{xy})\mathbb{E}_x \\ (-\varepsilon_{xy} \pm i\varepsilon_{xx})\mathbb{E}_x \\ 0 \end{pmatrix} = \begin{pmatrix} (\varepsilon_{xx} \pm i\varepsilon_{xy})\mathbb{E}_x \\ (\varepsilon_{xx} \pm i\varepsilon_{xy})\mathbb{E}_y \\ 0 \end{pmatrix} \tag{3.4}$$

$$\varepsilon_{\pm} = \varepsilon_{xx} \pm i\varepsilon_{xy} \tag{3.5}$$

Therefore the left and right circularly polarised contributions experience a different electrical displacement vector and this difference leads to the observable change in polarisation of the reflected beam.

Hence, by monitoring the polarisation change in the reflected beam as a function of external magnetic field, a relative measure of the magnetisation of the ferromagnetic sample can be determined. This allows the determination of the hysteresis loop of the material and allows a deep insight into the magnetic reversal occurring.

There are three main categories of MOKE: polar, longitudinal and transverse, each defined by the orientation of the sample magnetisation (figure 3.1). Polar is when the magnetisation lies out of plane of the sample, longitudinal is when the magnetisation is directed across the sample and is in line with the plane of incident light, and transverse is when the magnetisation is perpendicular to the plane of incidence but also in the sample plane. In general, if the sample is magnetised in an arbitrary direction then any combination of these effects can be present.

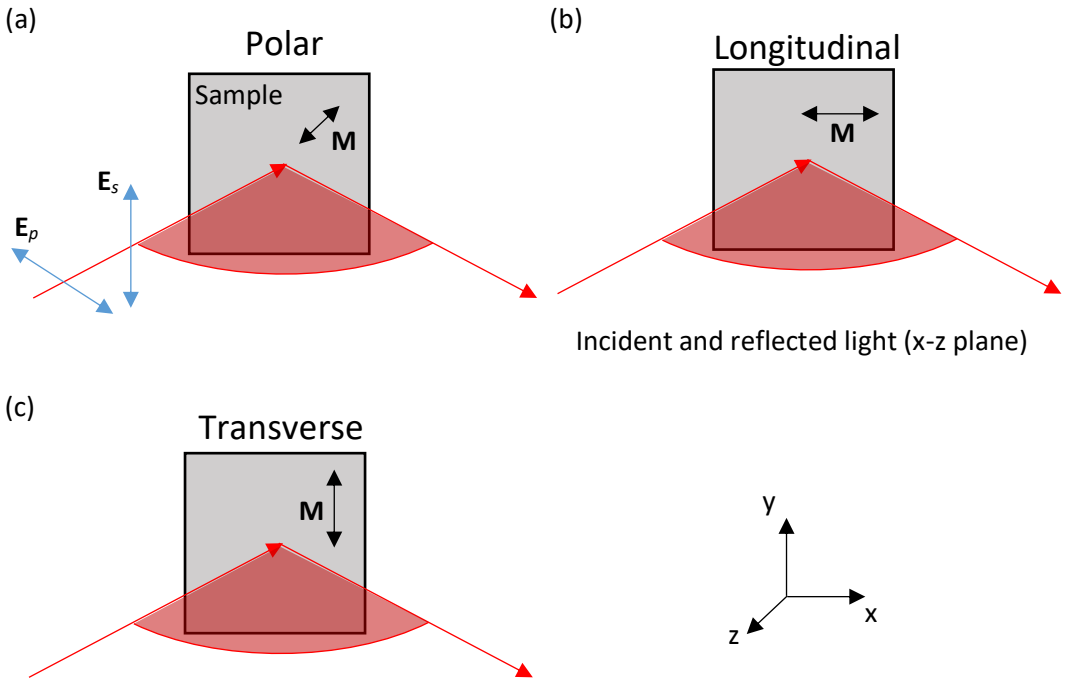

Figure 3.1: Representation of the three MOKE configurations: (a) Polar, (b) Longitudinal, (c) Transverse. The incident and reflected light lie at some angle within the x-z plane. For polar MOKE the light is usually near-normal to the sample, while for longitudinal and transverse more oblique angles are typically the case.

The incident light is usually linearly polarised in one of two directions as shown in figure 3.1(a), where $\mathbf{E}_p$ represents p-polarisation and $\mathbf{E}_s$ represents s-polarisation. If the sample is not magnetised then the reflected beam will retain these polarisations (Ali, 1999).

When the linearly polarised light reflects off a magnetic surface in the polar and longitudinal cases, the reflected light becomes elliptically polarised with two perpendicular electric field components: the standard Fresnel reflection amplitude, independent of magnetisation, and the Kerr coefficient which is directly proportional to the magnetisation vector parallel to the plane of the incident light. While the Kerr coefficient is usually smaller than the Fresnel amplitude, the difference in signal observed when switching the magnetisation is observable by using a second polariser ('analyser') to extract the Kerr signal from the reflected beam (Allwood et al., 2003).

To understand what happens to the reflected beam in these three cases, it is possible to consider the Kerr signal using the classical case of the Lorentz force that is induced when

the beam hits the sample, and the effect this has on the electrons in the sample. The Lorentz force can be written as (Young and Freedman, 2008):

$$\mathbf{F} = q(\mathbf{E} + \mathbf{v} \times \mathbf{B}) \tag{3.6}$$

Where **F** is the force experienced by a moving charged particle through a combination of electric and magnetic fields, *q* is the charge of the particle, **E** is the electric field, **v** is the velocity of the particle and **B** is the magnetic field.

If the effect of this force on the polarisation is considered, it follows that the electric field component of light accelerates the electrons along the direction of the incident polarisation and so will not alter its rotation. However, if the sample has a magnetisation then **B** = **M** and the magnetic field component is also included. From the geometry of the setup the resulting Lorentz force can cause the electrons to oscillate with a slight rotation with respect to the incident polarisation. The oscillating electrons emit electromagnetic waves and so the polarisation of the reflected light is rotated slightly (Ali, 1999).

In the longitudinal and polar setup, the resultant force is orthogonal to the incident polarisation for both s and p polarisations, and so rotates the polarisation. In the transverse setup however, for p-polarisation the resultant force remains directed parallel with the incident polarisation, while in s-polarisation the induced excitation and magnetisation are parallel resulting in no magnetic component to the force. For the transverse case only the polarisation amplitude is changed when the incident light is p-polarised. As a result this causes the transverse signal to become negligible when the incident light is s-polarised.

3.3 Description of apparatus

The setup used is similar to that presented by Allwood *et al*. and is shown in figure 3.2 (Allwood et al., 2003). A laser of power ≈40mW at source and wavelength 635nm has its beam expanded to approximately 1cm in diameter before it is passed through a Glan-Taylor polariser aligned to s-polarise the incident beam in the horizontal plane. The polarised light is then focused down to a spot size ≈50μm in diameter on the sample using a 1” diameter achromatic doublet lens with focal length 300mm. The reflected beam is passed through a Glan-Taylor analyser to extract the signal and reference beams which are focused onto a pair of high-speed silicon photodetectors by a ½” diameter doublet lens with focal length 100mm. A variable neutral density filter is used with the reference beam to adjust the intensity to approximately that of the signal beam. A camera is positioned

perpendicular to the sample as an entirely separate optical system and is used when aligning the laser spot onto the structures.

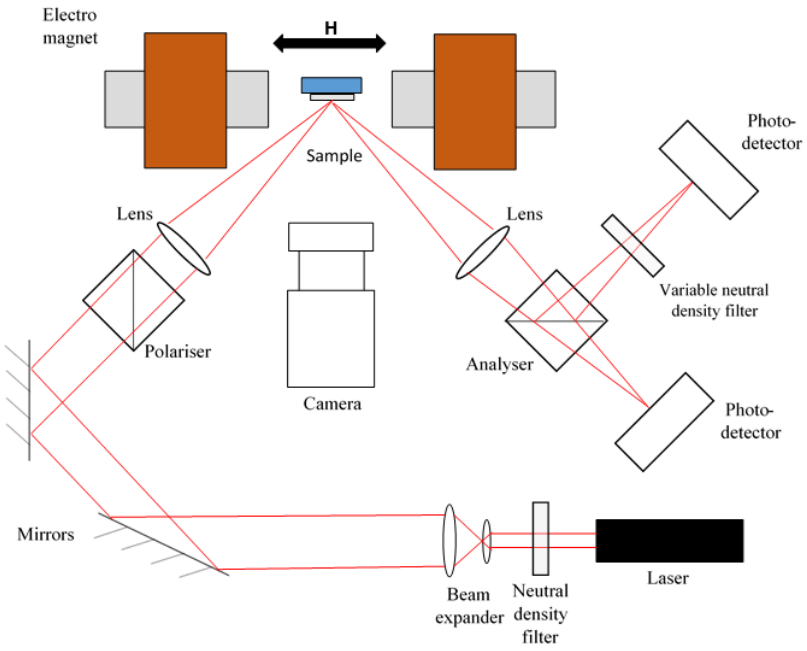

Figure 3.2: Schematic of apparatus used in MOKE setup. Image represents configuration for longitudinal MOKE.

The operational procedure for taking a measurement is then as follows:

The sample to be investigated is affixed to its holder using standard vacuum grease.

It is then positioned within the electromagnet with its poles retracted to give plenty of operating space.

The laser is aligned onto the sample within the field of view of the camera by careful adjustments of the mirrors, polariser and lens.

Once in view, the spot size is reduced to a minimum by use of a z translation stage to bring the sample to the focal point.

The spot is then positioned over the required structure on the sample by use of an x, y translation stage with analogue control and an attached rotation dial, as well as visual feedback from the camera.

The poles of the electromagnet are then carefully extended into the air-gap as close as possible to the sample without disturbing it and are secured in place.

The second lens is then positioned within the path of the reflected beam and the signal detector is translated to intercept the focal point. A 10% transmittance neutral density filter is placed at the laser source to protect the detector during alignment.

The Glan-Taylor analyser is then placed between the second lens and the signal detector. The analyser is rotated until an approximate minimum is observed from the signal detector and the neutral density filter removed.

The analyser is systematically rotated until the detected signal is at minimum intensity then adjusted to the required angular rotation offset from the minimum position.

A variable neutral density filter is placed within the path of the reference beam emitted by the analyser and an optional lens used if the reference beam requires focusing.

The reference detector is then moved to the new location of the focused reference beam spot.

Using visual feedback of the differential signal strength, the reference beam intensity is altered by use of the variable filter until the differential signal (with zero applied magnetic field) is approximately zero.

A continuous field cycle for the driving voltage of the electromagnet is set using software as well as the sampling rate for the two detectors. A data acquisition card (DAC) relays this voltage to a bipolar power supply which supplies a current to the electromagnet proportional to the voltage sent from the DAC. The software can then begin the measurement by cycling the magnetic field at a constant rate with continuous input from the detectors.

The program that runs the MOKE magnetometer was developed in house at Cardiff alongside the instrument itself. The program was coded using LabVIEW from National Instruments due to its compatibility with the data acquisition card.

A schematic block diagram of the program is shown in figure 3.3. The initial parameters that can be adjusted that are relevant for MOKE operation are: number of steps for the DAC output voltage, maximum/minimum output voltage for the DAC, output cycle period for the DAC voltage and number of read points for the DAC inputs. Channel selection and maximum/minimum input values for the detectors can also be set. From the input parameters the program generates the data for a sine wave for the output driving voltage using a LabVIEW function, which takes the period and number of output steps as

arguments, starting and ending at the positive maximum. Arrays with length equal to the set number of read points are generated and populated with zero values for the three read inputs: the signal detector, reference detector and gaussmeter.

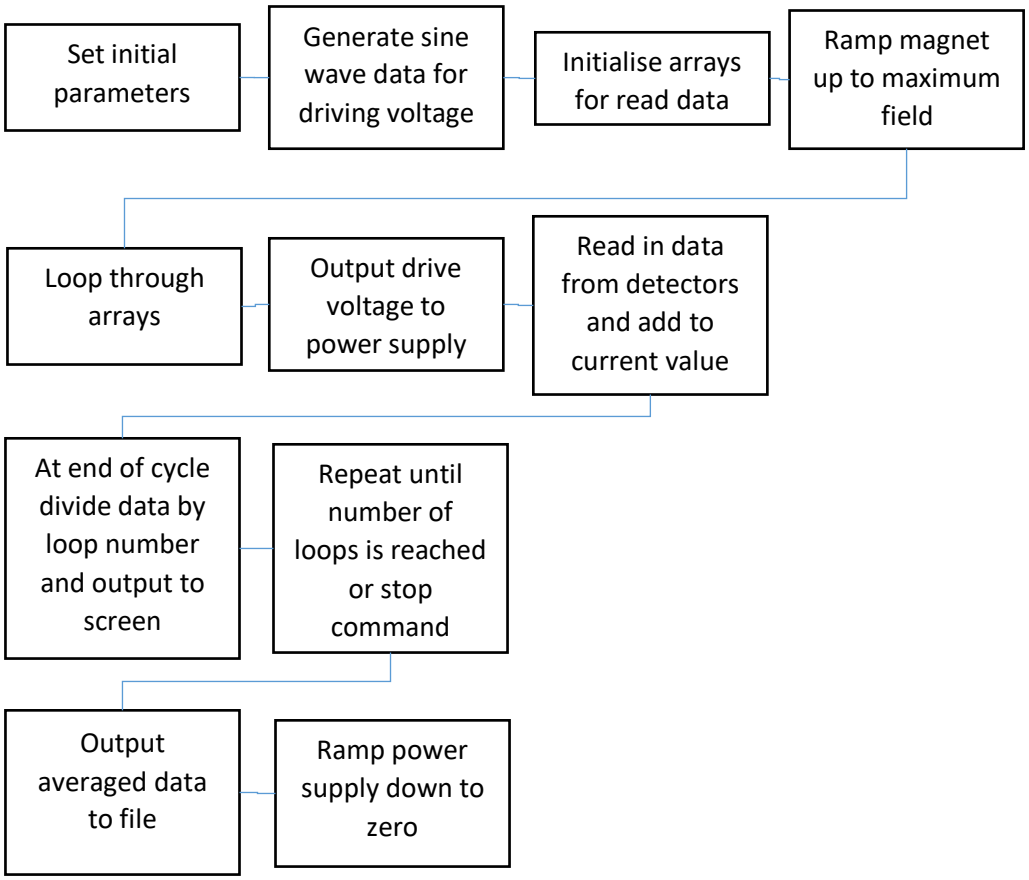

Figure 3.3: Block diagram representation of the MOKE program.

The output voltage is then transmitted to the Kepco bipolar power supply which generates a current proportional to the received voltage. The output voltage is increased to the maximum set output value to start. The program then progresses through the driving voltage array and at each point takes a reading averaged over 100 individual sample measurements from each of the detectors. At the end of the array the program averages the detector voltage values for each field point, outputs this to the GUI and plots them as a hysteresis loop.

The program then checks if either the desired number of loops has been reached or if a stop signal has been received. If not, the program loops back to the start of the driving voltage array and repeats. The measured values of detector voltage and magnetic field are added to the previous result for each driving point so that the arrays held in memory store

the cumulative loop data. Once the desired number of loops has been reached or the program receives the signal to stop the readings are divided by the number of loops taken and the results saved to file while the output voltage is ramped down to 0V and transmission to the supply stopped.

3.4 Sheet film measurements

Once the initial setup had been completed it was important to test that the system worked correctly. A magnetic sheet film such as cobalt (Co) has been well characterised in other studies (Aboaf et al., 1983) and produces a defined hysteresis loop with a large signal. A sheet film of magnetic material also ensured that no background from the substrate was included in the MOKE signal making it ideal as an initial test. The coercive field for a Co film can range from 1.5-38mT (García-Torres et al., 2009). A thin film of electrodeposited Co with thickness 180±15nm and cut down to an area of 4.0±0.1mm by 3.5±0.1mm was measured using the MOKE system with the resulting average of 5 loops shown in figure 3.4(a). The loop shows a large, clean hysteresis signal with a remanent magnetisation of 0.81±0.01M and a coercive field value of approximately 11.0±0.6mT, which lies within the accepted range for Co. The same sample was also measured in a commercial vibrating sample magnetometer (VSM) and the resulting hysteresis loop shown in figure 3.4(b). The VSM loop shows a qualitatively similar shape to that measured with the MOKE and has a remanent magnetisation of 0.77±0.01M and a coercive field of approximately 8.2±1.2mT. From figure 3.4(b), the sample saturates at approximately 4.3×10^{-3}emu and has a volume of approximately $(2.5 \pm 0.2) \times 10^{-6} cm^3$, which results in a saturation magnetisation of 1700±180emu cm^{-3} or equivalently $(1700 \pm 180) \times 10^3 Am^{-1}$ to two significant figures, which is close to the accepted value for Co (approximately $1425 \times 10^3 Am^{-1}$) (Cantu-Valle et al., 2015).

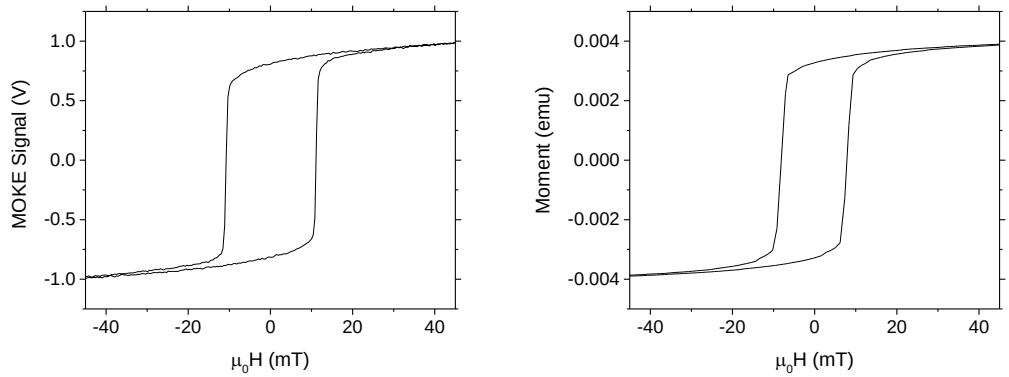

Figure 3.4: (a) Example hysteresis loop on a Cobalt film taken using the MOKE setup in this chapter, (b) Hysteresis loop measured on the same sample using VSM.

The approximately 25% discrepancy in coercive fields between the two loops can be explained by accounting for MOKE being a surface sensitive technique, probing local magnetisation, whereas VSM probes the average bulk magnetisation of the thick film. Because of this the coercive field as measured by MOKE can be expected to be up to 30% greater than that measured by VSM (Wrona et al., 2004). From the similarity of the two loops and the closeness of the remanent magnetisations and coercive fields it can be concluded that the measurements from the MOKE magnetometer are valid.

3.5 Nanostructured arrays

Having measured a sheet film, attention turned to sparse arrays of 2D nanostructures to perform initial calibration for small structures. The sample tested held several 7x7 arrays of individual structure cells comprised of nano-islands in a radial pattern on a silicon oxide substrate. Each cell structure consisted of six 1µm by 100nm by 10nm thick Permalloy ($Ni_{81}Fe_{19}$) nano-islands arranged at 60° rotations at fixed radius from the central point of the cell (figure 3.5 inset), with an array spacing of approximately 15µm between cells. Using the newly built MOKE it was possible to successfully observe hysteresis loops for each array set. An example is shown in figure 3.5.

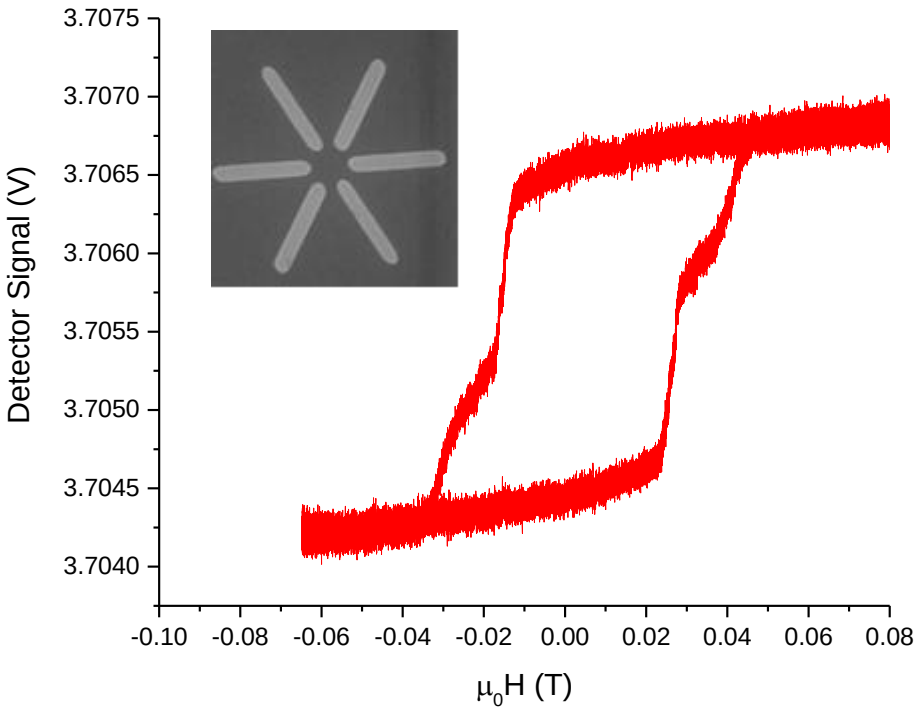

Figure 3.5: Time averaged hysteresis loop taken over 1500 cycles, using only the signal detector data. Inset shows scanning electron microscope image of one structure from the array probed.

While it was immediately possible to observe the 2D structures, some effort had to be put in to improve the resolution of the loops in order to draw useful comparisons with expected results from simulations.

3.6 Optimisation of signal to noise

To achieve a maximum signal-to-noise ratio (SNR) there are several factors that must be considered. As described in section 3.2, the MOKE signal is related to the magnitude of the Kerr coefficient in the reflected light. While a number of factors affect the magnitude of the Kerr coefficient, the most easily accessible one for the MOKE magnetometer is the spot size of the laser at the sample. This should be as small as possible so that the fraction of reflected light from the structures compared to the substrate is large, hence providing a larger intensity factor for the magnetic structures which contain the Kerr coefficient, whereas the background reflection contains no Kerr signal. This tight focusing also aids resolution of the system when investigating small structures. The spot size can be kept small by careful focusing when mounting samples and by using lenses with small focal lengths. However, it can be beneficial to use a lens with a long focal length to reduce the angular range of light incident on the sample in order to reduce the effects of depolarisation in the beam (Porto, 1966). For such long focal length lenses an achromatic coating helps in maintaining a small spot size. For the laser wavelength of 635nm, lens of focal length 300mm and a beam-width at the lens of approximately 12.5mm, the calculated spot size at the focal point is approximately 20µm (Self, 1983). In practice it was possible to regularly achieve spot sizes of approximately 50µm using a 300mm focal length, 1" diameter, bi-convex lens with an achromatic coating.

In designing the system, the optical component holders used were chosen to be of a non-magnetic material to remove any possible movement during magnetic field cycling, which could have interfered with the signal by shifting the spot position on the sample.

3.6.1 – Analyser angle

The overall SNR for a MOKE setup due to the properties of the hardware components was modelled simply by Allwood *et al.* by consideration of the various contributing factors and determining their contribution to the voltage output from a single detector. Their final expression for total SNR as a function of the current range produced by the full MOKE signal (Δi), the dark (i_D), shot (i_S) and Johnson (V_J) noises for the detector, and the intrinsic laser noise (i_L) is shown to be (Allwood et al., 2003):

$$SNR = \frac{R\Delta i}{\left[R^2(i_D+i_S+i_L)^2+V_J{}^2\right]^{\frac{1}{2}}} \tag{3.7}$$

where:

$$\Delta i = \upsilon P_0 \sin 2\phi_A \sin 2\theta_K \tag{3.8}$$

$$i_D = \upsilon(NEP)\beta^{\frac{1}{2}} \tag{3.9}$$

$$i_S = (2e\beta\upsilon P_0 \sin^2 \phi_A)^{\frac{1}{2}} \tag{3.10}$$

$$i_L = f_L \upsilon P_0 \sin^2 \phi_A \tag{3.11}$$

$$V_J = (4k_B TR\beta)^{\frac{1}{2}} \tag{3.12}$$

where ϕ_A is the rotation angle of the Glan-Taylor analyser with respect to its position of minimum signal transference ('analyser angle') and the remaining parameters are properties intrinsic to the detectors or the MOKE setup itself and are detailed in table 3.1.

Parameter	**Value**
Kerr rotation angle, θ_K	3.3x10^{-6} rad
Noise equivalent power, *NEP*	2.1x10^{-12} W Hz$^{-½}$
Bandwidth, β	5000 Hz
Load resistance, *R*	50 Ω
Temperature, *T*	301 K
Detector responsivity, υ	0.42 A W^{-1}
Incident laser power, P_0	40x10^{-3} W
Laser noise fraction, f_L	1x10^{-4}

Table 3.1: List of parameters for the MOKE system. NEP, β, R and υ taken from detector data sheet.

Of all of these terms, the only readily changeable value is the analyser angle, ϕ_A, and so the effect of this on the SNR achieved experimentally was compared with the theoretical prediction using equation 3.7. The calculated SNR curve as a function of analyser angle is shown on figure 3.6 along with experimental data points up to 4.5°. The experimental SNR is calculated by taking the ratio of the voltage difference of the magnetic transition to the magnetisation independent voltage fluctuation of the trace for a measured hysteresis loop at each angle. All other experimental settings were kept the same and each MOKE measurement was averaged over 25 loops.

From the calculated curve it is expected to see a peak in SNR just below 2° for analyser rotation angle. For the experimental results however, an upwards trend in SNR for increasing angle is observed and the maximal position remains in question. Error bars calculated from the precision of signal measurement for figure 3.6 are too small (largest value ±0.03) to be visible on the plot. The deviation of the experimental results from the theoretical expectation could be due to misalignment of the incident beam polarisation which would affect the Kerr rotation and analyser angles, or a reduction in the laser power after reflection from the sample (as it was assumed for the calculation that the reflected beam was of the same power as the incident beam).

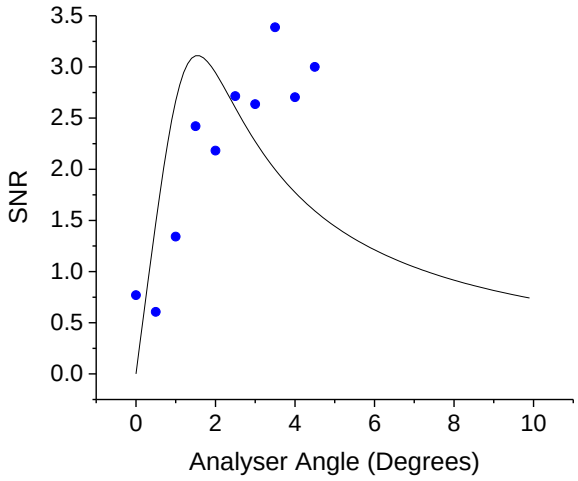

Figure 3.6: Measured SNR values as a function of analyser angle for values up to 4.5°. The black curve represents the calculated trend using equation 3.7 above and fitting parameters shown in table 3.1.

While the experimental results would indicate that a higher analyser angle would lead to better SNR, there are several restraints on the analyser angle from the experimental setup. At values above 4.5° the signal is strong enough to saturate the detector meaning access to higher angles would require a reduction in laser power which in turn reduces the Kerr signal (see section 3.6.4). Furthermore, at higher angles the reference beam is directed out of the plane of the optical bench housing the setup, making it impractical to use a second detector to monitor the reference signal (see differential detection below) and keep all components within the optical bench. As such, for general measurements a default analyser angle of 2° is used to achieve reasonable SNR while allowing for practical considerations.

3.6.2 Differential detection and time-averaging

Time averaging is a standard way of improving SNR for any general measurement system, with the SNR improving by a factor proportional to the square-root of the number of loops taken (Bhargava and Levin, 2002). The system was constructed with such time-averaging capabilities in mind and the method is essential for obtaining clean loops. A potential issue with averaging over long time scales is the stability of the laser power: if the power drifts or jumps then the end loop can become deformed or contain discontinuities. As shown in figure 3.7, after reflection from the sample the laser signal measured at the detector drifts by approximately 3mV over a period of 45s, separate from the noise in the signal. At the largest field range of ±500mT the field cycle period used is 5s. From figure 3.7 the potential change in signal across this cycle is approximately 1mV which can lead to the observed hysteresis loop being open ended.

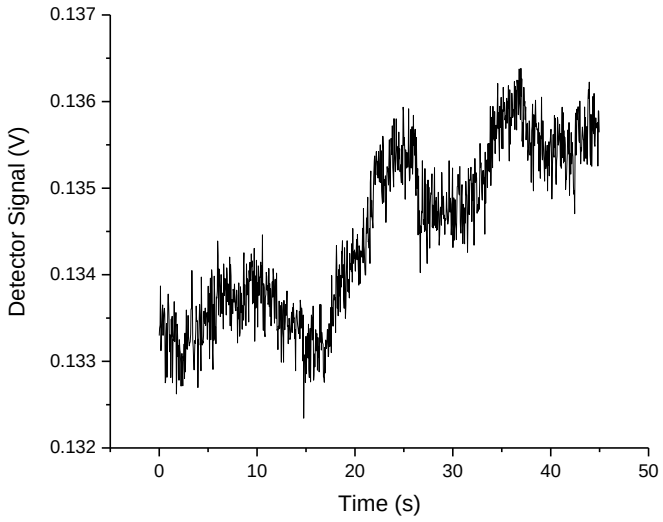

Figure 3.7: Detector signal measured as a function of time. No external field was applied during this measurement.

A way to mitigate this effect is to perform differential detection, i.e. to monitor the laser power using a separate photodetector and subtract this reference signal from the main signal. The results of these methods on SNR is shown in figure 3.8, making it clear that time-averaging over a large number of loops causes a significant increase in SNR compared to other options. Currently the system will run safely at a rate of one loop every 2 seconds at a field range of ±100mT (or 5s per loop at ±500mT), meaning that a 400 loop average can be taken within 15 minutes. While using two detectors increases the overall noise compared to using only one, and hence reduces the SNR value, the ability to take the difference between the measured signal and reference to the laser power helps to

minimise the effect of drift in the laser power and helps to reduce the number and magnitude of discontinuities within the overall hysteresis loop.

As for figure 3.6, calculated error bars are too small to be visible on the plots in figures 3.8, 3.9 and 3.10. It should be noted that the anomalous 50 loop data points at 40mW in figures 3.8 and 3.9 had the largest error value, and from examination of the hysteresis loop a periodic noise component not present in the other measurements could be seen. The source of this extra noise is likely mechanical vibration incurred during the experimental setup for that measurement as it is an isolated case. Due to the periodic nature, the differential signal suppresses that component which explains why the differential SNR is greater than that of a single detector for that data point.

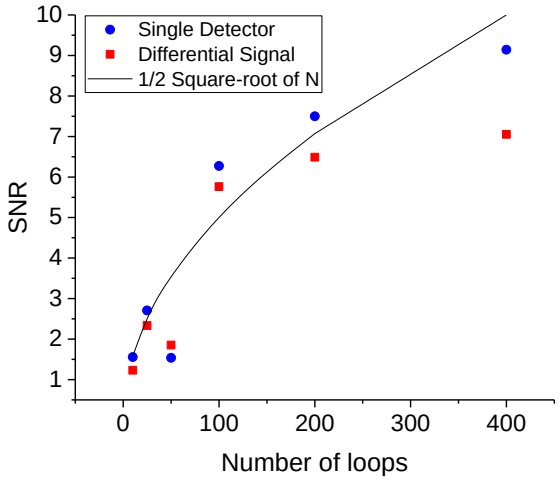

Figure 3.8: Measured SNR values for single detector and differential signal as a function of number of time averaged hysteresis loops. The black curve shows the trend of half the square-root of the number of loops and is a guide for the eye.

3.6.3 Laser power

As the Kerr signal magnitude is dependent upon the incident laser power (Allwood et al., 2003) it is intuitive to want to use the highest power available. However, at high power it is possible for the heating effect from the laser to add significant noise to the signal. To test this a 10% transmittance neutral density filter was placed at the laser source to attenuate the beam from 40mW to 4mW and the above test of SNR vs number of loops repeated. As is evident from the comparison in figure 3.9, the reduction in signal magnitude from the decreased laser power has a far more detrimental effect on the measured SNR than any heating effects that can be found at the highest power. Following from this, the maximum

laser power of 40mW is used for all measurements. At higher powers it can be expected that the effect of heating will become more important and so a compromise between power and heating would be required.

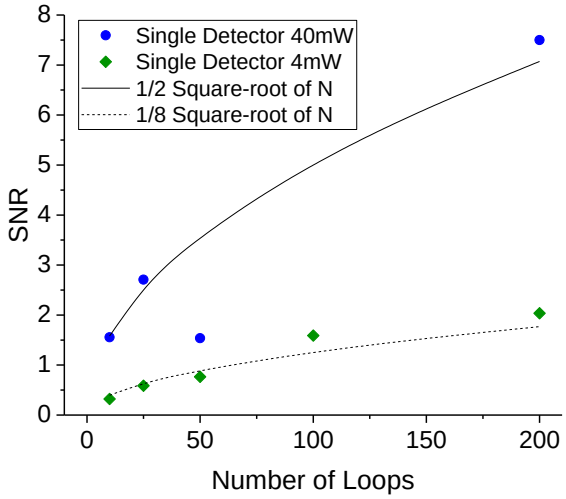

Figure 3.9: Comparison of SNR vs number of loops for laser powers 40mW and 4mW. The black curves show the trend of half the square-root of the number of loops for 40mW and one-eighth the square-root of the number of loops for 4mW and are guides for the eye.

3.6.4 Detector gain

The Si photodetectors used have a switchable gain from 0 to 70dB in 10dB increments. From the data sheet it is shown that as the gain increases so too does the intrinsic detector noise, shown in table 3.2. To check if there is an optimum setting, the gain for both detectors was systematically reduced and the SNR for a 50 loop time-averaged signal at each setting calculated.

dB Setting	RMS Noise (μV)
30	260
40	340
50	400
60	800
70	1100

Table 3.2: Listed noise values for Si photodetectors with dB gain setting.

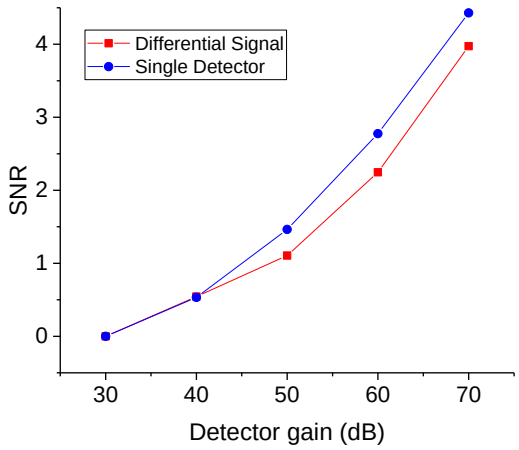

Figure 3.10: Variation of SNR with detector gain setting, time averaged over 50 loops.

Again, as for laser power, it is apparent from the results shown in figure 3.10 that the loss of signal magnitude from decreasing the detector gain outweighs any improvements in noise level. As such the detectors are kept at the maximum setting of 70dB for all measurements.

3.6.5 Data thinning

In operation the software reads in the detector voltages at a much faster rate (maximum 1.25×10^6 samples per second) than it drives the magnetic field, in a ratio of 100 read points to every field step. As such it is reasonable to take a rolling average to thin the number of points to the same order that the magnetic field is driven at. Care must be taken not to thin the data too much or important information in the hysteresis loop will be lost.

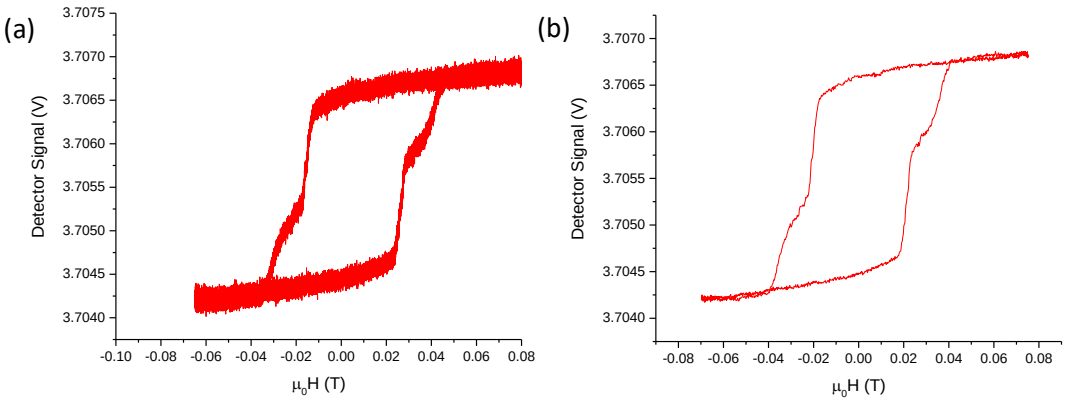

Figure 3.11: The effect of data thinning on the raw detector data. The loop in (a) was driven with a waveform consisting of 5000 points but the detected loop consists of 500000 points. The loop in (b) is the same data but with a rolling average every 100 points applied. Note the small magnetisation plateaus in the switching events visible in (b).

Figure 3.11 shows how careful application of this method greatly improves the visibility of features within a loop.

3.6.6 Optimal SNR settings

In summary, to achieve high SNR hysteresis loops for the 2D nano-island structures, the following practices were observed:

- Focus the laser spot on the sample such that the spot size is as small as possible.
- Set the analyser angle to a rotation of 2^{o} from minimum.
- Use the maximum laser power during measurement.
- Set the photodetectors to 70dB gain setting.
- Time-average the data for as long as is reasonable per measurement.
- Thin the data using a rolling average to match the resolution of the magnetic field driving voltage.

3.7 Challenges of measuring 3D magnetic nanostructures using MOKE

Moving to the measurement of 3D structures using MOKE brings additional challenges not present when probing 2D samples. For example, studies have shown that vibrational noise of the structures can be an issue (Fernández-Pacheco et al., 2013). Additionally, depending on the 3D structures, any combination of the three modes of MOKE can be present in the measured signal and so it can be difficult to deduce what is occurring if steps are not taken to suppress unwanted modes (by using s-polarised light to remove transverse MOKE effects for example).

The arrays of 3D structures investigated in this PhD produced a large diffraction pattern in the reflected light. To avoid diffractive MOKE effects in the signal, only the zeroth order reflected beam was selected by positioning the lens so that only the zeroth beam was focused through the secondary polariser. The polariser itself had a large surround that blocked higher order beams, and lens tubes were attached to the detectors to block unwanted reflections.

The samples measured were fabricated on a transparent glass substrate (see section 3.10), as such when mounting the sample the mount was blacked using a permanent marker pen and the structures positioned in front of the blacked area. The glass substrate introduced a linear background to the signal due to the Faraday effect (Schatz and McCaffery, 1969), as well as interference fringes in the reflected beam from thin-film interference. As such,

background measurements were performed on the substrate only, and these were subtracted from the signal measured on the magnetic structures.

Further discussion on the challenges encountered is presented in Chapter 5 alongside consideration of the results obtained.

3.8 Imaging techniques

While MOKE magnetometry was the main technique used to investigate the magnetic properties of the fabricated structures, a number of standard imaging techniques were also employed to check the dimensions of the structures probed as well as their composition and surface roughness. Scanning electron microscopy (SEM) including spin-polarised SEM (spin-SEM), energy dispersive X-ray (EDX) analysis, atomic force microscopy (AFM) and vibrating sample magnetometry (VSM) are discussed below.

3.8.1 Scanning electron microscopy

SEM is a widely used technique for imaging samples at scales beyond the diffraction limited resolution of optical light microscopes (approximately 200-250nm for white light with average wavelength 550nm). Another advantage of SEM over high-magnification optical imaging is that it has a larger depth of field and so is more suited to viewing samples with three-dimensional features, as much more of the sample will be in focus at once (Vernon-Parry, 2000).

The instrument is comprised of an electron gun (i.e. source of free electrons) that sits at the top of a column of electromagnetic lenses which focus the beam of accelerated electrons. There are three main types of electron gun: tungsten filament, lanthanum hexaboride filament and field effect guns. The tungsten filament is the most common and is the electron source used in the scanning electron microscopes used in this thesis. A tungsten filament is heated to over 2500^{o}C by passing a large current through it causing the thermal emission of electrons from the filament tip. The emitted electrons are then accelerated in the direction of the column using a potential difference applied across anode plates. Electromagnetic lenses consist of short coils which produce a non-uniform axial field that is rotationally symmetric about the axis column. As electrons enter the lens' field they are deflected according to equation 3.6 and the symmetry of the field causes them to be focused at a point (Egerton, 2005). By varying the current supplied to the lens coil and hence changing the strength of the magnetic field, the focal point position in the column axis can be adjusted. The focused beam is directed at the sample to be observed in a

chamber under vacuum. At the base of the column are a pair of defection coils that are used to raster scan the beam across the sample. The incident electrons from the beam are referred to as primary electrons and penetrate into the sample to the depth of a few microns (dependent upon the accelerating voltage used) and interact with the sample in a number of different ways.

The most important interaction for the context of this thesis is the inelastic scattering of the primary electrons, which leads to secondary electron emission and the generation of characteristic X-rays. When the primary electrons scatter they transfer some of their energy to an electron in the sample; this process can continue until the primary electron loses all of its energy and this results in a large amount of secondary electrons at lower energy (Allenspach, 2000). Secondary electrons that are near the surface of the sample are able to escape into the sample chamber and these are used for typical SEM imaging (referred to throughout this thesis as 'SEM images'). The secondary electrons are picked up by a detector placed within the chamber and an image is reconstructed by a computer from the raster scan. Additional detectors can be included in the chamber in order to view other signals generated from the electron beam (e.g. X-rays). A schematic representation of a scanning electron microscope is shown in figure 3.12, and an example image can be seen in the inset of figure 3.5.

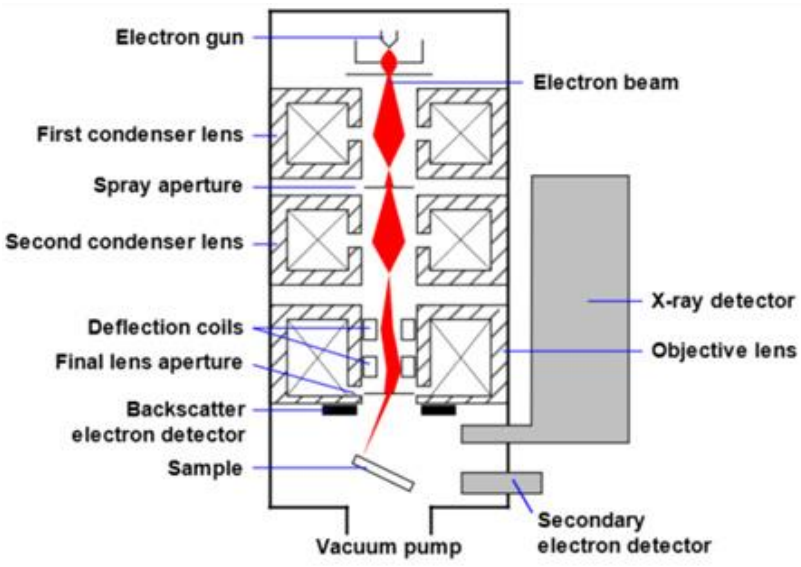

Figure 3.12: Schematic diagram of a scanning electron microscope. Image reproduced from Choudhary and Priyanka (Choudhary and Priyanka, 2017).

At Cardiff, use was made of two SEM systems, one in the School of Physics and Astronomy clean room for SEM imaging only, and one at the School of Earth Sciences for SEM imaging

and EDX analysis. Standard SEM imaging allowed for viewing of the topographical properties and geometry of fabricated structures as well as quantification of structure diameters by use of image manipulation software (see chapter 5).

When imaging a sample it was mounted on an SEM stub and the conducting substrate grounded to the holder by use of a small clamp or dots of carbon paint. As the structures are metallic, grounding the substrate in this way prevented charge build up from the incident electrons that can distort the image. The sample was then mounted on an xy-movement stage with tilt capabilities within the sample chamber. The chamber was then placed under vacuum and emission of electrons started. Control of the SEM properties was done via proprietary software on a connected computer.

An SEM that included spin-polarised detectors was also utilised at IBM, Zurich for Spin-polarised SEM (spin-SEM) magnetometry of structures produced at Cardiff, the results of which are discussed in chapter 5. The additions required for spin-polarised SEM and EDX analysis are discussed below.

3.8.2 Spin-polarised SEM

Spin-polarised SEM is an extension of the standard SEM technique that makes use of one or more specialised detector arrangements capable of discerning the polarisation of the secondary electrons. For ferromagnetic materials the polarisation of the secondary electron spin is proportional to the magnetisation of the magnetic domain they were emitted from and so, by discerning this polarisation, information about the magnetisation of the sample surface in one axis can be probed (Allenspach, 2000). The spin polarisation is dependent upon the energy of the secondary electrons, increasing with lower energy so electrons are typically collected in the range of 0eV to 10eV. This polarisation enhancement at low energy is fortuitous as the secondary electron intensity peaks in this low energy range. However, these low energy secondary electrons must come from the surface of the sample probed as they have a travel distance of the order of 1nm in 3*d* ferromagnetic materials. As such, spin-SEM is highly sensitive to the sample surface, which requires measurements to be performed in ultrahigh vacuum and on a clean sample.

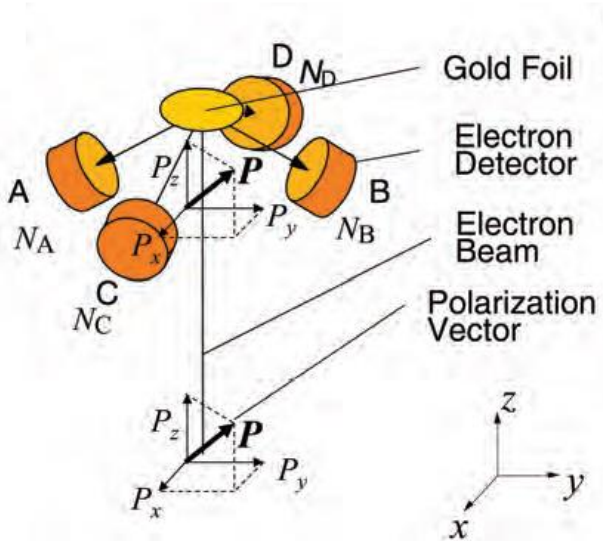

Figure 3.13: Representation of the spin-polarised detector arrangement. Image reproduced from Koike et al. (Koike, 2013).

An example of a polarised spin detector is the Mott detector (figure 3.13), which functions by accelerating the low energy electrons (up to 50-100keV) and scattering them off of a foil with a high atomic number, such as gold (Allenspach, 2000; Koike, 2013). The electrons have a large spin-orbit interaction with the foil and so are backscattered asymmetrically according to their spin orientation onto four detectors set at orthogonal positions (detectors A, B, C, and D in figure 3.13). By comparing the number of detections in each detector (N_A, etc. in figure 3.13) the polarisation of the secondary electrons can be determined; e.g. $(N_A-N_B)/(N_A+N_B)$ is proportional to the spin polarisation for the x-axis in figure 3.13. A standard topographical SEM image can also be constructed from a spin-SEM measurement using the overall total of detected electrons.

Due to the large depth of focus in SEM, a property that is also extended to spin-SEM, the technique is able to probe the magnetisation of 3D surfaces, making it ideal for this study in comparison to other domain viewing methods that suffer from a short depth of focus (such as Kerr microscopy).

The spin-SEM measurements presented in chapter 5 were performed and carried out by Dr. Rolf Allenspach and his group at IBM, Zurich, who provided the results for interpretation here. Before imaging with spin-SEM, the samples underwent a mild ion bombardment (using Kr^+ ions, 2000eV) to prepare a clean surface as required.

3.8.3 Energy dispersive X-ray analysis

Energy dispersive X-ray analysis (EDX) systems can be built into a SEM setup by adding a specialised detector to capture the characteristic X-rays generated during the SEM process. During the formation of the secondary electrons an inner shell electron can be displaced. An electron from one of the outer shells can undergo a transition to fill the vacant inner shell and in doing so can release an X-ray photon. The X-ray photons that are emitted from the sample have an energy equal to the transition that generated them (Bell and Garratt-Reed, 2003). The transitions are element-specific so the elemental composition of the sample can be determined by comparing the peaks of the detected X-ray energy spectrum with reference to a library of such transition values. To ensure generation of these X-rays a typical accelerating voltage of 20kV is used for the electron beam of the SEM (Welton and Company, 1984).

There are a number of limitations with this technique however. Firstly, the interaction volume for the generation of characteristic x-rays is much larger than for secondary electrons, leading to a lateral resolution typically of the order of 1µm (Vernon-Parry, 2000). As such the resolution of the EDX spectrum is less than the SEM image, meaning that care must be taken to focus on a relatively large section of the sample to ensure that the spectra is from the sample only. Secondly, the EDX detector has a finite energy resolution (approximately 150eV (Welton and Company, 1984)) and so it is possible to confuse elements whose signature transitions have an energy difference below that resolution.

The EDX measurement discussed in chapter 5 was performed at the School of Earth Sciences at Cardiff, using the same method as for standard SEM imaging discussed above. A larger sample was used to mitigate the chance of examining the substrate during measurement and several locations on the sample were probed. The composition data for each position was then averaged to provide overall values for the sample.

3.8.4 Atomic force microscopy

AFM is a widely employed technique that allows three-dimensional imaging of a sample's surface topography at the nanometre scale, and under certain circumstances atomic scale. The basic operational procedure is to measure an interaction or force between a sharp probe tip and the sample surface. There are a number of modes for AFM measurement, a complete and detailed explanation of which are discussed by Meyer (Meyer, 1992). However the technique employed during the course of this PhD was a non-contact tapping

mode and so only that is discussed here briefly. In addition to topography measurements, specialised AFM probe tips allow the probing of other surface properties such as magnetic stray field (this mode is known as magnetic force microscopy or MFM).

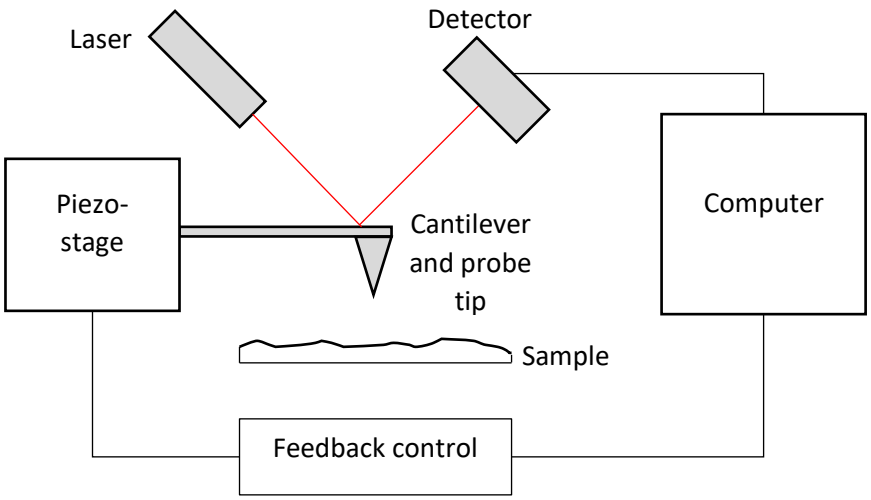

Figure 3.14: Schematic of AFM setup including feedback control loop.

A schematic of the AFM operation is shown in figure 3.14. The instrument is comprised of a cantilever with a sharpened tip that is set to oscillate close to the cantilever's resonant frequency. A laser is reflected off the cantilever and onto a set of detectors that are sensitive to position. The tip is brought into close proximity to the sample surface causing it to experience van der Waals forces which displace the equilibrium position of its oscillations. By using the piezo-stage to perform a raster scan at a fixed height (typically around 10-100nm from the surface) and monitoring the equilibrium position the surface topography of the sample can be mapped. Alternatively, feedback control can be used to keep the equilibrium position constant by raising or lowering the tip, and monitoring this vertical displacement likewise maps out the topography. For MFM the probe tip is fabricated from a magnetic material and the deflection caused by magnetic force (typical lift height of approximately 100nm), rather than van der Waals forces, is measured to produce an image of the magnetic contrast from the surface.

Despite the utility of AFM/MFM, the technique is not well suited to the measurement of samples with a large 3D component, such as those presented in this thesis. The AFM used in this thesis was a Bruker Dimension 3100 model, and had a maximum lift height of 5µm, which is lower than the height of the structures to be investigated. As such AFM was limited to investigating the surface roughness of single wires that had fallen over on the

substrate, as discussed in chapter 5, and the film thickness for determining the volume of magnetic material for the VSM analysis above. The measurements were performed at room temperature and the field of view restricted to image only the fallen structure to avoid damaging the tip by collision with an upright structure. The film thickness was measured using an offcut of the same film used for VSM and MOKE that had a trench fabricated into it using resist, such that the film height could be measured relative to the substrate. Spin-SEM was utilised in place of MFM for imaging the surface magnetic domains as it is more suited to three-dimensional structures as noted above.

3.8.5 Vibrating sample magnetometry

Vibrating sample magnetometry is a method that measures the average magnetic moment of a bulk sample. The sample is placed within a uniform magnetic field and vibrated at a known frequency. The distortion in the uniform field due to the magnetisation of the vibrating sample is detected by a number of coils as a measurable induced voltage. A reference signal is provided by use of a permanent magnet attached to the same drive rod as the sample but spatially separated and with separate detection coils. The reference signal thus has the same amplitude and phase as the measured signal. The uniform field the sample sits in can be swept, allowing for measurement of hysteresis (Foner, 1996).

Because it is the sample's magnetic moment that causes the induced voltage, this technique provides a direct measurement and the numerical value for sample magnetisation can be derived. While VSM can be made very sensitive (so that it approaches the sensitivity of superconducting quantum interference device magnetometers (Foner, 1981)), the absolute signal depends on the volume of magnetic material within the sample. Additionally, the measurement provided is an average of the total magnetic volume in the sample. This differs in comparison to MOKE which is an indirect measurement of magnetisation and so can only provide normalised results. However MOKE is sensitive to a localised surface area and so is better suited to the measurement of nanostructures where the overall magnetic volume is very small compared to that of a bulk film or sample.

A commercial VSM was used to measure the hysteresis loop of a cobalt film (section 3.4) for comparison with a MOKE measurement of the same film to validate the MOKE magnetometer performance. After taking the MOKE measurement the film was mounted to the VSM holder and a measurement performed at room temperature.

3.9 Micromagnetic simulations

Micromagnetic simulations of small structures are a useful tool when investigating nanostructures composed of a ferromagnetic material. Currently there are a number of micromagnetic simulation packages available either commercially, as freeware, or privately developed, which are used widely by researchers. Simulations can provide an idea of a number of magnetic properties, such as domain structure and wall regime, allowing for dimensions of structures to be investigated before committing to fabrication, or for complex or theoretical geometries to be investigated without the need for fabrication (which may be difficult or impossible with current technologies). However, care must be taken when defining the simulation parameters, otherwise the data produced can be misleading. This section will present the basic principles and models for micromagnetic simulations and describe the software packages used as well as the various investigations into simulation parameter space and their results.

3.9.1 Basic principles

There are two main methods when carrying out micromagnetic simulations – finite difference and finite element. In finite difference the model of the structure is tessellated onto a structured grid of cubic cells of fixed size, whereas in finite element the structure is mapped by a tetrahedral mesh (figure 3.15).

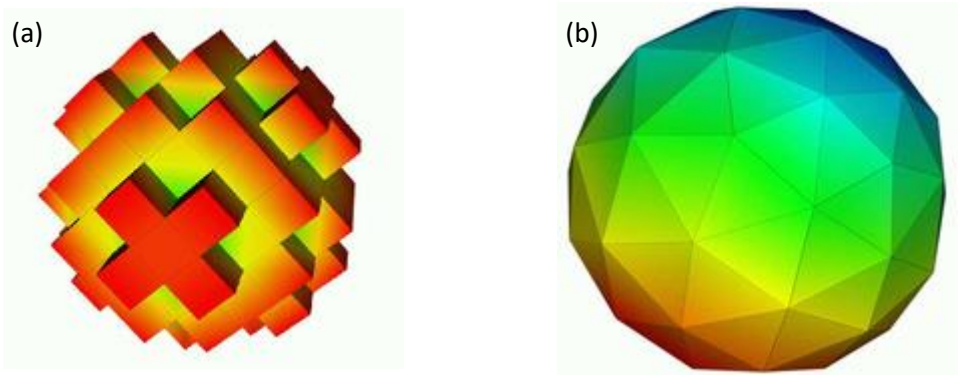

Figure 3.15: Sphere approximated by (a) a course finite difference grid and (b) a course finite element mesh. Image reproduced from Fangohr et al. (Fangohr et al., 2011).

Finite element is typically better suited for structures with a number of curved sections or very open geometries. Both methods use the Landau-Lifshitz equation (equation 3.13) (Yoshinobu Nakatani et al., 1989) to evolve the dynamics with time.

$$\frac{d\mathbf{M}}{dt} = -\gamma \mathbf{M} \times \mathbf{H}_{eff} - \lambda \mathbf{M} \times (\mathbf{M} \times \mathbf{H}_{eff}) \quad (3.13)$$

where **M** is the magnetisation, $\mathbf{H}_{eff}$ is the effective magnetic field strength, γ is the gyromagnetic ratio and λ is a damping term.

The Landau-Lifshitz equation describes the damped precession of the magnetic moments around the resultant field (as shown in figure 3.16) from the various contributions discussed in Chapter 2:

$$\mathbf{H}_{eff} = \mathbf{H}_{Zeeman} + \mathbf{H}_{Demag} + \mathbf{H}_{Anisotropy} + \mathbf{H}_{\text{Exchange}} \quad (3.14)$$

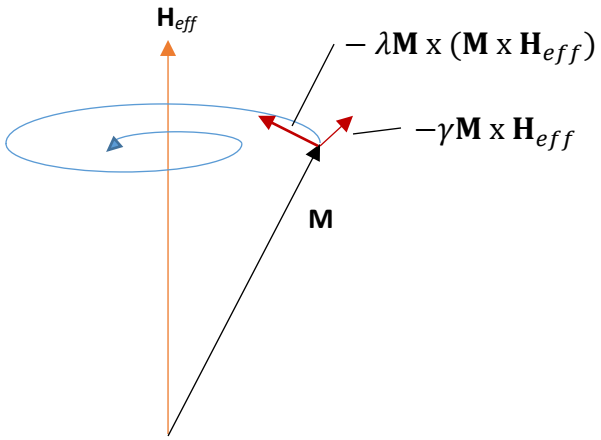

Figure 3.16: Representation of the terms in the Landau-Lifshitz equation.

The Landau-Lifshitz equation can be transformed into the Landau-Lifshitz-Gilbert (LLG) equation below:

$$\frac{d\mathbf{M}}{dt} = -\gamma' \left(\mathbf{M} \times \mathbf{H}_{eff} - \alpha \mathbf{M} \times \frac{d\mathbf{M}}{dt} \right) \quad (3.15)$$

where α replaces the damping constant from the Landau-Lifshitz equation, γ' is a precessional term and the other parameters are as described above.

The LLG equation replaces the damping term with one that is dependent on the time-derivation of magnetisation. This causes the precessional term (**M** x $\mathbf{H}_{eff}$) to depend on the damping term which is a more accurate representation of the behaviour of real ferromagnets for large damping.

The algorithms solve the LLG equation across all points or cells at iterative time steps, with $\mathbf{H}_{eff}$ updating at each step in response to the changes of the moments, and ultimately aims to minimise the free energy until a threshold parameter is reached (typically when $\frac{d\mathbf{M}}{dt}$ falls

below a threshold target) (Brown, 1963). Nmag uses the backward differentiation formula numerical method to calculate the time integration, with a default order of two. The method approximates the derivative of a given function for a given time-step and uses information from previously computed times to improve the accuracy of the approximation (Brayton et al., 1972).

At each time step the collective information for each point can be saved to an output data file, allowing for later extraction and investigation of key parameters, such as magnetisation.

3.9.2 General procedure for simulations

The initialisation of the parameter space for a simulation is critical to producing reliable results. For micromagnetic simulations the parameter space, that is the geometrical shape of the magnetic object to be investigated, defines the shape anisotropy, while the cell size or mesh-spacing (for finite difference and element methods respectively) can dictate the contribution from the exchange energy (Fangohr et al., 2011).

In general, the spacing should be kept below the exchange length of the magnetic material to be simulated, i.e. the length above which the exchange interaction diminishes rapidly. Exchange lengths are typically on the order of nanometres which puts a constraint on the overall dimensions of the simulated object, as the required computer memory usage scales with the number of cells/mesh points.

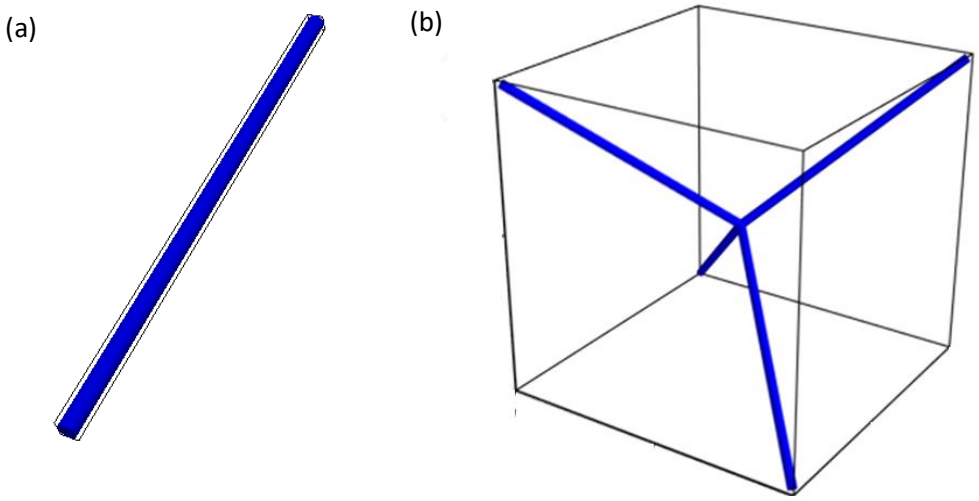

Figure 3.17: Visualisation of the mesh objects used for the simulations in Chapter 4; (a) A flat-ended cylinder with aspect ratio of 30 and (b) a tetrapod comprised of four cylinders as shown in (a). The meshes are scaled according to the simulation script.

The objects of interest for this PhD were cylindrical magnetic nanowires and conjoined networks of such wires. As such, a finite element method was preferred over finite difference due to the curved surface of the wire and open 3D nature of the networks. A flat-ended cylinder mesh file and a mesh file of four such wires conjoined at a central vertex and oriented radially outwards in a tetrahedral pattern ('tetrapod' structure) were produced from geometry files and are shown in figure 3.17.

The mesh files were used in simulation script files written in the python programming language. The scripts define the scale of the mesh object, the material parameters (namely exchange energy, saturation magnetisation and magnetocrystalline anisotropy), the initial magnetisation configuration and the externally applied magnetic field (if any) magnitude and direction. The magnetic field is defined as a series of field steps and at each field step the simulation performs a 'relax' command, i.e. the LLG equation is solved until dM/dt reaches a threshold value. In this way a complete hysteresis cycle can be simulated. The required data is then extracted from an output file.

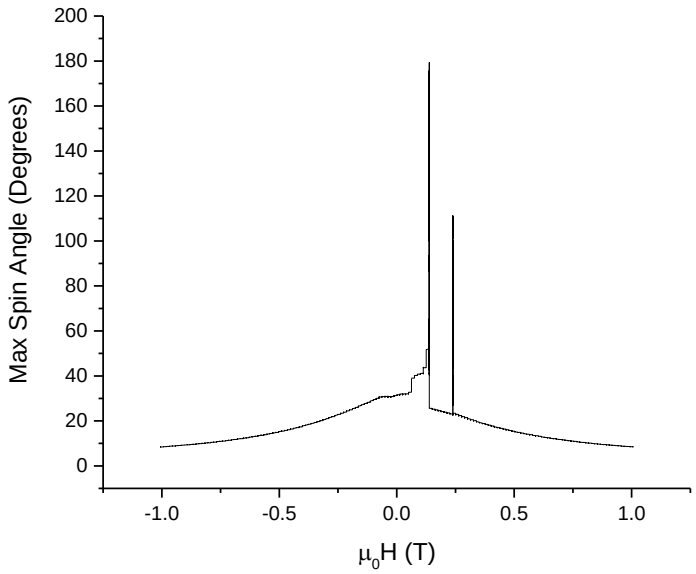

Figure 3.18: Plot of maximum spin angle against magnetic field step for the upsweep (-1T to 1T) of a simulated hysteresis loop on a tetrapod structure (see Chapter 4), the plot is typical for the simulations performed during the course of the PhD.

A measure of whether the simulation results are reliable or not is to investigate the maximum angle between adjacent spins present in the mesh. A typical plot of the maximum angle against magnetic field for an upsweep ranging from -1T to 1T of a hysteresis simulation performed during this PhD is shown in figure 3.18, from which it is

readily observed that at two points in the simulation the angle spikes to >100°. However, these spikes are explainable as the fields at which they occur coincide with the observation of Bloch point propagation within the simulated structure. Generally, if the maximum angle is above 90° then the results are unreliable, while an angle below 30° can be considered reliable (Fangohr et al., 2011). As discussed in Chapter 2, Bloch point domain walls are characterised by a vanishing local magnetisation which manifests itself as a singularity (where two local spins align at 180° to one another). As such it can be taken that the simulation is performing completely accurately as it has successfully reproduced the Bloch point (see chapter 4, section 4.2), which is consistent with literature (Da Col et al., 2014). Furthermore, this set of simulations serves to illustrate that the criteria proposed by Fangohr/Donahue in the above reference is only valid for micromagnetic textures that do not possess a Bloch point. The majority of the literature (see chapter 2, section 2.3.2) that involve Bloch point simulations make use of the same freely available micromagnetic simulation packages (Da Col et al., 2014; Ferguson et al., 2015; Ivanov et al., 2013; Piao et al., 2013; Salazar-Aravena et al., 2014), and so will observe the same effects. As an additional check, the results presented in chapter 4 are compared with reference (where possible) to check agreement with published results.

3.9.3 Software packages

Over the course of the PhD, a number of freely available simulation and visualisation packages were utilised. A brief overview of each is given here along with their usage in the PhD (for a more detailed description of each package and its operation see the relevant references for each).

Object-oriented micromagnetic framework (OOMMF) is a finite difference simulation package developed by NIST and has been widely accepted throughout the magnetic community. OOMMF provided a databank for material parameters as well as a way to visualise magnetisation files in ovf format (as output by both OOMMF and Mumax3) (Donahue, 2016).

Mumax3 is a finite difference software package that is graphical processing unit (GPU)-based. This means that it is generally more efficient than computing processor unit (CPU)-based packages (such as OOMMF) but comes with the caveat of requiring specific graphics cards (Nvidia CUDA based). There are typically far less GPU processors on super computer clusters and so total memory available for processing is more limited. Mumax3 was used

for several large scale simulations of simple geometries including the single nanowires considered for the discussion in Chapter 5 (Vansteenkiste and Van de Wiele, 2011).

Nmag is a finite element micromagnetic simulation package developed by Southampton University. The package has a high integration with the python programming language. A meshing package, Netgen 4.0, was used in conjunction to provide the mesh object files for Nmag. Nmag was used for all of the simulations covered in Chapter 4 (Fischbacher et al., 2007).

Mayavi2 (from the pythonxy package) and Paraview (stand-alone software) are both 3D visualisation packages were used for visualisation of vtk files of the magnetisation for the simulated objects (Ayachit, 2015; Ramachandran and Varoquaux, 2012).

Use was made of the Raven supercomputer cluster at Cardiff University for running the Nmag simulations. The use of a supercomputer allowed for relatively large mesh objects to be simulated that would otherwise be too resource intensive for personal computers to run efficiently. Using the cluster, simulations can be run using parallel processing via message passing interface (MPI) splitting the mesh into a number of partitions. Care must be taken to be consistent with number of processors used for long simulations that require restarting mid-run, otherwise the ordering inherent to partitioning the mesh is lost.

3.10 Fabrication of structures using two-photon lithography

The fabrication of the structures examined in chapter 5 was performed by another student (G. Williams) and so the process is only briefly considered here to provide context for the measurements and discussion in chapter 5.

Two-photon lithography (TPL) is a method that uses a femtosecond laser to expose a 3D pattern within a layer of photoresist. The focal point of the laser can be moved with respect to the substrate by using either a piezo stage to move the substrate or galvo-mirrors to move the beam. Hence by using TPL it is possible to create templates of arbitrary geometry within standard photoresists. These templates can be used with a variety of deposition techniques provided that consideration of the technique to be used is taken account of in the design of the template. Due to the complex shape geometry of structures such as tetrapods, electrodeposition was chosen due to not requiring direct line of sight to the substrate. This allows for structures with ‘buried’ or twisting geometry to be fabricated provided that there is a continuous opening from the substrate up to the resist surface. While TPL has been used previously for the fabrication of structures in other areas such as

micro-optics (Dietrich et al., 2017; Thiele et al., 2017) and microbiology (Brigo et al., 2017), the use of TPL to fabricate magnetic nanostructures is a novel technique.

The use of electrodeposition requires that the substrate be electrically conductive so as to act as one of the electrodes. For TPL, a commercially available system, a Photonic Professional GT from Nanoscribe (Nanoscribe GmbH, 2017a), was used. Due to the mechanics of the setup, the laser is incident through the substrate layer which requires that the substrate used be optically transparent. To satisfy these requirements, the substrate used was glass with a 500nm thick coating of indium tin oxide (ITO) on one face. Both glass and ITO are optically transparent at the wavelength of the laser in the photonic professional GT (780nm) and the ITO is electrically conductive for the purposes of electrodeposition.

The resist was spun onto the ITO side to the desired thickness for the structures to be fabricated (8µm for single wires) according to the spin-curve on the resist's data sheet (figure 3.19).

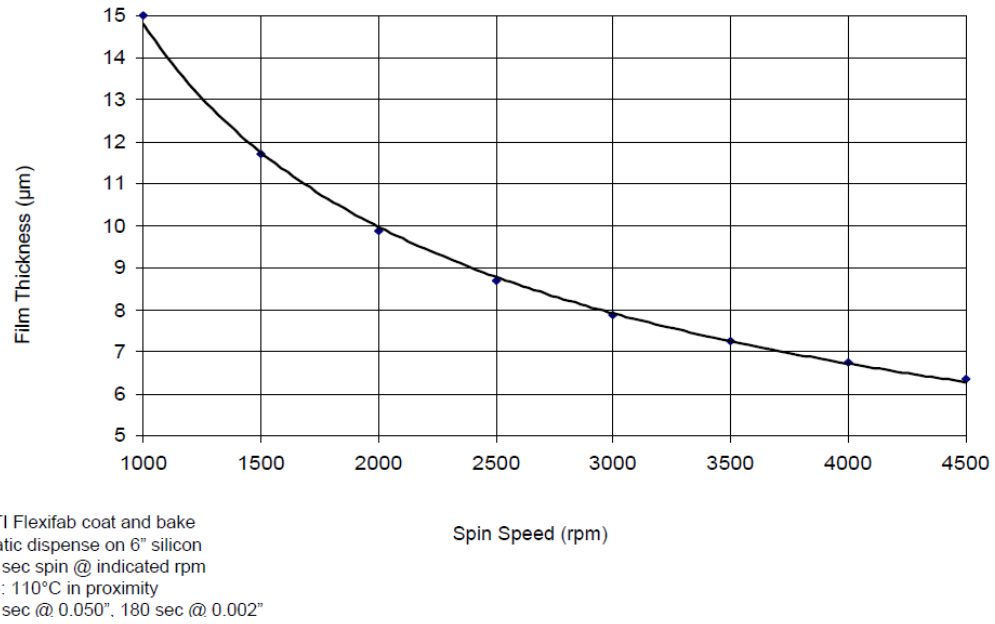

Figure 3.19: Spin curve for AZ9260 photoresist for 30s spin onto silicon. Image reproduced from technical sheet for resist.

As the film thickness is too large to measure using AFM, an alternative method of checking the thickness had to be employed. Typically the thickness would be measured using ellipsometry, however we did not have the facilities available to perform such measurements. Instead the thickness was checked from SEM images of overfilled structures by measuring the height up until the overfill point as shown in figure 3.20.

When electroplating, a typical method of determining when the structures are filled is to monitor the current until a sharp change occurs, indicating that the deposited material has reached the surface of the template. That method could not be employed here, as by the time a change in current is observed the structures have begun to overfill and leave mushroom-like caps on the nanowires (figure 3.20). Instead, a number of arrays of structures (typically at least 4) were exposed in the resist using TPL for each sample, with the intersection point placed at various heights within the resist. The electrodeposition was then timed and the resulting structure inspected, until an optimum time was determined. The use of four different heights for the intersection point improved the probability of obtaining an array of structures where the ratio of upper to lower wire lengths was approximately equal.

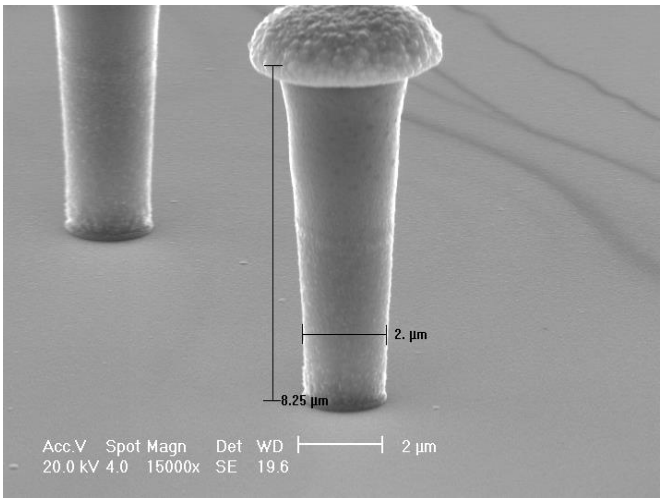

Figure 3.20: Example of an overfilled nanostructure with height measurement of 8.25µm.

The fabrication procedure is outlined in figure 3.21 and is described below:

A standard photoresist (AZ9260) is spin-coated onto the glass/ITO substrate on the ITO side and baked.

TPL is used to expose the required structure designs in the resist. The laser power was varied between 3-10.5mW and the scan speed varied between 5-20µms^{-1}. The sample is placed in a developer to remove the exposed regions leaving empty channels. Development time was varied between 15-120minutes.

Cobalt is electrodeposited into the channels using a two electrode (Co anode) constant current (1mA) approach and a standard 600ml bath consisting of cobalt sulphate (90g), cobalt chloride (27g), boric acid (14g), and sodium lauryl sulphate (1g).

The sample is then placed in acetone for 24 hours to remove the resist and leave the structures free-standing on the substrate. Free-standing tetrapod structures manufactured via this methodology are studied in chapter 5.

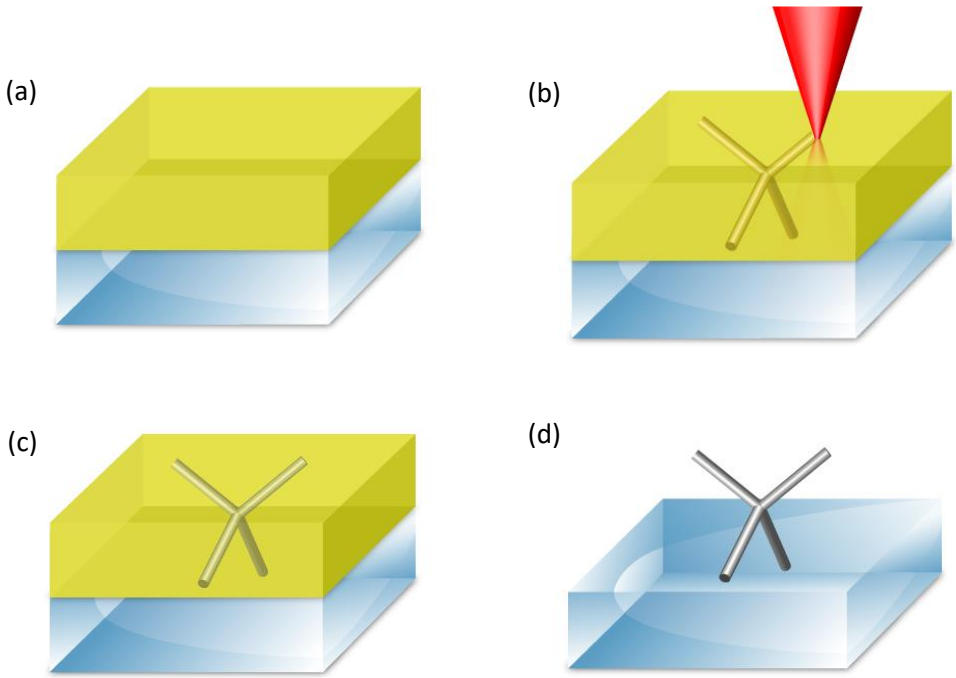

Figure 3.21: Outline of the fabrication procedure; (a) A standard photoresist is used to spin coat onto a conductive substrate, (b) TPL is used to expose the structure geometry, (c) Magnetic material is electrodeposited into the template, (d) The photoresist is removed using a standard lift off procedure. (Williams et al., 2017)

3.11 Montana cryostat

At Cardiff we have available a closed cycle cryostat with optical access from Montana instruments. During the course of the PhD it was intended to construct an additional MOKE magnetometer utilising the cryostat so that low temperature MOKE studies could be performed. While the setup was not completed during this course it remains a goal for the near-future and so a brief overview of the cryostat is included here. The cryostat is a standard 'cryostation' model from 2013 ("Cryostation | Montana Instruments," accessed 2018.) and consists of a compressor, control unit, the cryostat itself and sample chamber, and a user interface computer (laptop). From the specifications the system has a minimum base temperature of 3K and a peak to peak temperature stability of <10mK. The sample chamber has five optical access ports (four on the sides and one in the top of the chamber) and has eight electrical feed-through terminals.

The main cooling is provided by a two-stage Gifford-McMahon cryo-cooler (Jakob and Lizon, 2010), which is part of a closed-cycle flow of pressurised helium from the compressor.

The cryostat is controlled by a laptop with proprietary software, however, there are also packages included that enable integration of the cryostat control into LabVIEW programs.

While the cryostat is engineered to eliminate mechanical vibration, the room-temperature MOKE measurements found in this thesis were performed with the cryostat switched off.

Chapter 4 – Micromagnetic Simulations

4.1 Introduction

As fabrication efforts utilising two-photon lithography commenced, micromagnetic simulations were performed in order to study the magnetic reversal mechanism in nanowires that exhibit single domain behaviour at remanence. Since one of the main aims within the PhD was to investigate a 3D artificial spin ice material, micromagnetic simulations were also performed upon more complex tetrapod structures.

In this chapter micromagnetic simulations of permalloy ($Ni_{81}Fe_{19}$) (Py) nanowires and 'tetrapod' structures (consisting of four nanowires arranged in a tetrahedral pattern and conjoined at a vertex) are presented. Permalloy was used as the material for these simulations as it is widely studied in the literature as discussed in Chapter 2. In addition, it was anticipated that within the next 18 months the two-photon lithography (TPL) system would be upgraded to make feature sizes of around 150nm achievable, at which point permalloy structures would be desirable for comparison with existing literature. As computational time is costly, it was decided to use the resource to produce simulations that would be more applicable for that eventuality and that could be held as their own study.

It was found that, for the dimensions used, the nanowires yield structures that are single domain at remanence and Bloch point domain walls are observed during the switching process. Hysteresis loops were performed on single nanowires with the external field applied at various angles with respect to the nanowire long axis. The loops agreed with previous results found at similar dimensions, and showed an increasing contribution of coherent rotation of the magnetisation as the external field was applied at increasing angles with respect to the wire axis. It was observed that as the angle increases the Bloch points within the walls are displaced away from the central axis of the wire, and that the magnetisation upon the circumference of the wire surface becomes canted.

Simulations on single tetrapod structures were performed to investigate the energy of different states and these were discussed by comparison with the states found within bulk spin ice. Visualisation of the micromagnetic configurations at the tetrapod vertex indicated that the two-in/two-out ice-rule state formed a stable configuration with 109.5^{o} domain walls centred upon the vertex. The three-in/one-out state also formed a stable

configuration with some curling of the three similarly aligned wires near the vertex. The four-in/out state was found to be unstable.

Hysteresis loops were performed on tetrapod structures along three principle symmetry directions. It was found for the [100] and [110] field directions that the hysteresis loops could be replicated by summing loops from single wires at the same field orientation. For the [111] field direction the addition of single wire loops could not fully replicate the loop of the tetrapod. A detailed look at the switching dynamics of the [111] loop is presented and shows that a Bloch point domain wall generates further walls after it enters the vertex of the tetrapod. The selection of paths for these additional walls differed between the forward and reverse applied external field directions.

4.2 Single Py nanowires

Micromagnetic simulations of hysteresis loops and zero-field magnetic relaxation for individual Py nanowires of finite length were performed. An initial study of the relaxed magnetisation state was used to determine the nanowire geometry for hysteresis simulations. The initial magnetisation was set parallel to the axis of the wire and the nanowire length was fixed at 1.5μm while the diameter was varied from 25nm to 90nm. The parameters for Py were taken from the OOMMF library (Donahue, 2016) such that $M_s = 860 \times 10^3 Am^{-1}$ and $A = 13 \times 10^{-12} Jm^{-1}$ with zero magnetocrystalline anisotropy constant. The Nmag mesh object was generated to have an average mesh-spacing of 3.5nm, below the typical exchange length of 5nm for permalloy (Shaker Salem et al., 2013).

Due to the wires being of fixed finite length, curling of the magnetisation was observed at the ends of the wire. The curling was more pronounced in wires of larger diameter as shown by the decrease in the m_z magnetisation component (figure 4.1(a)) and visualisations of the magnetisation (figure 4.1(b),(c)), due to the decreasing aspect ratio resulting in a reduced shape anisotropy contribution to the energy.

Nanowire dimensions of diameter 50nm and length 1.5μm were chosen when moving to hysteresis simulations. The 50nm diameter mesh was chosen as it maximised the shape anisotropy of the wire while remaining within the Bloch point domain wall regime (See Chapter 2, section 2.3).

Simulations of hysteresis in the wires were performed with the external field ranging from approximately -1T to 1T and applied at varying angles with respect to the wire axis.

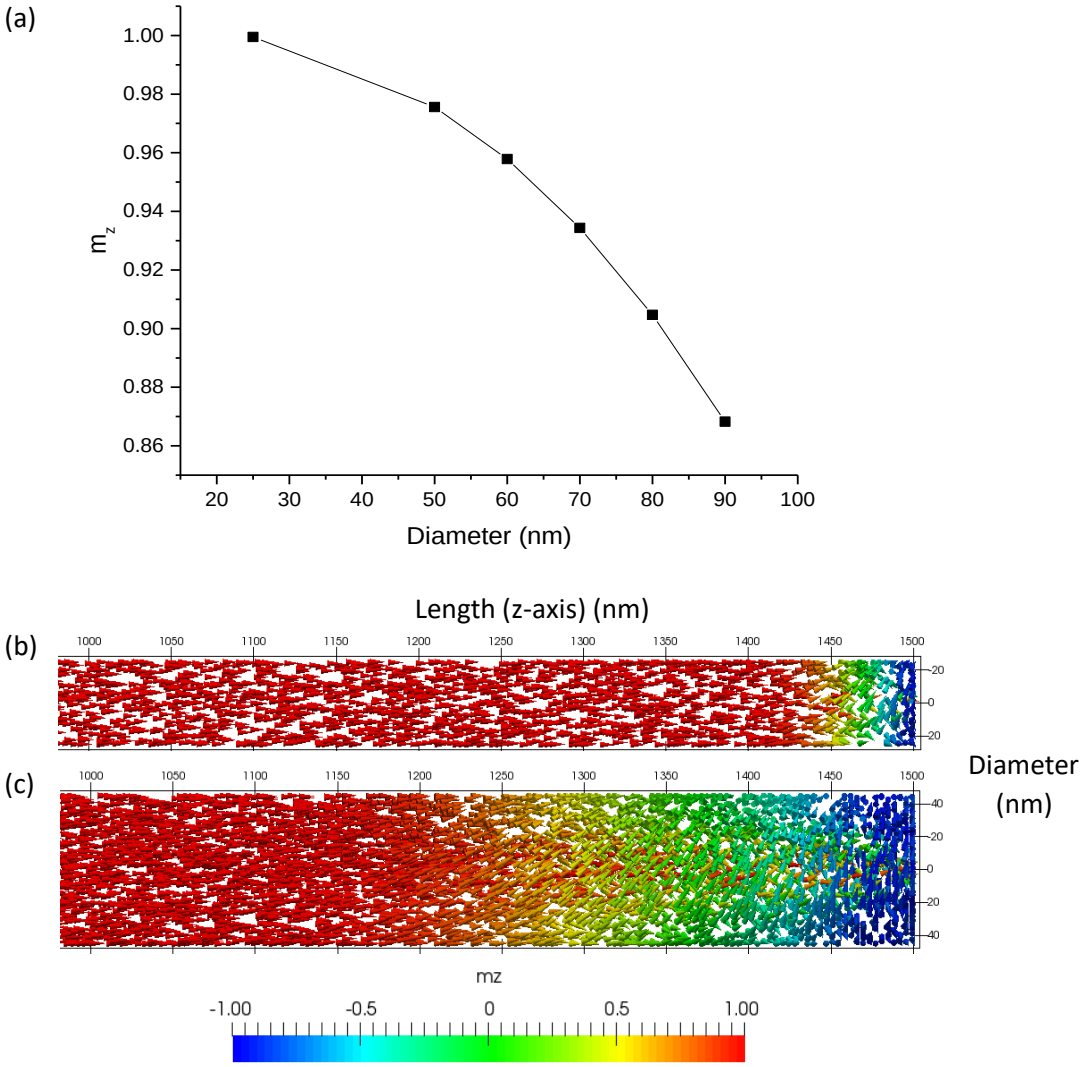

Figure 4.1: (a) Variation of m_z with diameter for nanowires of fixed length (1.5um), (b) Visualisation for magnetisation at the end of a nanowire with diameter 50nm, (c) Visualisation for magnetisation at the end of a nanowire with diameter 90nm.

The external magnetic field for each hysteresis loop simulation was applied at distinct angles chosen for direct comparison to more complex simulations performed upon tetrapod structures. The angles with respect to the wire long-axis were 0°, 35.25°, 54.75°, 70.5° and 90°. The resulting hysteresis loops are shown in figure 4.2. The loops shown in figures 4.2(a) and 4.2(e) which had angles of 0° and 90° respectively, show the typical easy- and hard-axis loops for single Py nanowires, with a coercive field for 0° of approximately 126mT, and qualitatively match the shape of loops reported previously on similar nanowire dimensions (diameter 40nm, length 2µm) (Ivanov et al., 2013). Likewise the loops in figures 4.2(b)-(d) for angles 35.25°, 54.75° and 70.5° are in qualitative agreement with results performed at similar angles (30°, 60°) on single nanowires of similar dimensions (diameter

30nm, length 1µm) (Salazar-Aravena et al., 2014), showing increasing contribution of magnetic rotation to the more square loop of figure 4.2(a).

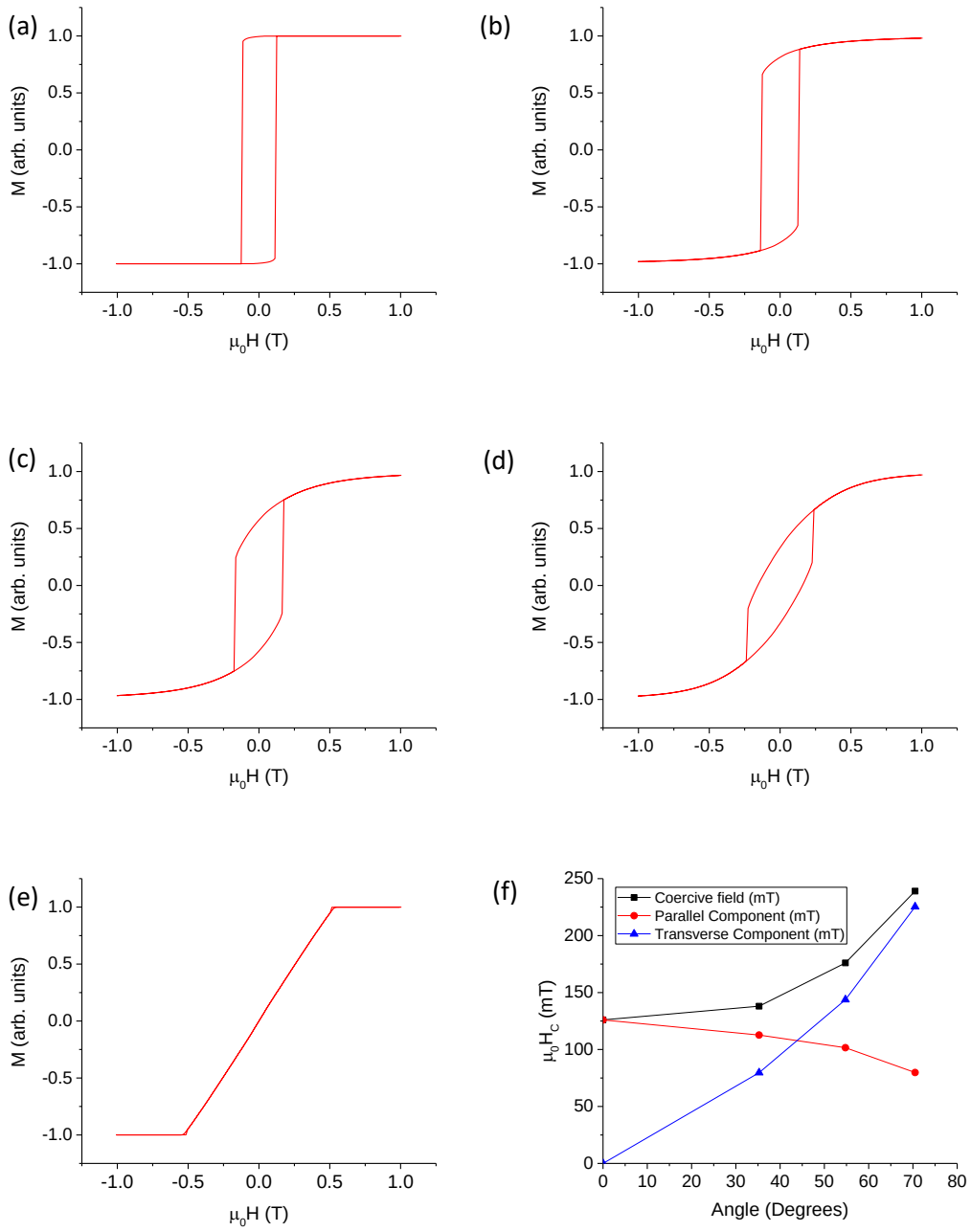

Figure 4.2: Simulated hysteresis loops performed on single nanowires with the applied field aligned at (a) 0°, (b) 35.25°, (c) 54.75°, (d) 70.5° and (e) 90°; with respect to the wire long axis; (f) variation of coercive field and components with angle between applied external field and nanowire axis.

The coercive field increases non-linearly as the angle of the external field is increased (figure 4.2(f)) and is of the same order as observed in the studies referred to above. The

saturation of the 90° loop at approximately 500mT also matches the equivalent loops in the above studies. As the switching event occurs at one field step in the simulation, the coercive fields are also equivalent to the nucleation field for the wire. As the external field is applied at an angle to the wire axis, it can be considered as the vector sum of a field component parallel to the wire axis and a component transverse to the wire axis. When the coercive fields are separated into these two components and plotted as a function of the external field angle (figure 4.2(f)), it becomes apparent that the parallel field required to cause a wall to nucleate is reduced when a transverse field is applied to the wire. The same trend was observed for planar permalloy wires by Glathe *et al.* (Glathe et al., 2008), who reasoned that the parallel nucleation field decreases because the change in shape of the domain wall induced by the transverse field lowers the exchange energy within the wall.

The behaviour of domain walls in a cylindrical nanowire under an oblique field has not been previously studied so the magnetisation structure in these simulations warrants investigation. From studying the magnetisation vector fields generated by the simulations, it is observed that wires of the dimensions used are single-domain at remanence with some curling of the magnetisation at the ends of the wire as noted above, and with further investigation of the switching event images it is observed that Bloch point domain walls are nucleated from the ends of the wires (figure 4.3(a), (b)). Both head-to-head and tail-to-tail Bloch point domain walls are observed.

When the field is completely parallel to the wire axis (0°), as the field increases rotation of the magnetisation occurs at the wire ends until at a critical field a single head-to-head Bloch point domain wall is nucleated, which propagates along the length of the wire before annihilating at the far end of the wire. The same is observed upon reversal of the external field direction. As the domain wall propagates, the Bloch point is observed to lag behind the vortex structure (figure 4.3(a)) as seen in previous studies (Piao et al., 2013).

For cases where the external field is applied at an angle >0° and <90°, as the field increases rotation of the magnetisation occurs at the wire ends similarly to the 0° case, until at a critical field it is observed that two walls (a head-to-head and a tail-to-tail) are nucleated and then propagate along the wire axis in opposite directions until they meet and annihilate in the middle of the wire. After this event the magnetisation of the wire then rotates to align with the external field as it increases. The same process is observed upon reversal of the field direction.

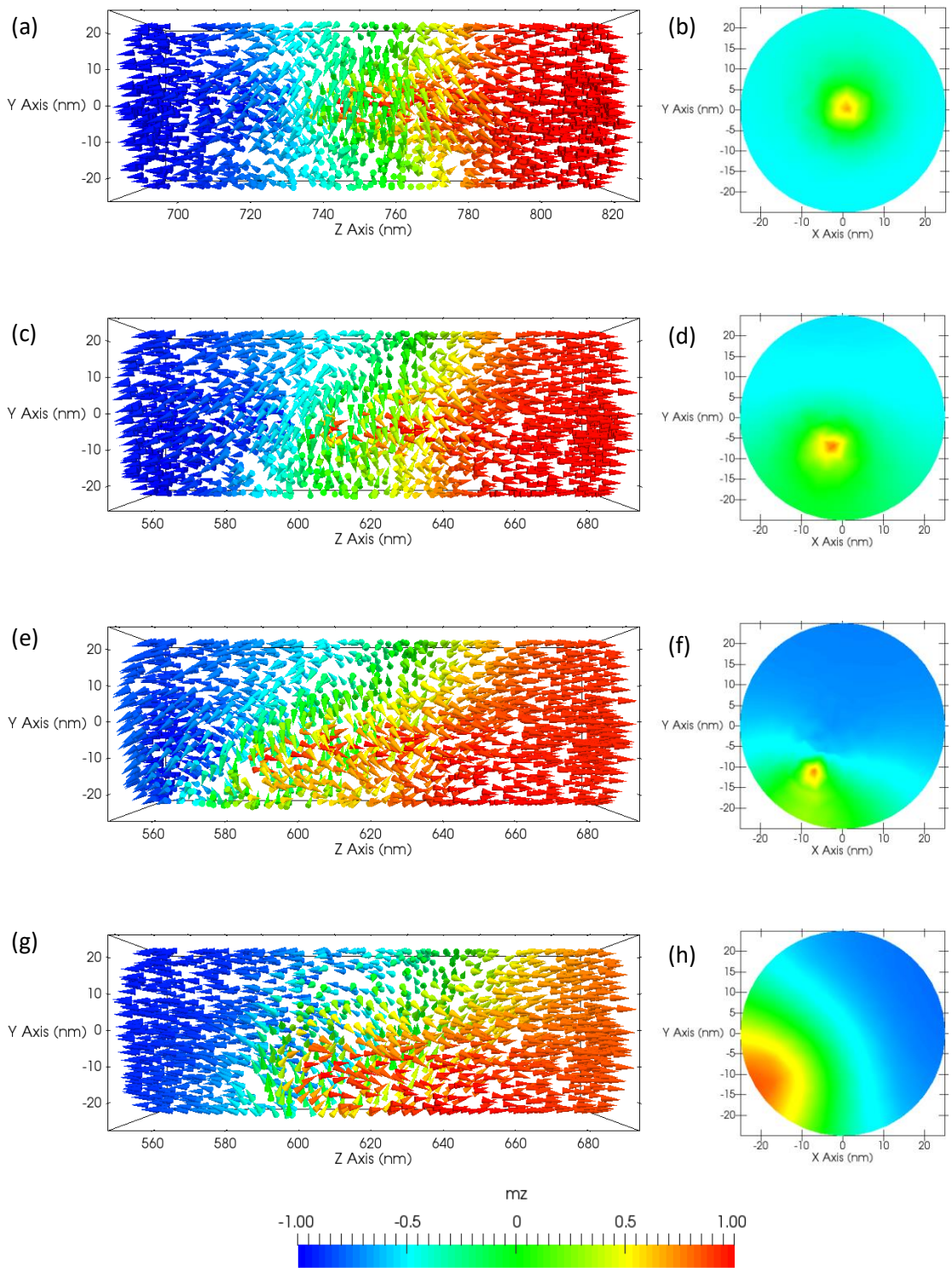

Figure 4.3: Representation of domain walls in a single nanowire with the external field applied at increasing angles with respect to the wire long-axis, colour scale is same for all images. (a) micromagnetic representation of magnetisation with external field parallel to wire axis, (b) slice presenting distribution of magnetisation a few nm from the Bloch point singularity; (c) & (d) same as for (a) & (b) with external field applied at 35.25°; (e) & (f) with external field applied at 54.75°; (g) & (h) with external field applied at 70.5°

As the angle is increased, the total field required for nucleation of the domain walls increases and the rate of magnetisation rotation also increases. When the field is perpendicular to the wire axis (90^o), as the field increases the magnetisation is observed to rotate until the wire reaches saturation and no domain walls are observed.

For the 0^o case, the curling of the magnetisation at each end of the wire is of different magnitude. This is likely due to subtle differences in the mesh ends due to the finite element approximation using tetrahedral volume elements. This ultimately leads to slightly different nucleation fields for domain walls at either end. Since the velocity of the Bloch point domain wall is high (see discussion on page 90), the single wall switches the wire magnetisation before a second wall can be nucleated. When the field is applied at an angle, there is a transverse component to the external field which affects the curling of the magnetisation at the wire's ends. This causes the curling to penetrate more evenly, and so two domain walls are nucleated at approximately the same time step.

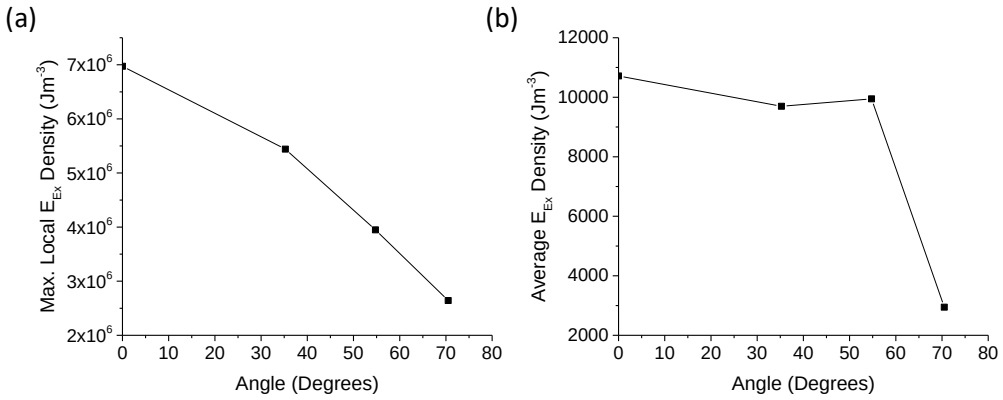

Figure 4.4: (a) Variation of maximum localised exchange energy density for simulated cylinder containing domain walls with angle of applied field (magnitude equal to coercive field as shown in figure 4.2(f)), (b) variation of averaged exchange energy density for simulated cylinder containing domain walls with angle of applied field.

By probing the maximum values of exchange energy in the wire over the switching process timescale, it is seen that as the angle is increased the maximum localised exchange energy decreases (figure 4.4(a)). As discussed in chapter 2, the Bloch point itself has no magnetisation and so is propagated only by the change in the exchange energy of the surrounding vortex structure. Hence, the decrease in exchange energy results in a lowering of the parallel field component required to nucleate a wall in a cylindrical wire. As noted above, this is the same trend as observed for nucleating domain walls in planar nanowires.

As the angle is increased the magnetisation on the outer edge of the domain wall becomes canted, leading to a linear increase in wall width. With the field applied at an angle to the wire axis, the Bloch points are seen to be displaced away from the central axis of the wire towards the outer surface (figure 4.3). At larger angles this shift causes the magnetisation to start to be directed out of the curved surface near to where the point has been displaced. With the external field applied at 70.5° the Bloch point is pushed to the outer surface of the wire (figure 4.3(g)) and the domain wall can no longer be considered a Bloch point domain wall. This is illustrated in figure 4.4(b) where the averaged exchange energy for the simulated cylinder containing domain walls shows an abrupt change for an applied field at 70.5°, indicating that the core of the Bloch point domain wall is no longer present.

The difference in trends between the averaged exchange energy density and the maximum localised density shown in figure 4.4 can be explained by considering what the two terms represent. The averaged density is summed over the entire cylinder, hence it indicates the energy of the vortex structure surrounding the Bloch point. As the angle of the applied external field increases the core is displaced, but the vortex structure remains as shown in figure 4.3(a)-(f), until it is destroyed at 70.5° shown in figure 4.3(g), (h). As such the averaged density varies little while the vortex structure is intact before decreasing dramatically when the structure is removed. In comparison, the maximum localised density will depend on the adjacent spins that are nearly anti-parallel at the Bloch point. As the field angle increases the transverse component increases, which causes the angle between these spins to be reduced which lowers the maximum exchange energy as returned by the simulation.

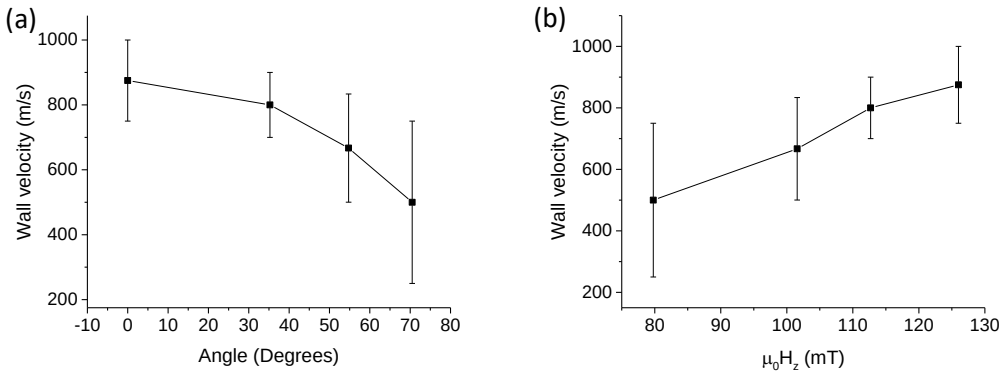

Figure 4.5: (a) Average wall velocity as a function of angle of external field to the wire axis, (b) Average wall velocity as a function of the external field component parallel to the wire axis.

One of the notable properties of domain walls in cylindrical nanowires is their high velocity. From a series of the above magnetisation images, velocities were calculated from the difference in position of a wall within a wire between time steps in the simulation. The wall velocity was found to decrease non-linearly with increasing angle (figure 4.5(a)), or equivalently increase linearly with increasing field component parallel with the wire axis (figure 4.5(b)), as would be expected for field-driven domain walls. Error bars were calculated using an estimate for the uncertainty of domain wall position (±50nm) and the interval of time between the two positions. The error for 70.5° is notably large (≈50%) due to the small number of time steps between measurements for that angle (2 x 10ps steps).

With the field parallel to the wire axis and with magnitude 128mT, the velocity of the Bloch point domain wall was approximately 850ms^{-1}. This value is less than half what was reported by Piau *et al.* who found that a Bloch point domain wall propagated with a velocity of approximately 2000ms^{-1} at a field of approximately 120mT in a permalloy wire of similar dimensions (50nm diameter and length 2μm) using the same material parameters (Piao et al., 2013). The discrepancy can be explained by the observation made by Forster *et al*. who found that the velocity of a Bloch point domain wall is dependent on the Gilbert damping parameter, α, used in the simulation (Forster et al., 2002). From their study, for an applied field of 188mT the velocity increased from around 375ms^{-1} with α = 1 to around 1750ms^{-1} with α = 0.05, for Co cylinders with diameter 40nm and length 600nm. Piao *et al.* used a damping parameter α = 0.01, whereas for this work α = 0.5, hence the large difference in velocities is to be expected.

With the hysteresis curves and domain wall regime found to be in agreement with previous literature for simulations on cylindrical nanowires, attention then turned to structures composed of such wires.

4.3 Tetrapod energy states

A tetrapod consists of four nanowires conjoined at the origin and directed along the [1 1 1], [-1 -1 1], [-1 1 -1] and [1 -1 -1] directions, such that the free ends of the nanowires form the vertices of a tetrahedron as shown in figure 4.6. In this arrangement, the wire long-axes mimic the constrained spin directions of the rare earth ions in the bulk pyrochlore spin ices such as dysprosium/holmium titanate. As such, provided that the wires are single domain at remanence and exhibit Ising-like behaviour, the tetrapod structure can be thought of as the most fundamental 3D artificial spin ice (3D ASI) building block. Understanding the nanomagnetism in these most simple structures will allow a better understanding of how

bulk frustrated systems can be mimicked using 3D nano-islands. Such structures can be fabricated, potentially in large lattices, by emerging 3D nano-fabrication techniques such as two-photon lithography (Williams et al., 2017).

When considering the realisation of a 3D ASI material, there are two primary components. Firstly, whether the stationary configuration and their associated energetics match what is seen in bulk spin ice. Secondly, whether the magnetic reversal of the 3D ASI system capture the exotic physics observed in spin ice, where monopole excitations are created and transported.

Initial simulations were carried out to see if static spin ice like states can be observed in tetrapod structures and to determine their relative energies. The nanowire dimensions were chosen to be the same as those used in the simulations on single nanowires, as were the material parameters for Py. For these simulations the initial magnetisation for each wire was set along the axis either 'in' or 'out' to a radius of 110nm from the vertex centre. The region within this radius (consisting of the vertex and remainder of the wires radiating from it) was given a random magnetisation. The magnetisations of the wires were placed in different states while the tetrapod was relaxed with no externally applied field.

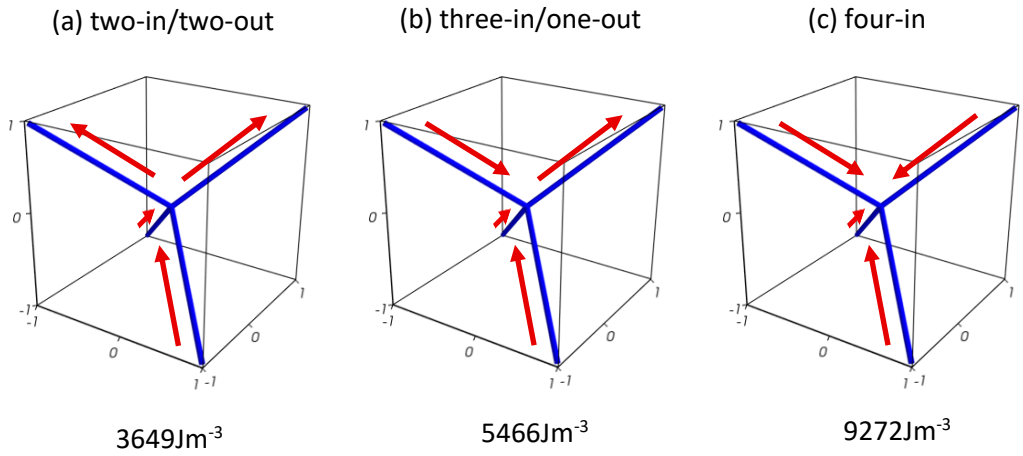

Figure 4.6: Configuration of different magnetic states and their associated energy densities, (a) the two-in/two-out state, (b) the three-in/one-out or one-in/three-out state, (c) the four-in or four-out state. Tetrapod cell volume ≈1.18x10^{-20}m^3

As shown in figure 4.6, the unit cell configurations follow the same trend as that of bulk pyrochlore spin ices (Levis, 2012), with the two-in/two-out state having the smallest energy density and the four-in/out state having the highest. The value presented in figure 4.6(c) for the energy value of the four-in/out state is an approximation as, for a tetrapod with

connected wires, this state is unstable and does not relax into a symmetrical four-in/out state. This can be seen in figure 4.7(e) where a domain wall has been pushed out of the vertex and against the pinned region of the wire. The two-in/two-out and three-in/one-out states were stable without the need to pin the magnetisation.

Figure 4.7 shows the micromagnetic visualisations at the vertex for the three states. For the two-in/two-out configuration shown in figure 4.7(a), the magnetisation has a smooth rotation from the 'in' wires to the 'out' wires, forming a symmetric arrangement of 109.5° domain walls (figure 4.7(b)).

For the three-in/one-out state shown in figure 4.7(c), the three wires pointing in have a curling in their magnetisation as they join the vertex. Shown for this case, one wire curls in the opposite sense to the others.

By viewing the vertex along the positive [111] axis, the three intersections of the 'in' wires can be observed simultaneously, and from figure 4.7(d) it can be seen that the localised total energy is different for each. This can be explained by considering that, at each intersection, the curling of the wires directs the magnetisation along either the positive [111] axis or the negative [111] axis. When this is directed in the positive sense for both of the 'in' wires it matches the magnetisation of the 'out' wire and has a smooth transition in magnetisation. When both are directed in the negative this acts against the 'out' magnetisation and so has a larger localised total energy. When one wire is directed positive and the other negative the intersection has a localised total energy between these two other states. The difference in localised energies could have an effect on domain wall propagation through the vertex. However, as shown and discussed later in section 4.4, during hysteresis simulations the curling in the three-in/one-out state was symmetric, causing the three intersections to be uniform.

The four-in/out state is observed to be very energetically unfavourable such that, as shown in figures 4.7(e) and (f), a domain wall has been ejected from the vertex up to the pinned site of a wire so that the vertex can attempt to reach a three-in/one-out state. The instability of this configuration is due to the extremely large energy that arises from the converging of the magnetisation of the four wires. This is consistent with observations in both bulk spin ice and the square lattice artificial spin ice where the four-in/out state is very unfavourable (R. F. Wang et al., 2006).

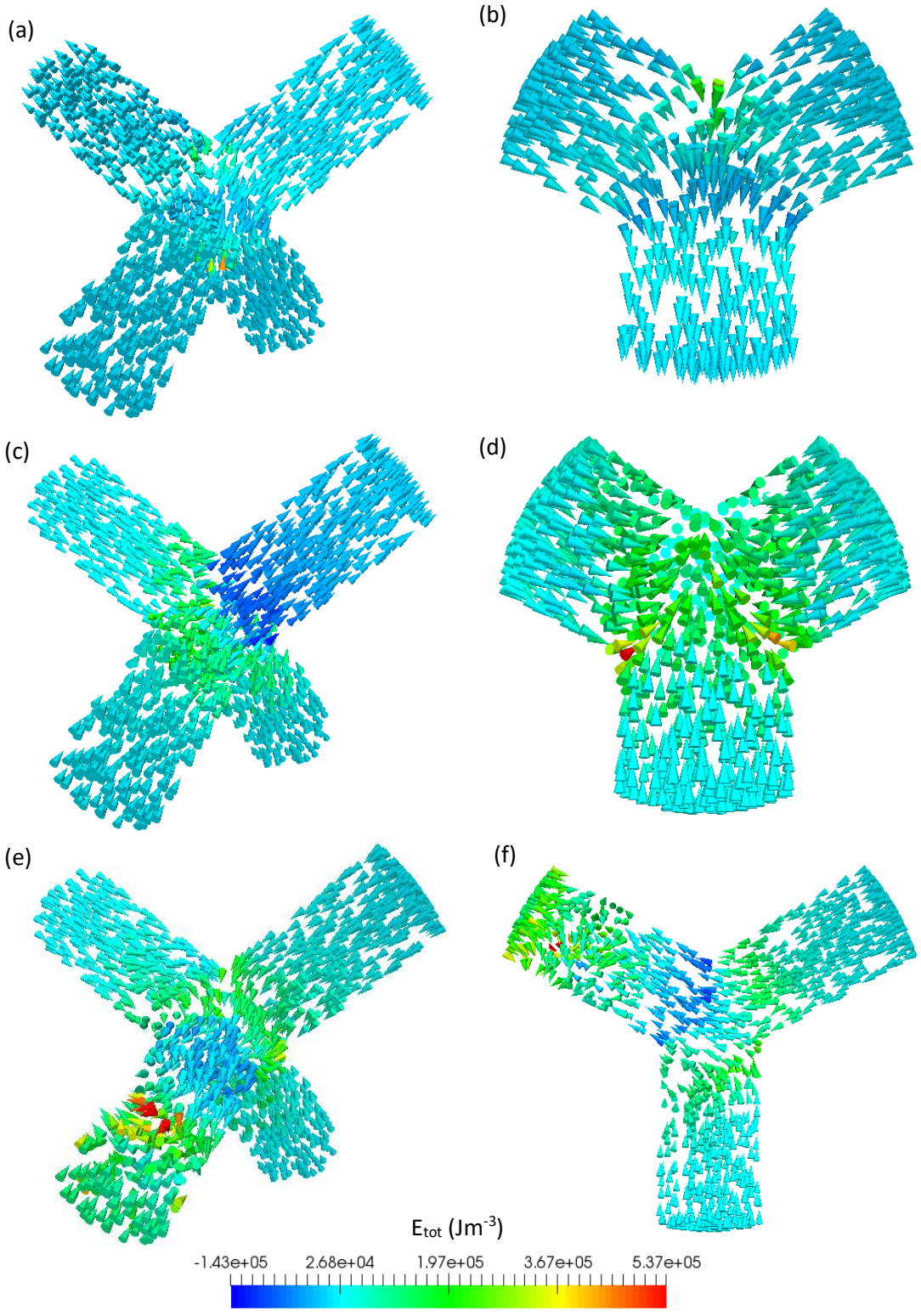

Figure 4.7: Micromagnetic visualisations of the vertex of a tetrapod cell showing localised total energy for states where the wires were pinned from a radius of 110 nm from the vertex centre; (a) two-in/two-out state, (b) view along [111] axis of (a), (c) three-in/one-out state, (d) view along [111] axis of (c), (e) four-in state, (f) view along [111] axis of (e).

4.4 Tetrapod hysteresis loops

With the energetics showing stable two-in/two-out and three-in/one-out states, the reversal of a cell became the next focus. Simulated hysteresis loops were performed on permalloy (Py) tetrapods with wire length 1.5μm and diameter 50nm to ensure the wires are single domain at remanence. Material parameters used were those found in OOMMF (Donahue, 2016). The loops were performed on the three symmetry axes of a tetrapod unit cell: the [100], [110] and [111] directions.

As seen in figure 4.8(a), for the [100] direction there is a single switching event as all four wires in the tetrapod have the same alignment with respect to the external field. As none of the wires are aligned parallel to the field, there is also significant rotation observed at higher fields up to saturation of approximately 1T. The coercive field of the transition is 170mT, consistent with that observed for the single nanowires in section 4.2.

From the micromagnetic visualisations it is observed that a domain wall nucleates from the free end of each of the four nanowires and they each travel toward the vertex. Interestingly, while the domains nucleate simultaneously, they travel through the wires at different speeds. It was seen for the reverse field direction that the two walls propagating in the same direction as the field arrived at the vertex first, while the two propagating against the field arrived later. The two walls in each set had similar speeds. For the forward field direction three of the walls arrived at the vertex at approximately the same time while one arrived later, this later wall propagating against the field direction. The first observation would suggest that the difference in speeds is due to the external field enhancing or impeding mobility depending on direction of travel, however the second perhaps implies delays in nucleation or a dip in mobility due to local perturbations in the magnetisation on a wall-by-wall case.

Compared with single wires, the tetrapods allow the possibility of interactions between the comprising wires which might explain these effects, however this is unlikely. One of the main possibilities for interaction is between the stray fields from the free ends of the wires, however from the geometry the distance between free ends is 2.45μm which is much greater than the length of a single wire. Another possibility would be domain walls interacting with each other or with the vertex, although these effects would be expected to be more pronounced as the walls approached closer to the vertex, and would be expected to have some symmetry due to the tetrapod geometry.

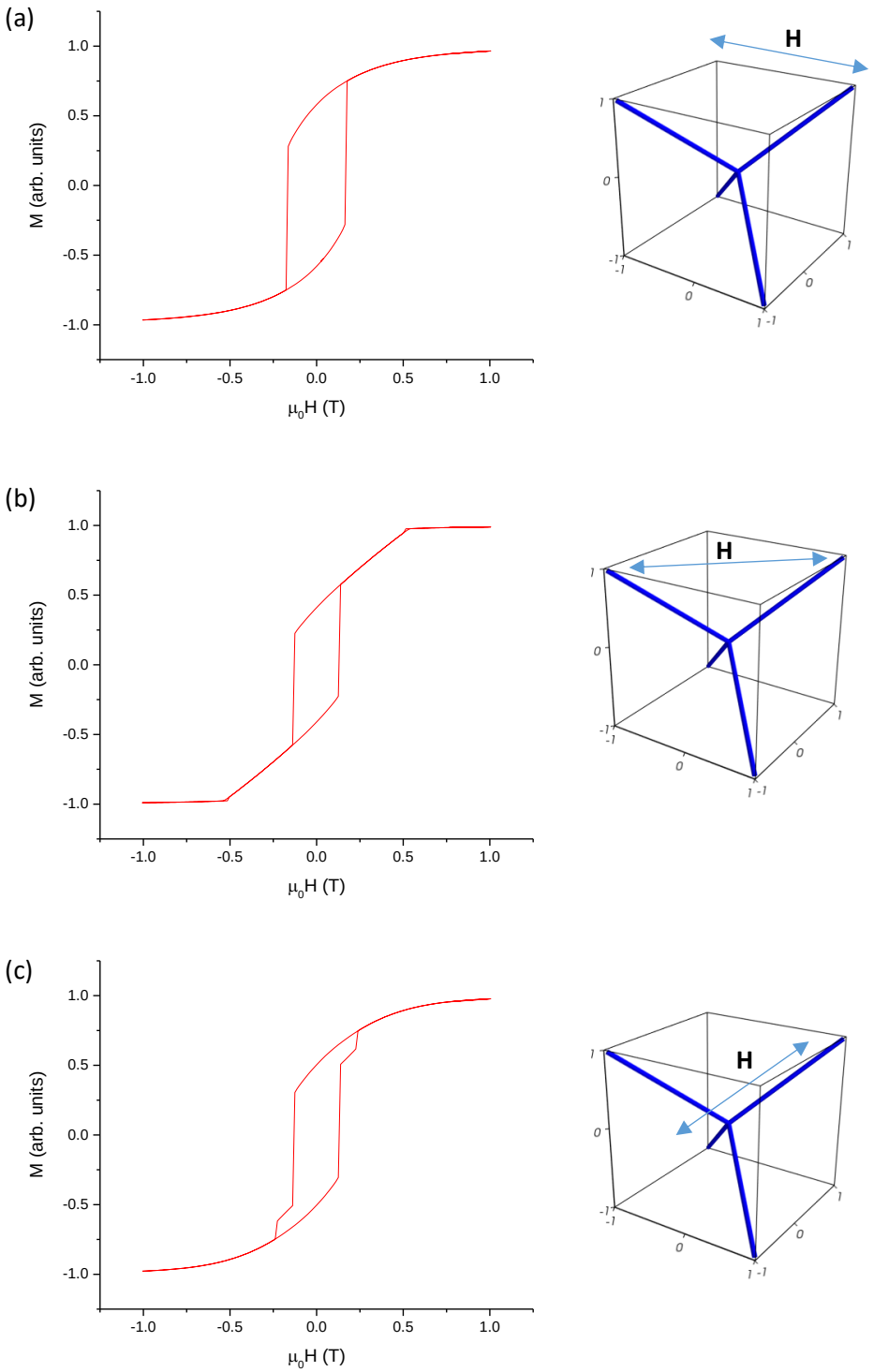

Figure 4.8: Hysteresis loops from simulations performed on a tetrapod cell with the external magnetic field applied in the following vector directions as shown in the cell image: (a) [1 0 0], (b) [1 1 0], (c) [1 1 1]. The magnetisation in each case is the component parallel to the external field.

From figure 4.8(b) it is seen that the [110] direction also has a single switching event from the two wires that are angled at 35.25° to the external field. The two wires that are perpendicular to the external field add a very hard-axis-like linear rotation until it saturates at just over 500mT (approximately 515mT). The coercive field of the transition is 132mT, which is lower than that seen in the [100] transition due to the larger component of the magnetic field along the wire axis as observed in the variation of coercive field with angle for single wires in section 4.2.

From the visualisations, a domain wall nucleates from the end of each of the wires parallel to the applied field and then annihilate when they meet. It was observed that for the reverse field direction the two walls met at the vertex, arriving at approximately the same time; whereas on the forward field direction one wall (strangely the one propagating against the field direction which further suggests differences in domain wall mobility are due to local effects for each wall) arrived at the vertex first and passed through it to annihilate with the second wall within the wire.

From figure 4.8(c), which shows the hysteresis loop shown for the [111] direction, there are two observed transitions, the initial larger transition has coercive field 132mT, the same as for the transition in [110], while the second transition has coercive field of 232mT. The full consideration of the domain wall dynamics during these switching events is detailed below after consideration of the loops in terms of the single nanowire loops. Interestingly, a plateau in the magnetisation curve along the [111] direction can also be observed in bulk pyrochlore spin ice (Borzi et al., 2016; Isakov et al., 2004; Matsuhira et al., 2002; Moessner and Sondhi, 2003). However the mechanisms for this plateau are different as the bulk spin ice compounds interact over a large lattice, whereas the simulations presented here concern only a single unit.

By comparing the hysteresis loops from the tetrapod structure to those on single nanowires, an immediate similarity can be noted between the 54.75° loop for a single wire (figure 4.2(c)) and the [100] loop for the tetrapod (figure 4.8(a)). When these are plotted together it is apparent that they are nearly identical (figure 4.9(a)). This follows from the visualisation of the magnetisation, as each wire comprising the tetrapod is angled at 54.75° to the external field. As such they all nucleate a wall at the same field and so the resultant normalised loop is nearly equivalent to that of a single wire, with some variation due to the interaction at the vertex in the tetrapod.

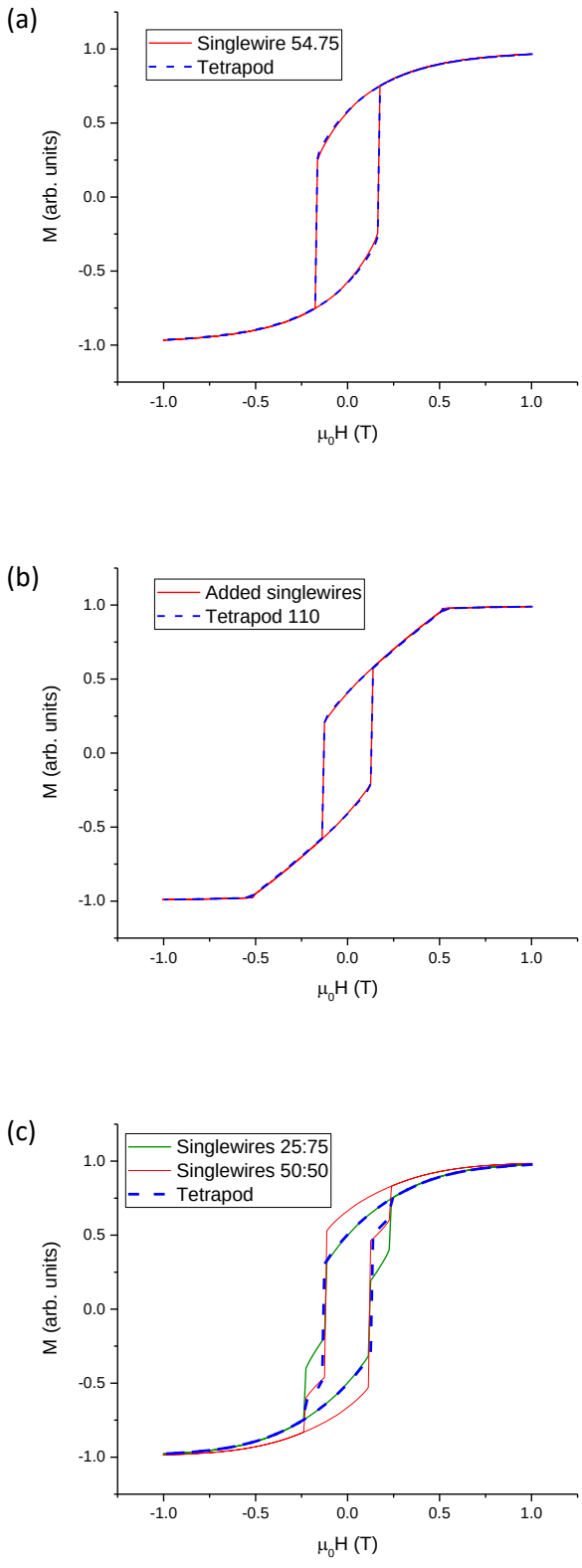

Figure 4.9: Comparison of tetrapod loops with those of single wires, (a) Tetrapod [100] and single wire at 54.75°, (b) Tetrapod [110] and added loops of single wires at 35.25° and 90°, (c) Tetrapod [111] and added loops of single wires at 0° and 70.5°.

Following on from this, by adding the loops for the 35.25° and 90° single wires (figure 4.2(b), (e)) in a 50:50 ratio, a loop is obtained that is similar to that of the [110] tetrapod (figure 4.8(b)). When plotted together, it is again readily apparent that the added loop is nearly identical to the tetrapod loop (figure 4.9(b)). As noted above, in the magnetisation images it is observed that the wires parallel to the plane of the field both propagate a wall at the same field, while the two wires that are perpendicular to the field only undergo rotation, so the normalised addition of the two cases in the single wires is able to reproduce this loop with some minor variation from the vertex again.

Moving onto the remaining loop, by adding the 0° and 70.5° loops for single wires together (figure 4.2(a), (d)), it is possible to obtain loops that partially match that of the [111] tetrapod loop (figure 4.8(c)). Adding the loops for the single wire in a 50:50 ratio manages to approximate the magnetisation change from the initial transition, but does not match the rotation of magnetisation, while adding them in a 25:75 ratio matches the rotation, but causes the magnetisation plateau from the initial transition to be at a lower value (figure 4.9(c)). In comparison to the previous two cases, the [111] loop bears a distinction in that the two wire subsets (0° and 70.5°) do not switch independently of each other. When the 0° wire switches it creates a four-in/out state at the vertex, and as mentioned above this is highly unstable. As such, and due to the vertex connecting the wires together, domain walls are propagated through two of the 70.5° wires but at the coercive field of the 0° wire, causing a further change in magnetisation than expected by considering only single wires. It is likely that the added loop in the 25:75 ratio is what would be observed for a disconnected tetrapod cell where the wires are sufficiently spaced apart that a four-in/out arrangement is allowed. From this however, it can be noted that the nanostructuring of the conjoined vertex in the cell does play a part when considering reversal mechanisms.

A series of magnetisation images for the [111] simulation are shown in figure 4.10, for different key points in the hysteresis loops as indicated by figure 4.10(a). At the largest applied field of just over 1T the entire cell is at saturation (figure 4.10(c)). As the field is reduced the magnetisation rotates to lie parallel with the wire long-axes (figure 4.10(d)) in a three-in/one-out state. After the initial transition at -132mT the cell is left in a two-in/two-out state (figure 4.10(e)). The switching mechanics are further explained by the time series shown in figures 4.11 and 4.13.

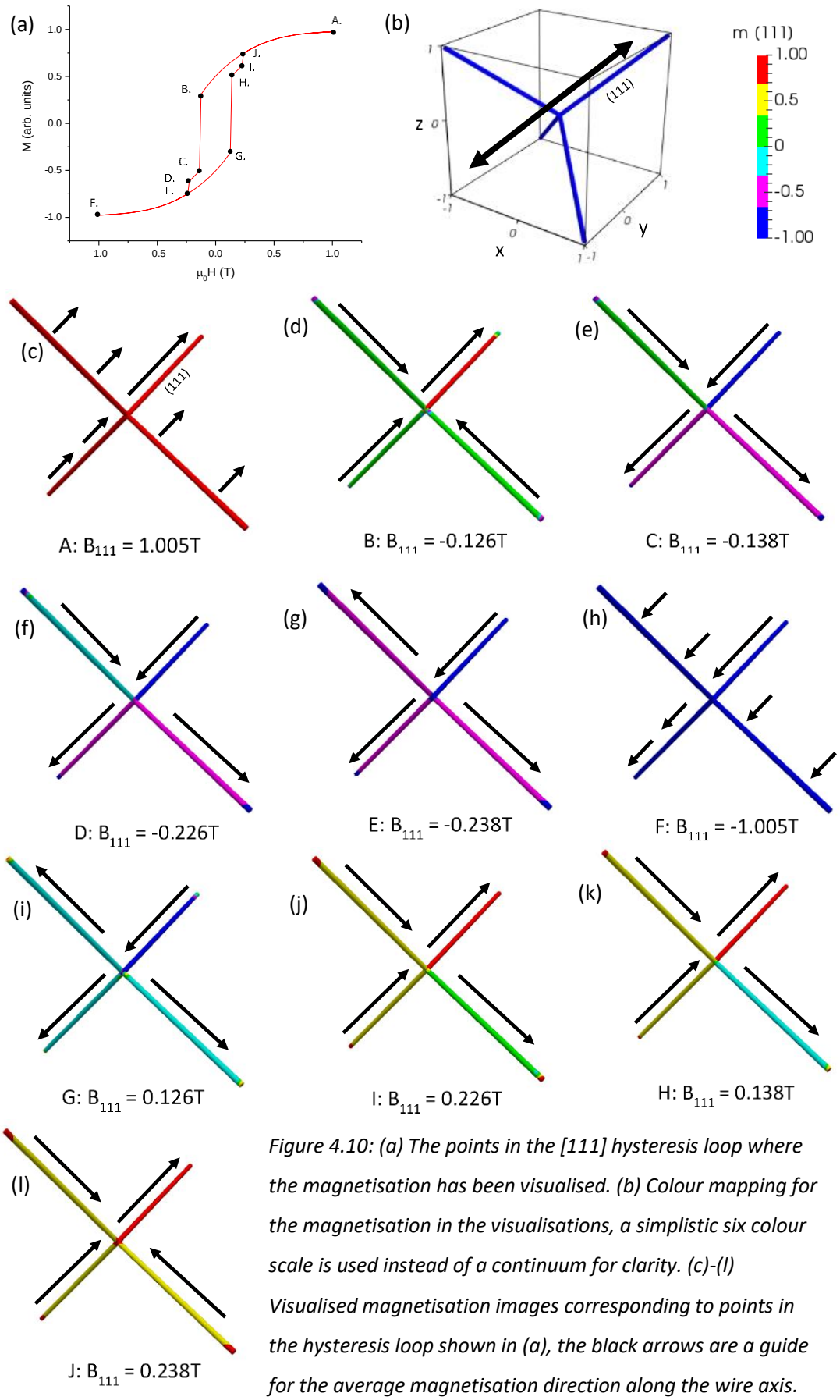

Figure 4.10: (a) The points in the [111] hysteresis loop where the magnetisation has been visualised. (b) Colour mapping for the magnetisation in the visualisations, a simplistic six colour scale is used instead of a continuum for clarity. (c)-(l) Visualised magnetisation images corresponding to points in the hysteresis loop shown in (a), the black arrows are a guide for the average magnetisation direction along the wire axis.

By visualising the magnetisation dynamics during the initial transition, it is observed that a domain wall nucleates from the free end of the wire aligned parallel to the field (figure 4.11(b)). When the wall enters the vertex it causes the nucleation of another domain wall in each of two of the three remaining wires. This process causes the structure to go from a three-in/one-out state to a four-in state (figure 4.11(c)). However, because of the high energy, further walls are immediately propagated (figure 4.11(d)), which leaves the cell in a two-in/two-out state at the end of the transition.

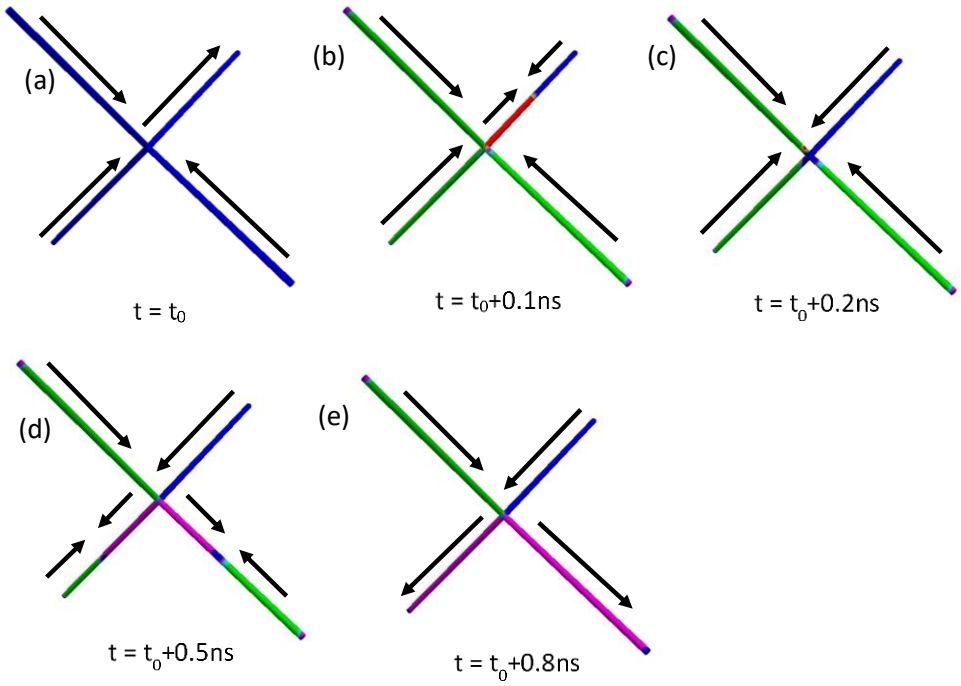

Figure 4.11: Time series of magnetisation during the switching event between figure 4.10(d) and figure 4.10(e), with t_0 being the time at which the external field step incremented.

When the wall enters the vertex, one of four situations would be expected: the wall could pin, creating a four-in state; the wall could cause the nucleation of a single wall resulting in a three-in/one-out state; the wall could clone once and cause two further walls to nucleate resulting in a two-in/two-out state; or the wall could clone an additional time causing three walls to nucleate, resulting in a one-in/three-out state.

Due to the finite width of the nanowires comprising the tetrapod structure, the vertex has a larger cross-sectional area compared to the wire diameter. It has been shown that a protrusion or increase in diameter of a cylindrical wire can act as a pinning site for domain wall motion (Berganza et al., 2016; Chandra Sekhar et al., 2014). However, there are several factors that could prevent a wall becoming pinned. Firstly, as seen in the magnetisation profiles for the propagating Bloch point domain walls in single nanowires

(figure 4.12(a)), the Bloch point itself lags behind the vortex structure surrounding it. The magnetostatic energy (and associated magnetic charge, $(\nabla \cdot \mathbf{M})$) of such a wall is concentrated at the Bloch point (figure 4.12(b)) but it is moved by the exchange energy of the vortex structure. Therefore, as the wall approaches the vertex, the vortex structure does not experience as large a magnetostatic repulsion as the Bloch point and so can enter the vertex before it can pin, and the exchange energy then pulls the Bloch point in afterwards. Secondly, as observed from the static energy states, a four-in state at the vertex is energetically unfavourable.

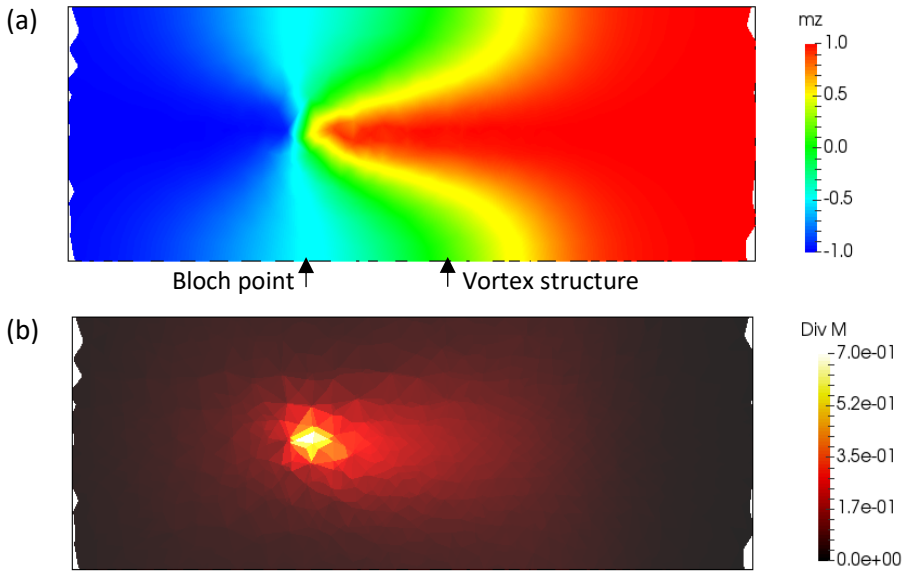

Figure 4.12: (a) Magnetisation profile of Bloch point domain wall in cylindrical nanowire with positions of Bloch point and leading vortex structure marked, wire axis is parallel to the z axis, (b) divergence of magnetisation for the same Bloch point domain wall.

Additionally, because the domain walls are not initially present in the simulation they must first be nucleated. Therefore in the simulation the external field is at the parallel wire's nucleation field when the domain wall approaches the vertex. For the three non-parallel wires the external field is angled at 70.5° which introduces a significant transverse component as seen in section 4.2. As a result the energy required to propagate a domain wall from the vertex into these wires is lowered and so it is unsurprising that the domain wall is not observed to pin during the simulation.

As was mentioned in chapter 2, it is possible for domain walls to clone at junctions in planar nanowires. For the tetrapod the cloning is possibly dictated by the energy states – the wall entering the vertex forms a four-in state, if only a single wall was nucleated out the state

would lower its energy and produce a three-in/one-out state. However, the nucleation of two further walls reduces the energy of the vertex even further. The static case energies showed that the two-in/two-out state is the least costly of the three types of vertex. As there is an energy cost for the formation of domain walls, coupled with the one-in/three-out state being of higher energy compared to the two-in/two-out state, it would seem unlikely for the wall to clone twice.

The secondary transition is then the remaining wire switching, resulting in a final state of one-in/three-out, completing the reversal of the whole cell. In this secondary switching the domain wall nucleates from the free end of the wire.

The magnetisation continues to rotate as the field is increased in the negative sense (figure 4.10(f)) until the remaining non-parallel wire switches at -232mT resulting in the cell being put into a one-in/three-out state (figure 4.10(g)). The cell is then fully saturated in the negative field direction at the same field magnitude of just over -1T (figure 4.10(h)).

As the field is increased from -1T to 1T, the same sequence of transitions occurs. It is notable however, that during the initial transition at 132mT, the two non-parallel wires that switch due to the propagation of the domain wall through the vertex are not the same two wires observed as switching in the inverse field ramp (figure 4.13(d)).

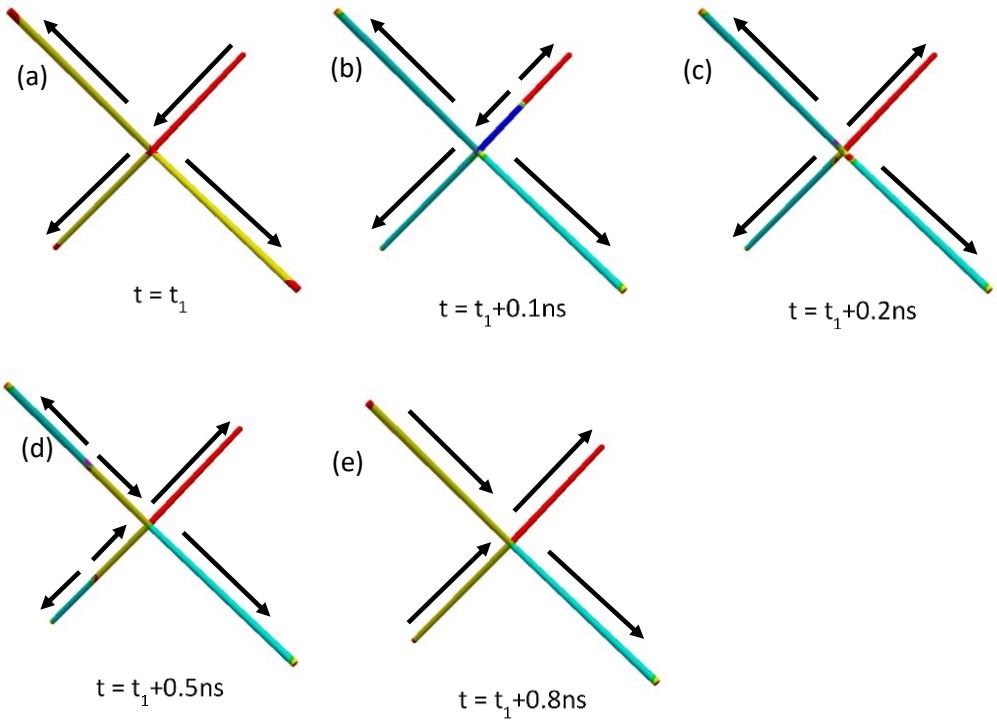

Figure 4.13: Time series of magnetisation during the switching event between figure 4.10(i) and figure 4.10(j), with t_1 being the time at which the external field step incremented.

Of note is that while the initial transition event contains multiple wires switching, there does not seem to be a preference for which of the three non-parallel wires have a domain propagate through. Looking at the micromagnetic configuration of the vertex before the wall enters, it shows that the three wires have the same rotational sense causing the vertex to be symmetric around the [111] axis (figure 4.14), differing from the three-in/one-out state shown in the static configuration in figure 4.7(c) where one wire has differing curling at the vertex, creating an asymmetry. As the Bloch point domain wall is rotationally symmetric in the parallel wire, there is thus no preference for any of the three wires for the case observed during the hysteresis loop as the localised total energy is approximately uniform between the wall and each of the wires close to the vertex. This differs from connected honeycomb 2D ASI where the chirality or type of domain wall shows a preference at Y-shaped junctions (Walton et al., 2015). It is possible that had the wires not been in a uniform chirality that the wall(s) may have preferentially selected a path. The differing selection of wires switching for forwards and reverse applications of the external field direction also suggests that there is no preferential distribution of mesh points influencing the selection process.

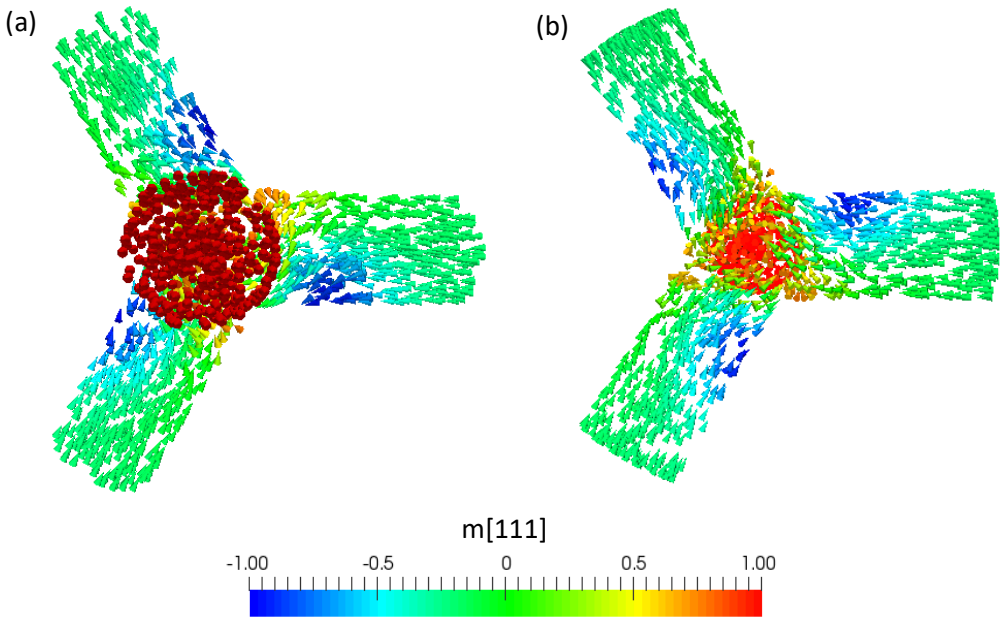

Figure 4.14: Micromagnetic visualisation of the vertex from figure 4.10(d) as viewed along (a) the negative [111] axis and (b) the positive [111] axis.

Also of note is that, while the tetrapod cell exhibits three-in/one-out 'monopole-like' states, unlike in 2D artificial spin ice these are the result of the remanent magnetisation in the vertex rather than pinned domain walls at junctions, as the Bloch point passes through

the vertex without pinning. This is a significant difference as the lack of pinned walls should mean that the 3D vertex is more stable in the face of thermal and magnetic fluctuations. It also raises the question of how mobile a monopole-like state would be in an extended 3D nanowire lattice, which is a potential future study if a computing architecture that can support such an extended simulation mesh becomes available.

Chapter 5 – Magnetometry of 3D Magnetic Nanostructures

5.1 Introduction

In this chapter a comprehensive analysis of 3D nanostructures fabricated in-house using two-photon lithography (TPL) is presented. The structures covered include vertical nanowires, angled nanowires and full tetrapod structures (mirroring the simulations covered in chapter 4).

A study of the lateral feature size was performed on cylindrical nanowires as a function of laser-write power and the minimum achieved feature size was measured to be 435nm. This closely matches the expected feature size of 424nm obtained by taking dark erosion into account with a theoretical model of two-photon polymerisation.

Arrays of angled nanowires and full tetrapod structures fabricated at a higher power were imaged using scanning electron microscopy (SEM), and the distribution of feature sizes within arrays was found. The angled nanowires were found to have an average lateral feature size of 750±40nm and an average perpendicular feature size of 910±30nm after correcting for parallax. The tetrapod structures were found to have a lateral feature size of 610±55nm and a perpendicular feature size of 900±75nm. Images of full arrays covering a total area of 300µm by 300µm showed that the structures were regularly ordered with a wire-length ratio of 0.95±0.04 between the two lower wires affixed to the substrate and the two upper wires.

Atomic force microscopy (AFM) was performed upon fallen nanowires and trenches within the resist to compare surface roughness between the two. They were found to be similar, with the roughness measured as ±3nm for the wire and ±5nm for the resist trench.

Spin-polarised SEM (spin-SEM) was performed in collaboration with IBM, Zurich. The study demonstrated that spin-SEM is a powerful methodology that can be utilised to measure 3D magnetic nanostructures.

The images showed the underlying magnetisation of the top-surface of a wire within a tetrapod sample and indicated that it was in a multi-domain regime. Images of the vertex showed that the vertex maintained a multi-domain structure despite application of a field in excess of the coercive field of the sample, directed out of the sample plane.

Magneto-optical Kerr effect (MOKE) magnetometry was performed on an array of individual angled nanowires. The obtained hysteresis loops for both polar geometry and

longitudinal with the field applied parallel to the projection of the wire axis on the substrate showed a steep initial rise in magnetisation. At higher fields the change of magnetisation with field was notably reduced and saturation was not achieved. Longitudinal loops with the field applied perpendicular to the projection of the wire axis on the substrate showed much more hard-axis-like behaviour and the sample once again did not reach saturation in the field range (≈450mT).

MOKE magnetometry was performed on an array of full tetrapod structures. The obtained hysteresis loop for polar geometry closely resembled that obtained for the individual angled nanowires. The longitudinal loops indicated a sharp initial transition, followed by further transitions at higher fields. When rotated by ninety degrees such that the applied field was parallel to the projection of the upper wire long-axis a similar looking loop was obtained.

5.2 Lateral feature size study

TPL is a relatively new fabrication technique that, while used in areas such as microfluidics and metamaterials, has not previously been explored for magnetic micro/nanostructure fabrication. In light of this it was useful as a first study to determine the range of feature sizes that are readily obtainable with the technique. This is an important property for magnetic structures as the size and geometry of such structures have significant effects on the magnetic properties – notably whether they are in a single- or multi-domain regime, and with shape anisotropy affecting the magnetostatic contribution to the energies.

As such, a study of the minimum possible feature size in magnetic nanostructures that could be achieved with a stock Nanoscribe system at Cardiff was performed. To perform the study, samples were produced where TPL was used to write an array of vertical channels in the resist layer, using single write-lines, while laser power was reduced systematically across the array. Development time was maintained for all arrays at 30 minutes. The templates were then filled with cobalt using electrodeposition and the resist removed to produce a ‘power array’ of vertical cobalt nanowires with a cylindrical cross-section (figure 5.1(a), (b)). From figure 5.1(c), it is clear that the lateral feature size decreases with laser power in a non-linear fashion, with a minimum achieved size of 435nm, taken from top-down SEM images.

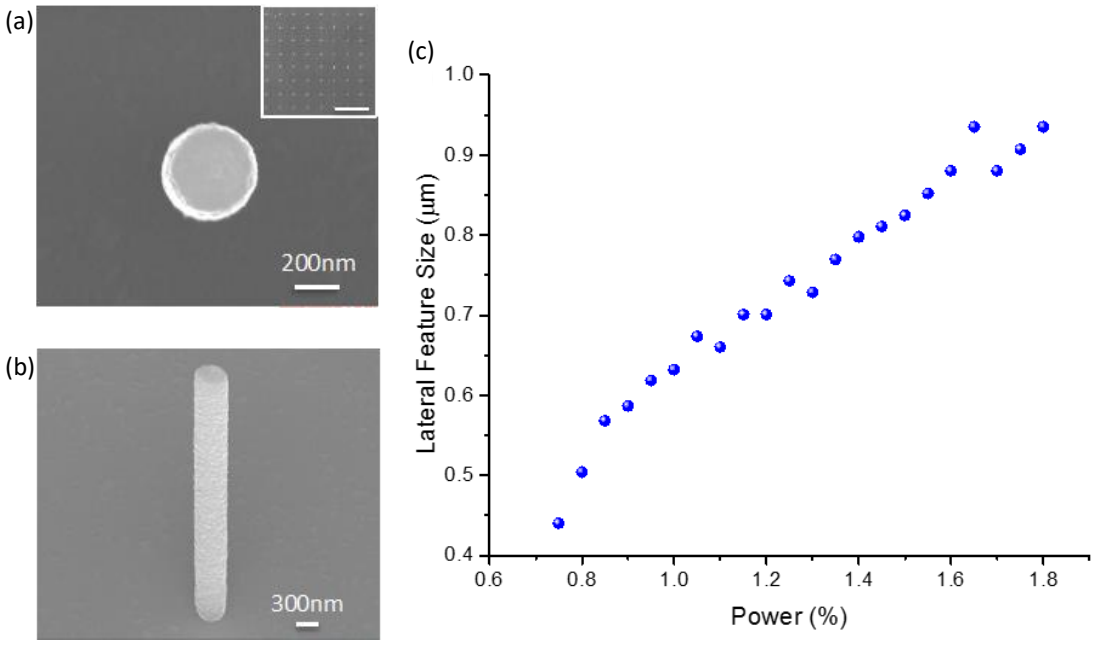

Figure 5.1: (a) Zoomed in SEM image of smallest nanowire in power array (top view), (inset shows further sub-500nm structures on sample, scale bar = 8µm); (b) Tilted SEM image of same nanowire; (c) Lateral feature size of wires plotted against power as a percentage of 180mW. (Williams et al., 2017)

By using the model for two-photon polymerisation discussed in chapter 2 it is possible to calculate the expected minimum feature size and compare with the results shown above. The expression for the lateral feature size is repeated here as equation 5.1 (Cao et al., 2013), and the parameters relating to the fabrication setup are presented in table 5.1.

$$d_{Vox} = w(z)\sqrt{ln\left[\frac{4C\eta^2 P_{laser}^2 t}{f\tau\left(\pi h\omega w^2(z)\right)^2 ln\frac{M_0}{M_{th}}}\right]} \tag{5.1}$$

$$C = \frac{\Phi\delta C_0}{A_E + C_0} \tag{5.2}$$

Where z = distance from laser focus, $w(z)$ = beam radius at position z, C = factor relating to the quantum efficiency (Φ) and two-photon absorption cross-section (δ) as well as the Einstein coefficient of absorption (A_E) and a rate constant (C_0), η = transmittance of the objective lens, P_{laser} = incident laser power, t = processing time, f = repetition frequency of the laser, τ = pulse width, ω = frequency of light, M_0 = initial concentration of photoinitiator in the ground state, M_{th} = threshold amount of dissolvable photoinitiator.

Symbol	Value	Units
C ($\Phi\delta$)	$3x10^{-63}$	m^4s
η	1	-
t	0.6	s
h	$6.63x10^{-34}$	Js
ω	$3.85x10^{14}$	Hz
w(z=0)	$1.04x10^{-7}$	m
f	$8.0x10^{7}$	Hz
τ	$1x10^{-13}$	s
M_0	1	-
M_{th}	0.98	-
P_{laser}	$0.0075 \cdot 180x10^{-3}$	W

Table 5.1: Parameters used for Equation 5.1 and the corresponding units. (Nanoscribe GmbH, 2017b; Zhou et al., 2015)

C_0 was assumed to be much larger than A_E such that C tended towards $\Phi\delta$.

It was hence determined that the theoretical minimum feature size that should have been achievable was 274nm, far smaller than the observed 435nm.

However, a known process that occurs with photoresists is dark erosion, where the unexposed resist is removed during the development phase of the lithography, leading to larger than expected feature sizes (MicroChemicals GmbH, 2013). Dark erosion occurs simultaneously with the development of the exposed regions but at a slower rate (figure 5.2). As a result it can be expected that the dark erosion will be uniform radially as the cylindrical channels are developed axially, increasing the overall diameter. Another result of this difference in dissolution rates is that the effect of dark erosion will be less noticeable toward the bottom of the cylindrical wires as the unexposed side walls will not be in contact with the developer solution until the exposed volume is removed. This is seen as a slight variation in diameter close to the substrate interface in figure 5.3, and is most noticeable in the larger cylinders shown in figure 5.3(b) and (c).

A method for controlling the dark erosion is to dilute the developer solution, as shown in figure 5.2. Dilution reduces both the development rate of the exposed regions of the resist and the dark erosion rate. However, the ratio of the development rate to dark erosion rate increases significantly to a factor of approximately 300 at a dilution of 4:1 water to developer.

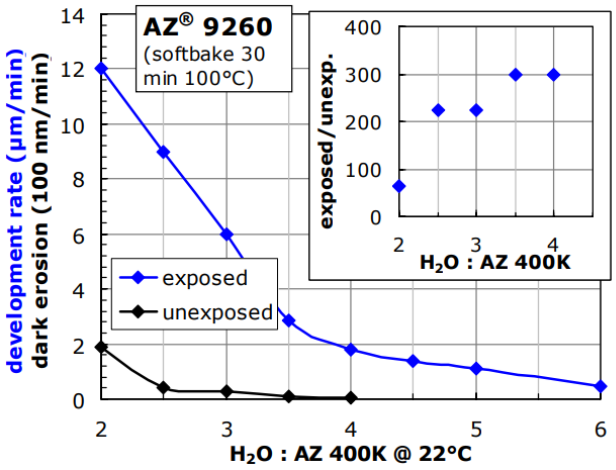

Figure 5.2: Variation of development rate of exposed resist and dark erosion rate with dilution of developer solution with water. Inset shows the variation in ratio of the two rates with dilution. Image reproduced from Microchemicals GmbH (MicroChemicals GmbH, 2013).

It was estimated that the dark erosion for the sample investigated occurred at a rate of approximately 5nm per minute for the dilution ratio of the developer used (4 parts water to 1 part developer). The above model used to calculate the expected feature size can be expanded to take this into account by simply adding a linear term dependant on the dark erosion rate and development time, with the assumption that dark erosion occurs from the start of the development process (which is valid for the top surface of the cylinders). With this addition, it was found that the expected minimum feature size increased from 274nm to 424nm for the 30 minute development. This closely matches the observations from the measurements seen in figure 5.1. This constraint on the minimum feature size will therefore mean that fabricated structures will be in the multi-domain regime.

Figure 5.3 shows tilted SEM images of the power array used in the feature size study at various regions of wire diameter. From these images it can clearly be seen that the top surface roughness of the wires varies considerably with the diameter of the wire - the smallest wires (figure 5.3(a)) have noticeably smoother tops compared to the larger structures (figure 5.3(c)). This variation in roughness of the top surface of structures is likely down to current-crowding effects during the electrodeposition (Luo et al., 2005). Current-crowding causes the electric field to be non-uniform at certain feature sizes as the resist channels constrain the electric field lines (figure 5.4). This variation in the electric field causes the deposited material (in this case cobalt) to be deposited unevenly. The effect is

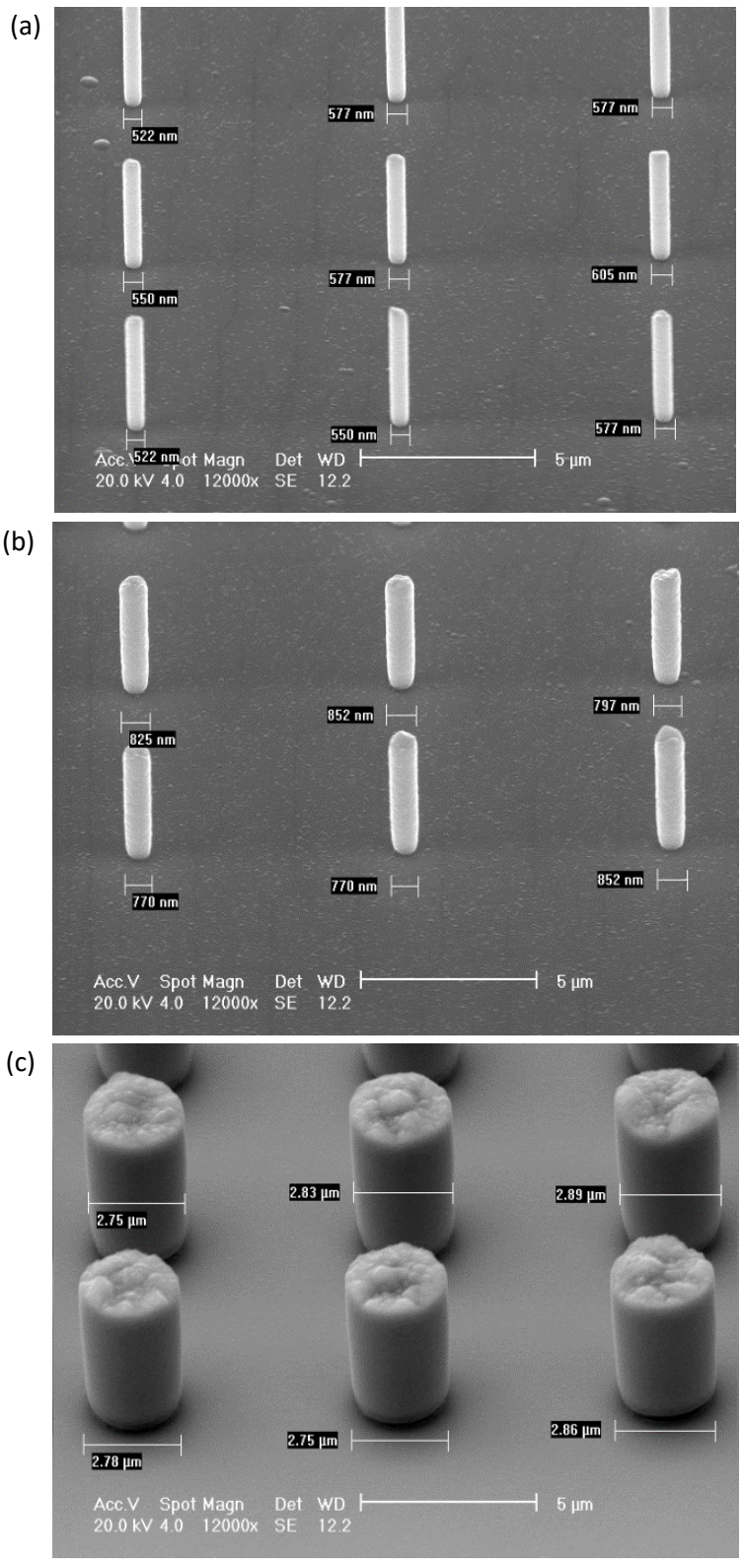

Figure 5.3: Tilted SEM images of vertical wires from a power array sample with size ranges: (a) 522-605nm, (b) 770-825nm, (c) 2.75-2.89µm.

less pronounced at very large sizes where the field is largely uniform, and at very small features where the crowding is so high that the field is forced into uniformity again. Between these two thresholds the effect can be significant.

From the tilted SEM images of the power array it becomes apparent that the threshold feature size for structures fabricated with the setup at Cardiff is within the range of 600-700nm, as evidenced by the average transition from smooth top below 600nm to irregular above 700nm (figure 5.3(b)). This effect is clearly apparent in the highly irregular surfaces of wires with diameters on the order of microns (figure 5.3(c)).

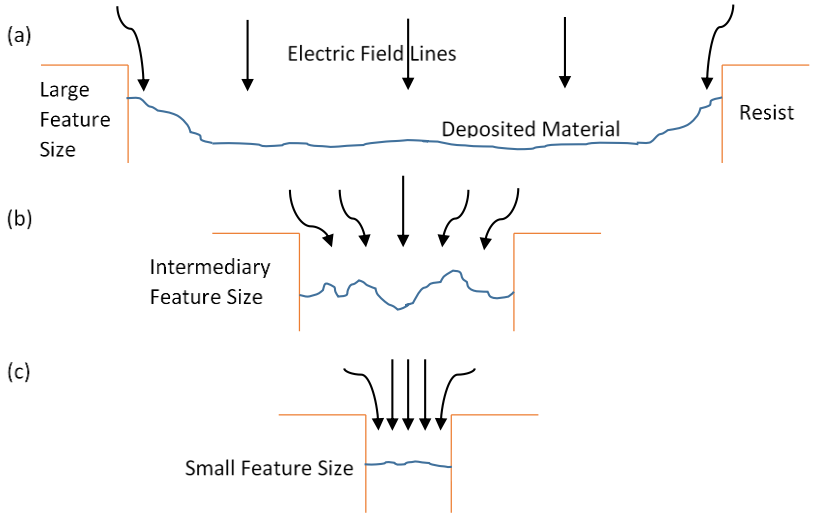

Figure 5.4: Diagram of current crowding effect at (a) large feature size, (b) intermediary feature size and (c) small feature size.

AFM was used to profile the side wall roughness of the structures by measuring the topography of a single wire of cross-section ≈1.5µm that had fallen over onto the substrate. This was then compared to a topography measurement of an exposed and developed trench within a layer of resist. Both topographies are comparable and show a low surface roughness of approximately ±3nm for the wire and ±5nm for the resist trench (figure 5.5). This is comparable to the edge roughness of 2D Co nanowires fabricated using electrodeposition (Ounadjela et al., 1997).

Energy dispersive X-ray (EDX) measurements of samples (figure 5.6) show that they are of high-purity cobalt, >95%, with low amounts of carbon and oxygen. The minor carbon deposition likely arises from the well-known carbon deposition effect from the SEM imaging process (Edgcombe and Valdrè, 2002). As the photoresist used contains organic

compounds, any residual resist on the structures probed could contribute the small amount of oxygen observed in addition to some additional carbon. Another possible source for the oxygen could be oxidation of the Co to CoO from the ashing process used to remove excess resist.

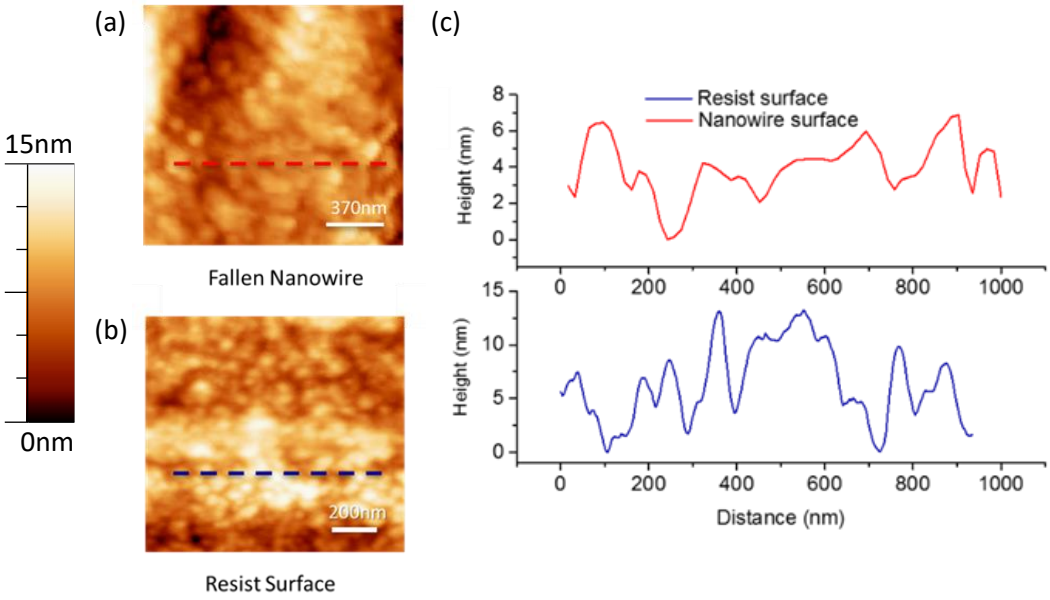

Figure 5.5: (a) AFM image of fallen microwire side surface; (b) AFM image of resist trench surface; (c) Plots of surface roughness using lines for AFM images shown in (a) and (b). (Williams et al., 2017)

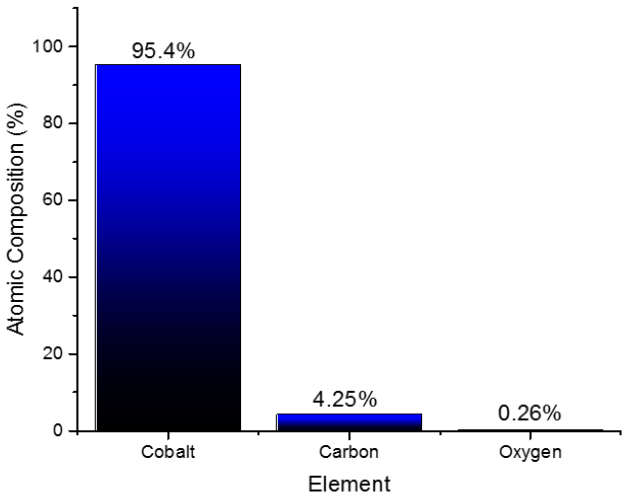

Figure 5.6: Energy dispersive X-ray analysis of cobalt structures grown using standard process for all samples fabricated in-house. (Williams et al., 2017)

Additionally, X-ray diffractive analysis (XRD) measurements (not included) of a Co film grown using the same bath and electrodeposition technique show that the electrodeposited Co is in the *hcp* phase.

Having investigated the topographical and chemical properties of electrodeposited cobalt structures fabricated with TPL, the magnetic properties of structures fabricated with this method could now be studied.

5.3 Angled magnetic nanowires

One of the attractive properties of TPL is the ability to produce 3D structures of almost any geometry. Moving on from the feature study of vertical cylindrical wires, more complex structures were fabricated and investigated. One of the possible uses of TPL would be to fabricate 3D artificial spin ice; this could be achieved by creating networks of nanowires arranged in the same tetrahedral pattern as the magnetic ions in the pyrochlore lattices of bulk spin ice materials. In addition to investigating 'tetrapod' structures (see chapter 4), the properties of 3D nanowires angled with respect to the substrate (the constituent components of tetrapods) were studied. For these more complex sample sets, a larger power than that used to produce the smallest features in the sample considered in section 5.2 was used to increase the yield of viable structures.

5.3.1 Nanowire dimensions

Figures 5.7(a)-(c) show the SEM images of individual nanowires inclined at an angle of 30.5° from the substrate. It is seen that the array is regularly ordered with no observable defects or 'fallen' structures. Despite only being anchored at a single point, it was observed that wires fabricated in this manner were remarkably resilient to breaking away from the substrate and falling, provided the samples were handled with typical care. Large arrays on the order of 300µm x 300µm were used for visibility and to increase the signal to noise in MOKE.

Tilted viewing angles of between 40° and 70° also allow measurements of the wire width and thickness to be made, however there will be an associated error from parallax depending on the angle (i.e. the angle at which the measurement is taken at dictates the proportional component of the true length). Using an imaging program (ImageJ) and the scale bar on the SEM images, the feature sizes were determined as follows. For individual nanowires the lateral feature size was found to have an average value of 750±40nm (figure 5.7 (d)) while the average perpendicular length as seen from a 50° tilt angle was

1190±40nm (figure 5.7 (e)). After correcting for the parallax viewing angle of 50° using trigonometry, the length perpendicular to the wire axis becomes 910±30nm.

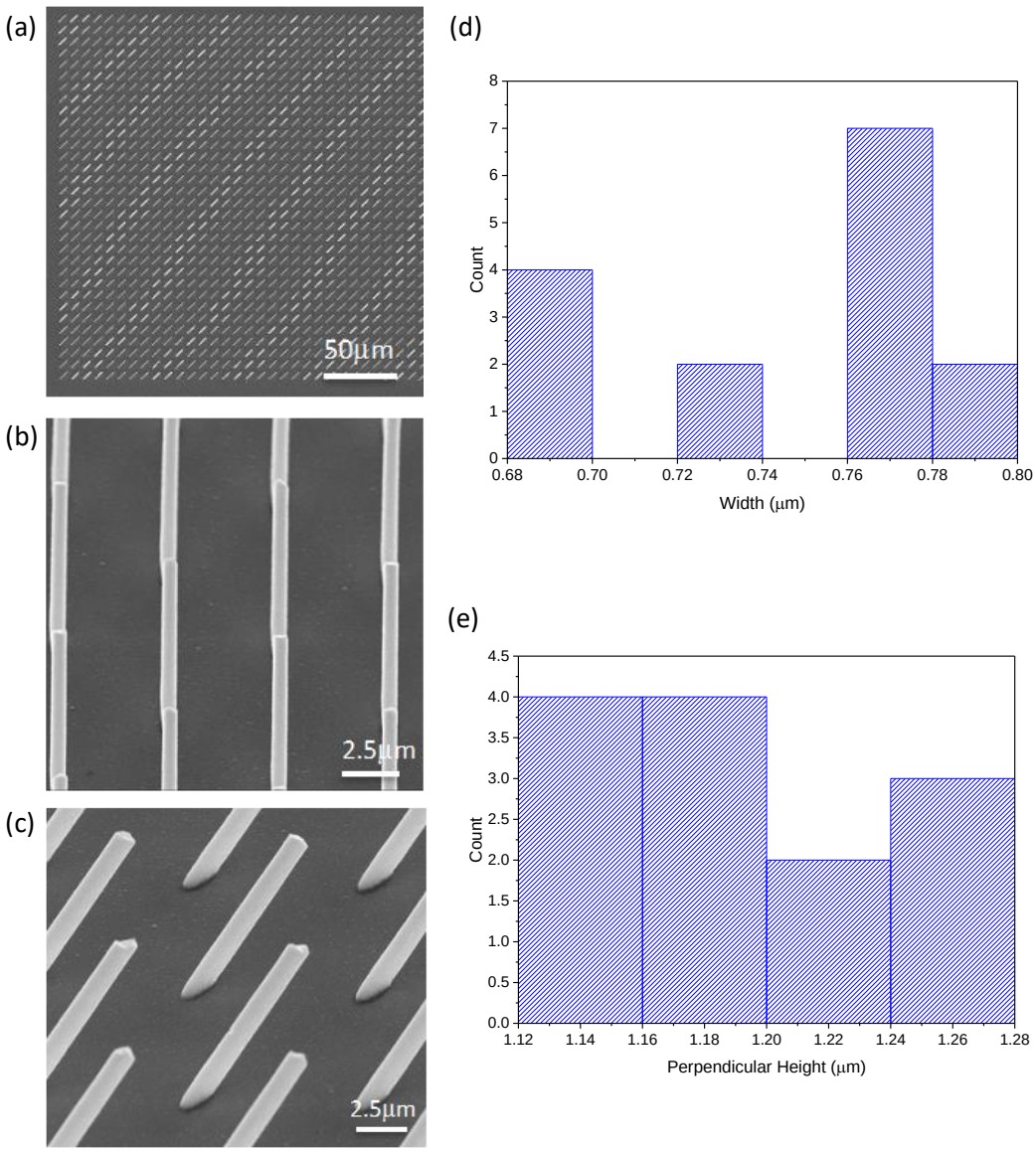

Figure 5.7: SEM images of an array of single angled nanowires: (a) Top-down view of array of single nanowires, (b) High magnification view of single nanowires after tilting stage, (c) High magnification of tilted nanowires after rotation (Williams et al., 2017)*; (d) Distribution of wire widths (sample size of 15 wires); (e) Distribution of perpendicular wire height at 50° viewing angle (sample size of 13 wires).*

The samples shown here are those used in the MOKE studies in section 5.3.2. As is evidenced from these measurements, the wires have an elliptical profile due to the point spread function of the Gaussian beam forming the voxel used in the writing (see chapter 2).

These dimensions are also outside the region where current crowding produces smooth top surfaces (as evidenced by variation seen in the SEM images), which could lead to variation in the nucleation field of domain walls if the wires were in the single domain regime. For the wire dimensions above however, the wires will likely be multi-domain and so the magnetisation reversal process will be dominated by the motion of walls already present within the wire. The wire ends that are affixed to the substrate have a different profile to the free ends as can be seen in figure 5.7(c). The bottom surface is chamfered at an angle of 59.5^{o} resulting in a wedge-shaped end, and the roughness will match that of the substrate which is much more uniform than the roughness of the top surface of the wires.

As previously shown by AFM measurements in section 5.2, the side wall surfaces have a low roughness in relation to the feature size (<1%), so this is unlikely to affect the magnetic properties in the way comparable roughness does on much smaller feature sizes (where roughness is approximately 15% of feature size) (Ounadjela et al., 1997). Therefore it is likely any observed pinning effects in the magnetometry will be due to the 3D geometry (notably the vertex of the tetrapod structures) or other factors.

5.3.2 MOKE measurements on single angled nanowires

MOKE measurements were performed on the above array of individual nanowires angled to the substrate at 30.5^{o}. The MOKE setup used was typical for longitudinal and polar measurements (see chapter 3), however the observed effects and analysis required for 3D structures is more complex than that usually required by 2D structures. There have been very few previous studies of MOKE on angled 3D nanowires in the literature, and due to the difficulty of fabricating such structures these have focused on only a single wire rather than an array of such structures (Fernández-Pacheco et al., 2013).

Upon aligning the laser spot on the array of structures, the reflected beam displayed a large diffraction pattern. The observed diffraction pattern was a 2D array of circular spots aligned on a square grid, matching the square array of structures as would be expected for a 2D diffraction grating. The pattern rotated in line with the sample rotation. The zeroth order spot was obviously apparent as it had a much higher intensity than the higher order spots and was positioned in the middle of the pattern. It was important to isolate and use only the zeroth order spot in measurements as higher order spots have their own complex set of properties when studied using MOKE (known as diffractive MOKE) (Grimsditch and Vavassori, 2004). As the reflected beam was expanding out from the sample, it was

possible to place the secondary lens such that the zeroth order spot completely filled the lens, thus ensuring that only the zeroth order was focused onto the detector.

Within the spots of the diffraction pattern an interference pattern was also observed. The origin of the interference pattern is likely the glass substrate – as the laser spot was much larger than a single structure a significant portion of it reached the substrate and so the reflected beam will be comprised of multiple reflected components – one from the structures, one from the top surface of the glass substrate and one from the bottom surface of the substrate from the light that was transmitted through it. The latter two components relating to the glass substrate will interfere in the well-known thin-film interface effect. As the beams producing the interference effect are from the substrate, they do not carry any information from the magnetic structures and so the interference should not have an effect on the MOKE signal.

Residual resist on the structures was a major challenge when examining the structures with MOKE and spin-SEM. At IBM the structures were first sputtered to remove a resist layer and expose the cobalt surface. At Cardiff a plasma asher was used in multiple stages to remove resist. As MOKE is sensitive to approximately the top 20nm of the structure, very careful experiments were required to get a measurable signal. The structures were measured after a series of plasma ashing trials. No ashing at all leads to a much reduced MOKE signal due to the presence of a residual semi-transparent resist layer. However, too much exposure to an oxygen plasma will remove all resist and start to oxidise the Co surface. As CoO is an antiferromagnetic material this would lead to a reduction in signal.

As the spot size at the sample of the MOKE apparatus covers multiple structures, a large linear background due to the Faraday effect of the laser light reflected back through the glass substrate is apparent (Tan and Arndt, 1997). When considering MOKE results, especially when the signal is small, it is useful to account for this background. Two techniques can be employed: a measurement away from the structures on the sample gives a measurement of the substrate only, as this is linear, and the gradient of the effect can be determined and then subtracted from the data. Alternatively, it can be assumed that at high fields the sample has saturated and so in this range the signal is of the background only. In this case a straight line can be subtracted from the graph by picking points from this range to use as the gradient (Sultan, 2013). The drawback of the first approach is that it assumes the gradient taken from the substrate is uniform across the sample, which is not necessarily the case. An average can be taken but this still does not

necessarily match the true value of the background at the space occupied by the structures. The second approach assumes that the structures are at saturation, this is almost certainly not the case as rotation of the magnetic domains lasts for a large field range.

Despite these challenges, measurements of the magnetic properties of the 3D structures presented in this chapter have been performed successfully. The polariser for the incident beam was set to s-polarisation; as such any contribution from the transverse MOKE signal should be negligible.

The external magnetic field was applied in the polar geometry and longitudinal geometry. In the polar setup the resulting loops obtained show a steep change in magnetisation at low fields indicative of domain wall motion, and a region where dM/dH was greatly reduced at high fields (figure 5.8(a)). Saturation was not obtained as the setup used had a maximal field of 0.5T which is far less than the calculated 1.7T needed to saturate such structures. The average coercive field for the polar MOKE loop was 22.5±0.8mT and the remanent magnetisation was 0.100±0.005M.

In the longitudinal setup, when the field was applied parallel to the projection of the wire long-axis on the substrate the resulting loops were similar to that from the polar setup – a steep initial change in magnetisation around zero field, followed by a gradual rotation at higher fields (figure 5.8(b)). The average coercive field for longitudinal MOKE parallel to the wire projection was 11.0±1.8mT with remanence 0.099±0.012M, and for anti-parallel the coercive field was 16.0±6.0mT with remanence 0.130±0.002M. The low values for remanence from these loops are a good indication that the wires are in a multi-domain regime.

When performing longitudinal MOKE with the field applied along the projection of the wire long axis, it should be noted that due to the 45^{o} angle of incidence of the MOKE laser and the 30.5^{o} raised angle of the wire that the magnetisation probed is different for when the wires are rotated through 180^{o} within the field. The resulting angular component in the product of $\mathbf{k}\cdot\mathbf{M}$ increases from ≈14^{o} to ≈80^{o} which affects the observed loops (Allwood et al., 2003). The difference of the dot product cosine for these angles suggests that the detected signal is reduced by a factor of 5.5 when rotating from 14^{o} (defined as parallel in figure 5.9(b)) to 80^{o} (defined as anti-parallel in figure 5.9(d)).

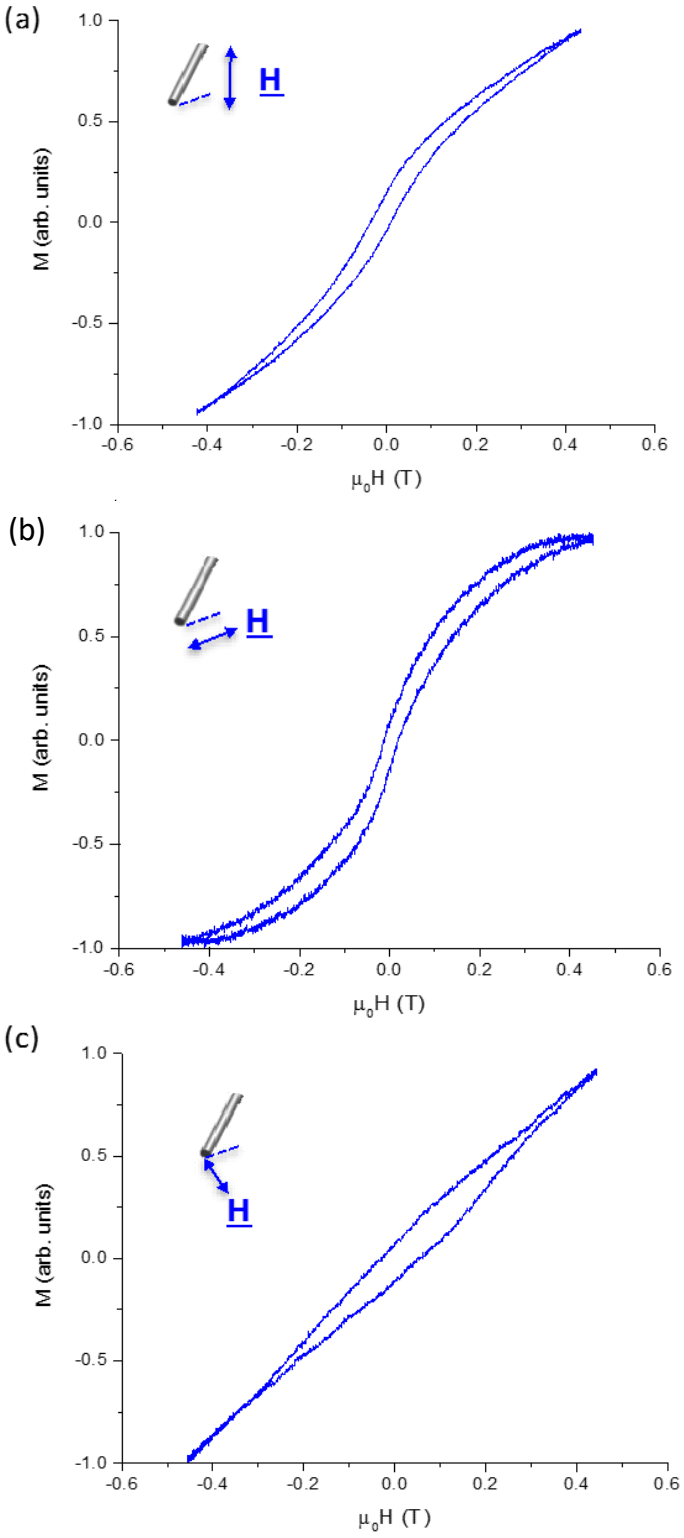

Figure 5.8: MOKE loops for single angled nanowires, (a) Polar MOKE configuration, (b) Longitudinal MOKE configuration with external field applied parallel to the projection of the wire long-axis onto the substrate, (c) Longitudinal MOKE configuration with external field applied perpendicular to the projection of the wire long-axis onto the substrate. (Williams et al., 2017)

However, when comparing between the parallel and anti-parallel MOKE loops shown as figures 5.9(a) and 5.9(c), there is no appreciable difference in the signal to noise ratio. This is likely due to the multi-domain and elliptical nature of the wires resulting in an overall even average of magnetisation vectors that each orientation is sensitive to. Both loops also show a similar shape, with rotation of the magnetisation occurring at high fields and a steeper transition occurring at low field. The most notable difference is the opening of the loop at high fields for the parallel orientation seen in figure 5.9(a) that is not seen for the anti-parallel case in figure 5.9(c). This is likely the result of the different magnetisation components being probed as the anti-parallel orientation is sensitive to a more transverse component which will have a more reversible rotation of magnetisation at the higher end of the field range. The parallel orientation on the other hand sees a more axial component, but as the field range does not go high enough to begin saturating the wires the opening from hysteresis is still observable at the higher end of the field range.

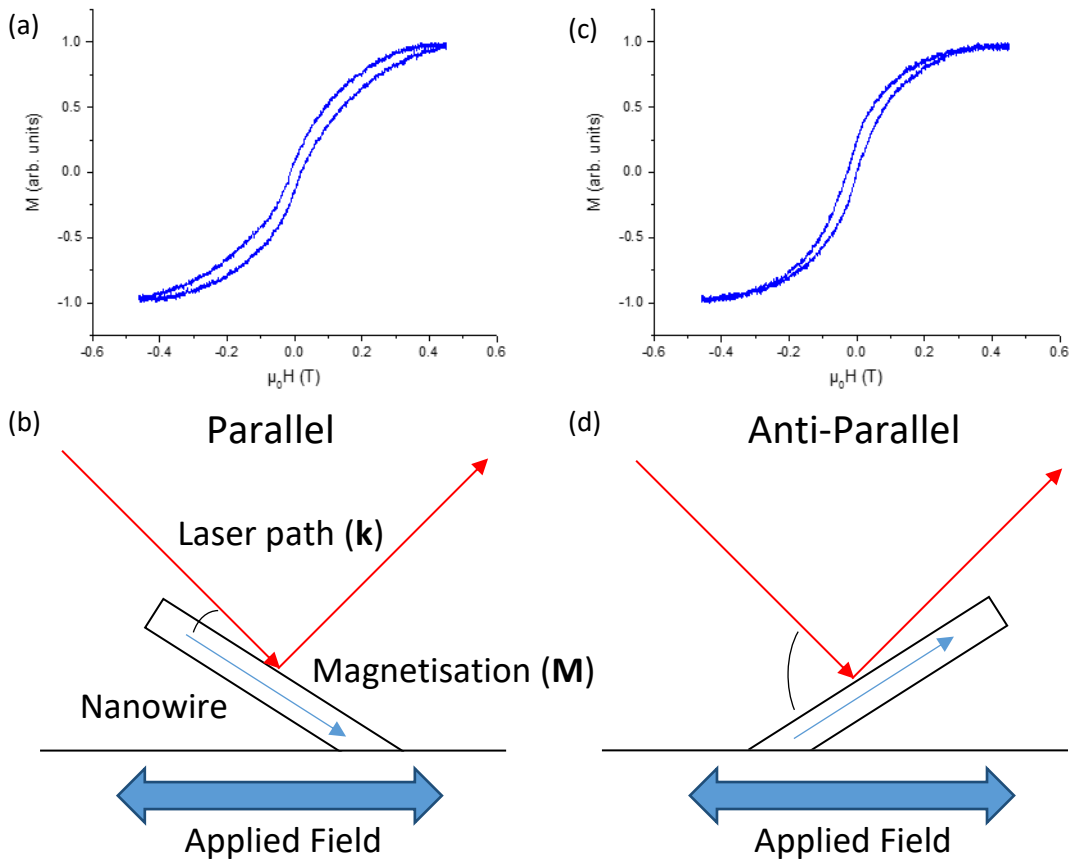

Figure 5.9: (a) MOKE loop performed on array of single angled wires aligned with the raised ends towards the incident laser path, (b) Schematic of alignment for (a); (c) MOKE loop performed on array of single angled wires aligned with the anchored ends towards the incident laser path, (d) Schematic of alignment for (c).

When the field was applied perpendicular to the projection of the wire long-axis (figure 5.8(c)), the loop showed a much more hard-axis-like shape with a remanent magnetisation of approximately 0.160M without reaching saturation and with opening of the loop. The loop shown is similar in shape to the low field perpendicular MOKE loops previously reported for cobalt nanowire arrays (Ounadjela et al., 1997; Vega et al., 2012).

In order to understand the shape of the above hysteresis loops, literature related to Co magnetic nanowires of similar size was consulted. Cylindrical cobalt wires made using electrodeposition and of similar diameter (400-500nm) have been shown to have coercive fields of the same order of magnitude as measured above, approximately 100 Oe or equivalently 10mT, when the external field is applied parallel to the wire axis (Fert and Piraux, 1999; Henry et al., 2001; Ounadjela et al., 1997). Furthermore, the hysteresis loops shown in the literature and measured by various techniques for fields applied parallel and perpendicular to the wire axis for large wires (>100nm diameter) qualitatively match the shape of the loops shown in figure 5.8 for the same field range (Bantu et al., 2001; Ferré et al., 1997; García et al., 1999; Henry et al., 2001). It is seen in such studies that the properties of such wires are similar for diameters greater than 150-200nm as the coercive fields, remanent magnetisation and anisotropy constants all show a greatly reduced rate of change with diameter for cobalt. Hence it is reasonable to assume similar processes for the wires presented here that are of diameter 750nm. One of the studies also mentions that wires up to 450nm diameter show evidence of the coexistence of domains aligned transverse and axial with respect to the wire from transport measurements (Fert and Piraux, 1999). The domain pattern in wires of 90nm diameter (Belliard et al., 1998) and 150nm diameter (Henry et al., 2001) are shown to be multi-domain by probing with magnetic force microscopy (MFM), with a structure similar to that mentioned above where axial- and transverse-oriented domains coexist. For such wires in a multi-domain regime it has been suggested that the domain walls are vortex-like and that the reversal mode is likened to a quasi-curling mode (Ferré et al., 1997; Ivanov et al., 2013).

From the above and given the similarities of the loops to those seen in the literature, it is likely that the wires studied here follow a similar magnetisation process: for polar and longitudinal, domain walls already present within the wire begin to move as the field is increased, causing the domains with components in the same direction of the field that are visible on the surface to grow. As the field is further increased the domain walls will be impeded by the wire boundaries at which point the magnetisation of the wire will start to uncurl and the magnetisation on the surface will gradually rotate to align with the field. As

the field is decreased, the magnetisation curls but may have regions of different chirality along the wire length, resulting in the formation of domain walls along the length. Such a domain pattern would be observable as a chequerboard pattern of MFM contrast as seen in the references above.

For the field applied perpendicularly to the wire axis, the vortex states will uncurl as the external field is increased, causing the visible top-surface magnetisation to gradually increase in the field direction. When the field is decreased the magnetisation will curl and form a number of domains similar to the polar and longitudinal case, however the domains visible on the surface will have a larger component remaining in the field direction hence the opening of the loop.

In order to obtain a deeper insight into the switching process for the specific geometry of the wires presented here, micromagnetic simulations were performed so that further comparisons could be made.

The finite difference micromagnetic simulation package mumax3 was used to simulate hysteresis loops on cobalt wires with elliptical cross-section of similar dimensions (800nm x 600nm x 7µm) to the single wires studied above and the wires comprising the tetrapod structures studied below. The material parameters used were $M_s = 1400 \times 10^3 Am^{-1}$ and $A = 30 \times 10^{-12} Jm^{-1}$ (Donahue, 2016) with an edge smooth parameter equal to 8 (the maximum) and a cell size of $(5nm)^3$, below the exchange length of 7nm for Co (Jamet et al., 2001). The simulations were performed at zero temperature. When considering magnetocrystalline anisotropy it was assumed that the polycrystalline electrodeposited cobalt would consist of many grains with randomly oriented anisotropy axes. As the package was limited to creating a maximum of 256 different grain regions, and could only do so in a 2D plane, it was instead assumed that the anisotropy axes of the grains average to zero across the whole wire. This has also been assumed within the literature (Fernández-Pacheco et al., 2009; Grujicic and Pesic, 2005), and so a magnetocrystalline anisotropy term was neglected due to these computational limits. The external field was varied from -1T to 1T with 10mT increments and the damping parameter was set to 0.9 to expedite the simulations. The external field was applied at an angle of 59.5° and 30.5° with respect to the wire length in the major axis plane and at 90° to the wire length in the minor axis plane so as to replicate the field geometry for polar, longitudinal parallel to the projection of the wire axis and longitudinal perpendicular to the projection of the wire axis, as measured using MOKE. The

resulting hysteresis loops from the simulations are shown in figures 5.10, 5.11 and 5.12, along with accompanying snapshots of the magnetisation at specific field steps.

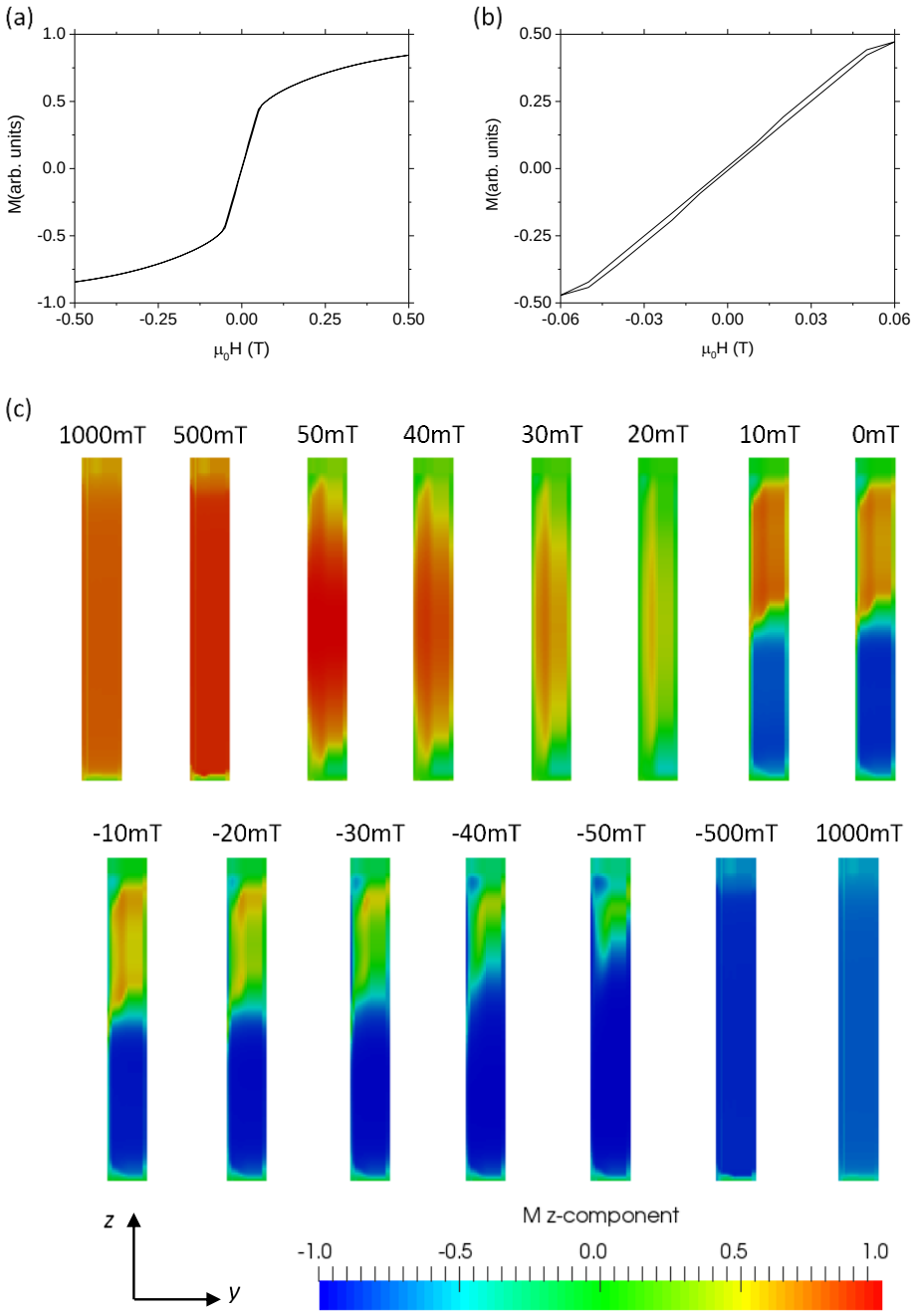

Figure 5.10: (a) Simulated hysteresis loop for a single wire with field applied in polar geometry (field applied at 59.5° with repsect to the wire axis), (b) zoomed in image of same loop showing hysteresis, (c) magnetisation snapshots of the wire upper surface at specified field points for the upper half of the loop. Colour represents the z-component of magnetisation as shown.

The polar loop shown in figure 5.10(a) shows a steep initial transition with hysteresis (figure 5.10(b)) at low field up to approximately M = 0.5 and lasting between the range of ±50mT, after which point rotation of the magnetisation begins and lasts as a long saturation tail up to the maximum field of 1T. The polar loop has a coercive field of approximately 0.8mT and a remanent magnetisation of ±0.007M. The overall loop shape matches that seen in the experimental data (figure 5.8(a)) and so the magnetisation method is likely similar. By studying the magnetisation of the upper surface of the wire through the snapshots shown in figure 5.10(c) it can be seen that at the extreme fields of ±1T the magnetisation is rotated to align with the field direction as indicated by the reduction of M_z compared to that at ±500mT where the reduced field means that the shape anisotropy of the wire causes the magnetisation to align more parallel to the wire axis.

The reversal of magnetisation between 50mT and -50mT is also captured in figure 5.10(c). At 50mT the onset of curling can be observed at the wire ends as indicated by the regions with zero z-component of magnetisation. The curling increases along the length as the field is reduced, with a vortex state observed to begin forming at the lower end of the wire visible by the small region of negative z-component in the 40mT, 30mT and 20mT images at the bottom of the wire. At 10mT the vortex state curls in such a way as to present a tail to tail domain pattern on the upper surface that appears to separate two regions of opposite magnetisation and remains roughly central in the wire through 0mT. As the field is then increased in the opposite direction, the wall moves along the wire length so as to grow the region with magnetisation component in the same sense as the field, as seen in the images for -10mT through to -50mT. At -50mT the wall has moved almost to the wire end leaving only regions with magnetisation component of zero or aligned with the field direction.

These observations match the reversal method proposed above for the fabricated wires.

The longitudinal loop shown in figure 5.11(a) is similar in shape to the polar loop, however the hysteresis has a steeper initial transition lasting up to approximately M = 0.75 and in the range between ±30mT before rotation of the magnetisation begins. The longitudinal loop has a coercive field of approximately 0.3mT and has a remanent magnetisation of ±0.0067M. This is again of similar shape to those observed for the longitudinal loops on the fabricated nanowires, and additionally the same differences in shape are observed between the polar and longitudinal loops for both the simulations and fabricated wires. Both are consistent with the shearing of hysteresis loops on nanowires as the angle of the external field with respect to the wire axis is increased.

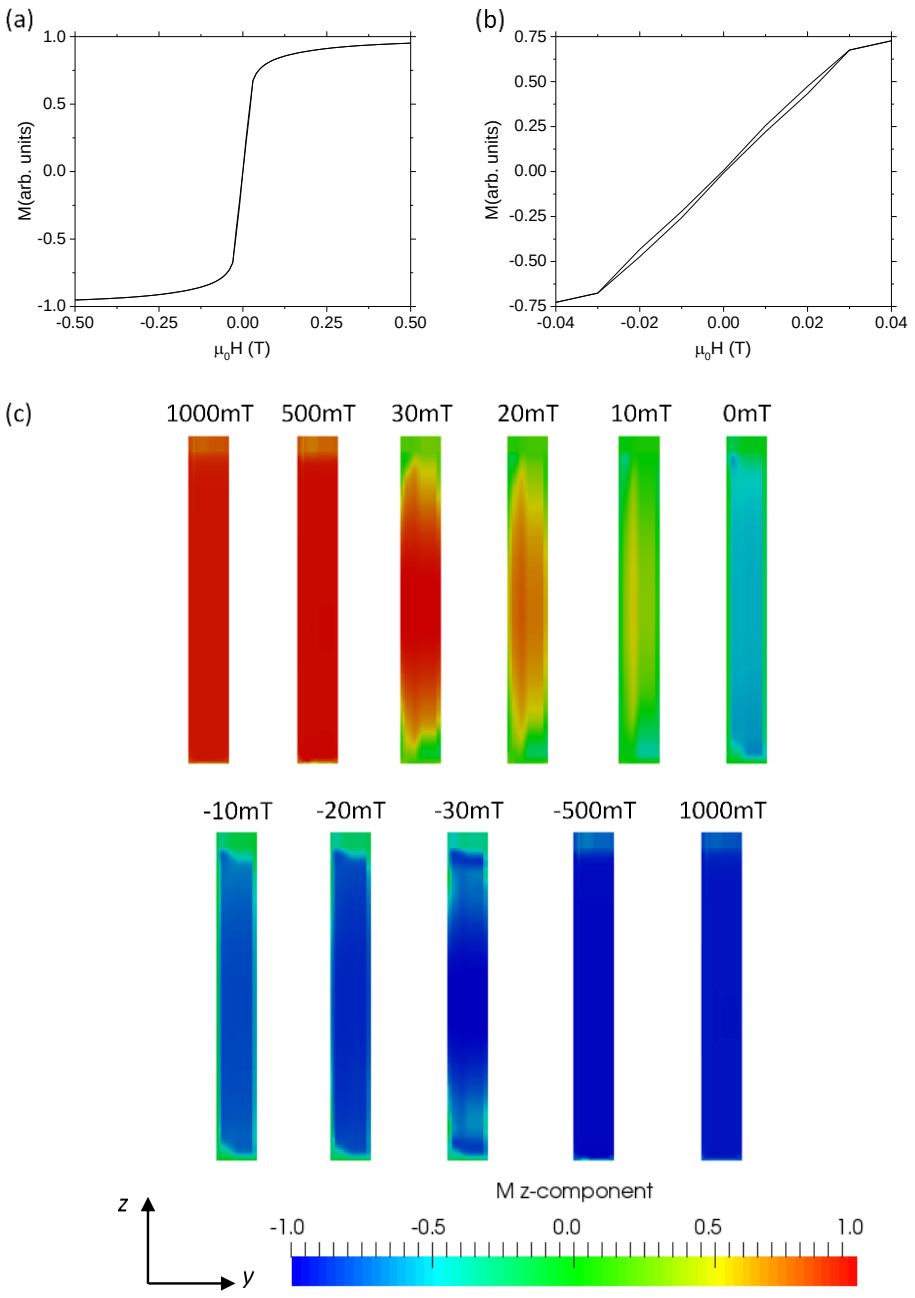

Figure 5.11: (a) Simulated hysteresis loop for a single wire with field applied in longitudinal geometry parallel to the projection of the wire axis (field applied at 30.5^{o} with respect to the wire axis), (b) zoomed in image of same loop showing hysteresis, (c) magnetisation snapshots of the wire upper surface at specified field points for the upper half of the loop. Colour represents the z-component of magnetisation as shown.

When considering the magnetisation snapshots in figure 5.11(c), at large fields the same observation as for the polar loop is seen – a decrease in magnetisation component along the wire axis at ±1T compared to ±500mT due to the field rotating the magnetisation away

from the wire axis. However this difference is less noticeable for longitudinal due to the reduced angle of the external field with respect to the wire axis resulting in a larger component parallel with the wire axis when compared to the polar loop.

When considering the transition from 30mT to -30mT shown in the snapshots, while the initial magnetisation change matches that observed for polar, no domain wall becomes apparent at low field around 0mT. Instead, at 0mT the upper surface magnetisation consists of a large region with a slight negative z-component. As the field is increased in the negative direction, this region becomes more aligned with the field as shown in the images from 0mT to -20mT. At -30mT. There is evidence of curling at the two ends which is likely hidden from the top-surface view, as is discussed below for the transversally applied field simulation.

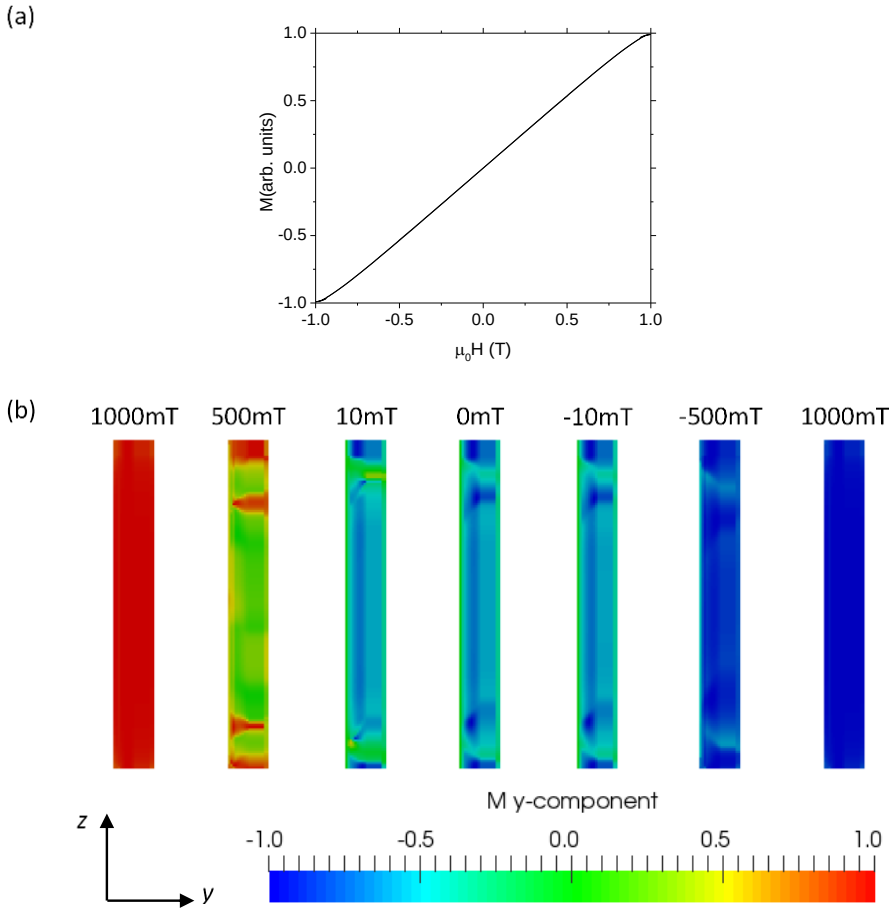

Figure 5.12: (a) Simulated hysteresis loop for a single wire with field applied in longitudinal geometry perpendicular to the projection of the wire axis (field applied at 90^o with respect to the wire axis), (b) magnetisation snapshots of the wire upper surface at specified field points for the upper half of the loop. Colour represents the y-component of magnetisation as shown.

The simulated loop where the field was applied perpendicular to the wire axis (figure 5.12(a)) shows a linear gradient with no opening of the loop, indicating wholly rotation based reversal of the magnetisation, saturating at approximately 1T and with a remanence magnetisation of approximately zero.

From the magnetisation snapshots of the y-component shown in figure 5.12(b), it is apparent that the wire is fully saturated at ±1T. As the field is decreased to 500mT the snapshots show that most of the surface magnetisation is directed along the wire axis, with two strongly aligned transverse regions near the wire ends indicative of vortex state formation. As the field is reduced further, the 10mT snapshot shows that the magnetisation is curling across most of the wire and in the opposite sense, with two regions where the magnetisation is axial towards the ends of the wire. The snapshots for 0mT and 10mT are almost identical, showing that a transversely applied field causes a much smaller change in magnetisation compared to fields with an axial component. The remaining image at 500mT shows the growth of the magnetisation in the same direction of the applied field.

The snapshots do not show the same magnetisation process that the loop in figure 5.12(a) indicates; at 0mT the top surface magnetisation shows a region where the average component is directed in the –y direction. Since the loop displays the properties of the whole wire, this shows that by probing the top-surface of the magnetisation information can be hidden and also helps to show why the measured loop for this orientation opens, whereas the simulated loop does not. If the bulk magnetisation of the wire is investigated, it is seen that as the field is reduced the magnetisation curls in such a fashion as to form a vortex state along the wire length, in the same fashion as seen in Ivanov *et al*.'s simulations on much smaller (50nm) cylindrical wires (Ivanov et al., 2013). A full glyph representation of this vortex state along the length of the simulated cylinder is shown in figure 5.13, from the snapshot at 0mT. From this it is readily apparent that while the bulk magnetisation is approximately zero as shown by the hysteresis loop, the surface magnetisation shows a distinct favourable direction.

Interestingly, the simulations of Ivanov *et al*. mentioned above were of polycrystalline Co and included magnetocrystalline anisotropy distributed in-plane of the nanowire diameter. As the same mechanism is observed in the much larger wires presented here it supports the assumption that magnetocrystalline anisotropy can be neglected for the case of a polycrystalline material with randomly distributed axes.

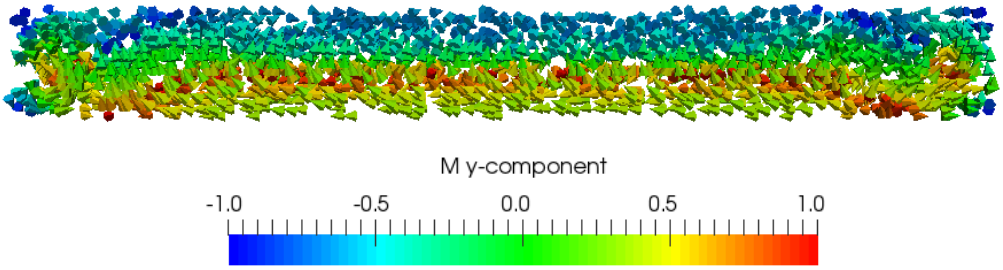

Figure 5.13: Glyph representation of magnetisation for 0mT snapshot in figure 5.12(c). View is along the y-axis.

Though the simulated loops qualitatively capture the shapes of the measured loops, there are some distinct differences. The fabricated loops show opening of the loops at the higher field rotation range whereas the simulated loops exhibit hysteresis only in the steep initial transition. In addition, the coercive fields for the fabricated loops are approximately two orders of magnitude greater than those of the simulated loops.

There are a number of factors that could explain the differences observed between the simulations and fabricated structures. The simulations were performed on a single wire with idealised geometry and field alignment and neglected thermal effects (the simulations run with T=0K). The magnetisation results from the simulations are also the bulk values for the entire wire whereas MOKE only probes the top surface to a depth of approximately 20nm. The fabricated structures are in an array and so the MOKE loops are an average across multiple wires. The wires themselves are of slightly larger dimensions than those used in the simulations and have variation in the roughness of the free end while the end affixed to the substrate has an angled wedge removed in comparison to a whole cylinder as discussed in section 5.3.1.

The discrepancy in coercive fields cannot be explained by physical reasoning; being at room temperature and of larger dimensions should reduce the coercive field. Therefore, it is likely that the large difference in coercive field is due to a number of other factors. It should be noted that both the simulations and the literature suggest that the initial magnetisation process occurs by domain wall motion, hence it is this process that must be inhibited in the fabricated structures. Firstly, the finite roughness of the wire edges, as well as the irregular tops, is likely to pin the domain walls close to the surface and so be measurable by MOKE. Such geometrical pinning centres can signficantly enhance the coercive field in films (Zhao et al., 2000), and the same is likely in this case. Secondly, the electrodeposited bath (as

stated in chapter 3) contains the additives sodium laurel sulfate and boric acid. These are essential in the fabrication of microstructures, however it is possible that some of these impurity chemicals will become embedded within the deposit and behave as defects, again acting as a pinning site for domain walls. Finally, though it was ignored within the simulations due to computational restraints, the fabricated samples will exhibit a magnetocrystalline anisotropy, which is likely to be randomly orientated. Any wall nucleation processes, which occur due to the rotation of localised spins, is likely to be suppressed. In addition, it has been observed that variations in anisotropy within nanowires behave as a series of pinning potentials of varying height, effectively increasing the field required to move the wall (Gerhardt et al., 2014).

With the above knowledge of the magnetisation processes in single nanowires, it should now be possible to interpret the magnetisation of more complex tetrapod structures which can be considered as being comprised of multiple nanowires.

5.4 Tetrapod structures

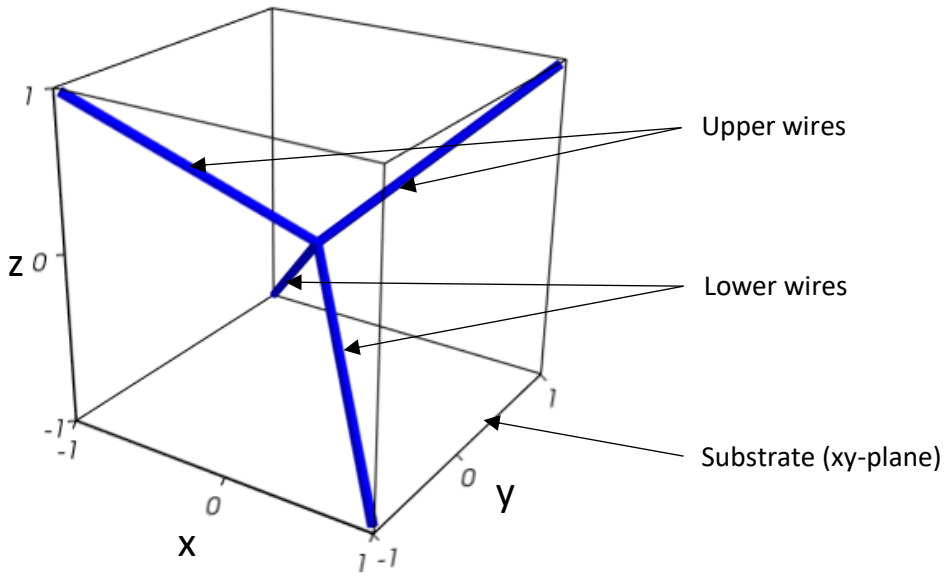

Figure 5.14: Visualisation of tetrapod geometry and labelling.

In this section the focus shifts to full tetrapod structures. The structure geometry was defined by arranging four nanowires around a central vertex such that, declaring the center of the vertex as the origin, the wires follow the vectors [1 1 1], [-1 -1 1], [1 -1 -1] and [-1 1 -1]. Throughout this section reference will be made regarding the 'lower' wires, that is the two wires below the vertex and anchored to the substrate, and the 'upper' wires, that

is the two wires above the vertex with free ends. These two subsets of wires are rotated by 90^{o} around the z-axis with respect to each other. This is illustrated by figure 5.14.

5.4.1 Tetrapod dimensions

Figures 5.15(a)-(c) show the SEM images of an array of tetrapods. As for the array of single wires, the images show that there are no obvious defects or fallen structures and that the tetrapod structures do not vary considerably across the array which can be shown by the wire length ratio. Top-down SEM images allow for quantification of the upper to lower wire-length ratio of tetrapods, from a sample set of 64 structures the average wire length aspect ratio was determined as 0.95±0.04 with a Gaussian distribution (figure 5.15 (d)). From the measurements taken to determine the aspect ratio and using tetrahedral geometry (the wires make a 35.25^{o} angle to the substrate or xy-plane), the average wire lengths were calculated to be 6.3±0.2µm for the upper wire subset and 6.6±0.2µm for the lower subset by using simple trigonometry and the measured length projections in the xy-plane (figure 5.15 (e)). The scale accuracy from the imaging software (ImageJ) used for these measurements was 0.2µm/pixel.

These results agree within errors to the values obtained by directly measuring the wire lengths individually from tilted SEM images: average 6.7±0.2µm for the upper wires and average 6.3±0.2µm for the lower wires.

For tetrapods the lateral feature size was found to be 610±95nm while the length perpendicular to the wire axis was 900±95nm. The large deviation in these values comes from a lack of resolution in the images used in the analysis. To investigate a large sample set required zoomed out images of multiple structures, leading to a scale accuracy of approximately 95nm/pixel.

The elliptical cross section of the wires means that the tetrapods do not have perfect symmetry when rotated within a magnetic field – the field can have a larger normal component to the major axis for some wires and to the minor axis for others. This could have unexpected effects on any magnetometry performed as the field would effectively be applied at differing angles on a wire by wire basis. This would be of most concern for the [111] field direction where the three non-parallel wires will present a ratio of 2:1 for either major or minor axes depending on the rotation. However, due to the constraints of the experimental setup and sample fabrication the [111] field direction cannot be probed.

For the [100] field directions, the two out of plane directions present only the minor axes of the wires, accessible by polar MOKE geometry, whereas the four field directions in the same plane as the substrate present only the major axes of the wires and can be accessible by longitudinal MOKE. As the field sees the same wire axis for each wire irrespective of the geometry (i.e. there is never any mixing of minor or major wire axes for these field directions), it can be expected that, while there may be some difference in the measured loops between the geometries, they should both show similar properties.

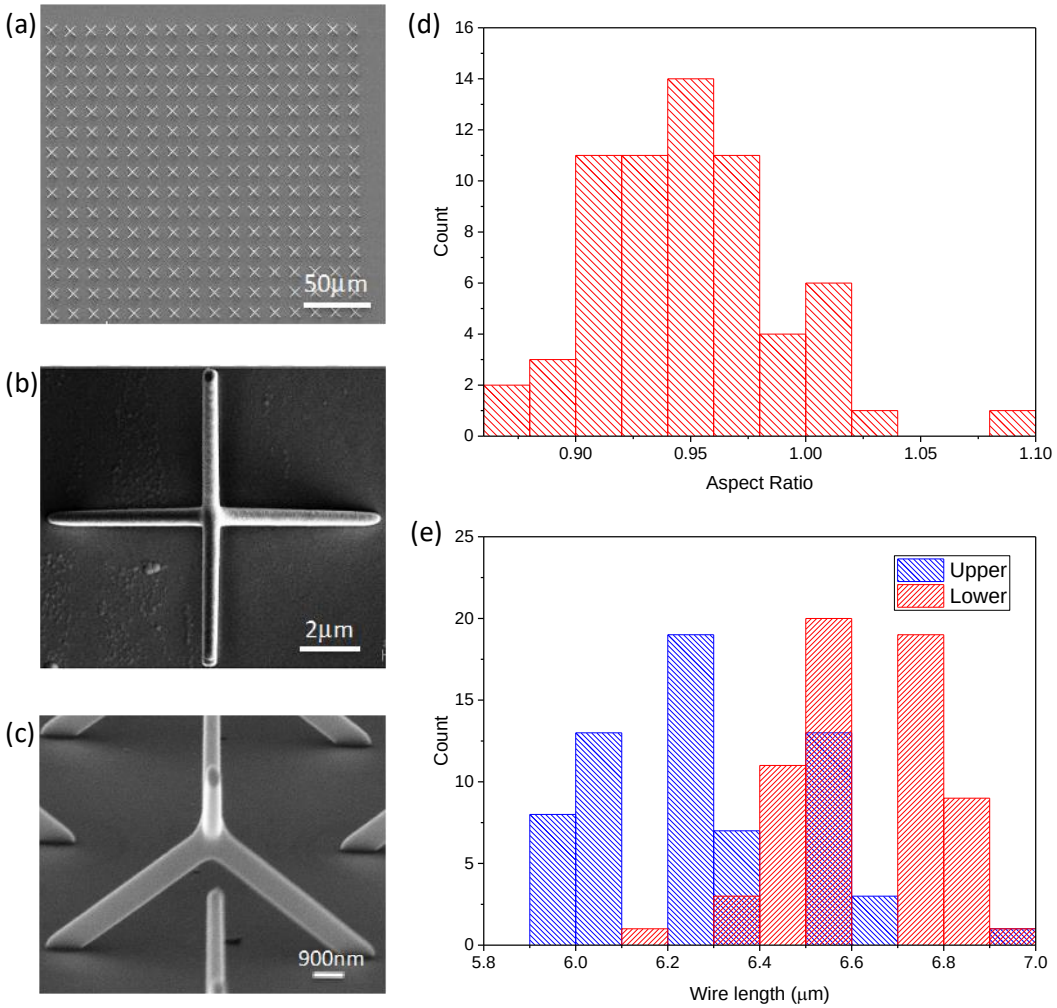

Figure 5.15: SEM images of an array of tetrapod structures: (a) Top-down view of array of tetrapods, (b) High magnification view of a single tetrapod, (c) High magnification view of a single tetrapod after tilting stage (Williams et al., 2017)*; (d) Distribution of aspect ratio of upper to lower wires in tetrapods (sample size of 64 structures); (e) Distribution of wire lengths (sample size of 64 structures).*

For the [110] field directions, the two directions in the plane of the substrate present the minor axes of both wires in one plane and the major axes of both wires in the orthogonal plane. By contrast in the remaining [110] field directions each of the orthogonal wire sets will present one major and one minor axis. However, only the first set of directions are accessible using longitudinal MOKE, while the remainder cannot be probed. As such, the measured [110] loops are expected to show similar properties.

5.4.2 Spin-SEM images

Spin-polarised SEM (spin-SEM) images were taken by collaborators within Dr. Rolf Allenspach's group, IBM Research, Zurich. Spin-SEM was performed on a tetrapod sample, with two sets of images focusing on one of the upper nanowires comprising the tetrapod, one set for virgin remanence state (figures 5.16(a)-(d)) and one after application of a small external field (figures 5.16(e)-(h)), and another set for the central vertex of the structure after application of a larger external field (figures 5.16(i)-(k)). The sample provided was of slightly smaller dimensions to those studied by MOKE in this thesis, with a lateral wire width of approximately 410nm as shown in figures 5.16(a), (e).

The spin-polarised images taken on the wire in its virgin remanence state indicate that the structure is in a multi-domain regime for the dimensions investigated (figures 5.16 (b), (c)), confirming that the larger wires investigated in the MOKE studies are in the multi-domain regime. This multi-domain structure persists after application of an 11.8mT field pulse directed parallel to the projection of the wire long axis, with evidence that the domain walls have moved along the wire (figures 5.16(f), (g)). The movement of these walls is evidence that for the low field range the magnetisation of nanowires is governed by domain wall motion as was stated in the discussion for single nanowires above.

A statistical analysis was performed by applying a grid to the magnetisation images and computing the net vector of magnetisation in each cell. The point vector images generated by this for both sets are shown in figures 5.16(d), (h) and allow for the surface magnetisation to be more easily interpreted. Due to the large shape anisotropy term of the tetrapod nanowire ($6.2 \times 10^5 Jm^{-3}$), it is expected that a significant component of the magnetisation lies parallel to the wire long axis. From the point vector images this is seen to be the case, however a spread of magnetisation angles is also observed. The magneto-crystalline anisotropy term of electrodeposited Co (5.9×10^5 Jm^{-3}) is found to be comparable to the shape anisotropy term, and only a factor of 4 less than the calculated demagnetisation field term for a tetrapod nanowire (2.3×10^6 Jm^{-3}).

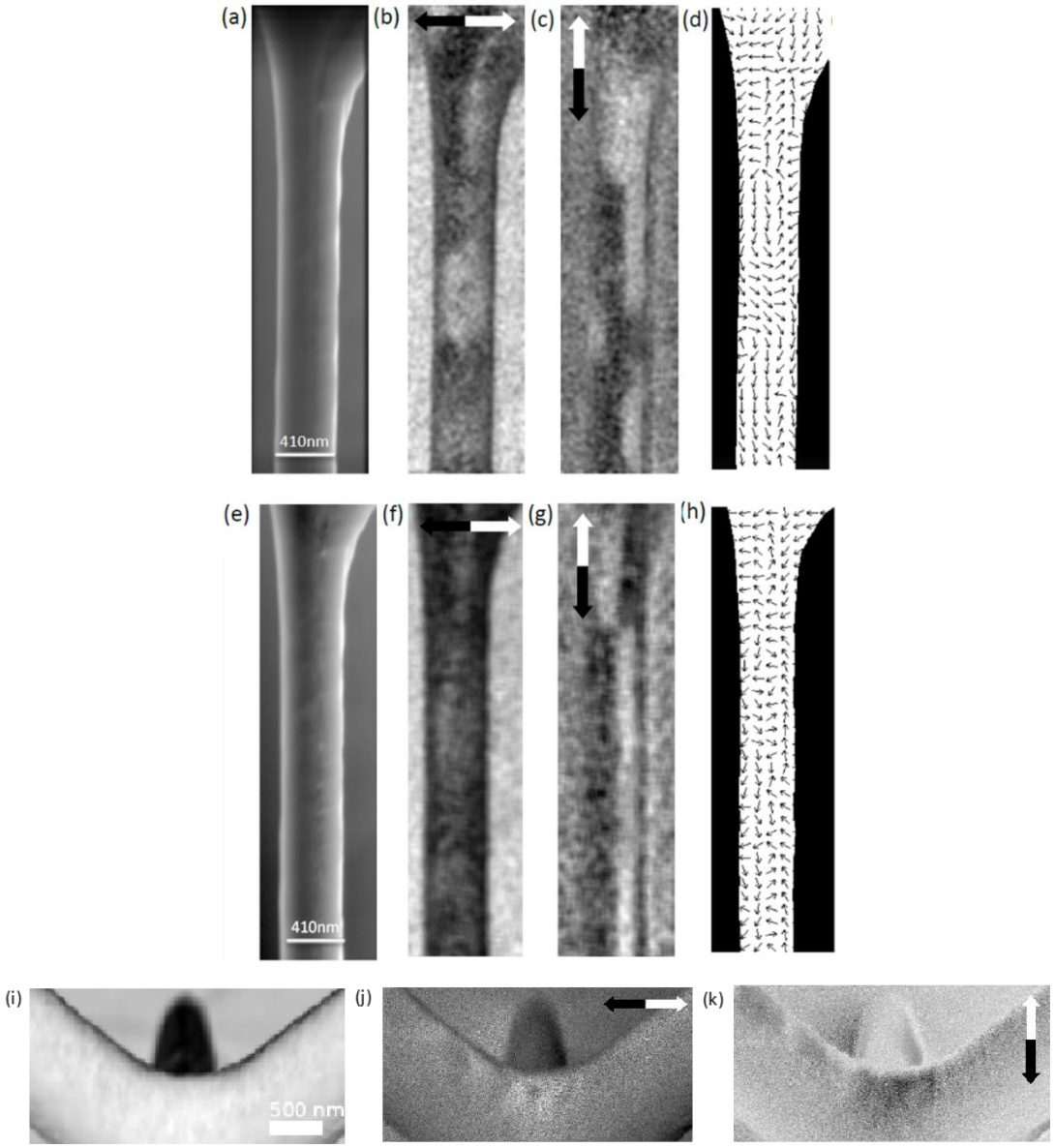

Figure 5.16: Spin-polarised SEM images of a tetrapod wire and vertex. (a) Standard SEM image of individual wire probed, (b) Spin-SEM image of x-component of magnetisation within wire at remanent field, (c) Spin-SEM image of y-component of magnetisation within wire at remanent field, (d) Vector arrow representation of magnetisation within wire at remanent field, (e)-(h) Same as (a)-(d) after application of 11.8mT field pulse along projection of wire long-axis, (i) Standard SEM image of vertex probed, (j) Spin-SEM image of x-component of magnetisation within vertex after application of a 250mT field normal to substrate, (k) Spin-SEM image of y-component of magnetisation within vertex after application of a 250mT field normal to substrate. (Williams et al., 2017)

As there is no good agreement on the preferential alignment of the magnetocrystalline anisotropy axis for electrodeposited *hcp* Co, it has been assumed in a similar manner as for the simulations on single wires that the fabricated 3D structures are composed of randomly oriented crystallites. As such, the distribution of magnetisation angles around the long axis observed in the spin-SEM images is to be expected due to the competition between the shape anisotropy and randomly distributed magnetocrystalline axes.

The spin-SEM images of the vertex (figures 5.16 (j), (k)) show that a complex arrangement of domains persist at the 3D vertex of the tetrapod structures even after application of a 250mT field directed normal to the substrate. This is surprising as the applied field is much stronger than the coercive field for this orientation (27mT), which would be expected to cause the vertex to reside in an approximately two-in/two-out state (chapter 4) upon returning to zero field. Instead, both of the upper wires emerging from the vertex do not have surface magnetisation favouring the transverse direction (figure 5.16(j)), which suggests that upon approaching the vertex the magnetisation has strong curling. From figure 5.16(k) it is apparent that there is a region at the vertex that has a large component of magnetisation different from the surrounding area. Nanostructuring has previously been shown to have an effect on the magnetic properties of a sample (C. C. Wang et al., 2006), and from the spin-SEM images it would appear that the 3D geometry of the vertex has a large effect on the domain patterns, acting as a mediating region between the four wire ends and potentially serving as a pinning site for domain walls.

The domain patterns observed in figures 5.16(b), (c) resemble those seen in 150nm diameter wires magnetised transverse to the wire axis (field 1.3T), imaged with MFM by Henry *et al.* (Henry et al., 2001). MFM is sensitive to the out of plane stray field component of magnetisation, while the spin-SEM images above are sensitive to the in-plane components. However, for cylindrical wires the out of plane and transverse components can be expected to show similar patterns due to the rotational symmetry about the wire axis and curling of magnetisation at the wire surface. For those wires the authors put forward a model for the domain pattern using the calculated MFM response for transverse and longitudinal magnetisation components with respect to the wire axis. After such wires were demagnetised in the direction of the wire axis a long stripe domain pattern was seen similar to figure 5.16(g).

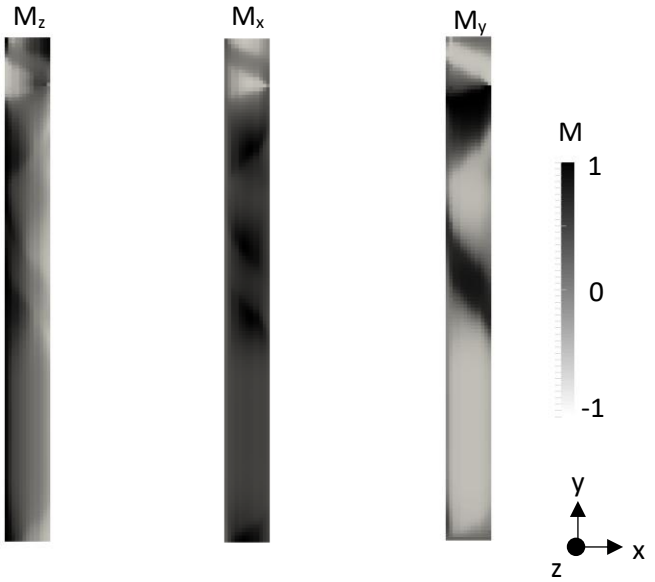

Figure 5.17: Zero-field remanence magnetisation for top surface of simulated wire. The three magnetisation components are provided with greyscale colouring for comparison with figure 5.16.

Figure 5.17 shows the magnetisation of the top surface of the simulated wire (section 5.3.2) after the initial relaxation in zero field. Both the components along and perpendicular to the wire axis are shown and the colour scale is used to match the spin-polarised scanning electron microsope images presented above. The magnetisation images show that the wire relaxes into a multi-domain state as would be expected for wires of these dimensions. The axial component (M_y) shows an alternating pattern of domains with components along the wire axis while the transverse component (M_x) show that for much of the wire the magnetisation curls in the positive y-direction, apart from a small region at the top that exhibits a component in the opposite sense. The out of plane component (M_z) shows contrast aligned with the wire axis.

There are similarities in the domain patterns from the remanence state of the simulated single wire (figure 5.17), those seen in the tetrapod wire in figures 5.16(b), (c) and the MFM images of the literature. All have alternating bands of varying lengths for both the axial and transverse components, and the out of plane component of the simulation has contrast along the axis similar to the MFM images from the above literature. One difference is that the x- and y- components of the simulation do not show any walls along the length of the wire as is seen in the spin-SEM images. This is likely due to the absence of magnetocrystalline anisotropy in the simulations. All show that the surface magnetisation

of such wires have a patchwork pattern of domains that are mobile with field, which will be important when considering the magnetisation processes of such structures as probed by MOKE.

5.4.3 MOKE measurements on tetrapods

Performing MOKE on complex 3D structures is a very challenging undertaking. Unlike with 2D structures consideration needs to be made for how the incident laser is reflected off of the 3D geometry. In addition, due to the use of glass as a substrate, the observed loops often contain a significant background that is comprised of the Faraday Effect and scattering defects within the glass and the mounting surface. The MOKE signal also observes the top surface of the 3D structure, in effect taking a 2D snapshot, and as such is unable to probe bulk properties, or features that are obscured by the bulk structure. Additionally, as the tetrapod structures presented here would be extremely challenging to fabricate using traditional means, as of writing there have been no previous studies in the literature on similar structures. As such the analysis of the results obtained in this study is a very challenging prospect.

Polar MOKE provides the simplest case for investigating the magnetisation of the structures under a time-varying external field. Due to the fabrication design, in this MOKE geometry only a single symmetry direction can be observed, that of the field applied along the [100] and orthogonal axes, and is independent of the in-plane rotation of the sample. Polar MOKE is more sensitive than longitudinal MOKE due to the normal incidence of the beam and so the signal to noise ratio is approximately a factor of 10 higher when compared to longitudinal (Allwood et al., 2003; Pathak and Sharma, 2014).

The polar MOKE loops for the tetrapod structures (figure 5.18(a)) strongly resemble the polar MOKE loops for single angled nanowires and have an average coercive field of 21.5±1.4mT. The coercive field agrees within errors with the value of 22.5±0.8mT found for polar MOKE on the single nanowires. This is to be expected, as the field arrangement is identical for each of the four nanowires comprising the tetrapod structures and at a similar angle of 35.25^{o} compared to 30.5^{o} for the single angled wire case. Because of the polar setup the field is applied approximately parallel to the [100] symmetry direction of the tetrapod. As such these loops are analogous to the simulated hysteresis loops seen for the [100] direction in Chapter 4, where the tetrapod loop was very similar to that of a single wire with the same field orientation.

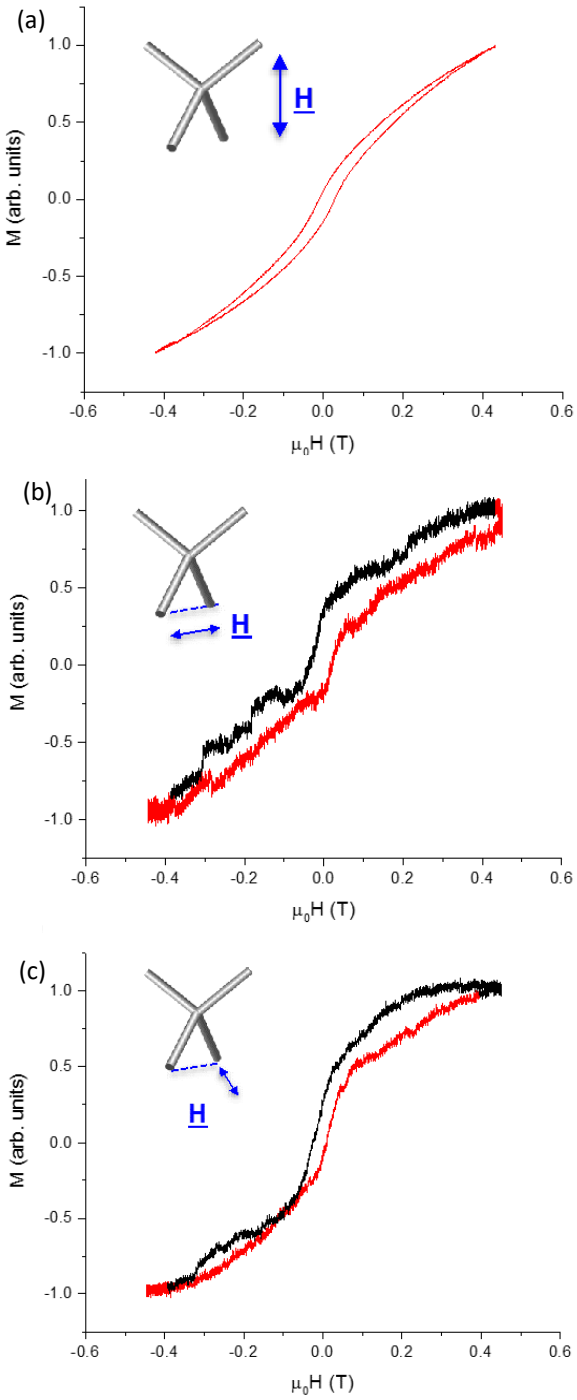

Figure 5.18: MOKE loops for tetrapod structures, (a) Polar MOKE configuration, (b) Longitudinal MOKE configuration with external field applied parallel to the projection of the lower wires, (c) Longitudinal MOKE configuration with external field applied perpendicular to the projection of the lower wires. The forward and reverse magnetisation sweeps are coloured red and black respectively for clarity in (b) and (c). (Williams et al., 2017)

While the tetrapod structures and single wires are multi-domain compared to the simulations which were single domain at remanence, a similar argument can be made that the similarities between the polar loops are due to the four tetrapod wires switching at approximately the same field and in the same manner as for the single wire. As all four wires in the tetrapod likely switch in the manner described in section 5.3.2 for single wires at the same time, the interaction at the vertex will not have a significant effect on the magnetisation dynamics for polar orientation, and so the single wire loop is able to reproduce the observable results.

Longitudinal MOKE was performed at two distinct sample rotations: with the external field applied parallel to the projection of the lower wires on the substrate (henceforth referred to as "lower parallel") (figure 5.18(b)), and with the sample rotated by 90^{o} so that the external field was now aligned parallel to the projection of the upper wires (henceforth referred to as "upper parallel") (figure 5.18(c)). Other rotations were attempted (notably with the field applied at 45^{o} to all wires), however the resultant loops contained a highly parabolic background which has proven extremely difficult to remove.

The longitudinal MOKE loops obtained on the tetrapods show an initial transition with an average coercive field 27±3mT for lower parallel and 24±8mT for upper parallel, approximately 10mT greater than those measured on the single angled nanowires for both parallel and anti-parallel configurations. At higher fields further transitions are consistently observed, three additional measured loops for each orientation are included in figures 5.19 and 5.20 to show this. The secondary transition is most prominent among the additional transitions and is found to have an average coercive field of 120±3mT for lower parallel and 130±8mT for upper parallel. The plateau length from the initial transition to the second has an average value of 67±6mT for lower parallel and 75±5mT for upper parallel.

Occasionally, odd features are observed within the measured MOKE loops such as an increase in magnetisation that is even with field (for example, as can be seen in figure 5.19(f)). These could potentially be due to second order MOKE effects (that are proportional to the products of the magnetisation vector components) (Kuschel et al., 2011), diffractive MOKE effects, or potentially transverse effects, and/or complex backgrounds. From the setup it is unlikely to be diffractive MOKE or transverse effects.

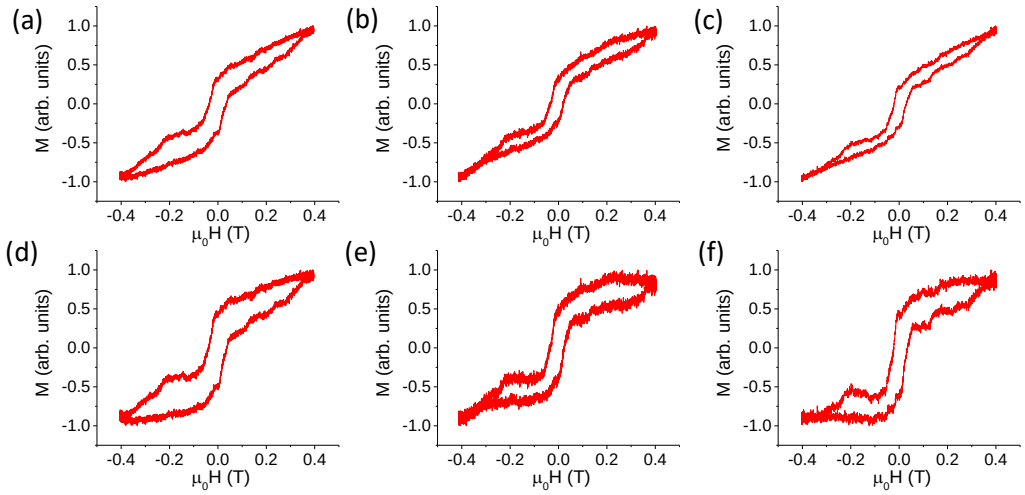

Figure 5.19: Multiple measurements in same MOKE configuration as figure 5.18(b) performed by moving laser focal point off structures and returning. For graphs (a), (b) and (c) a straight line with gradient -5.5mVT^{-1} has been subtracted. For graphs (d), (e) and (f) a straight line with gradient taken from one of the saturation tails has been subtracted. Transitions in the high field range are consistently observed across all figures regardless of the background subtraction method used.

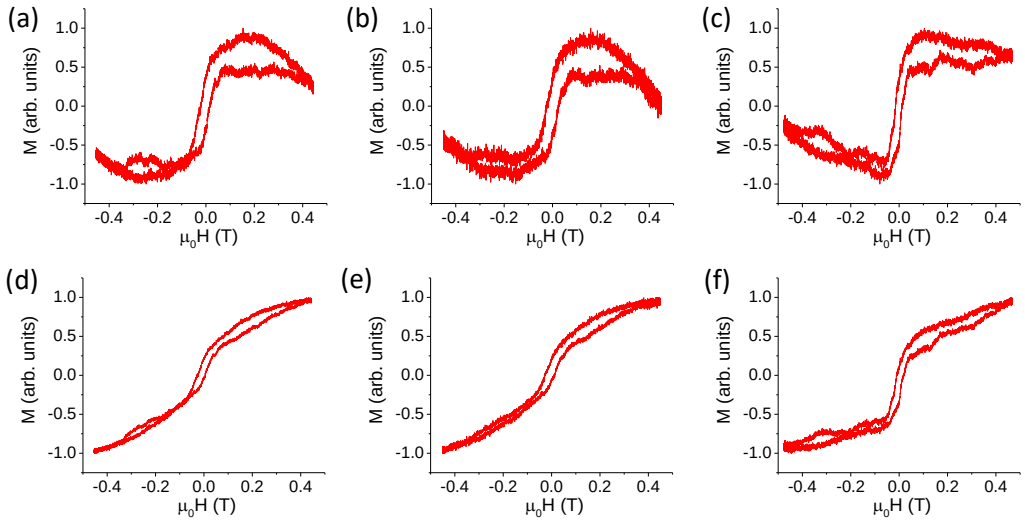

Figure 5.20: Multiple measurements in same MOKE configuration as figure 5.18(c) performed by moving laser focal point off structures and returning. For graphs (a), (b) and (c) a straight line with gradient -5.5mVT^{-1} has been subtracted however a negative gradient background remains. For graphs (d), (e) and (f) a straight line with gradient taken from one of the saturation tails has been subtracted. Transitions in the high field range are consistently observed across all figures regardless of the background subtraction method used.

As discussed earlier in section 5.3.2, the incident light was s-polarised which will suppress any transverse signal. A clear diffraction pattern was observed in the reflected beam from the structures which disperses enough such that only the 0^{th} order spot is selected and focused down onto the detector. The analyser body coupled with a lens tube on the detector to block any of the higher order spots from reaching the detector active area. As such, for diffractive MOKE to have any effect on the resulting loops, it would require higher diffractive order effects to be present within the 0^{th} order spot.

While the observed background in certain orientations was quite complex (likely due to imperfections within the glass substrate), for longitudinal MOKE in the two configurations presented in this chapter the background from the glass was linear and varied little with rotation. Several loops were taken with the laser focused only on the substrate and produced featureless linear plots with average gradient values of $-5.5\pm3.6 mVT^{-1}$ for lower parallel and $-5.5\pm1.4 mVT^{-1}$ for upper parallel. When subtracting linear backgrounds from the raw MOKE loop data, a flat gradient of $-5.5 mVT^{-1}$ was used. While this removes the observed background from the lower parallel loops (figure 5.19(a)-(c)), in the upper parallel loops a negative slope background remains after the subtraction (figures 5.20(a)-(c)).

If the alternate method for background subtraction by using the gradient from the saturation tail is used for the same graphs, it removes the background gradient from the upper parallel loops (figures 5.20(d)-(f)), but does not return the lower parallel loops to the same state as removing the fixed glass background does (figures 5.19(d)-(f)). From comparison between figures 5.19 and 5.20, the two rotations are most similar to each other when a different background subtraction is used on each. The reasoning for this is not clear as the substrate measurements for both orientations were very similar, yet the upper parallel measurements require a larger gradient than measured to remove the linear background despite having a smaller variation in measured backgrounds as shown by the relative errors. However, the further transitions in the loops at higher fields are consistently observed in all loops, despite the method used.

There are a number of possible sources for the further transitions, such as stochastic effects in the sample or domain wall pinning and de-pinning. As the MOKE loops are averaged over many hundreds of cycles, and the consistency with which the transitions are observed, it seems unlikely that they arise from stochastic effects of the sample set. While it cannot be said with certainty that they are due to domain wall pinning, it seems the most

likely case given the nature of the sample geometry when compared to the pinning of domain walls in similar 2D junctions (Petit et al., 2009).

The errors for the second transition coercive fields and plateau lengths are low, below 10%, and the histograms shown in figure 5.21 indicate that the distribution of the multiple coercive field measurements is favourably grouped around the average value for both orientations. This suggests that the plateaus and second transition are not the result of some random effect (which would have a larger error and broader distribution of values) but are in fact intrinsic features for the structures.

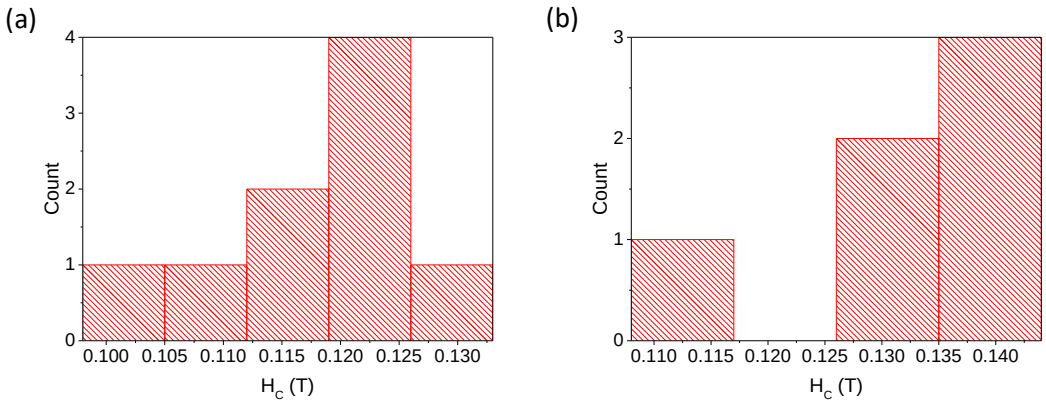

Figure 5.21: Histograms of second transition coercive field distribution for MOKE loops taken on (a) lower parallel orientation (n=9) and (b) upper parallel orientation (n=6).

From the normalised graphs, the initial transitions are often seen to end at approximately ±0.25M, ±0.50M, and ±0.75M. This would seem to indicate magnetisation reversals of individual and multiple wires that comprise the structure; as each structure is composed of four wires each would account for ≈25% of the magnetisation. Further transitions have more variation, but are also often observed to end at these values. These are perhaps due to stochastic pinning events which would account for the variation observed over multiple measurements and loops (Muñoz and Prieto, 2011).

The loops for lower parallel and upper parallel are similar in shape as would be expected due to the symmetry of the structures, however the loop for lower parallel is much more linear at higher field in comparison to the upper parallel loop which shows non-linear change in magnetisation in that range. This high field difference can be explained if the signal is dominated by the component from the upper wires – in the lower parallel orientation the upper wires are perpendicular and so a linear response is expected from

them as seen in the single wire studies (figure 5.8(c)), whereas in upper parallel orientation a more non-linear change is expected from the single wire studies (figure 5.8(b)).

The remaining differences between the lower parallel and upper parallel loops can be put down to the slight differences between the MOKE orientations. When using MOKE the top-most surface of the structures is probed to a depth of ≈20nm. As such, it can be expected to see differences from when the upper wires are parallel to the field compared with when the lower wires are parallel, as in effect opposite sides of the vertex are viewed as domain walls pass through it. The free ends of the upper wires of the tetrapod structures differ to the ends of the lower wires anchored to the substrate – the upper wire free ends are closer to the ends of a cylinder but with some variation in surface roughness, whereas the ends of the lower wires anchored to the substrate are chamfered at the join with the substrate (and therefore likely have a lower variation in surface roughness matching that of the substrate). If the wires were in the single domain regime then this difference in wire ends would likely contribute an observable difference to the measured coercive fields as they would modify how domain walls are nucleated. However, since the wires are multi-domain this effect will be diminished as many of the domain walls will already exist within the bulk wires. This likely helps to explain why the coercive fields for the initial transition agree within errors for the two orientations. Additionally, the higher field transitions are less prominent in the upper parallel case. This supports the proposed switching mechanism detailed below if the upper wires component is more significant than the lower wires component, and if the additional transitions are the result of domain wall motion in the perpendicular wires.

As these structures are too large to realistically simulate at the same scale, the interpretation of their hysteresis loops is restricted to intuitive arguments and reference to existing literature, the single wire simulations discussed in section 5.3.2 and the spin-SEM results discussed above. A proposed, simplified switching mechanism based off of the observations noted previously is shown in figure 5.22.

Let it be assumed that at zero field each wire of the tetrapod is in a 4-domain chequerboard state (figure 5.22(a)), which is a simplified version of the domain pattern observed in the spin-SEM images and the MFM studies from the literature. At the vertex the four wires likely make some complex arrangement of 109.5^{o} domain walls, which will act much like 90^{o} walls (O'Handley, 2000). When a small field (H_1) is applied in a direction parallel to two of the wires and perpendicular to the remaining two, domain walls in the

two ‘parallel’ wires will move resulting in a steep change in magnetisation with field (figure 5.22(b)), as was observed for the single wires (figure 5.8(b) and figure 5.11(a)). Hence, the initial transition observed in the measured tetrapod loops (figure 5.18(b), (c)) is most likely the result of domain wall motion in the wires aligned parallel to the field. Depending on the configuration of the domains in the wires and at the vertex, the magnetostatic interaction between them could act to reduce the mobility of domain walls approaching the vertex or assist in pulling them into the vertex. In this manner the walls may experience either a potential well or barrier at the vertex.

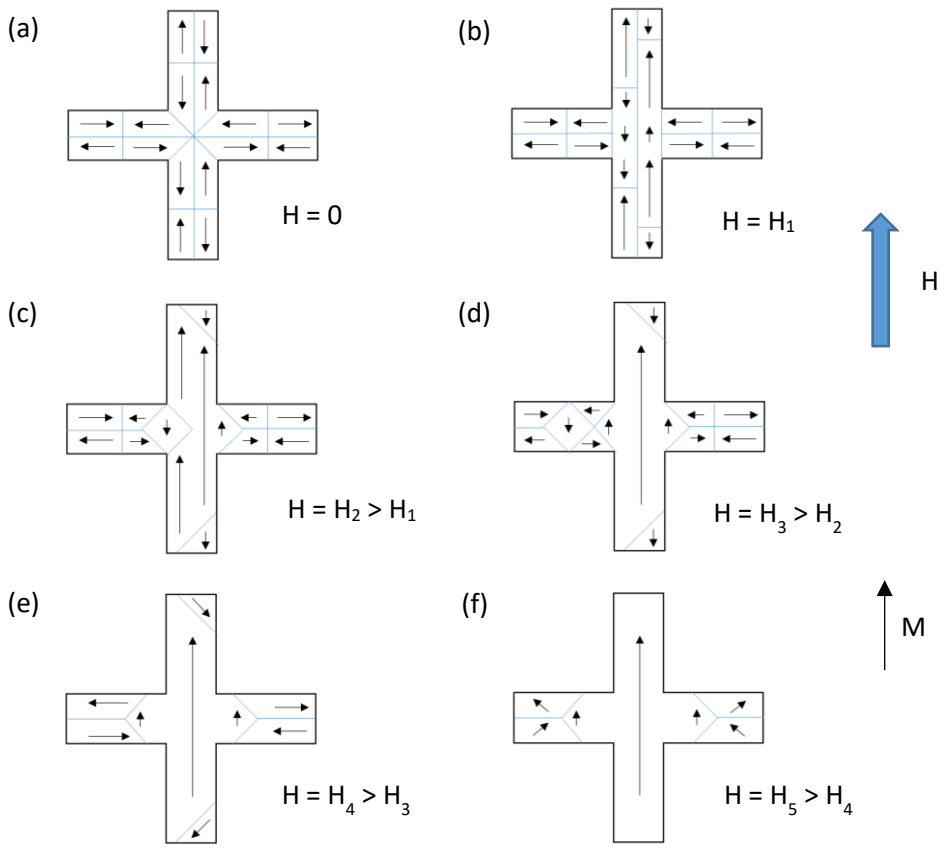

Figure 5.22: Proposed switching mechanism for tetrapod structure represented on a 2D plane.

At the end of this transition it will be possible for domain walls to be pinned at the vertex (figure 5.22(c)). As the field increases further, the vertex should become more aligned to the field which would have an effect of pushing the domain walls against the base of the perpendicular wires, and will result in a much reduced change in magnetisation with field while this occurs, observable as the plateau in the measured loops. As the field increases

further, any pinned walls at the vertex could be depinned and propagate into the perpendicular wires (figure 5.22(d)). The depinning event and subsequent motion of domains will have a sharper change in magnetisation which would be observed as additional transitions in the measured loops. It should be noted that these additional transitions are unlikely to be due to Barkausen noise (random jumps in magnetisation) as the transitions favour specific positions as mentioned above. Instead, they are more likely to be a stochastic selection between several depinning fields mediated by thermal fluctuations, as seen previously in nanowires (Hayward, 2015).

Once all the walls have been depinned there is no more possibility for additional transition events (figure 5.22(e)) and so as the field is increased even further the magnetisation of the perpendicular wires will undergo rotation as seen at the highest fields in the measured loops (figure 5.22(f)). As the field is then reduced, there are no walls present initially and so the magnetisation decreases without transition events, likely in a curling type mode which can introduce domain walls again at low field as seen in the simulations of the single wires. These introduced domains can then facilitate the same switching process as described above for the field increasing in the reversed sense.

It is possible for one or both of the parallel wires to contribute to the initial transition as, from the experimental setup, the sample is likely to have some small angle deviation from being perpendicular to the field which would result in slightly different orientations of the field to the parallel wires. However as this angle is small ($<2^{o}$) it is unlikely for there to be an obvious split in coercive fields for the two parallel wires. As both parallel and anti-parallel wires are measured in these structures, it might be expected that there would be a split in coercive fields as seen in the single wire measurements (figure 5.9). However, the coercive fields for the tetrapod are greater than both orientations of the single wires, 27mT and 24mT compared to 11mT and 16mT. This increase could be due to the reduced wire dimensions in the tetrapod (610nm lateral for the tetrapod wires compared to 750nm lateral for the single wires), but also because of the conjoined nature of the wires restricting the movement of domain walls at the vertex.

It is tempting to try and explain the possible domain wall depinning and propagation into the perpendicular wires using arguments based on the simulated hysteresis loops from chapter 4 for more simplistic single-domain wire tetrapods. There it was observed that a single domain wall entering the vertex of the structure led to the propagation of walls down multiple wires for the [111] field direction. It was also observed that in the [110]

direction, while both wires aligned with the field direction switched at the same coercive field, one wall could lag and cause the other to enter the vertex alone. While in that idealised simulation case the wall passed through the vertex without generating further walls in the perpendicular wires, such assisted wall depinning was observed in single-domain, planar crosses (O'Brien et al., 2012b) and while the exact mechanism is likely different, for a more complex multi-domain system such an event might be possible.

It should be noted however that for the single-domain regime structures discussed in chapter 4, it was possible to replicate the [110] field tetrapod loop by combining the loops of single isolated wires. When trying a similar technique to construct loops for the longitudinal configurations in figure 5.18(b) and (c) from the measured loops of the individual wires (using parallel, anti-parallel and perpendicular loops from single wires shown in figure 5.8 with varied contributions), it is possible to manufacture loops that begin to approach the general shape of the measured tetrapod loops but they are unable to reproduce the observed transitions at higher fields. As the measured results for the single fabricated wires largely agreed with previous literature and simulation data, this inability to reproduce the loops for the tetrapod structures indicates that the effect of nanostructuring on the larger multi-domain systems produces a much more complex magnetisation process than that of single-domain structures.

Chapter 6 – Conclusions

The work presented in this thesis has demonstrated a new method for the fabrication of magnetic nanostructures that addresses the limitations of the currently employed techniques. It was shown that two-photon lithography (TPL) can be employed to design 3D nanostructure templates, which can then be filled using electrodeposition to produce arrays of high purity magnetic structures. This combination represents a significant advance in the study of experimental 3D nanomagnetism as it enables the largescale production of geometries that would previously have been extremely challenging to fabricate. The results of this PhD are among the first to examine what is possible, and have shown that the standard surface techniques of magneto-optical Kerr effect (MOKE) magnetometry and spin-polarised scanning electron microscopy (spin-SEM) can be used to probe the magnetisation reversal of complex 3D nanostructures. Additionally, simulations performed on complex 3D structures of the same geometry of experimentally produced structures were included as an initial study of the behaviour of domain walls at 3D nanowire junctions and for future reference in experimental work.

In chapter 4, a study on micromagnetic simulations of single cylindrical nanowires of finite length and 'tetrapod' structures, a combination of four nanowires of the same dimensions arranged so as to mimic the spin orientations of bulk pyrochlore spin ice, were presented. For the single nanowires, hysteresis loops were performed where the angle of the uniform external field with respect to the wire long axis for single nanowires was varied. The angles were chosen so as to match the wire orientations with respect to the external field when hysteresis loops were applied at principle symmetry axes for the tetrapod structure. The coercive field was observed to increase as the angle was increased from 0^{o}, while for the field applied at 90^{o} to the wire axis no hysteresis was observed as the magnetisation reversal was due solely to rotation. The hysteresis loops generated were found to match those found in previous literature studies on cylindrical nanowires. From visualisation of the magnetisation at time steps during the simulations, the switching events in the cylindrical wires were observed to be due to the nucleation and propagation of Bloch point domain walls, as predicted for the wire dimensions (50nm diameter and 1.5μm length) by a phase diagram from literature (Ferguson et al., 2015). As the angle of the applied external field with respect to the wire axis increased, it was noted that by splitting the field into an axial and transverse component, the axial component required to nucleate a domain wall decreased. This trend was explained by considering the maximum localised exchange

energy within the wire mesh, which decreased as the transverse component of the field increased. The same trend was observed for domain walls under angled fields in planar Py nanostrips (Glathe et al., 2008). The magnetisation images also showed that the vortex part of the domain wall became more canted as the angle increased while the Bloch point itself was displaced away from the centre of the wire axis. With the field applied at 70.5° the domain wall propagated was so displaced that it no longer resembled a Bloch point domain wall, which was evidenced as a sharp decrease in average exchange energy of the nanowire. When comparing the Bloch point domain wall velocity to other studies in the literature it was found to increase with axial field component as expected and observed the same dependence upon the Gilbert damping parameter.

As the single wire simulations were in agreement with the literature, static zero-field magnetic relaxation simulations were performed on the tetrapod structure to check the three distinct energy states analogous to bulk spin ice: two-in/two-out, three-in/one-out and four-in. The averaged total energy density for these states was found to follow the trend for bulk spin ice, with two-in/two-out being the lowest energy state and four-in the highest. Both the two-in/two-out state and three-in/one-out state were stable configurations, whereas the four-in state was not stable, even with pinning of the magnetisation in the wires, due to the large energy associated with the state. This was the same observation seen for 2D artificial spin ice (R. F. Wang et al., 2006).

With it established that the tetrapod mesh exhibits the expected trend in states, hysteresis loops were performed on the tetrapod along three principle symmetry axes: [100], [110] and [111]. The loop for the [100] direction was found to be replicated by the single wire loop with the field applied at 54.75°. This is due to each of the four wires comprising the tetrapod being aligned at that angle with respect to the external field meaning that, during the switch event, a domain wall is nucleated from the free end of each wire and propagates down the respective wires before annihilating at the vertex of the structure to complete the reversal of the two-in/two-out state. The loop for the [110] direction was found to be obtainable by the addition of the single wire loops for 35.25° and 90°, as two of the four wires are aligned at each of those angles respectively. The switching event was observed to be due to the nucleation of domain walls from the free ends of the two wires aligned at 35.25° which behaved in a similar manner as seen for the [100] direction.

The [111] loop however could not be obtained from the addition of the single wire loops with the same angles (0° and 70.5°) and featured two switching events. Upon inspecting

the visualisations of the switching events, it was observed that for the initial transition a Bloch point domain wall is nucleated at the free end of the 0° wire and then propagates down to the vertex. Despite the vertex potentially acting as a pinning site as seen in a previous study (Berganza et al., 2016; Chandra Sekhar et al., 2014), it was seen that the domain wall enters the vertex for every simulation. The lack of pinning was reasoned to be due to the vortex structure of the domain wall leading ahead of the Bloch point and screening it from magnetostatic interaction, the energetically unfavourable nature of a four-in state at the vertex and the nucleation field of the domain wall assisting propagation into the remaining wires. Upon entering the vertex, the domain wall then induced the nucleation of two further domain walls that each propagate down two of the three wires at 70.5° at the same field step. Domain wall cloning had been observed previously in 2D nanostrip junctions and it was suggested that the cloning at this 3D junction was mediated by reducing the energy of the vertex to a two-in/two-out state. The second switching event was the remaining 70.5° wire propagating a domain wall. The selection of the two 70.5° walls during the initial transition event was observed to be different during reversal of the external field direction. This was reasoned to be due to the symmetry of magnetisation curling for the three 70.5° nanowires at the vertex join not providing an imbalance in energy to influence selection.

Compared with connected 2D artificial spin ice, the stable monopole-like three-in/one-out state or vice versa in the tetrapod was not the result of domain wall pinning but rather the remanent magnetisation at the vertex. It is believed that this will have important ramifications for the stability of the monopole-like defects in an extended 3D artificial spin ice lattice. The above study demonstrates that 3D geometries exhibit complex behaviour that warrant further investigations, especially with the emergence of fabrication techniques capable of producing such structures.

In chapter 5, 3D nanostructures fabricated using TPL and electrodeposited cobalt were characterised and measured using spin-polarised SEM and MOKE magnetometry. Initially an array of vertically aligned cylindrical nanowires, where the write power was reduced across the array, was inspected by scanning electron microscopy (SEM), atomic force microscopy (AFM) and energy dispersive X-ray analysis (EDX). By measuring the diameter of the cylinders from SEM images the smallest lateral feature size was determined as 435nm. This did not agree with the theoretical minimum for the parameters used in the fabrication until an addition was made to the model to account for dark erosion. The topographical surface measurements taken by AFM were found to agree with those reported on

electrodeposited cobalt. EDX analysis showed that the structures were of high-purity (>95%) Co with minor amounts of carbon and oxygen which originated from the SEM process and residual photoresist on the sample surface.

The next sample to be investigated was an array of 3D nanowires angled at 30.5^{o} with respect to the substrate. The array was written using one power only and a larger power than that used to produce the smallest cylinder in the previous study was used to provide a good yield of structures in the array. Previous studies of such wires using focused electron beam induced deposition investigated samples consisting of a single wire only. From topographical inspection of the array it was found that there were no observable defects among structures and that the wires had an elliptical cross-section. The two wire ends were observed to have different profiles, the lower end dictated by the join to the substrate and the upper end with some variance in roughness from the electrodeposition process and a consequence of the larger structure size. The sample was prepared for MOKE measurement by using a series of plasma ashing trials to remove residual photoresist from the surface. The result of the ashing process was measureable hysteresis loops for the array.

The loops were taken in the polar and longitudinal MOKE geometries, with the field applied parallel and perpendicular to the projection of the nanowire axis onto the substrate for the longitudinal case. For the polar hysteresis loop it was seen that for low field there was a steep change in magnetisation with field. The rate of change decreased as the field was increased, and the maximum applied field was not strong enough to fully saturate the sample, resulting in an open hysteresis loop. A similar trend was observed for the longitudinal geometry with the field parallel or anti-parallel, with some variance in coercive field due to the change of angle between the wire axis and incident laser of the MOKE. The hysteresis loop taken in longitudinal geometry with the field applied perpendicular showed a much more linear relationship with field, with opening of the loop. From the size of the wires and low remanence of the loops it was surmised that they were in the multi-domain regime. These results were compared to existing literature on arrays of cobalt nanowires with large (>100nm) diameters and were found to be in qualitative agreement. From comparison with the literature it was concluded that the reversal mechanism was domain wall motion at low field (as indicated by the steep initial change shown by the experimental loops), followed by a reduction in domain wall mobility as the wire boundaries constrain the motion and then rotation of the magnetisation at high fields.

Supporting micromagnetic simulations of hysteresis loops were performed at the same geometries for wires of dimensions approaching those of the fabricated wires. The polar and parallel longitudinal simulated loops were in qualitative agreement with the trends observed for the experimental loops, however the perpendicular longitudinal loop exhibited a closed loop with linear relationship of magnetisation with field, indicative of a wholly rotation based reversal mechanism. The discrepancy for the perpendicular loop was shown to be due to the surface-sensitive nature of MOKE, which was unable to account for other magnetisation changes within the bulk structure.

Once the single wire structures had been characterised and their reversal mechanism compared with the literature, a more complex 3D structure was investigated. The structure of choice was the tetrapod arrangement of nanowires as studied in chapter 4, due to its potential use as a unit cell for a 3D artificial spin ice lattice. From inspection of SEM images it was found that, like the single nanowire array, there were no observable defects among the structures. From measurements of the wire dimensions for the tetrapod structures it was determined that all of the wire lengths were approximately equal with a ratio close to unity (0.95±0.4).

A tetrapod array sample of smaller dimensions was sent to collaborators at IBM for spin-SEM analysis. The sample was prepared by use of a mild bombardment of Kr^+ ions to create a clean surface as required by spin-SEM, and the top surface of one of the tetrapod upper wires was imaged before and after a small field pulse directed parallel to its axis projection. The tetrapod vertex was also imaged after application of a large out of plane field. The images provided by IBM showcased that spin-SEM is a powerful technique for probing the magnetic domain surface map of 3D structures, and revealed that the structures were multi-domain as expected. The images exhibited features that were comparable to magnetic force microscopy images of the domain patterns on the surface of cylindrical wires from the literature, as well as surface magnetisation profiles of the zero-field remanence state for the simulated wire used to compare with the fabricated arrays above. From a statistical analysis of the magnetisation presented with the IBM images, there was a preference for magnetisation to lie along the wire axis. This was determined to be due to the competing interactions between randomly aligned magnetocrystalline anisotropy axes and the shape anisotropy of the wire.

Finally, hysteresis loops were taken using MOKE on the tetrapod structures in the same geometries as for the single nanowire array. The sample was prepared using plasma asher

trials as before. The hysteresis loop for the polar case was qualitatively similar to the polar loop measured for the single angled nanowires. This was explained using similar reasoning as for the [100] tetrapod loop in chapter 4, and demonstrated that MOKE is a viable technique for probing magnetisation of complex 3D geometries despite the difficulties involved both experimentally and for analysis. The longitudinal hysteresis loops performed on the tetrapod structures showed an initial switching event at low field and further transitions at higher fields. These latter transitions were consistently observed and could not be explained by considering multiple contributions from the loops for single nanowires, using a similar method as was employed to recreate loops for the [110] simulation in chapter 4. Instead, a reversal mechanism was proposed based on the experimental observations of the previous studies in the chapter and with reference to the literature. The mechanism proposed that the initial transition at low field was due to domain wall motion in the two tetrapod wires parallel to the applied field. The domain walls can then be pinned at the vertex. As the field is increased further the walls can become unpinned and expand into the perpendicular wires causing the secondary transitions. At larger fields again the magnetisation in the perpendicular wires then rotates to align with the field.

The results of this chapter have shown that the act of 3D nanostructuring on magnetic samples leads to complex behaviour that cannot be replicated by considerations of the constituent parts of such structures only.

Building on the results from this thesis, there is great scope for future work. Following from the simulations performed in chapter 4, a study focusing on a more detailed analysis of domain wall interaction at branching 3D nanowire junctions could be made. This could take the form of simple Y-shaped junctions of cylindrical nanowires in a single plane, or of more complex junctions that expand into 3D space such as three cylindrical wires aligned along orthogonal axes. Such a study would potentially give a better insight into the path selection mechanism for domain walls in 3D nanowires, as well as the importance of the magnetisation within the junction itself. Additionally the parameters governing the cloning of domain walls in 3D nanowires could be investigated. For further simulation studies of the 3D ASI unit cell, simulations could be performed on smaller wires so that they are in the transverse wall regime and compare the switching mechanisms with those for Bloch point domain walls. A unit cell that is disconnected (i.e. separated nanowires with no vertex) would potentially better match the spin dynamics of a bulk spin ice material cell and would remove the propagation effects of domain walls through the vertex. Extending the simulation to multiple joined cells would also be of interest to observe domain wall

propagation over an extended lattice and the mobility or stability of the monopole-like three-in/one-out remanent states at the vertices. Simulations of other 3D geometries that could be fabricated would also be useful for future experimental work as the fabrication technologies are improved.

One of the limitations of the TPL and electrodeposition technique is that of the feature sizes achievable, which are currently restricted to the multi-domain regime. As such the immediate future work involving this technique should focus on reducing the obtainable feature size of the structures down to a regime where they are single domain at remanence for the nanowire constituents. Doing so will help reduce the complexity of the analysis of the measurements and can potentially be realised by using negative-type photoresists (Yeh et al., 2010). TPL using negative resists creates a template by exposing the resist in negative space and so changes the minimum feature size from dependence on the voxel diameter within the focal point to the convolution between two line scans. Another method for reducing the feature size would be to install a shorter wavelength laser (such as 405nm) in the TPL setup so that other resists could be used for two-photon polymerisation (Mueller et al., 2014). Reducing the wavelength decreases the achievable width of the focal point and so reduces the lateral feature size of the TPL voxel.

The remaining obvious area for future work would be the fabrication of 3D nanostructures with different geometry. One option would be to use TPL and negative resist to produce a polymer scaffold. A magnetic material could then be deposited on top of this scaffold using a line of sight deposition technique such as thermal evaporation. This would result in nanostrips with an out of plane curvature upon the top surface of the scaffold. Such samples could exhibit interesting magnetic properties as the topic of curvature is an emerging research area in magnetism (Streubel et al., 2016). Additionally such structures would be better suited for measurement using MOKE as they would not be bulk structures so the surface magnetisation would be a good representation of the whole wire.

References

Aboaf, J., Herd, S., Klokholm, E., 1983. Magnetic properties and structure of cobalt-platinum thin films. IEEE Trans. Magn. 19, 1514–1519. https://doi.org/10.1109/TMAG.1983.1062575

Ali, M., 1999. Growth And Study Of Magnetostrictive FeSiBC Thin Films For Device Applications. University of Sheffield.

Allenspach, R., 2000. Spin-polarized scanning electron microscopy. IBM J. Res. Dev. 44, 553–570. https://doi.org/10.1147/rd.444.0553

Allwood, D.A., Xiong, G., Cooke, M.D., Cowburn, R.P., 2003. Magneto-optical Kerr effect analysis of magnetic nanostructures. J. Phys. Appl. Phys. 36, 2175. https://doi.org/10.1088/0022-3727/36/18/001

Allwood, D.A., Xiong, G., Cowburn, R.P., 2007. Domain wall cloning in magnetic nanowires. J. Appl. Phys. 101, 024308. https://doi.org/10.1063/1.2424525

Andrzejewska, E., 2016. Chapter 2 - Free Radical Photopolymerization of Multifunctional Monomers, in: Baldacchini, T. (Ed.), Three-Dimensional Microfabrication Using Two-Photon Polymerization, Micro and Nano Technologies. William Andrew Publishing, Oxford, pp. 62–81. https://doi.org/10.1016/B978-0-323-35321-2.00004-2

Atkinson, D., Allwood, D.A., Faulkner, C.C., Xiong, G., Cooke, M.D., Cowburn, R.P., 2003. Magnetic domain wall dynamics in a permalloy nanowire. IEEE Trans. Magn. 39, 2663–2665. https://doi.org/10.1109/TMAG.2003.815548

Atkinson, D., Allwood, D.A., Xiong, G., Cooke, M.D., Faulkner, C.C., Cowburn, R.P., 2003. Magnetic domain-wall dynamics in a submicrometre ferromagnetic structure. Nat. Mater. 2, 85–87. https://doi.org/10.1038/nmat803

Atkinson, D., Eastwood, D.S., Bogart, L.K., 2008. Controlling domain wall pinning in planar nanowires by selecting domain wall type and its application in a memory concept. Appl. Phys. Lett. 92, 022510. https://doi.org/10.1063/1.2832771

Ayachit, U., 2015. The ParaView Guide: A Parallel Visualization Application. Kitware, Inc., USA.

Balke, B., Wurmehl, S., Fecher, G., Felser, C., Kübler, J., 2008. Rational design of new materials for spintronics: Co2FeZ (Z=Al, Ga, Si, Ge). Sci. Technol. Adv. Mater. 9, 014102. https://doi.org/10.1088/1468-6996/9/1/014102

Bantu, A.K.M., Rivas, J., Zaragoza, G., López-Quintela, M.A., Blanco, M.C., 2001. Structure and magnetic properties of electrodeposited cobalt nanowires. J. Appl. Phys. 89, 3393–3397. https://doi.org/10.1063/1.1345857

Bell, D.C., Garratt-Reed, A.J., 2003. Energy Dispersive X-ray Analysis in the Electron Microscope. Garland Science.

Belliard, L., Miltat, J., Thiaville, A., Dubois, S., Duvail, J.L., Piraux, L., 1998. Observing magnetic nanowires by means of magnetic force microscopy. J. Magn. Magn. Mater. 190, 1–16. https://doi.org/10.1016/S0304-8853(98)00282-0

Berganza, E., Bran, C., Jaafar, M., Vázquez, M., Asenjo, A., 2016. Domain wall pinning in FeCoCu bamboo-like nanowires. Sci. Rep. 6, 29702. https://doi.org/10.1038/srep29702

Bhargava, R., Levin, I.W., 2002. Effective Time Averaging of Multiplexed Measurements: A Critical Analysis. Anal. Chem. 74, 1429–1435. https://doi.org/10.1021/ac011153n

Biziere, N., Gatel, C., Lassalle-Balier, R., Clochard, M.C., Wegrowe, J.E., Snoeck, E., 2013. Imaging the Fine Structure of a Magnetic Domain Wall in a Ni Nanocylinder. Nano Lett. 13, 2053–2057. https://doi.org/10.1021/nl400317j

Borzi, R.A., Albarracín, F.A.G., Rosales, H.D., Rossini, G.L., Steppke, A., Prabhakaran, D., Mackenzie, A.P., Cabra, D.C., Grigera, S.A., 2016. Intermediate magnetization state

and competing orders in $Dy_2Ti_2O_7$ and $Ho_2Ti_2O_7$. Nat. Commun. 7, ncomms12592. https://doi.org/10.1038/ncomms12592
Bramwell, S.T., Giblin, S.R., Calder, S., Aldus, R., Prabhakaran, D., Fennell, T., 2009. Measurement of the charge and current of magnetic monopoles in spin ice. Nature 461, 956–959. https://doi.org/10.1038/nature08500
Bramwell, S.T., Gingras, M.J.-P., 2001. Spin Ice State in Frustrated Magnetic Pyrochlore Materials. Science 294, 1495–1501. https://doi.org/10.1126/science.1064761
Brayton, R.K., Gustavson, F.G., Hachtel, G.D., 1972. A new efficient algorithm for solving differential-algebraic systems using implicit backward differentiation formulas. Proc. IEEE 60, 98–108. https://doi.org/10.1109/PROC.1972.8562
Brigo, L., Urciuolo, A., Giulitti, S., Della Giustina, G., Tromayer, M., Liska, R., Elvassore, N., Brusatin, G., 2017. 3D high-resolution two-photon crosslinked hydrogel structures for biological studies. Acta Biomater. 55, 373–384. https://doi.org/10.1016/j.actbio.2017.03.036
Brown, W.F., 1963. Micromagnetics. Interscience Publishers.
Brown, W.F., 1962. Magnetostatic Principles in Ferromagnetism. North-Holland Publishing Company.
Bryan, M.T., Schrefl, T., Atkinson, D., Allwood, D.A., 2008. Magnetic domain wall propagation in nanowires under transverse magnetic fields. J. Appl. Phys. 103, 073906. https://doi.org/10.1063/1.2887918
C. Castelnovo, R. Moessner, Sondhi, S.L., 2012. Spin Ice, Fractionalization, and Topological Order. Annu. Rev. Condens. Matter Phys. 3, 35–55. https://doi.org/10.1146/annurev-conmatphys-020911-125058
Cantu-Valle, J., Betancourt, I., Sanchez, J.E., Ruiz-Zepeda, F., Maqableh, M.M., Mendoza-Santoyo, F., Stadler, B.J.H., Ponce, A., 2015. Mapping the magnetic and crystal structure in cobalt nanowires. J. Appl. Phys. 118. https://doi.org/10.1063/1.4923745
Cao, H.-Z., Zheng, M.-L., Dong, X.-Z., Jin, F., Zhao, Z.-S., Duan, X.-M., 2013. Two-photon nanolithography of positive photoresist thin film with ultrafast laser direct writing. Appl. Phys. Lett. 102, 201108. https://doi.org/10.1063/1.4807678
Castelnovo, C., Moessner, R., Sondhi, S.L., 2008. Magnetic Monopoles in Spin Ice. Nature 451, 42–45. https://doi.org/10.1038/nature06433
Chandra Sekhar, M., Goolaup, S., Purnama, I., Lew, W.S., 2014. Depinning assisted by domain wall deformation in cylindrical NiFe nanowires. J. Appl. Phys. 115, 083913. https://doi.org/10.1063/1.4867004
Chern, G.-W., Reichhardt, C., Nisoli, C., 2014. Realizing three-dimensional artificial spin ice by stacking planar nano-arrays. Appl. Phys. Lett. 104, 013101. https://doi.org/10.1063/1.4861118
Choudhary, O.P., Priyanka, 2017. Scanning Electron Microscope: Advantages and Disadvantages in Imaging Components. Int. J. Curr. Microbiol. Appl. Sci. 6, 1877–1882. https://doi.org/10.20546/ijcmas.2017.605.207
Claudine Lacroix, 2011. Introduction to Frustrated Magnetism. Springer.
Cryostation | Montana Instruments [WWW Document], n.d. URL https://www.montanainstruments.com/Products/Cryostation/?tab=product-overview (accessed 1.27.18).
Cumings, J., 2011. Frustrated magnets: Artificial ice goes thermal. Nat. Phys. 7, 7–8. https://doi.org/10.1038/nphys1898
Curtis R. Menyuk, 2010. Symmetry of the Dielectric Tensor.
Da Col, S., Jamet, S., Rougemaille, N., Locatelli, A., Mentes, T.O., Burgos, B.S., Afid, R., Darques, M., Cagnon, L., Toussaint, J.C., Fruchart, O., 2014. Observation of Bloch-

point domain walls in cylindrical magnetic nanowires. Phys. Rev. B 89, 180405. https://doi.org/10.1103/PhysRevB.89.180405
Dietrich, P.-I., Harris, R.J., Blaicher, M., Corrigan, M.K., Morris, T.J., Freude, W., Quirrenbach, A., Koos, C., 2017. Printed freeform lens arrays on multi-core fibers for highly efficient coupling in astrophotonic systems. Opt. Express 25, 18288–18295. https://doi.org/10.1364/OE.25.018288
Donahue, M., 2016. OOMMF: Object Oriented MicroMagnetic Framework. https://doi.org/D3XS5JJ23
Eastwood, D.S., King, J.A., Bogart, L.K., Cramman, H., Atkinson, D., 2011. Chirality-dependent domain wall pinning in a multinotched planar nanowire and chirality preservation using transverse magnetic fields. J. Appl. Phys. 109, 013903. https://doi.org/10.1063/1.3525733
Edgcombe, C.J., Valdrè, U., 2002. Experimental and computational study of field emission characteristics from amorphous carbon single nanotips grown by carbon contamination. I. Experiments and computation. Philos. Mag. Part B 82, 987–1007. https://doi.org/10.1080/13642810208218357
Egerton, R.F., 2005. Physical Principles of Electron Microscopy: An Introduction to TEM, SEM, and AEM. Springer US.
Eisberg, R.M., Resnick, R., 1974. Quantum physics of atoms, molecules, solids, nuclei, and particles. Wiley.
Elhajal, M., Canals, B., Lacroix, C., 2004. Ordering in pyrochlore compounds due to Dzyaloshinsky–Moriya interactions: the case of Cu 4 O 3. J. Phys. Condens. Matter 16, S917. https://doi.org/10.1088/0953-8984/16/11/049
Fangohr, H., Thomas Fischbacher, Matteo Franchin, Giuliano Bordignon, Jacek Generowicz, Andreas Knittel, Michael Walter, Maximilian Albert, 2011. 11. Mini tutorial micromagnetic modelling — NMAG User Manual v0.2.1 documentation [WWW Document]. URL http://nmag.soton.ac.uk/nmag/0.2/manual/html/tutorial/doc.html (accessed 9.9.17).
Faulkner, C.C., Allwood, D.A., Cooke, M.D., Xiong, G., Atkinson, D., Cowburn, R.P., 2003. Controlled switching of ferromagnetic wire junctions by domain wall injection. IEEE Trans. Magn. 39, 2860–2862. https://doi.org/10.1109/TMAG.2003.816247
Ferguson, C.A., MacLaren, D.A., McVitie, S., 2015. Metastable magnetic domain walls in cylindrical nanowires. J. Magn. Magn. Mater. 381, 457–462. https://doi.org/10.1016/j.jmmm.2015.01.027
Fernández-Pacheco, A., Serrano-Ramón, L., Michalik, J.M., Ibarra, M.R., De Teresa, J.M., O'Brien, L., Petit, D., Lee, J., Cowburn, R.P., 2013. Three dimensional magnetic nanowires grown by focused electron-beam induced deposition. Sci. Rep. 3. https://doi.org/10.1038/srep01492
Fernández-Pacheco, A., Streubel, R., Fruchart, O., Hertel, R., Fischer, P., Cowburn, R.P., 2017. Three-dimensional nanomagnetism. Nat. Commun. 8, ncomms15756. https://doi.org/10.1038/ncomms15756
Fernández-Pacheco, A., Teresa, J.M.D., Szkudlarek, A., Córdoba, R., Ibarra, M.R., Petit, D., O'Brien, L., Zeng, H.T., Lewis, E.R., Read, D.E., Cowburn, R.P., 2009. Magnetization reversal in individual cobalt micro- and nanowires grown by focused-electron-beam-induced-deposition. Nanotechnology 20, 475704. https://doi.org/10.1088/0957-4484/20/47/475704
Ferré, R., Ounadjela, K., George, J.M., Piraux, L., Dubois, S., 1997. Magnetization processes in nickel and cobalt electrodeposited nanowires. Phys. Rev. B 56, 14066–14075. https://doi.org/10.1103/PhysRevB.56.14066

Fert, A., Piraux, L., 1999. Magnetic nanowires. J. Magn. Magn. Mater. 200, 338–358. https://doi.org/10.1016/S0304-8853(99)00375-3
Fischbacher, T., Franchin, M., Bordignon, G., Fangohr, H., 2007. A Systematic Approach to Multiphysics Extensions of Finite-Element-Based Micromagnetic Simulations: Nmag. IEEE Trans. Magn. 43, 2896–2898. https://doi.org/10.1109/TMAG.2007.893843
Foner, S., 1996. The vibrating sample magnetometer: Experiences of a volunteer (invited). J. Appl. Phys. 79, 4740–4745. https://doi.org/10.1063/1.361657
Foner, S., 1981. Review of magnetometry. IEEE Trans. Magn. 17, 3358–3363. https://doi.org/10.1109/TMAG.1981.1061748
Forster, H., Schrefl, T., Suess, D., Scholz, W., Tsiantos, V., Dittrich, R., Fidler, J., 2002. Domain wall motion in nanowires using moving grids (invited). J. Appl. Phys. 91, 6914–6919. https://doi.org/10.1063/1.1452189
García-Torres, J., Gómez, E., Vallés, E., 2009. Modulation of magnetic and structural properties of cobalt thin films by means of electrodeposition. J. Appl. Electrochem. 39, 233–240. https://doi.org/10.1007/s10800-008-9661-9
García, J.M., Asenjo, A., Velázquez, J., García, D., Vázquez, M., Aranda, P., Ruiz-Hitzky, E., 1999. Magnetic behavior of an array of cobalt nanowires. J. Appl. Phys. 85, 5480–5482. https://doi.org/10.1063/1.369868
Gerhardt, T., Drews, A., Meier, G., 2014. Current-driven domain wall depinning from an anisotropy boundary in nanowires. J. Phys. Condens. Matter 26, 206001. https://doi.org/10.1088/0953-8984/26/20/206001
Gerlach, W., Stern, O., 1922. Der experimentelle Nachweis der Richtungsquantelung im Magnetfeld. Z. Für Phys. 9, 349–352. https://doi.org/10.1007/BF01326983
Glathe, S., Berkov, I., Mikolajick, T., Mattheis, R., 2008. Experimental study of domain wall motion in long nanostrips under the influence of a transverse field. Appl. Phys. Lett. 93, 162505. https://doi.org/10.1063/1.2993329
Grimsditch, M., Vavassori, P., 2004. The diffracted magneto-optic Kerr effect: what does it tell you? J. Phys. Condens. Matter 16, R275. https://doi.org/10.1088/0953-8984/16/9/R01
Grujicic, D., Pesic, B., 2005. Micromagnetic studies of cobalt microbars fabricated by nanoimprint lithography and electrodeposition. J. Magn. Magn. Mater. 285, 303–313. https://doi.org/10.1016/j.jmmm.2004.08.003
Gunnarsson, K., Roy, P.E., Felton, S., Pihl, J., Svedlindh, P., Berner, S., Lidbaum, H., Oscarsson, S., 2005. Programmable Motion and Separation of Single Magnetic Particles on Patterned Magnetic Surfaces. Adv. Mater. 17, 1730–1734. https://doi.org/10.1002/adma.200401880
Harris, M.J., Bramwell, S.T., McMorrow, D.F., Zeiske, T., Godfrey, K.W., 1997. Geometrical Frustration in the Ferromagnetic Pyrochlore ${\mathrm{Ho}}_{2}{\mathrm{Ti}}_{2}{O}_{7}$. Phys. Rev. Lett. 79, 2554–2557. https://doi.org/10.1103/PhysRevLett.79.2554
Hayward, T.J., 2015. Intrinsic Nature of Stochastic Domain Wall Pinning Phenomena in Magnetic Nanowire Devices. Sci. Rep. 5, 13279. https://doi.org/10.1038/srep13279
Henry, Y., Ounadjela, K., Piraux, L., Dubois, S., George, J.-M., Duvail, J.-L., 2001. Magnetic anisotropy and domain patterns in electrodeposited cobalt nanowires. Eur. Phys. J. B - Condens. Matter Complex Syst. 20, 35–54. https://doi.org/10.1007/s100510170283
Hubert, A., Schäfer, R., 1998. Magnetic Domains: The Analysis of Magnetic Microstructures. Springer Science & Business Media.

Isakov, S.V., Raman, K.S., Moessner, R., Sondhi, S.L., 2004. Magnetization process of spin ice in a [111] magnetic field. Phys. Rev. B 70. https://doi.org/10.1103/PhysRevB.70.104418
Ivanov, Y.P., Vázquez, M., Chubykalo-Fesenko, O., 2013. Magnetic reversal modes in cylindrical nanowires. J. Phys. Appl. Phys. 46, 485001. https://doi.org/10.1088/0022-3727/46/48/485001
Jakob, G., Lizon, J.-L., 2010. Advanced high-cooling power 2-stage Gifford-McMahon refrigerator systems. p. 77393I. https://doi.org/10.1117/12.856231
Jamet, M., Wernsdorfer, W., Thirion, C., Mailly, D., Dupuis, V., Mélinon, P., Pérez, A., 2001. Magnetic Anisotropy of a Single Cobalt Nanocluster. Phys. Rev. Lett. 86, 4676–4679. https://doi.org/10.1103/PhysRevLett.86.4676
Jaubert, L.D.C., Holdsworth, P.C.W., 2011. Magnetic monopole dynamics in spin ice. J. Phys. Condens. Matter 23, 164222. https://doi.org/10.1088/0953-8984/23/16/164222
Jeon, S., Malyarchuk, V., Rogers, J.A., Wiederrecht, G.P., 2006. Fabricating three dimensional nanostructures using two photon lithography in a single exposure step. Opt. Express 14, 2300–2308. https://doi.org/10.1364/OE.14.002300
Jiles, D., 2015. Introduction to Magnetism and Magnetic Materials, Third Edition. CRC Press.
Kadowaki, H., Ishii, Y., Matsuhira, K., Hinatsu, Y., 2002. Neutron scattering study of dipolar spin ice ${\mathrm{Ho}}_{2}{\mathrm{Sn}}_{2}{\mathrm{O}}_{7}:$ Frustrated pyrochlore magnet. Phys. Rev. B 65, 144421. https://doi.org/10.1103/PhysRevB.65.144421
Kasuya, T., 1956. A Theory of Metallic Ferro- and Antiferromagnetism on Zener's Model. Prog. Theor. Phys. 16, 45–57. https://doi.org/10.1143/PTP.16.45
Keatley, P.S., 2008. Time-Resolved Magneto-Optical Investigations of Picosecond Magnetisation Dynamics in Arrays of Non- Ellipsoidal Ferromagnetic Nano-Elements. University of Exeter.
Koike, K., 2013. Spin-polarized scanning electron microscopy. Microscopy 62, 177–191. https://doi.org/10.1093/jmicro/dfs092
Ku, J.G., Liu, X.Y., Chen, H.H., Deng, R.D., Yan, Q.X., 2016. Interaction between two magnetic dipoles in a uniform magnetic field. AIP Adv. 6, 025004. https://doi.org/10.1063/1.4941750
Kunz, A., 2009. Field induced domain wall collisions in thin magnetic nanowires. Appl. Phys. Lett. 94, 132502. https://doi.org/10.1063/1.3112577
Kunz, A., Reiff, S.C., 2008. Enhancing domain wall speed in nanowires with transverse magnetic fields. J. Appl. Phys. 103, 07D903. https://doi.org/10.1063/1.2829032
Kuschel, T., Bardenhagen, H., Wilkens, H., Schubert, R., Hamrle, J., Pištora, J., Wollschläger, J., 2011. Vectorial magnetometry using magnetooptic Kerr effect including first- and second-order contributions for thin ferromagnetic films. J. Phys. Appl. Phys. 44, 265003. https://doi.org/10.1088/0022-3727/44/26/265003
Laan, G. van der, 1998. Microscopic origin of magnetocrystalline anisotropy in transition metal thin films. J. Phys. Condens. Matter 10, 3239. https://doi.org/10.1088/0953-8984/10/14/012
Ladak, S., Read, D., Tyliszczak, T., Branford, W.R., Cohen, L.F., 2011. Monopole defects and magnetic Coulomb blockade. New J. Phys. 13, 023023. https://doi.org/10.1088/1367-2630/13/2/023023
Ladak, S., Read, D.E., Branford, W.R., Cohen, L.F., 2011. Direct observation and control of magnetic monopole defects in an artificial spin-ice material. New J. Phys. 13, 063032. https://doi.org/10.1088/1367-2630/13/6/063032
Ladak, S., Read, D.E., Perkins, G.K., Cohen, L.F., Branford, W.R., 2010. Direct observation of magnetic monopole defects in an artificial spin-ice system. Nat. Phys. 6, 359. https://doi.org/10.1038/nphys1628

Lago, J., Blundell, S.J., Baines, C., 2007. μSR investigation of spin dynamics in the spin-ice material Dy 2 Ti 2 O 7. J. Phys. Condens. Matter 19, 326210. https://doi.org/10.1088/0953-8984/19/32/326210

Levis, D., 2012. Two-dimensional Spin Ice and the Sixteen-Vertex Model (Theses). Université Pierre et Marie Curie - Paris VI.

Liu, C.H., 1967. Effective Dielectric Tensor and Propagation Constant of Plane Waves in a Random Anisotropic Medium. J. Math. Phys. 8, 2236–2242. https://doi.org/10.1063/1.1705148

Luo, J.K., Chu, D.P., Flewitt, A.J., Spearing, S.M., Fleck, N.A., Milne, W.I., 2005. Uniformity Control of Ni Thin-Film Microstructures Deposited by Through-Mask Plating. J. Electrochem. Soc. 152, C36–C41. https://doi.org/10.1149/1.1833320

Maruo, S., 2016. Microfluidic Devices Produced by Two-Photon-Induced Polymerization, in: Stampfl, J., Liska, R., Ovsianikov, A. (Eds.), Multiphoton Lithography. Wiley-VCH Verlag GmbH & Co. KGaA, pp. 315–334. https://doi.org/10.1002/9783527682676.ch12

Matsuhira, K., Hiroi, Z., Tayama, T., Takagi, S., Sakakibara, T., 2002. A new macroscopically degenerate ground state in the spin ice compound Dy 2 Ti 2 O 7 under a magnetic field. J. Phys. Condens. Matter 14, L559. https://doi.org/10.1088/0953-8984/14/29/101

McMichael, R.D., Donahue, M.J., 1997. Head to head domain wall structures in thin magnetic strips. IEEE Trans. Magn. 33, 4167–4169. https://doi.org/10.1109/20.619698

McQuarrie, D.A., Simon, J.D., 1997. Physical Chemistry: A Molecular Approach. University Science Books.

Meena, J., Min Sze, S., Chand, U., Tseng, T.-Y., 2014. Overview of Emerging Non-volatile Memory Technologies. Nanoscale Res. Lett. 9, 1–33. https://doi.org/10.1186/1556-276X-9-526

Merzbacher, E., 1998. Quantum Mechanics. Wiley.

Meyer, E., 1992. Atomic force microscopy. Prog. Surf. Sci. 41, 3–49. https://doi.org/10.1016/0079-6816(92)90009-7

MicroChemicals GmbH, 2013. Development of Photoresists.

Mistonov, A.A., Grigoryeva, N.A., Chumakova, A.V., Eckerlebe, H., Sapoletova, N.A., Napolskii, K.S., Eliseev, A.A., Menzel, D., Grigoriev, S.V., 2013. Three-dimensional artificial spin ice in nanostructured Co on an inverse opal-like lattice. Phys. Rev. B 87, 220408. https://doi.org/10.1103/PhysRevB.87.220408

Moessner, R., Sondhi, S.L., 2003. Theory of the [111] magnetization plateau in spin ice. Phys. Rev. B 68. https://doi.org/10.1103/PhysRevB.68.064411

Mougin, A., Cormier, M., Adam, J.P., Metaxas, P.J., Ferré, J., 2007. Domain wall mobility, stability and Walker breakdown in magnetic nanowires. EPL Europhys. Lett. 78, 57007. https://doi.org/10.1209/0295-5075/78/57007

Mueller, P., Thiel, M., Wegener, M., 2014. 3D direct laser writing using a 405 nm diode laser. Opt. Lett. 39, 6847–6850. https://doi.org/10.1364/OL.39.006847

Muñoz, M., Prieto, J.L., 2011. Suppression of the intrinsic stochastic pinning of domain walls in magnetic nanostripes. Nat. Commun. 2, ncomms1575. https://doi.org/10.1038/ncomms1575

Nakatani, Y., Thiaville, A., Miltat, J., 2005. Head-to-head domain walls in soft nano-strips: a refined phase diagram. J. Magn. Magn. Mater., Proceedings of the Joint European Magnetic Symposia (JEMS' 04) 290–291, 750–753. https://doi.org/10.1016/j.jmmm.2004.11.355

Nakatani, Y., Thiaville, A., Miltat, J., 2003. Faster magnetic walls in rough wires. Nat. Mater. 2, 521–523. https://doi.org/10.1038/nmat931

Nanoscribe GmbH, 2017a. 3D printing on the micrometer scale - Nanoscribe GmbH [WWW Document]. URL http://www.nanoscribe.de/en/ (accessed 9.13.17).
Nanoscribe GmbH, 2017b. Photonic Professional GT Technical Manual.
Nasirpouri, F., 2007. Template electrodeposition of magnetic nanowire arrays. Transw. Res. Netw. 37661.
O'Brien, L., Beguivin, A., Fernandez-Pacheco, A., Petit, D., Read, D.E., Cowburn, R.P., 2012a. Magnetic domain wall induced, localized nanowire reversal. Appl. Phys. Lett. 101, 062415. https://doi.org/10.1063/1.4742746
O'Brien, L., Beguivin, A., Petit, D., Fernandez-Pacheco, A., Read, D., Cowburn, R.P., 2012b. Domain wall interactions at a cross-shaped vertex. Philos. Transact. A Math. Phys. Eng. Sci. 370, 5794–5805. https://doi.org/10.1098/rsta.2012.0089
Odom, B., Hanneke, D., D'Urso, B., Gabrielse, G., 2006. New Measurement of the Electron Magnetic Moment Using a One-Electron Quantum Cyclotron. Phys. Rev. Lett. 97, 030801. https://doi.org/10.1103/PhysRevLett.97.030801
O'Handley, R.C., 2000. Modern Magnetic Materials.
Ohgai, T., Enculescu, I., Zet, C., Westerberg, L., Hjort, K., Spohr, R., Neumann, R., 2006. Magneto-sensitive nickel nanowires fabricated by electrodeposition into multi- and single-ion track templates. J. Appl. Electrochem. 36, 1157–1162. https://doi.org/10.1007/s10800-006-9200-5
Ohgai, T., Hjort, K., Spohr, R., Neumann, R., 2008. Electrodeposition of cobalt based ferro-magnetic metal nanowires in polycarbonate films with cylindrical nanochannels fabricated by heavy-ion-track etching. J. Appl. Electrochem. 38, 713–719. https://doi.org/10.1007/s10800-008-9499-1
Okoshi, T., 1965. Demagnetizing Factors of Rods and Tubes Computed from Analog Measurements. J. Appl. Phys. 36, 2382–2387. https://doi.org/10.1063/1.1714495
Osborn, J.A., 1945. Demagnetizing Factors of the General Ellipsoid. Phys. Rev. 67, 351–357. https://doi.org/10.1103/PhysRev.67.351
Ounadjela, K., Ferré, R., Louail, L., George, J.M., Maurice, J.L., Piraux, L., Dubois, S., 1997. Magnetization reversal in cobalt and nickel electrodeposited nanowires. J. Appl. Phys. 81, 5455–5457. https://doi.org/10.1063/1.364568
Parkin, S.S.P., Hayashi, M., Thomas, L., 2008. Magnetic Domain-Wall Racetrack Memory. Science 320, 190–194. https://doi.org/10.1126/science.1145799
Pathak, S., Sharma, M., 2014. Polar magneto-optical Kerr effect instrument for 1-dimensional magnetic nanostructures. J. Appl. Phys. 115, 043906. https://doi.org/10.1063/1.4862908
Pauling, L., 1935. The Structure and Entropy of Ice and of Other Crystals with Some Randomness of Atomic Arrangement. J. Am. Chem. Soc. 57, 2680–2684. https://doi.org/10.1021/ja01315a102
Petit, D., Jausovec, A.-V., Zeng, H.T., Lewis, E., O'Brien, L., Read, D., Cowburn, R.P., 2009. Mechanism for domain wall pinning and potential landscape modification by artificially patterned traps in ferromagnetic nanowires. Phys. Rev. B 79, 214405. https://doi.org/10.1103/PhysRevB.79.214405
Petit, D., Jausovec, A.-V., Zeng, H.T., Lewis, E., O'Brien, L., Read, D., Cowburn, R.P., 2008. High efficiency domain wall gate in ferromagnetic nanowires. Appl. Phys. Lett. 93, 163108. https://doi.org/10.1063/1.3005586
Piao, H.-G., Shim, J.-H., Djuhana, D., Kim, D.-H., 2013. Intrinsic pinning behavior and propagation onset of three-dimensional Bloch-point domain wall in a cylindrical ferromagnetic nanowire. Appl. Phys. Lett. 102, 112405. https://doi.org/10.1063/1.4794823
Porto, S.P.S., 1966. Angular Dependence and Depolarization Ratio of the Raman Effect. JOSA 56, 1585–1589. https://doi.org/10.1364/JOSA.56.001585

Prinz, G.A., 1998. Magnetoelectronics. Science 282, 1660–1663. https://doi.org/10.1126/science.282.5394.1660
Pushp, A., Phung, T., Rettner, C., Hughes, B.P., Yang, S.-H., Thomas, L., Parkin, S.S.P., 2013. Domain wall trajectory determined by its fractional topological edge defects. Nat. Phys. 9, 505. https://doi.org/10.1038/nphys2669
Qi, Y., Brintlinger, T., Cumings, J., 2008. Direct observation of the ice rule in an artificial kagome spin ice. Phys. Rev. B 77, 094418. https://doi.org/10.1103/PhysRevB.77.094418
Ramachandran, P., Varoquaux, G., 2012. Mayavi2: 3D Scientific Data Visualization and Plotting. Astrophys. Source Code Libr. ascl:1205.008.
Ramirez, A.P., Hayashi, A., Cava, R.J., Siddharthan, R., Shastry, B.S., 1999. Zero-point entropy in 'spin ice.' Nature 399, 333–335. https://doi.org/10.1038/20619
Rougemaille, N., Montaigne, F., Canals, B., Hehn, M., Riahi, H., Lacour, D., Toussaint, J.-C., 2013. Chiral nature of magnetic monopoles in artificial spin ice. New J. Phys. 15, 035026. https://doi.org/10.1088/1367-2630/15/3/035026
Ruderman, M.A., Kittel, C., 1954. Indirect Exchange Coupling of Nuclear Magnetic Moments by Conduction Electrons. Phys. Rev. 96, 99–102. https://doi.org/10.1103/PhysRev.96.99
Saha, S.K., Divin, C., Cuadra, J.A., Panas, R.M., 2017. Effect of Proximity of Features on the Damage Threshold During Submicron Additive Manufacturing Via Two-Photon Polymerization. J. Micro Nano-Manuf. 5, 031002-031002-10. https://doi.org/10.1115/1.4036445
Salazar-Aravena, D., Palma, J.L., Escrig, J., 2014. Angular dependence of the magnetic properties of cylindrical nanostructures with wire–tube morphology. Mater. Res. Express 1, 026112. https://doi.org/10.1088/2053-1591/1/2/026112
Salhi, E., Berger, L., 1993. Current-induced displacements and precession of a Bloch wall in Ni-Fe thin films. J. Appl. Phys. https://doi.org/10.1063/1.352611
Scaife, B.K.P., 1989. Principles of dielectrics.
Schatz, P.N., McCaffery, A.J., 1969. The Faraday effect. Q. Rev. Chem. Soc. 23, 552–584. https://doi.org/10.1039/QR9692300552
Schryer, N.L., Walker, L.R., 1974. The motion of 180° domain walls in uniform dc magnetic fields. J. Appl. Phys. 45, 5406–5421. https://doi.org/10.1063/1.1663252
Self, S.A., 1983. Focusing of spherical Gaussian beams. Appl. Opt. 22, 658–661. https://doi.org/10.1364/AO.22.000658
Seo, S.-M., Lee, K.-J., Jung, S.-W., Lee, H.-W., 2010. Controllable chirality switching of a moving domain wall by oblique magnetic field. Appl. Phys. Lett. 97, 032507. https://doi.org/10.1063/1.3467456
Shaker Salem, M., Sergelius, P., M. Corona, R., Escrig, J., Görlitz, D., Nielsch, K., 2013. Magnetic properties of cylindrical diameter modulated Ni 80 Fe 20 nanowires : interaction and coercive fields. Nanoscale 5, 3941–3947. https://doi.org/10.1039/C3NR00633F
Spin-transfer Torque MRAM Technology | Everspin [WWW Document], n.d. URL https://www.everspin.com/spin-transfer-torque-mram-technology (accessed 2.25.18).
Streubel, R., Fischer, P., Kronast, F., Kravchuk, V.P., Sheka, D.D., Yuri Gaididei, Schmidt, O.G., Makarov, D., 2016. Magnetism in curved geometries. J. Phys. Appl. Phys. 49, 363001. https://doi.org/10.1088/0022-3727/49/36/363001
Sulka, G.D., Brzózka, A., Liu, L., 2011. Fabrication of diameter-modulated and ultrathin porous nanowires in anodic aluminum oxide templates. Electrochimica Acta 56, 4972–4979. https://doi.org/10.1016/j.electacta.2011.03.126

Sultan, M., 2013. Experimental and micromagnetic study of magnetisation behaviour in isolated ferromagnetic nanowires (Doctoral). Durham University.
Tan, C.Z., Arndt, J., 1997. Faraday effect in silica glasses. Phys. B Condens. Matter 233, 1–7. https://doi.org/10.1016/S0921-4526(97)80001-T
Teresa, J.M.D., Fernández-Pacheco, A., Córdoba, R., Serrano-Ramón, L., Sangiao, S., Ibarra, M.R., 2016. Review of magnetic nanostructures grown by focused electron beam induced deposition (FEBID). J. Phys. Appl. Phys. 49, 243003. https://doi.org/10.1088/0022-3727/49/24/243003
Thiaville, A., Nakatani, Y., Miltat, J., Suzuki, Y., 2005. Micromagnetic understanding of current-driven domain wall motion in patterned nanowires. EPL Europhys. Lett. 69, 990. https://doi.org/10.1209/epl/i2004-10452-6
Thiele, S., Arzenbacher, K., Gissibl, T., Giessen, H., Herkommer, A.M., 2017. 3D-printed eagle eye: Compound microlens system for foveated imaging. Sci. Adv. 3, e1602655. https://doi.org/10.1126/sciadv.1602655
van Dorp, W.F., Hagen, C.W., 2008. A critical literature review of focused electron beam induced deposition. J. Appl. Phys. 104, 081301. https://doi.org/10.1063/1.2977587
Vansteenkiste, A., Van de Wiele, B., 2011. MuMax: A new high-performance micromagnetic simulation tool. J. Magn. Magn. Mater. 323, 2585–2591. https://doi.org/10.1016/j.jmmm.2011.05.037
Vega, V., Böhnert, T., Martens, S., Waleczek, M., Montero-Moreno, J.M., Görlitz, D., Prida, V.M., Nielsch, K., 2012. Tuning the magnetic anisotropy of Co–Ni nanowires: comparison between single nanowires and nanowire arrays in hard-anodic aluminum oxide membranes. Nanotechnology 23, 465709. https://doi.org/10.1088/0957-4484/23/46/465709
Vernon-Parry, K.D., 2000. Scanning electron microscopy: an introduction. III-Vs Rev. 13, 40–44. https://doi.org/10.1016/S0961-1290(00)80006-X
Walton, S.K., Zeissler, K., Burn, D.M., Ladak, S., Read, D.E., Tyliszczak, T., Cohen, L.F., Branford, W.R., 2015. Limitations in artificial spin ice path selectivity: the challenges beyond topological control. New J. Phys. 17, 013054. https://doi.org/10.1088/1367-2630/17/1/013054
Wang, C.C., Adeyeye, A.O., Singh, N., 2006. Magnetic antidot nanostructures: effect of lattice geometry. Nanotechnology 17, 1629. https://doi.org/10.1088/0957-4484/17/6/015
Wang, R.F., Nisoli, C., Freitas, R.S., Li, J., McConville, W., Cooley, B.J., Lund, M.S., Samarth, N., Leighton, C., Crespi, V.H., Schiffer, P., 2006. Artificial “spin ice” in a geometrically frustrated lattice of nanoscale ferromagnetic islands. Nature 439, 303–306. https://doi.org/10.1038/nature04447
Wanzenboeck, H.D., Hochleitner, G., Mika, J., Shawrav, M.M., Gavagnin, M., Bertagnolli, E., 2014. Mapping of local argon impingement on a virtual surface: an insight for gas injection during FEBID. Appl. Phys. A 117, 1749–1756. https://doi.org/10.1007/s00339-014-8755-y
Welton, J.E., Company, C.O.F.R., 1984. SEM petrology atlas. American Association of Petroleum Geologists.
Wieser, R., Vedmedenko, E.Y., Weinberger, P., Wiesendanger, R., 2010. Current-driven domain wall motion in cylindrical nanowires. Phys. Rev. B 82, 144430. https://doi.org/10.1103/PhysRevB.82.144430
Williams, A., Moruzzi, V., Malozemoff, A., Terakura, K., 1983. Generalized Slater-Pauling curve for transition-metal magnets. IEEE Trans. Magn. 19, 1983–1988. https://doi.org/10.1109/TMAG.1983.1062706
Williams, G., Hunt, M., Boehm, B., May, A., Taverne, M., Ho, D., Giblin, S., Read, D., Rarity, J., Allenspach, R., Ladak, S., 2017. Two-photon lithography for 3D magnetic

nanostructure fabrication. Nano Res. 1–10. https://doi.org/10.1007/s12274-017-1694-0
Wrona, J., Stobiecki, T., Czapkiewicz, M., Rak, R., Ślęzak, T., Korecki, J., Kim, C.G., 2004. R-VSM and MOKE magnetometers for nanostructures. J. Magn. Magn. Mater., Proceedings of the International Conference on Magnetism (ICM 2003) 272–276, 2294–2295. https://doi.org/10.1016/j.jmmm.2003.12.933
X Ke, 2007. Nonmonotonic Zero-Point Entropy in Diluted Spin Ice. Phys. Rev. Lett. 99.
Yan, M., Andreas, C., Kákay, A., García-Sánchez, F., Hertel, R., 2011. Fast domain wall dynamics in magnetic nanotubes: Suppression of Walker breakdown and Cherenkov-like spin wave emission. Appl. Phys. Lett. 99, 122505. https://doi.org/10.1063/1.3643037
Yan, M., Kákay, A., Gliga, S., Hertel, R., 2010. Beating the Walker Limit with Massless Domain Walls in Cylindrical Nanowires. Phys. Rev. Lett. 104, 057201. https://doi.org/10.1103/PhysRevLett.104.057201
Yeh, W.-M., Noga, D.E., Lawson, R.A., Tolbert, L.M., Henderson, C.L., 2010. Comparison of positive tone versus negative tone resist pattern collapse behavior. J. Vac. Sci. Technol. B Nanotechnol. Microelectron. Mater. Process. Meas. Phenom. 28, C6S6-C6S11. https://doi.org/10.1116/1.3518136
Yin, L.F., Wei, D.H., Lei, N., Zhou, L.H., Tian, C.S., Dong, G.S., Jin, X.F., Guo, L.P., Jia, Q.J., Wu, R.Q., 2006. Magnetocrystalline Anisotropy in Permalloy Revisited. Phys. Rev. Lett. 97, 067203. https://doi.org/10.1103/PhysRevLett.97.067203
Yoshinobu Nakatani, Yasutaro Uesaka, Nobuo Hayashi, 1989. Direct Solution of the Landau-Lifshitz-Gilbert Equation for Micromagnetics. Jpn. J. Appl. Phys. 28, 2485. https://doi.org/10.1143/JJAP.28.2485
Yosida, K., 1996. THEORY OF MAGNETISM.: Edition en anglais. Springer Science & Business Media.
Yosida, K., 1957. Magnetic Properties of Cu-Mn Alloys. Phys. Rev. 106, 893–898. https://doi.org/10.1103/PhysRev.106.893
Young, H.D., Freedman, R.A., 2008. University Physics with Modern Physics, 12th ed. Pearson International.
Zeissler, K., Walton, S.K., Ladak, S., Read, D.E., Tyliszczak, T., Cohen, L.F., Branford, W.R., 2013. The non-random walk of chiral magnetic charge carriers in artificial spin ice. Sci. Rep. 3. https://doi.org/10.1038/srep01252
Zhao, Y.-P., Gamache, R.M., Wang, G.-C., Lu, T.-M., Palasantzas, G., De Hosson, J.T.M., 2000. Effect of surface roughness on magnetic domain wall thickness, domain size, and coercivity. J. Appl. Phys. 89, 1325–1330. https://doi.org/10.1063/1.1331065
Zhou, X., Hou, Y., Lin, J., 2015. A review on the processing accuracy of two-photon polymerization. AIP Adv. 5, 030701. https://doi.org/10.1063/1.4916886